NASA CR-161,611

NASA-CR-161611
19810004186

VOLUME I

DEVELOPMENT OF

CO_2 LASER DOPPLER INSTRUMENTATION

FOR

DETECTION OF CLEAR AIR TURBULENCE

FINAL REPORT

10 FEBRUARY 1972 - 27 DECEMBER 1978

ER78-4392-1   September 1979

CONTRACT NAS8-28424

RAYTHEON

RAYTHEON COMPANY
EQUIPMENT DIVISION

VOLUME I

DEVELOPMENT OF

CO_2 LASER DOPPLER INSTRUMENTATION

FOR

DETECTION OF CLEAR AIR TURBULENCE

FINAL REPORT

10 FEBRUARY 1972 - 27 DECEMBER 1978

Prepared for

GEORGE C. MARSHALL SPACE FLIGHT CENTER

NASA

HUNTSVILLE, ALABAMA 35812

By

C. E. Harris

A. V. Jelalian

RAYTHEON COMPANY
Equipment Division
Equipment Development Laboratories
Electro-Optics Systems Laboratory
Wayland, Massachusetts 01778

N81-12697 #

Page intentionally left blank

TABLE OF CONTENTS

TABLE OF CONTENTS (Continued)

TABLE OF CONTENTS (Continued)

TABLE OF CONTENTS (Continued)

LIST OF ILLUSTRATIONS

LIST OF ILLUSTRATIONS (Continued)

LIST OF ILLUSTRATIONS (Continued)

SECTION 1
INTRODUCTION AND SUMMARY

1.1 GENERAL

This final report describes the activities performed by Raytheon Company from February 1972 to December 1978 under NASA Contract NAS8-28424 for the modification, construction, test and operation of an advanced airborne CO_2 laser Doppler system for detecting clear air turbulence (CAT). The earlier instrument, which established the current program, was developed by Raytheon under NAS8-24742, 6 June 1969, and is fully described in Raytheon Publication ER72-4243, May 1972. This report covers the second-generation CAT program and those auxiliary activities required to support and verify such a first-of-a-kind system: aircraft interface, ground and flight verification tests, data analyses, and laboratory examinations. Study efforts which were contributions to the state-of-the-art of CAT technology or which are of special interest to those working in CAT-related technologies have been made a part of this report.

1.2 THE CAT SYSTEM

1.2.1 THE PROTOTYPE SYSTEM

Using laser Doppler heterodyne techniques, Raytheon developed a research system (see Figure 1-1) which detected and measured the range and intensity of CAT events. This prototype instrumentation, described in Raytheon Publication ER72-4243, can be described in terms of its two major subsystems - transmitter and receiver. The transmitter is composed of a CO_2 laser oscillator, modulator, folded laser amplifier, heterodyne recombination optics, and external optics. The receiver consists of a detector, signal processors, and signal display and recording apparatus. The system operates by measuring the Doppler spectrum of laser light backscattered from naturally suspended aerosols in the atmosphere. If the atmospheric velocity is uniform, all aerosols move at the same velocity, resulting in a narrow spectrum; while in the case of a turbulent atmosphere, a variety of different velocity components are encountered and a broad Doppler spectrum is
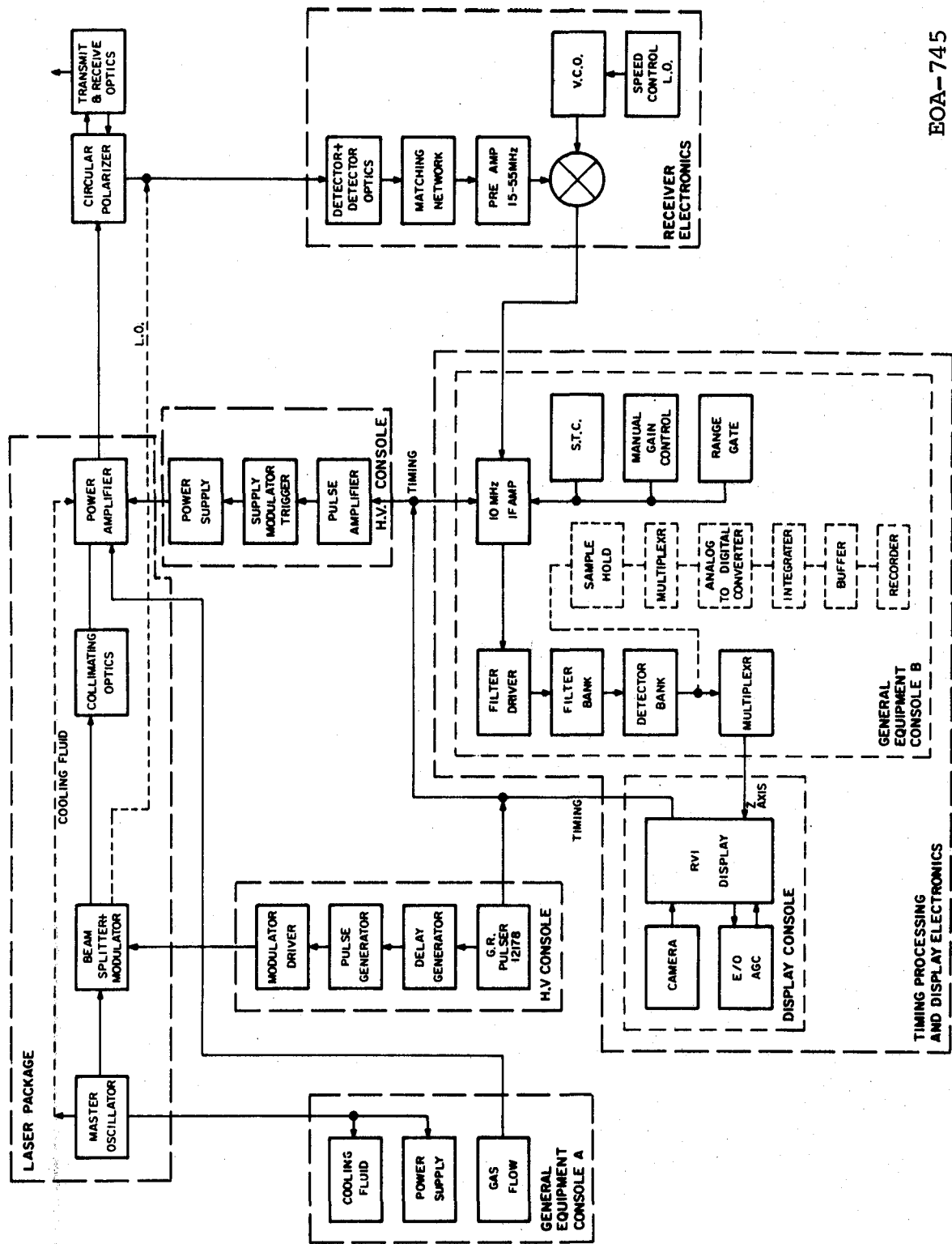
Figure 1-1. System Block Diagram

observed. The Doppler spectrum is obtained by heterodyning with a stable CW reference laser. The spectra, thus obtained, are displayed in real time and recorded on digital tape. This system is described in Section 2.1.

1.2.2 THE OFFSET SYSTEM

As originally configured, the CAT system employed a master oscillator-power amplifier design with the CW master oscillator serving as the local oscillator. In order to provide directional sense in ground test operations and to simulate flight conditions, the system was modified by installing a second CW laser oscillator offset by 10 MHz (see Figures 1-2 and 1-3). Reconfiguration was accomplished by remounting optical components and injecting a variable electronic mixing signal to control the Doppler signal within a specific IF band. This offset system is described in Section 2.2.

1.3 ORGANIZATION OF THIS REPORT

This report is organized in such a way as to reflect the evolution of the CAT system to its present configuration.

The system was designed in 1970 and tested in 1972 and 1973. Subsequently, modifications were made, of which the most significant was the addition of an offset local oscillator. During the modifications, many tests, measurements, and analyses were performed in order to establish the final configuration. To provide a self-contained system description, both the initial and final configurations are addressed in Section 2 with 2.1 describing the original system and 2.2 the additions and modifications.

Section 2 of this report describes the instrumentation of the CAT system - the modules, interrelation of components, operational modes and performance characteristics. Section 3 describes the system test and evaluation programs in laboratory measurements which led to the final configuration. Other sections detail specific contractual tasks: Section 4, signal processing and atmospheric analyses; Section 5, aircraft interface; Section 6, site selection activities; Section 7, ground verification tests; Section 8, field
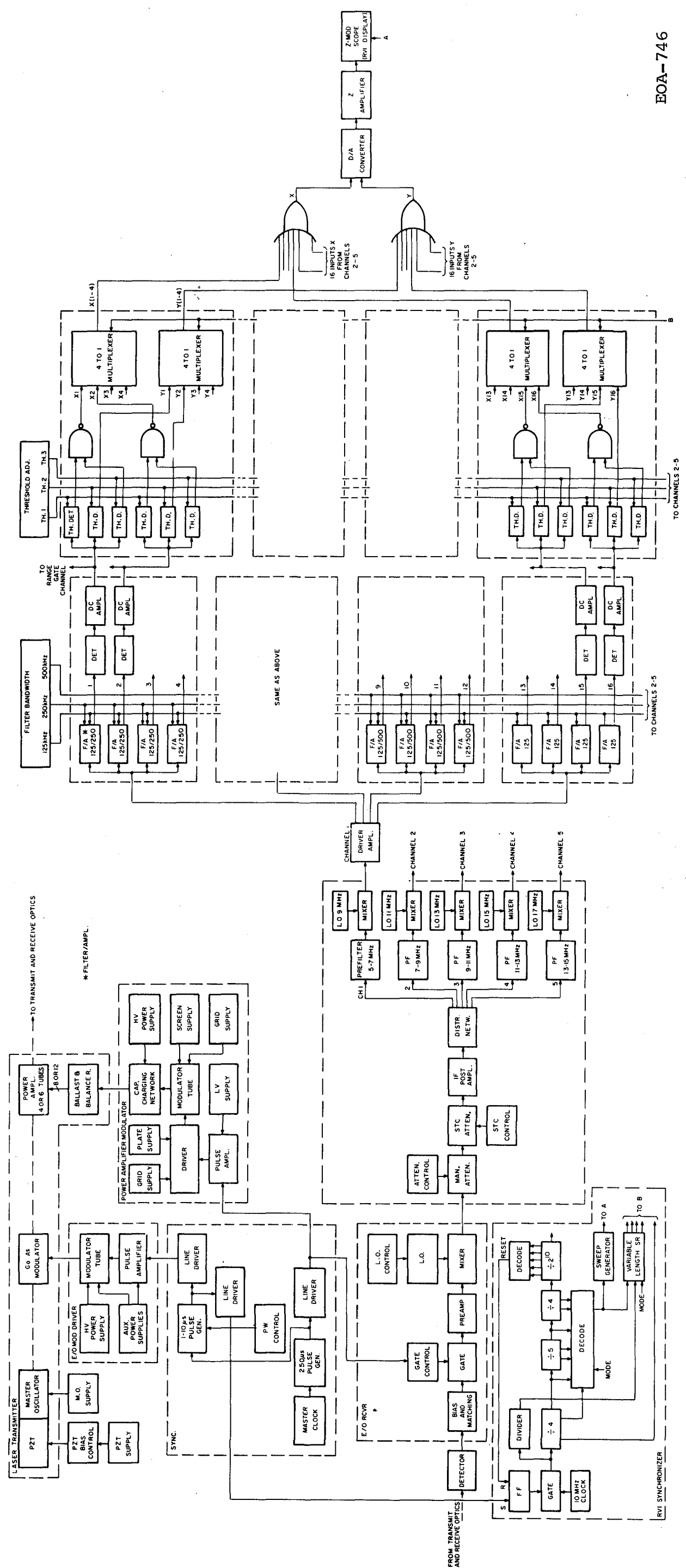
Figure 1-2. Updated System Block Diagram

EOA-746

1-4
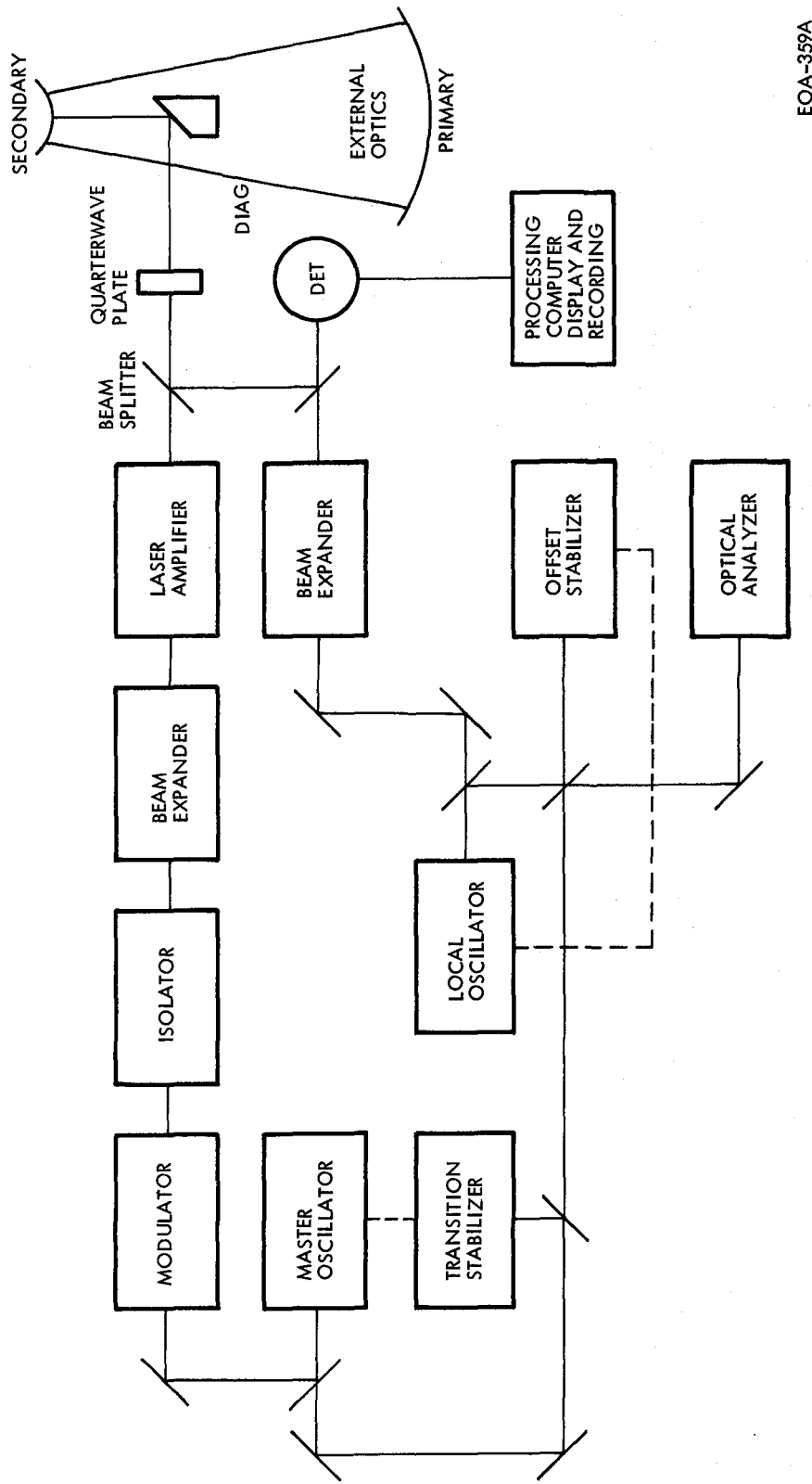
Figure 1-3. Offset CAT Instrument Optical Schematic

EOA-359A

tests - offset system; Section 9, flight tests and verification; and Section 10, flight data analyses.

Volume II of this report contains as appendices the studies referenced in this volume and descriptions of studies and investigations of significance to those in CAT-related areas. One appendix also contains an abbreviated set of ground operating instructions and alignment procedures for the offset system. These appendices are not essential to an understanding of the system operating principles or concepts, but are intended as complete documentation of topics discussed briefly or incompletely in Volume I.

SECTION 2

SYSTEM DESCRIPTIONS

2.1 INTRODUCTION

This section is presented in two parts. The first briefly
describes the earlier CAT system designed in 1970 and flight-tested
in 1972 and 1973. It is presented as a basis for understanding the
current configuration developed in 1976 and identified as the CAT
System with offset local oscillator. It is discussed in Section 2.3.
Because the CAT program is an ongoing effort, a detailed discussion
of the programs, tests, experiments, and examinations leading to
this configuration of the system is postponed until Section 3.

2.2 THE BASIC SYSTEM

2.2.1 CAT SYSTEM OPERATION

The basic CAT system transmitter can be considered in a master-
oscillator power-amplifier (MOPA) configuration (Figure 2-1) wherein
coaxial transmit and receive optics are used for homodyne detection
of optical backscatter from atmospheric aerosols. In operation, the
output of a CW master oscillator is passed through a switch operating
on the transverse electro-optical effect. The output of this switch
is a series of pulses with widths ranging from 2 to 10 microseconds
at repetition rates up to 200 pulses per second. This pulsed beam is
expanded in diameter to approximately 1.5 centimeters and directed
into a pulsed CO_2 amplifier. The pulses are amplified by more than
30 dB within the amplifier. Exiting from the amplifier, the beam
passes through a germanium Brewster plate set to pass the pulses,
through a cadmium-sulphide quarter-wave plate which converts the
linear polarization of the pulsed beam to circular, and into the
atmosphere by way of a 12 inch diameter telescope. The returning
signals follow the reverse path through the telescope, and through
the quarter-wave plate which linearly polarizes the beam making it
orthogonal to the amplifier output beam. The signal beam is then
reflected from the Brewster plate and down to the recombining beam-
splitter where the signal and the local oscillator beam (derived from
the master oscillator beam) are combined and focused on the detector.

2-1
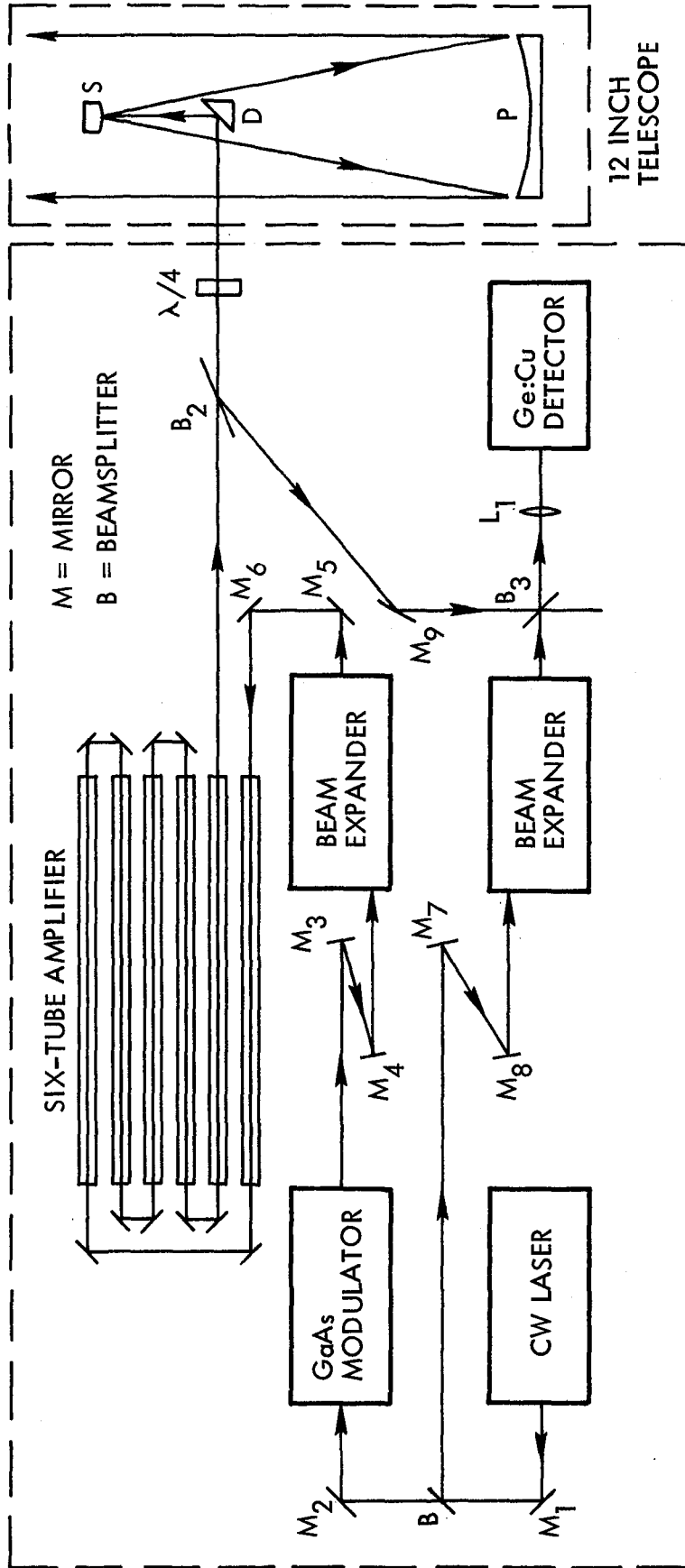
Figure 2-1. CAT System Master-Oscillator Power-Amplifier Arrangement

EOA-747

The homodyned electrical output of the detector is amplified and heterodyned to an intermediate frequency (IF). The IF signal is then amplified and analyzed by a filter bank appropriately matched to the pulse length. The output of each filter is individually detected and displayed. This display is in the form of a range velocity indication (RVI) where velocity is plotted as a function of range, and a record channel display which indicates the velocity information in a single range cell.

The basic system components are described below.

2.2.2 TRANSMITTER COMPONENTS

2.2.2.1 Master Oscillator

The master oscillator in the basic system is a Honeywell CO_2 laser, later modified by Raytheon to permit user replacement of the fill gas. The unit features an adjustable rear reflector and ZnSe intra-cavity Brewster's angle polarizer. The output beam is in the TEM_{00} mode. The unit operates on several P-lines as well as R-lines with the specific signature depending upon the condition of the gas fill. Output power is in the range of 7 to 8 watts. Problems with and improvements to this original master oscillator are discussed in Section 3.3.7.

2.2.2.2 Optical Modulators

The two optical modulators each consist of two voltage controlled electro-optic crystals of gallium arsenide, 7 x 7 x 40 mm, located between two polarizing elements. The beam diameter of this point is about 7 mm, so that truncation occurs at the $1/e^2$ diameter. When a voltage is applied to the gallium arsenide, the relative phase of the two polarization components of light passing through the crystal is changed. If a sufficiently high voltage is applied, the phase difference becomes equal to 180° and the polarization of the light passing through the crystal is altered by 90°. Since the two polarizing elements in the first modulator are crossed under the zero voltage condition, no energy is passed; while under the 180° or half-wave condition, all the energy is passed. Under operation, a 2 to 10 microsecond

high voltage pulse is applied to the modulator crystal which results in an optical pulse of the same length. The second modulator is normally transmissive and is switched off at the end of the pulse to suppress ringing effects associated with switching the first one.

2.2.2.3 Beam Expander

An off-axis parabolic beam expander is used in the basic system to increase the laser beam diameter to the 1.5 centimeters required for the amplifier. An off-axis design was used to reduce scattering back into the amplifier. The beam expander is provided with a carrier for a spatial filter if necessary for very high gain conditions.

2.2.2.4 CO_2 Amplifier

The amplifier consists of six tubes, each containing 3/4 meter of discharge in a CO_2 flowing gas mix. The discharge, driven by a high-voltage DC power supply fed to the amplifier through a high-voltage modulator, is longitudinal and split into two portions of 3/8 of a meter each in order to reduce the high voltage requirements. The discharge tubes provide a gain of approximately 6 dB per tube or a total of approximately 36 dB of small-signal gain.

2.2.2.5 Output Telescope (Beam Expander)

The output telescope is a 12-inch (30.5 cm) diameter f/3 afocal Newtonian-Cassegrain telescope configuration. It features Invar construction to minimize focus variations due to temperature changes, and Cer-Vit optical elements.

2.2.2.6 Heterodyne Detector

In the course of the CAT program, several types of infrared detectors were used. The original detector was a copper-doped germanium detector requiring helium cooling. The second detector was a SAT HgCdTe photovoltaic detector using nitrogen cooling; PbSnTe detectors were evaluated. Laboratory measurements on these detectors showed that with the doped germanium detector a coherent quantum efficiency of 10% was achieved. Abbreviated measurements of the SAT HgCdTe detector indicated a quantum efficiency on the order of 25 - 30% which, together with the expected 3 dB improvement in noise characteristics, would have resulted in a 7 dB improvement over the germanium. The HgCdTe detectors have been the most consistently employed in both systems. The characteristics of the currently used detector are discussed in detail in Section 3.3.6.

2.2.3 RECEIVER COMPONENTS

2.2.3.1 IF Amplifier and Sensitivity Time Control

The IF amplifier consists of a voltage controlled attenuator followed by five stages, each stage providing a 10 dB gain. A step attenuator precedes the amplifier so that signals larger than the 6 to 22 dB range used may be accommodated.

The sensitivity time control varies signal attenuation as a function of time, or equivalently, range. This attenuation compensates for the change in strength of the collected optical signal as a function of range so that the average signal intensity is range (time) independent. The sensitivity time control is a function generator, which approximates a function with ten straight lines, with the slope of each line segment adjustable.

2.2.3.2 Filter Bank

The filter bank consists of five prefilter amplifiers, mixers, local oscillators, and driver amplifiers feeding to five groups of sixteen comb filter amplifiers and detectors (see Figure 2-2). Briefly, the 5 - 15 MHz signal bandwidth is divided into five 2 MHz channels by the prefilters with each 2 MHz section of the original signal spectrum heterodyned to a common 2 - 4 MHz spectrum. The narrow band comb filters then divide each of these 2 MHz bands into the proper number of channels depending on the transmitted pulse width; i.e., sixteen 125 kHz bands; eight 250 kHz bands; or four 500 kHz bands. Thus, the entire 5 to 15 MHz band is divided into 80, 40 or 20 narrow bands.

2.2.3.3 RVI Display

Each filter in the filter bank can be sampled at time intervals equal to the reciprocal of the filter's bandwidth. The signal from successive samples, taken at time intervals $\Delta \tau$ arises from portions of the atmosphere located at distances displayed by $c \Delta \tau/2$. A series of samples gives the velocity distribution over all ranges within the system detection capability. Thus, all the data required to present the velocity distribution in the path of the aircraft at all ranges are available.

EOA-748

Figure 2-2. Filter Bank, Block Diagram

From IF Amp 5-15 MHz (See Figure 1-2)

The function of the RVI is to display the data from the filter bank. The vertical axis represents velocity, the horizontal axis - range. (In other words, each individual filter corresponds to a specific y coordinate while each time sample is represented by an x coordinate.) Within a time $\Delta \tau$, equal to 1/B, all of the filters in the bank are sampled and displayed on a vertical line on the RVI. The filters are sampled again during the next $\Delta \tau$ interval and portrayed on an adjacent vertical line. This procedure continues from the minimum range, determined by switching transients to the maximum, limited by the minimum detectable signal.

The RVI is a Tektronix R453, with a long-persistence phosphor. The phosphor decay time is significantly longer than the time between pulses, so the effects of several pulses ($\sim$ 60) are integrated on the RVI screen.

2.2.3.4 Record Channel

The 80 filter bank outputs are sampled at a time corresponding to a specific range in front of the aircraft. These 80 signals are then multiplexed onto one line. Five 16:1 multiplexers and a 5:1 multiplexer comprise the 80:1 multiplexer. The multiplexed output is converted to digital format and fed to a digital video integrator where the 80 signals are integrated for 50 periods. The integrated samples are dumped into a buffer which reads them onto the tape during the next fifty periods. The digital data are recorded in PCM format on one track with other tracks free for analog signals.

A Tektronix R422 scope is included to monitor the output of the record channel with viewing capability before or after integration, and a 14 track Ampex tape recorder is employed for recording the integrated data in PCM format along with time codes and auxiliary aircraft data.

2.3 THE CAT SYSTEM WITH FREQUENCY OFFSET

The modifications made in 1976 to the basic system described in 2.2 can be seen from Figure 2-3. These modifications are the net gain from the tests, evaluations, and examinations described in Section 3, Evaluation and Redesign Program.
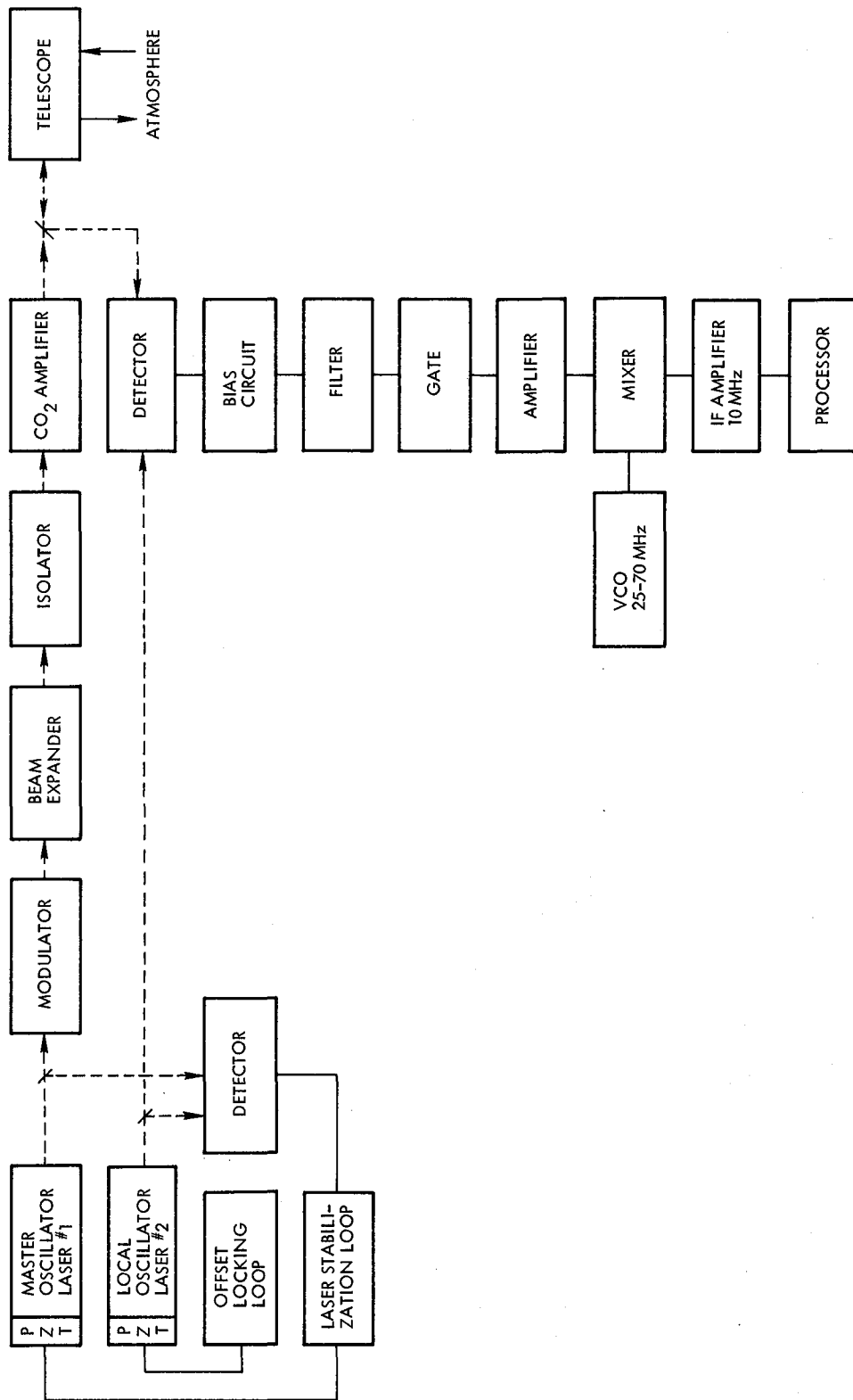
Figure 2-3. Offset System Block Diagram

EOA-749A

2.3.1 OFFSET LOCAL OSCILLATOR

The purpose of the offset local oscillator is to provide a means of determining the directional sense of the Doppler target with respect to a ground operated CAT system. Such a capability is especially important in measurements of complex storm structures in which both receding and advancing components are present, and in addition, in giving the ground based system the opportunity to evaluate phenomena under system conditions simulating aircraft forward motion. The offset local oscillator is a separate local oscillator laser installed in the system and locked to a frequency offset from the transmitter by a fixed amount. This scheme requires a second laser in the system, a locking detector, an interferometer designed to provide a local oscillator and a means of comparing oscillator frequencies, and a locking loop.

The laser will be discussed followed by the interferometer, locking detector, and locking loop.

2.3.1.1 Local Oscillator Laser

The local oscillator used in the offset system is a Sylvania Model 941 CO_2 laser with a PZT adjustable cavity. The first laser when first received had the following characteristics:

Output Power	2.2 – 3.1 watts depending upon transition; Maximum power on P(20)
Signature	$00^{\circ}1 - 10^{\circ}0$, R(20) – 10.25 μm
	R(24) – 10.22 μm
	R(26) – 10.21 μm
	P(18) – 10.57 μm
	P(20) – 10.59 μm
	P(22) – 10.61 μm
Power Stability	Better than 3% over one hour after 30 minute warm-up period
Beam Parameters	Diameter $(1/e^2)$ = 3.8 mm Divergence $(1/e^2)$ = 3.8 mrad
Beam Steering	Not detectable. Estimated to be less than 10% of beam divergence.

2.3.1.2 Offset Laser Interferometer

The offset laser interferometer has two functions: first, it provides a local oscillator for the receiver; and secondly, it combines a portion of the master oscillator and a portion of the local oscillator beams for detection by the locking detector whose output is used to drive the locking loop which stabilizes the offset frequency at 10 MHz.

An important component in the interferometer is the local oscillator attenuator which is located in front of the local oscillator beam expander in a position such that both the master oscillator LO and the offset LO passes through it before entering the beam expander. This attenuator consists of a half-wave plate and a wire-grid polarizer. Rotation of the half-wave plate rotates the polarization of the beam entering the polarizer, thus varying the attenuation of the local oscillator beam without altering its polarization.

2.3.1.3 Locking Detector

The locking detector is used to detect the beat frequency between the local oscillator and the master oscillator and provide this signal to the locking loop. Because of the relatively large powers of both beams available to this detector, it is not necessary that it be as sensitive as the receiver detector materials tested for use in this detector. A pyroelectric detector was chosen for this component because of its large power handling capability which relates directly to heterodyne sensitivity.

2.3.1.4 Locking Loop

This section briefly describes the principle of a locking loop. A block diagram of the locking loop incorporating the lasers and locking detector is shown in Figure 2-4.

The transmitter laser (Laser #1) is the frequency reference which the loop tracks. The local oscillator (Laser #2) is the tuned element. Since the two lasers are offset in frequency in the RF range, an optical detector is used to detect the heterodyned outputs of the lasers. The output of this device is the beat frequency of the two lasers.
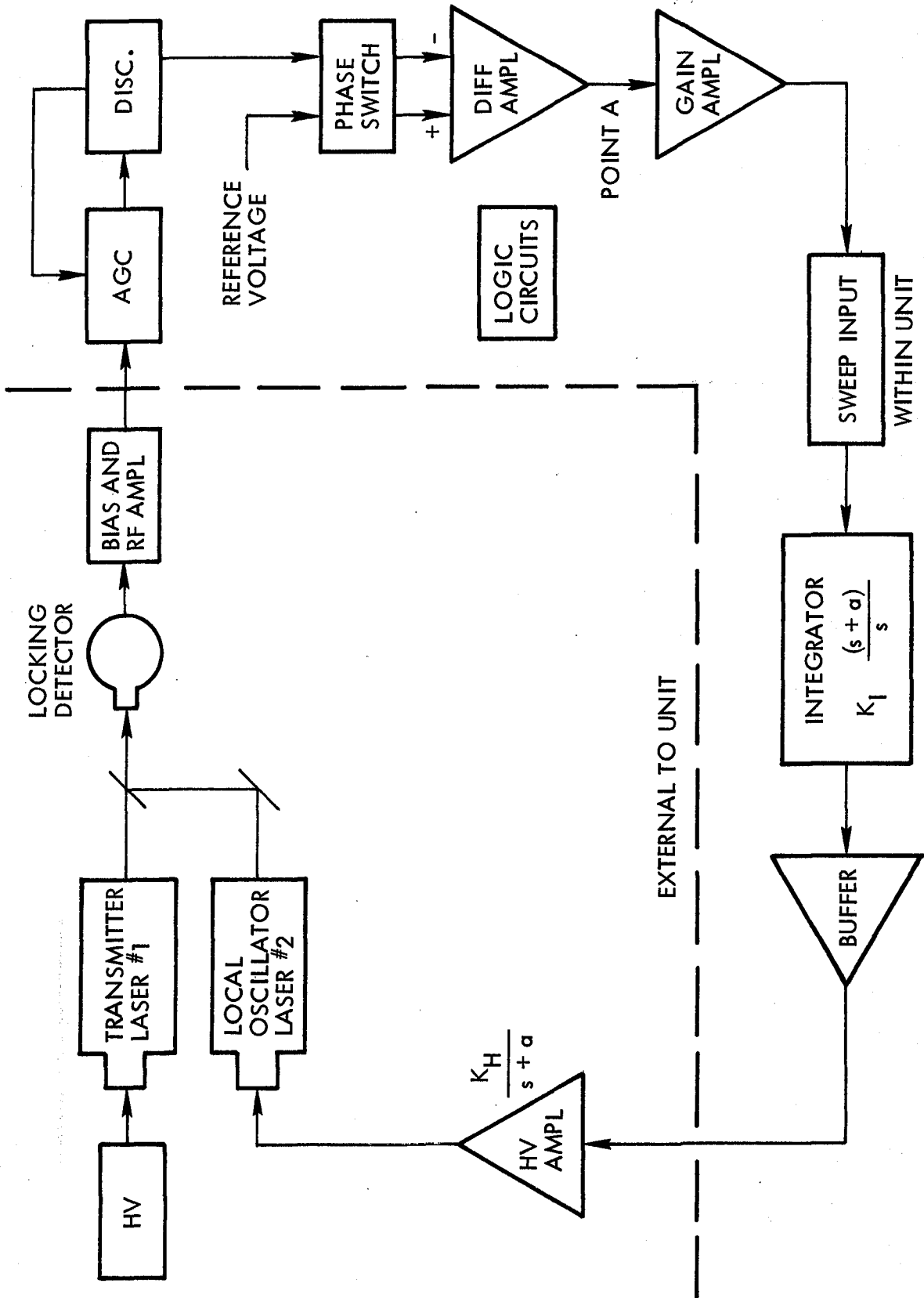
Figure 2-4. Locking Loop Description

EOA-750A

2-11

The RF signal is amplified and fed into an AGC and then a discriminator. The AGC holds the amplitude approximately constant while the discriminator converts the RF signal to a DC level proportional to the frequency of the latter.

The reference is a DC voltage corresponding to the frequency at which the two lasers are to lock. Point A should have 0 volts when the system is locked. When there is drift or some other frequency change on either laser, a voltage proportional to the frequency error is generated. The phase switch exchanges the reference and the discriminator outputs to the differential amplifier and they are subtracted by the differential amplifier. In one position, an increase in the discriminator results in an increasing error voltage at point A. In the other, an increasing discriminator decreases the error voltage at point A.

The error voltage is amplified by the gain amplifier (K_g) and enters the sweep switch. When locked, the error voltage passes into the integrator. When sweeping, a sweep current is injected into the integrator which produces a sweeping voltage output. When locked, the error voltage appears across a resistor producing an error current which is integrated. The integrator feeds integrated error voltage to the output buffer. This produces a low-impedance output to drive a high-voltage amplifier. The high-voltage amplifier drives the PZT of laser 2. This adjusts the frequency of laser 2 and, therefore, its heterodyne frequency relative to laser 1. This forms a frequency locked loop similar to a "tracker" in which the frequency generating elements are lasers instead of electronic oscillators. The logic circuits control lock, unlock and sweep functions.

2.3.2 ELECTRO-OPTIC MODULATOR

The principal problem with the basic system electro-optic GaAs modulator was the high reflection value of the AR coatings and the truncation of the beam by the seven-millimeter crystal aperture.

Difficulties were also found in using a four crystal modulator in the flight B CAT test flights where the primary problems appeared to be of correct orientation of all four crystals, or with residual birefringence in some of the crystals. The improved electro-optic modulator includes increased aperture size, better AR coatings on the crystal faces, and modification of the modulator to operate with only two crystals rather than four (see Section 3.3.9.1).

2.3.3 HALF-WAVE PLATE

In the course of tests on the transmitter (Section 3.1) it becomes obvious that it would be advantageous to be able to align the system with a CW CO_2 laser beam. This had been done in some cases by rotating the output polarizer of the electro-optical modulator or by removing the input polarizer and placing a half-wave plate before the modulator to rotate the laser polarization to match the output polarizer. In returning the system to its operating configuration, however, both of these methods resulted in misalignment. To overcome this problem, a half-wave plate was incorporated in a carrier which could be slid into the modulator housing between the input polarizer and the first modulator crystal and which rotated the polarization of the laser beam so that it passed through the modulator with the correct polarization when the modulator was not being pulsed.

2.3.4 BEAM EXPANDERS

The first beam expanders were designed before the characteristics of the master oscillator could be checked. Using information provided by the master oscillator vendor, the original expander design called for 2.5 times expansion using a 4.0 cm focal length mirror at the location of M_1 shown in Figure 2-5. This design was based on a 6 mm diameter MO beam. As it turned out, the beam was actually 8 mm diameter, forcing the use of a 5 cm M_1 to maintain the correct output diameter. The holes bored in the body of the beam expander were located for the geometry of 2.5 times expansion. Changing the focal length of M_1 forced the entering beam to strike M_1 lower, closer to the edge, in order for the reflection to reach M_2. To adjust for this, the body

2-13

17.5 mm offset

57 mm diameter

22 mm diameter

.25

1 inch

EOA-751
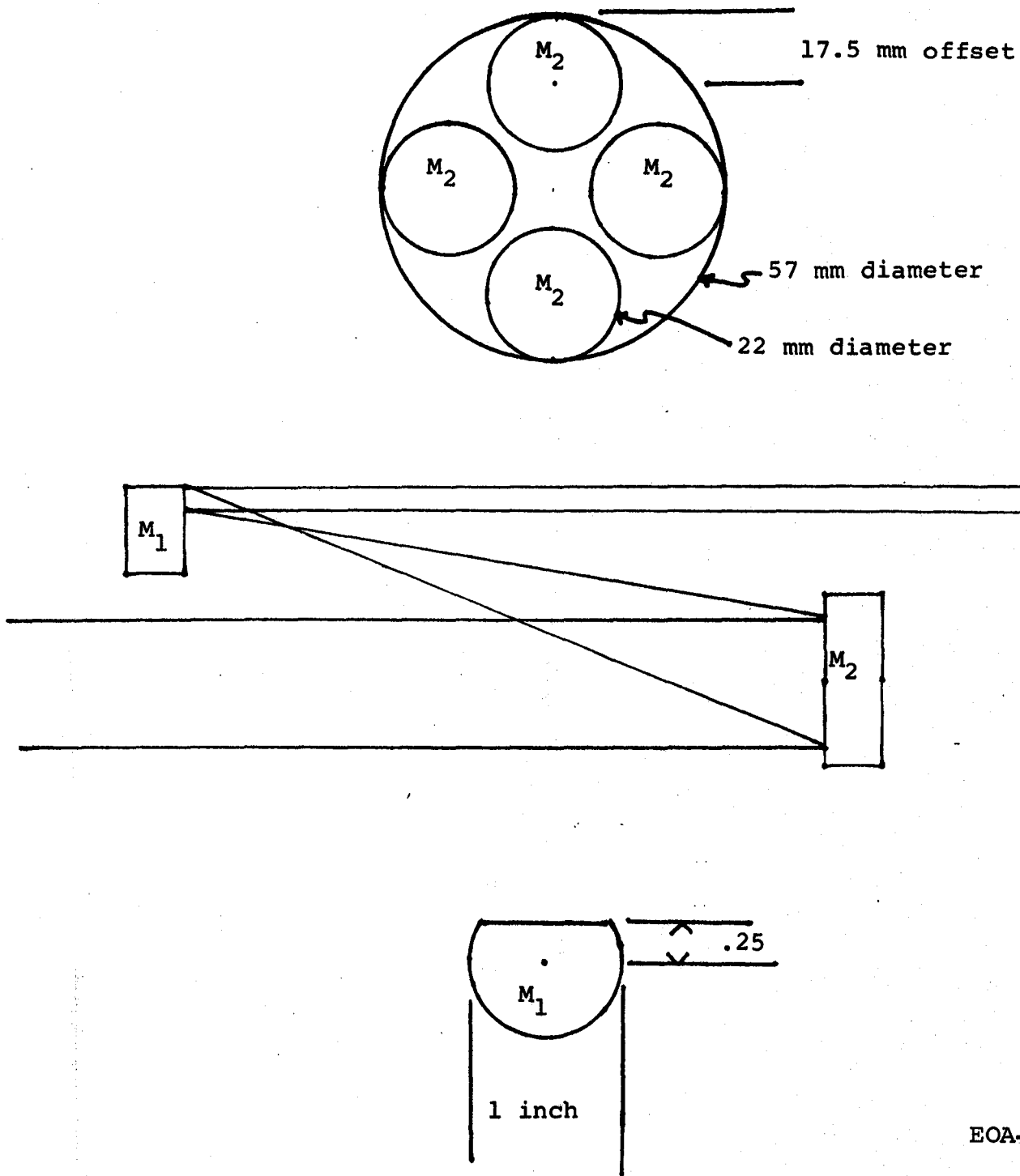
Figure 2-5. Beam Expander Mirror Geometry

had to be bored out with a hole 9 mm in diameter closer to the mounting surface than the original hole.

The Gaussian beam on entry into the entrance bore had a measured diameter of 8.5 mm at its $\frac{1}{e^2}$ points. This means that the beam was clipped at points slightly larger than this diameter when the beam travels exactly on center down the bore. However, it was discovered that in order for the axes of both mirrors to be common and have the exiting beam leave on its proper axis, the entering beam had to be sent in 1.61 mm below the axis, closer to the mounting surface. No elongation of the expanded beam was noticed.

When the beam is expanded two times, an output beam of 17 mm diameter was derived at the $\frac{1}{e^2}$ points, while the output bore had a diameter of 16.6 mm which contributed to the beam clipping and degradation. M_1 had about 3.9 mm clearance from its edge to the axis of the incoming beam and this was not enough for unclipped reflectance of the beam; therefore, the new M_1 was increased in diameter, a new mounting made, and a new input mirror installed to correct the problems in the transmitter beam expander.

2.3.5 MIRRORS

It was found in lab tests that the mirrors external to the amplifier showed signs of corrosion to the degree that the gold reflecting surface had been perforated in many places. Mirrors internal to the amplifier showed signs of degradation in areas masked by the mount. This could be due to optical erosion by the beam, by charged particles in the discharge, or by the ultra-violet discharge. It was also found that in the case of mirrors contaminated by oil or dust particles, effective cleaning was not possible on soft gold reflective coatings.

As a result, new types of mirrors were specified in all locations within the redesigned system. These mirrors used multi-layer dielectric enhanced metallic coatings on silicon substrates. Considerable experience in the last several years with this type of mirror under field conditions has shown no measurable coating degradation. To the degree possible, these mirrors approach military standards for adhesion

abrasion and water exposure, but at this time no manufacturer has met these abrasion and water exposure specifications.

2.3.6. DETECTOR/RECEIVER

2.3.6.1 Detector

A HgCdTe detector manufactured by Honeywell, Electro-Optics Center, replaces the photoconductive copper-doped germanium detector used in the early tests. The detector specifications are:

Material	Photovoltaic HgCdTe
Operating Wavelength	10.6 μ
Quantum Efficiency	$\geq$ 40%
Bandwidth	$\geq$ 80 MHz
D* (10.6 μ)	$\geq$ 5 x 10^9 cm Hz 1/2 Watt
Shunt Resistance	$\geq$ 100 Ω
Series Resistance	$\leq$ 20 Ω
Dimension of Active Area	0.25 mm x 0.25 mm $\pm$ 10%
Contact	Cryogenic Associates IR-13 with SMA bulkhead connector
Window	BaF_2

With the increased quantum efficiency and lower noise figure, this detector provides a 7 dB increase in performance over the CuGe detector at low frequencies and a slightly greater increase at frequencies above the 8 MHz cut-off frequency of the CuGe detector.

2.3.6.2 Receiver Electronics

The receiver for the offset system is designed around the characteristics of the HgCdTe detector and provides shot noise limited operation for maximum useful sensitivity and dynamic range for the signal processor. The offset system has two modes of operation (base-band and offset) selectable by switching filters. Figure 2-6 is a block diagram of the receiver system.

The HgCdTe photovoltaic detector has an impedance of approximately 200 - 1000 Ω matched to the receiver input by a bias circuit which
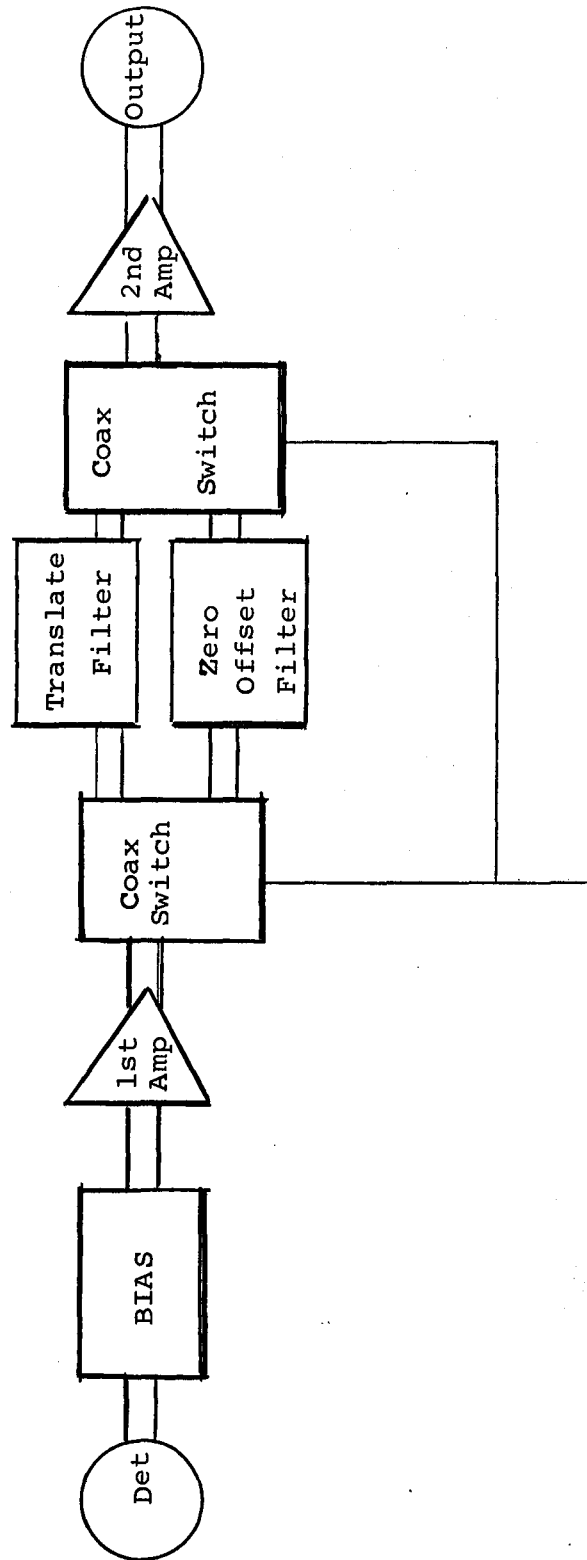
Figure 2-6. Receiver Block Diagram

EOA-752

also supplies the optimum bias current and voltage for the range of local oscillator power used. These parameters vary from detector to detector and must be properly set to produce maximum signal-to-noise ratio.

The first amplifier is important both for S/N ratio and dynamic range. A low noise high-dynamic range amplifier is used here with a gain adequate to raise the detector shot noise above Johnson and amplifier noise, but small enough that large spurious signals do not cause it to saturate. The bandwidth is approximately from 200 kHz to 100 MHz to accommodate both modes.

The second amplifier provides most of the gain, since the filters following the first amplifier attenuate out-of-band interference.

The two coax switches select the appropriate filter for the mode by using either the translate filter or the zero offset filter. The translate filter combines a bandpass function with a stopband function around the modulator frequency to remove feedthrough and harmonic products. This is used whether the acousto-optic modulator or the offset locking loop is used. The high pass filter rejects the 1/f noise which becomes significant below 1 MHz, while the stopband filter attenuates scattering and feedthrough around the modulator drive frequency.

The zero offset filter is a simple 100 kHz high-pass filter for eliminating as much 1/f and supply ripple noise as practical while keeping the low frequency response adequate.

2.3.7 TELESCOPE MODIFICATION

A significant problem resulted from the backscatter of radiation by the telescope secondary mirror into the amplifier. This feedback caused the amplifier to behave somewhat as an independent oscillator and spontaneously emit optical pulses prior to modulator switching. In the original telescope design, an attempt was made to prevent this problem by boring a hole in the center of the 45° plane mirror which

directs the beam to the secondary mirror. It has since been determined that because of the small size of this hole, the optical field filled in and the feedback factor was not significantly affected by the bored hole.

It was found experimentally, however, that a small blackened ball located in front of the secondary mirror would reduce the backscatter by an order of magnitude. This approach was used and found to provide sufficient reduction when combined with the isolator and master oscillator frequency chirper.

2.3.8 PZT HV POWER SUPPLY

The PZT HV power supply provides a linear voltage control from 0 to 2000 V to the PZT crystal. This control enables an operator to manually tune the PZT over its entire range, and set the CAT laser to a desired operating point. The voltage is adjustable by means of a front panel potentiometer connected to a digital counting dial displaying the operating voltage. The HV control network is shown in Figure 2-7.

The manner in which the control circuit operates is to regulate the DC input voltage at + 24 VDC to reduce the effects of source voltage irregularities. After this the + 24 VDC passes to a transistor control network that linearly adjusts the DC input voltage to a small modular HV power supply. The power supply is connected to the PZT and to a fixed resistive load for better overall performance. As the input to the HV power supply is varied, its output voltage changes in a linearly proportional manner. In other words, E_{out} is equal to a constant times E_{in}. This drives the PZT crystal directly for the desired HV control tuning.

2.3.9 OFFSET SYSTEM OPTO-MECHANICAL DESIGN

The design and fabrication of the offset system has been completed. The opto-mechanical design is shown in Figures 2-8 and 2-9. A Sylvania 941S-PZT laser provides the local oscillator beam through an attenuator which can be varied over a 100:1 range. A portion of the laser output is mixed with an attenuated beam from the Honeywell master oscillator
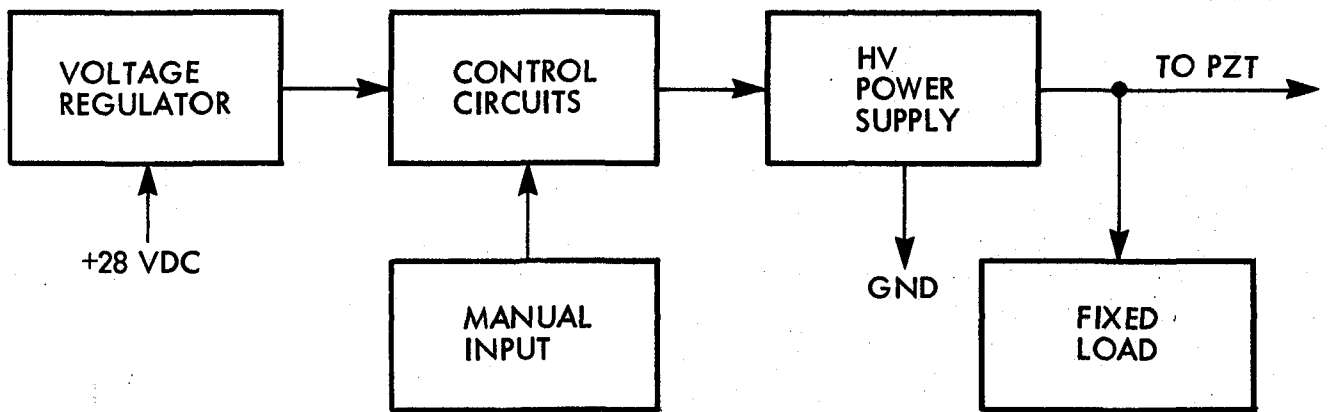
Figure 2-7. PZT HV Control - Block Diagram
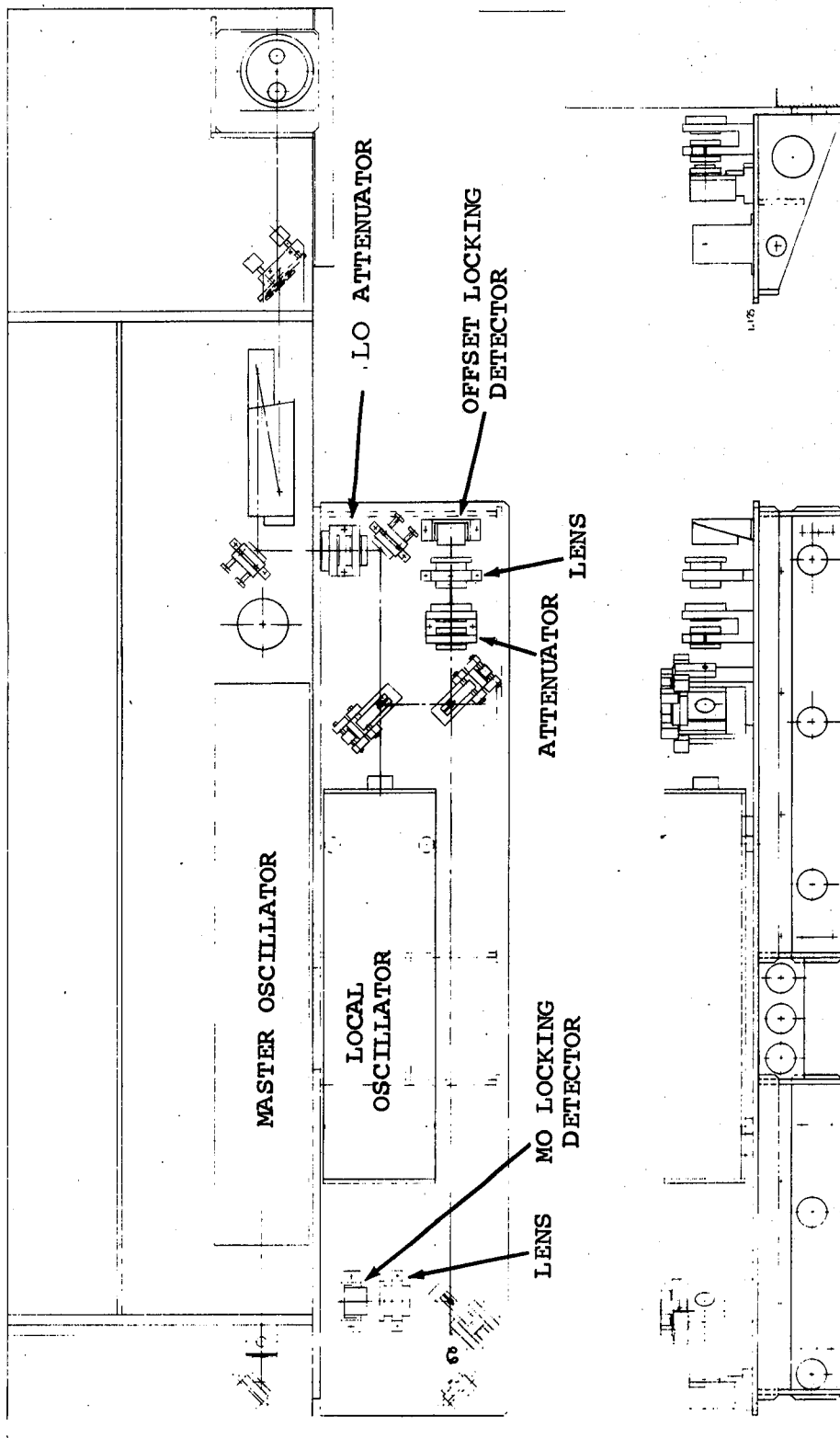
Figure 2-8. Offset System Components Layout

MASTER OSCILLATOR

LOCAL OSCILLATOR

LO ATTENUATOR

OFFSET LOCKING DETECTOR

LENS

ATTENUATOR

MO LOCKING DETECTOR

LENS
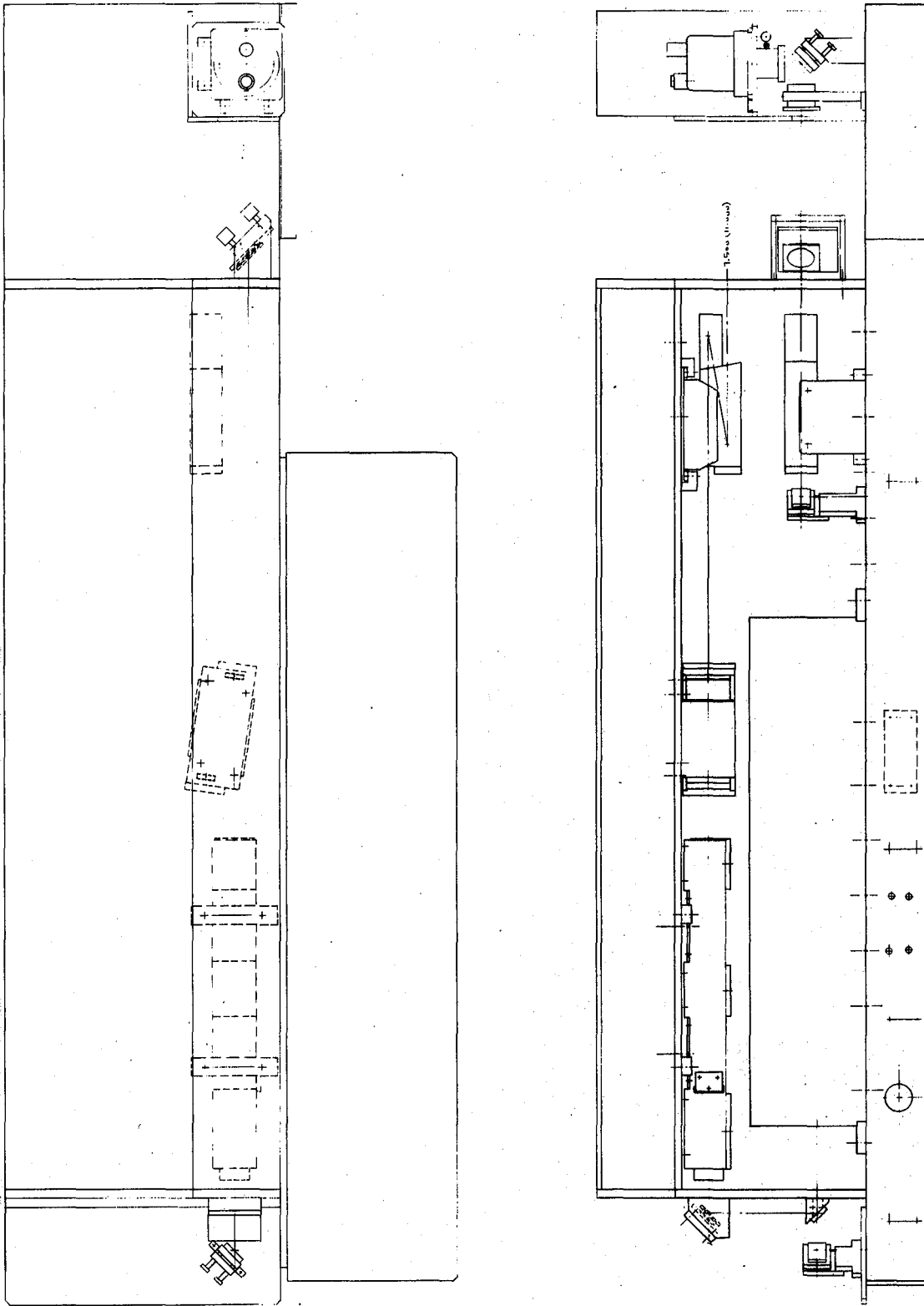
Figure 2-9. Offset System Optical Path

EOA-755

by the offset locking detector and the difference frequency is sensed
by an offset frequency locking loop which adjusts the Sylvania laser
to maintain a 10 MHz offset. The master oscillator is stabilized
to the center of various possible transitions by dithering its cavity
length and sampling its output power variations with the master
oscillator locking detector.

SECTION 3
SYSTEM TEST AND EVALUATION PROGRAMS

3.1 INTRODUCTION

Following the 1971-72 flight test and ground test programs, it
was determined that a substantial system performance improvement was
required to achieve meaningful detection ranges at the operational
altitudes of jet transports. This determination is detailed in Section
10 and Appendix F. The first step toward this improvement was a
detailed evaluation of the system performance in laboratory measurements.
A series of measurements were developed which sought to determine the
level of performance and the practical possibilities for improvement
in the following areas:

1. Output power

2. Coherence of output beam

3. Receiver heterodyne efficiency

4. Detector and receiver electronic efficiencies

5. Oscillation characteristics

The results of the measurement program are described in
Section 3.2.

On the basis of the measurement program, the following were
identified as areas in which substantial improvements should be made.

1. Isolator

2. Telescope

3. Beam expanders

4. Detector and receiver

5. Modulator

In addition, it was decided that in order to facilitate ground testing and to make the system useful for ground based measurements of storms and fronts, a frequency offset system was necessary to provide vector-velocity direction sense. This required the addition of a separate local oscillator laser and the implementation of a frequency offset stabilization loop together with room temperature detectors to drive it. In order to facilitate atmospheric probing, the processor was modified to allow automatic range sequencing and variable integration. The modifications are detailed in Section 3.3.

3.2 TRANSMITTER MEASUREMENT PROGRAM

3.2.1 VISUAL EXAMINATION OF OPTICAL SURFACES

All optical surfaces were periodically examined. On first examination, it was found that a number of surfaces had degenerated due to what appeared to be etching of the coatings by particles which had settled on them. The tenaciousness of these particles and the softness of many of the gold-coated mirror surfaces made cleaning difficult. In some cases, mirror surfaces were perforated and mirrors in the amplifier appeared to have been etched by exposure to charged particles or UV radiation in the discharge. Beamsplitters were generally in good condition except that AR coatings were not effective in some cases as indicated by power losses and secondary reflected beams. Periodic maintenance procedures were instituted which eliminated most of these problems.

3.2.2 POWER LOSSES IN OPTICAL COMPONENTS

Beam power was periodically measured at several points through the transmitter. For these CW measurements, a half-wave plate was used before the modulator to rotate the plane of polarization passing through the modulator. Typical measurement results are shown in Figure 3-1. Major losses have been incurred with the degraded mirrors M1 and M2, the beamsplitter BS1 (poor AR coating) and the modulator whose 7 mm aperture is smaller than the 8 mm beam. Amplifier optical loss is considered reasonable for the degree of beam spread and
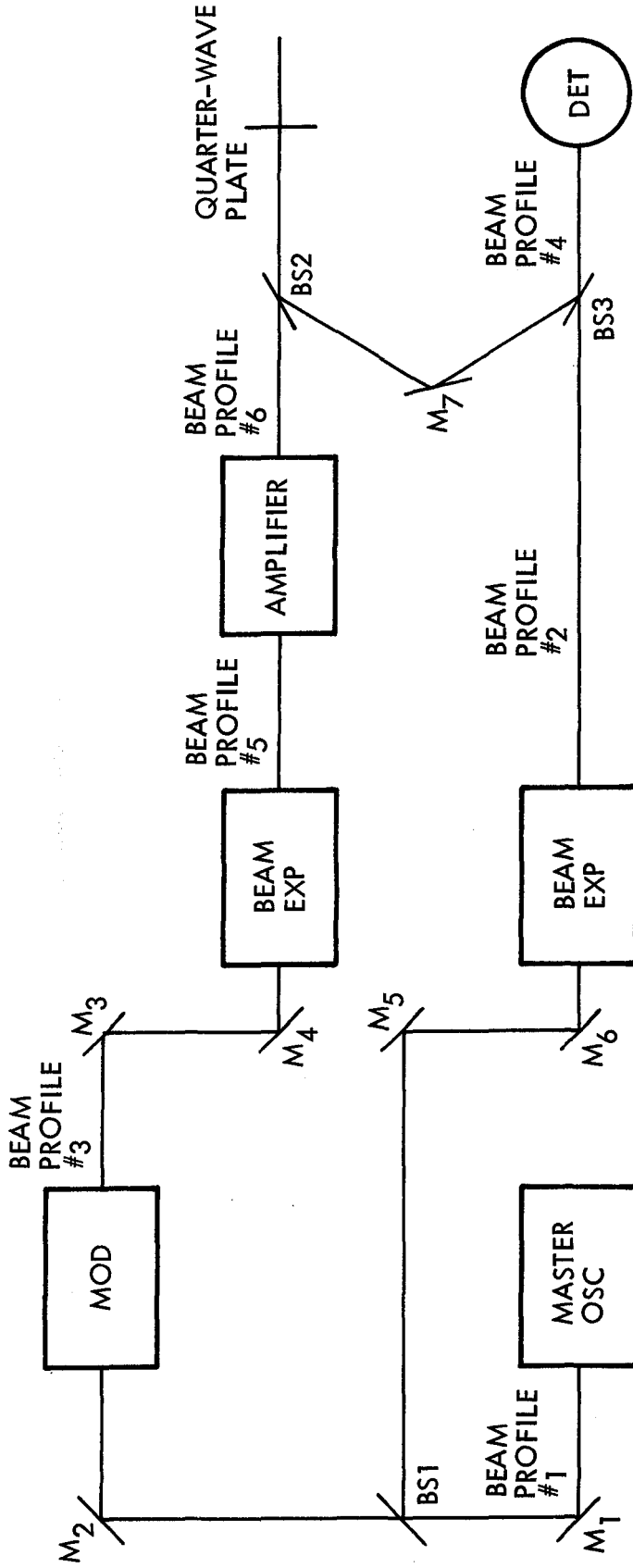
COMPONENT	OUTPUT	LOSS	CUMULATIVE LOSS
MASTER OSCILLATOR	4.75W	--	--
M1, M2, BS1	2.2 W	3.3dB	3.3
MODULATOR	1.4 W	2.0dB	5.3
M3, M4, BEAM EXPANDER	1.17W	.8dB	6.1
AMPLIFIER	.73W	2.0dB	8.1

EOA-756A

Figure 3-1. Transmitter Optical Efficiency

aperturing in the amplifier. Procedures for measuring these losses are detailed in Appendix G.

3.2.3 MEASUREMENT OF BEAM PROFILES

During transmitter realignment, beam patterns were observed visually on liquid crystal and fluorescent infrared sensitive materials and a PbSnTe detector was scanned horizontally through the beam to generate intensity profiles following each of the major optical elements in the system. Two techniques were used to obtain large signal-to-noise ratios. At points in front of the electro-optic modulator, a synchronous amplifier was used in conjunction with a beam chopper to reduce the effective noise bandwidth. At points following the modulator, where the average power is one milliwatt or less, a sample-and-hold circuit synchronized with the modulator driver was used to improve the S/N ratios. The detector size used was 100 μm prior to the beam expander and 400 μm following the beam expander. Figures 3-2 through 3-8, explained below, are typical beam profiles obtained at the major optical element test points.

Figure 3-2 shows the master oscillator output beam profile before it has reached any of the optical elements. It has the Gaussian shape expected of a single mode laser. The diameter at the $1/e^2$ intensity points is 6.28 mm.

Figure 3-3 shows the profile of the local oscillator beam after it emerges from the beam expander. The fluctuations are circular patterns resulting from the slight overfilling of an aperture in the beam expander by the laser beam. The diameter at the $1/e^2$ intensity points is approximately 14 mm which compares well with the 15 mm design diameter. It is to be expected that fringes will somewhat degrade the heterodyne efficiency of the system.

Figure 3-4 shows the effect on the local oscillator beam of interference within the recombining beamsplitter. The fringes are straight and nearly vertical indicating a wedge near the horizontal plane. The depth of the fringes indicates that the AR coating on the beamsplitter has degraded.

MASTER OSCILLATOR BEAM PROFILE
DISTANCE: 105 CM FROM LASER

6.28mm

1mm
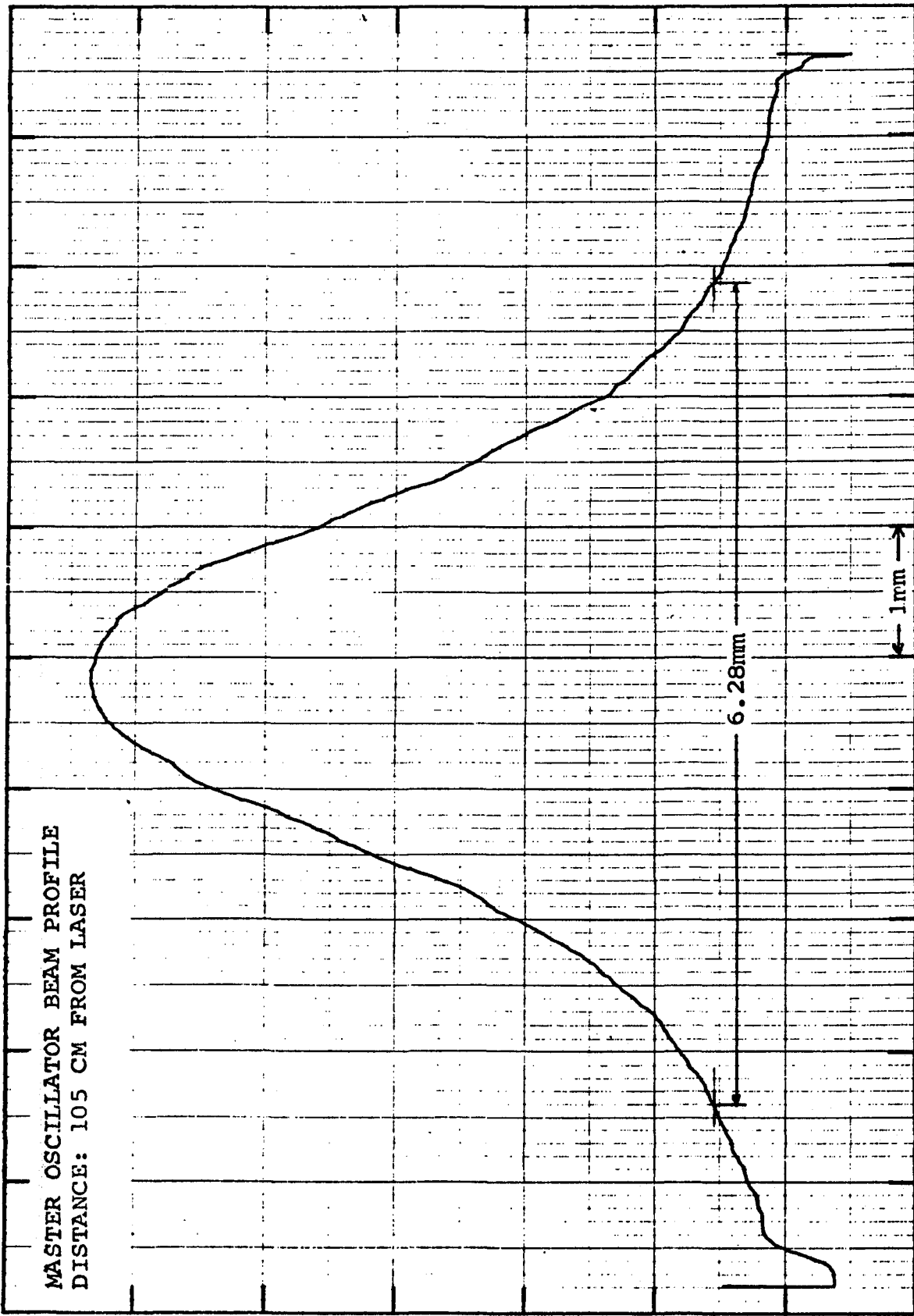
EOA-757

Figure 3-2. Master Oscillator Intensity Profile

3-5

EXPANDED LOCAL OSCILLATOR BEAM PROFILE
DISTANCE: 125 CM FROM EXPANDER
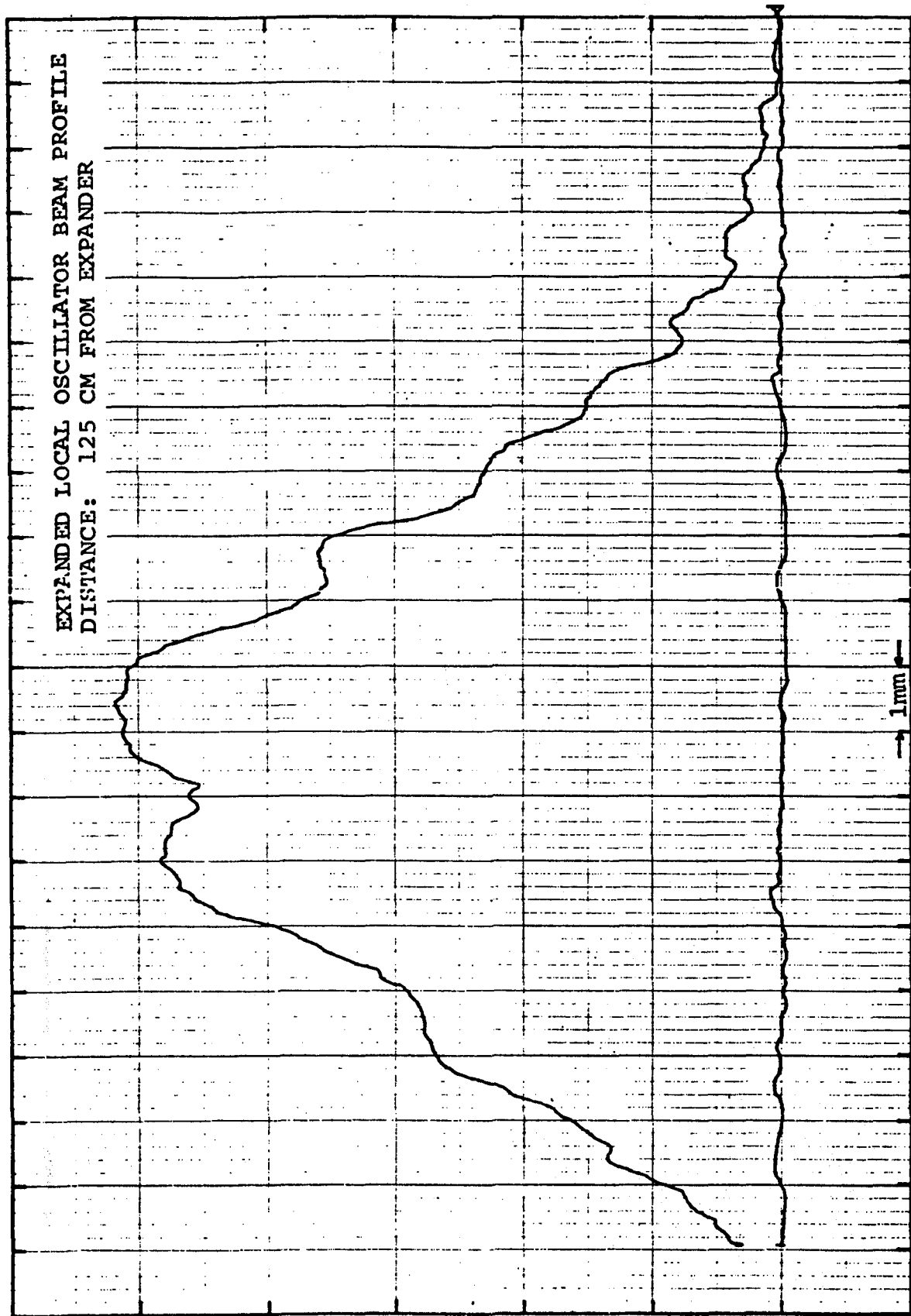
EOA-758

Figure 3-3. Local Oscillator Beam Profile

MASTER OSCILLATOR BEAM PROFILE
FOLLOWING RECOMBINING BEAMSPLITTER
DISTANCE: 115 CM FROM BEAMSPLITTER

1mm
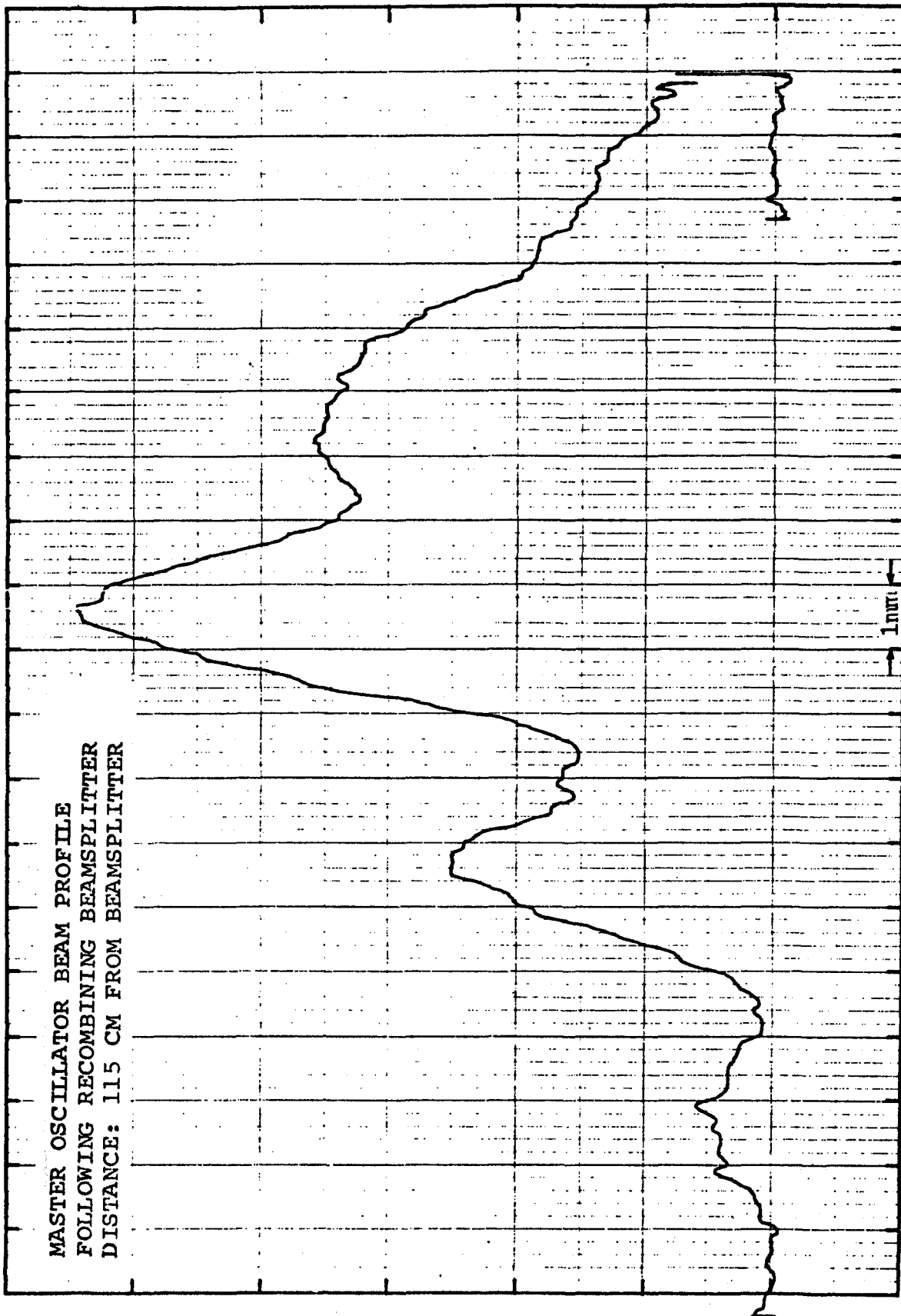
EOA-760

Figure 3-4. Master Oscillator Output Beam Profile

Figure 3-5 shows the transmitter beam after passing through the electro-optic modulator. It shows that the large 7 mm x 7 mm crystals permit the beam to pass with minor clipping of the beam.

Figure 3-6 shows the transmitter beam following the beam expander and demonstrates the same fringe pattern seen in the local oscillator leg.

Figure 3-7 shows the transmitted beam after it passes through the six unexcited amplifier tubes. The precise pattern is very sensitive to the beam alignment and appears to be due to reflections off the walls of the discharge tubes. Wall bounces with power loss at the tube ends are also consistent with the approximately 10 dB of optical loss seen in the amplifier.

Figure 3-8 shows what appears to be preferential amplification of the axial portions of the beam structure with the amplifier excited. (The small scale structure ~ 0.1 mm on the profile is due to interference from the amplifier driver and should be ignored.)

3.2.4 INTERFEROMETRIC TESTING OF FLAT MIRRORS

Several of the mirrors were tested in their mountings to determine if the mounts were stressing the mirrors. This proved to be so with both the steering mirrors and the mirrors mounted in the amplifier turn-around blocks. Figure 3-9 demonstrates the improvement achieved by improving the mirror mounting geometry. This is typical of the mountings.

3.2.5 DETECTOR AND PREAMPLIFIER MEASUREMENTS

Efficiency measurements of the flight test CuGe detector/receiver were made and the signal (S), noise (N), preamplifier noise (N_{TH}) and S/N frequency characteristics were determined. The receiver efficiency at 10 MHz was determined to be 18%. The frequency dependence of the various parameters is shown in Figure 3-10. These curves show that despite the limited detector frequency response, the receiver sensitivity should be 13% $\pm$ 0.5 dB in the 20 - 30 MHz frequency range.

MASTER OSCILLATOR BEAM PROFILE
DISTANCE: 160 CM FROM MODULATOR OUTPUT

8.3mm

1mm

EOA—759
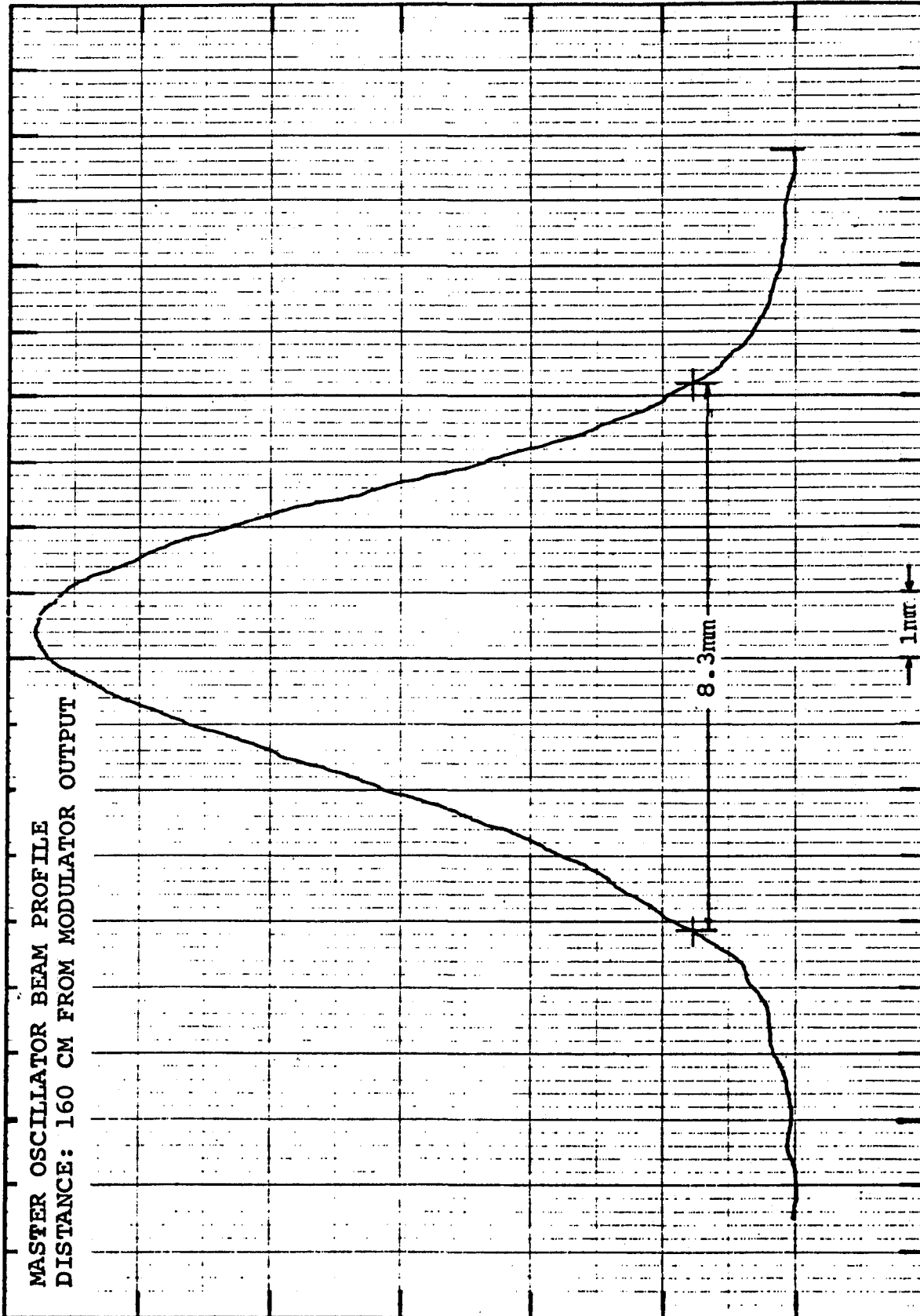
Figure 3—5. Master Oscillator Beam Profile

TRANSMITTER EXPANDER OUTPUT BEAM PROFILE
DISTANCE: 130 CM FROM OUTPUT PORT

EOA-761

1mm
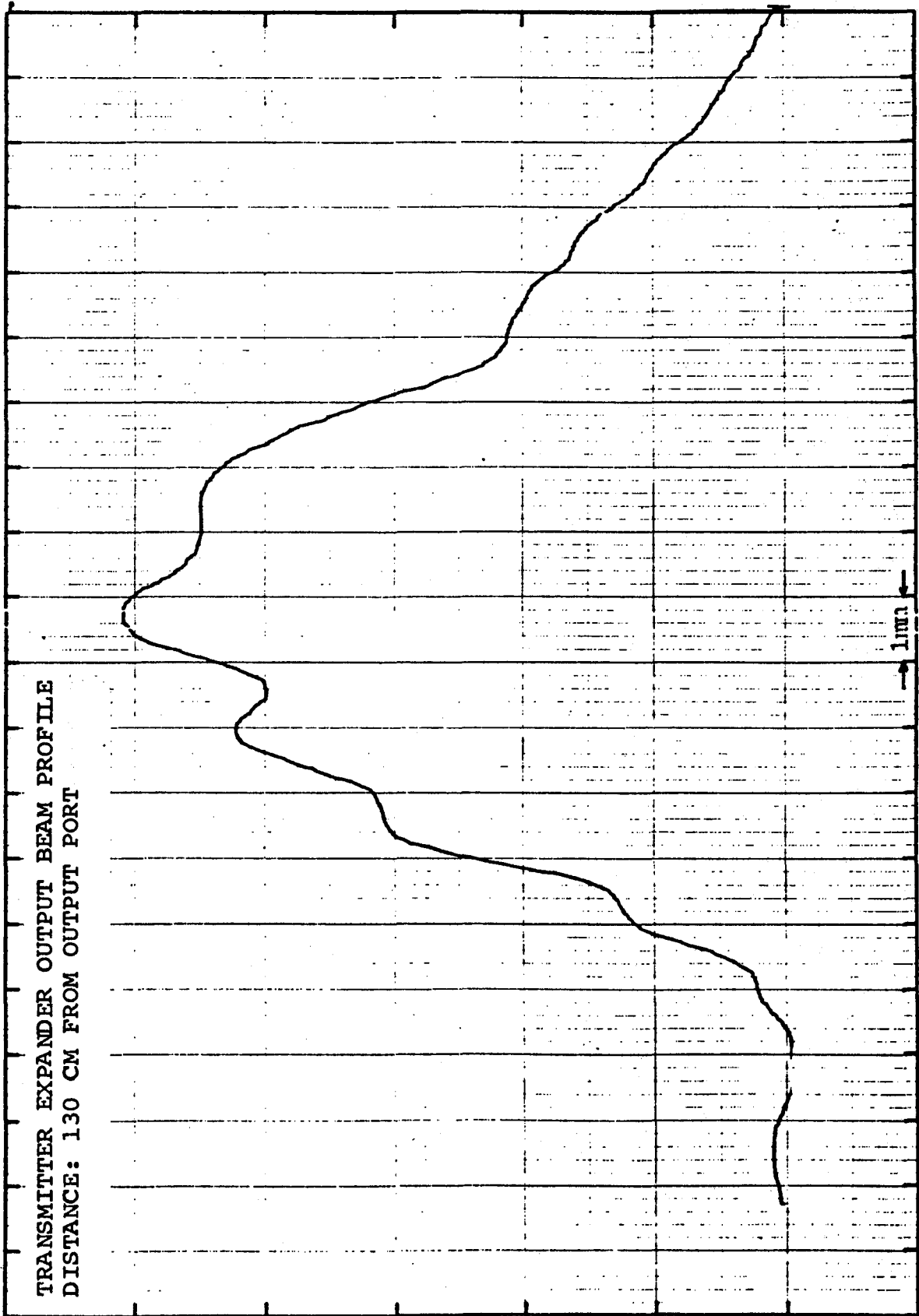
Figure 3-6.   Transmitter Beam Expander Beam Profile

The chart contains the following labels within the plot area:

AMPLIFIER OUTPUT BEAM PROFILE -
AMPLIFIER OFF
DISTANCE: 503 CM FROM OUTPUT
WINDOW OR
5.03 METERS FROM OUTPUT
WINDOW

EOA-762

1mm
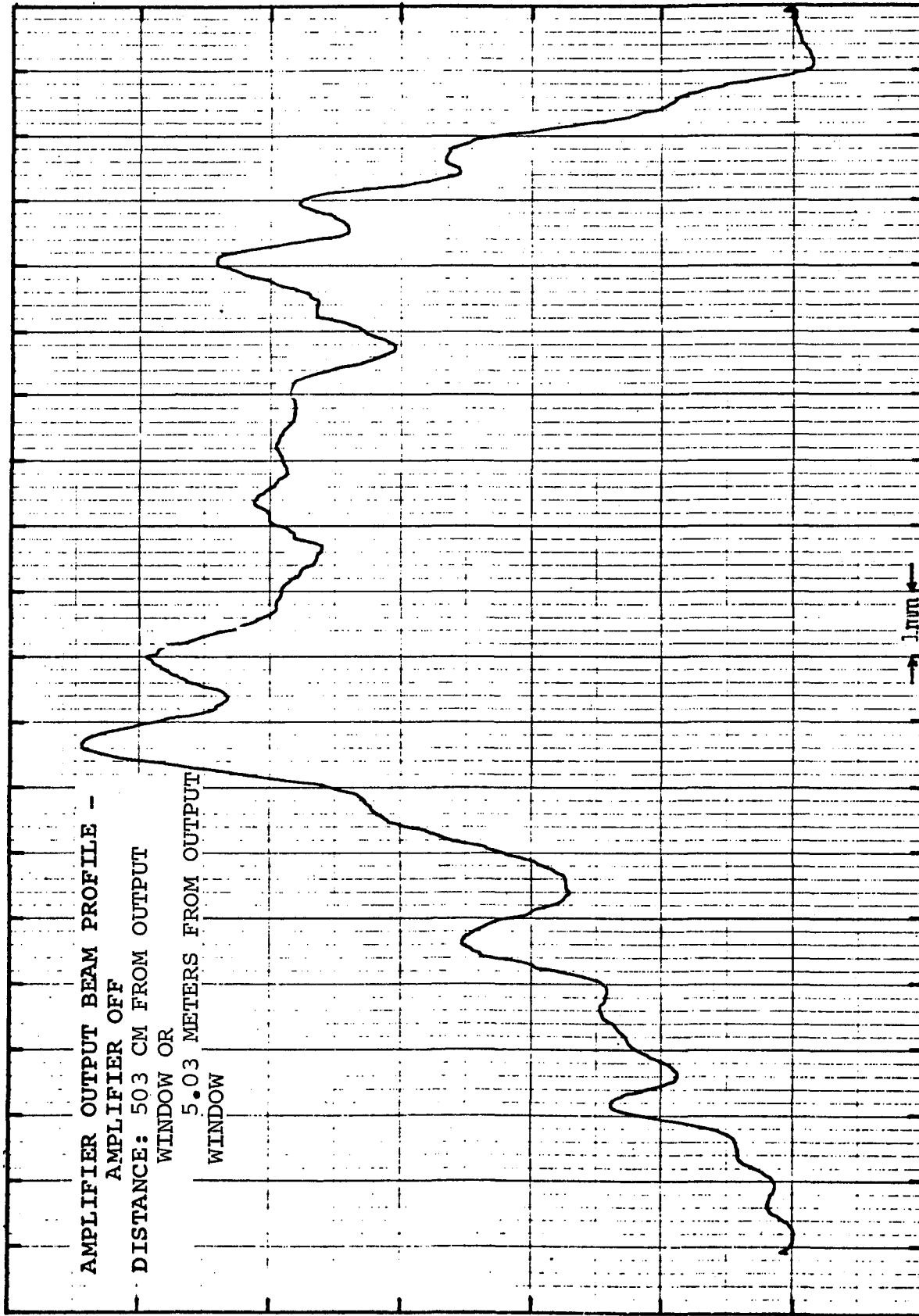
Figure 3-7. Amplifier Output Beam Profile - Amplifier Off

AMPLIFIER OUTPUT BEAM PROFILE -
AMPLIFIER ON
DISTANCE: 503 CM FROM OUTPUT WINDOW OR
5.03 METERS FROM OUTPUT WINDOW

EOA-763

1mm
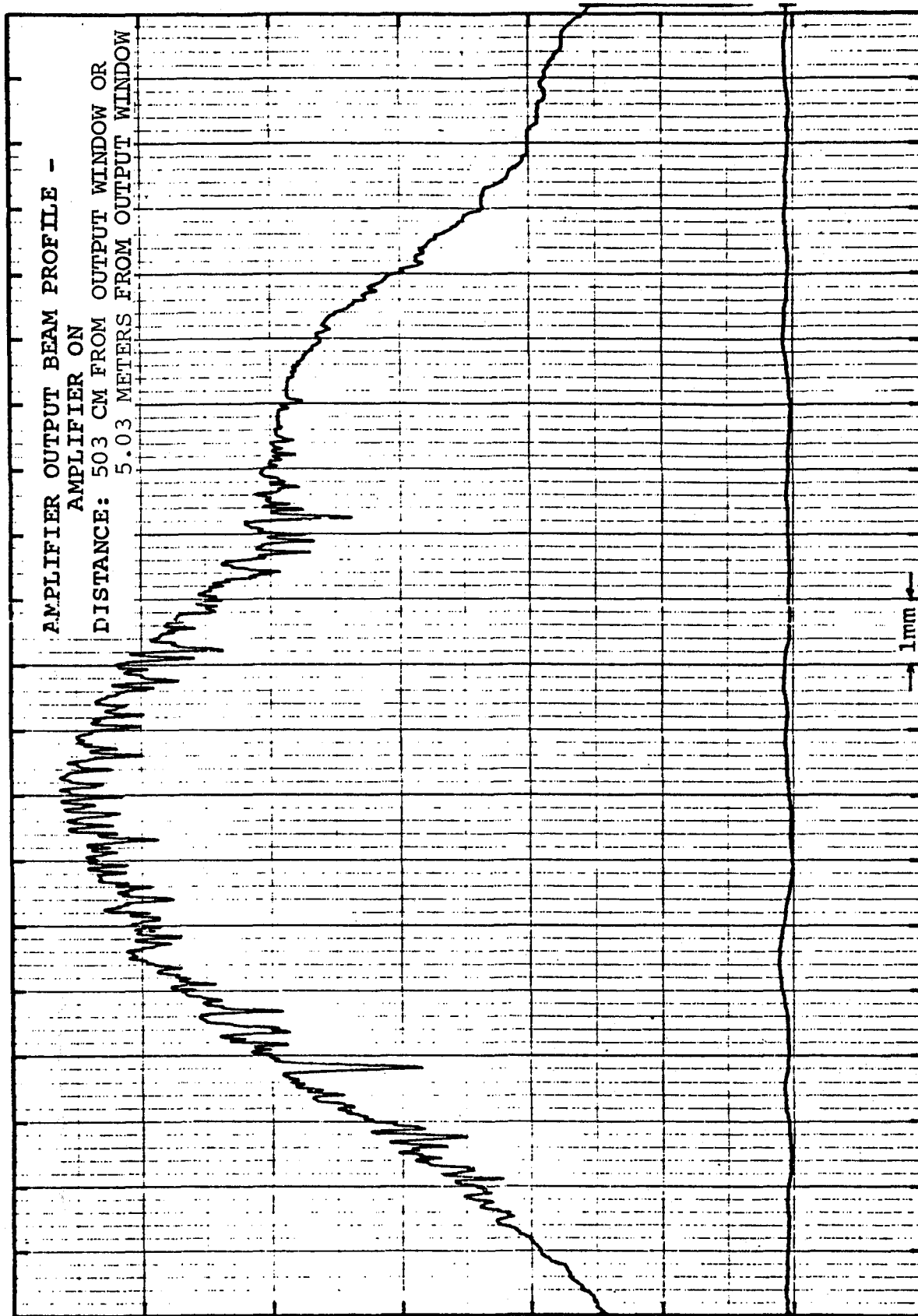
Figure 3-8. Amplifier Output Beam Profile - Amplifier On
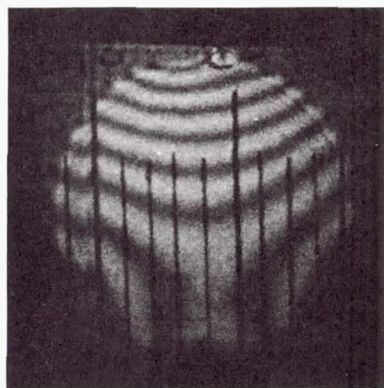
Double Pass Interferogram of Turn-Around Block
Before Remounting -   λ/40 @ 10.6 μm   1 Div = 2 mm
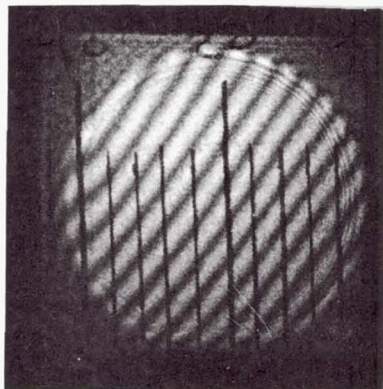
Double Pass Interferogram of Turn-Around Block
After Remounting

EO-451

Figure 3-9. Distortion of Mirrors in Turn-Around Blocks
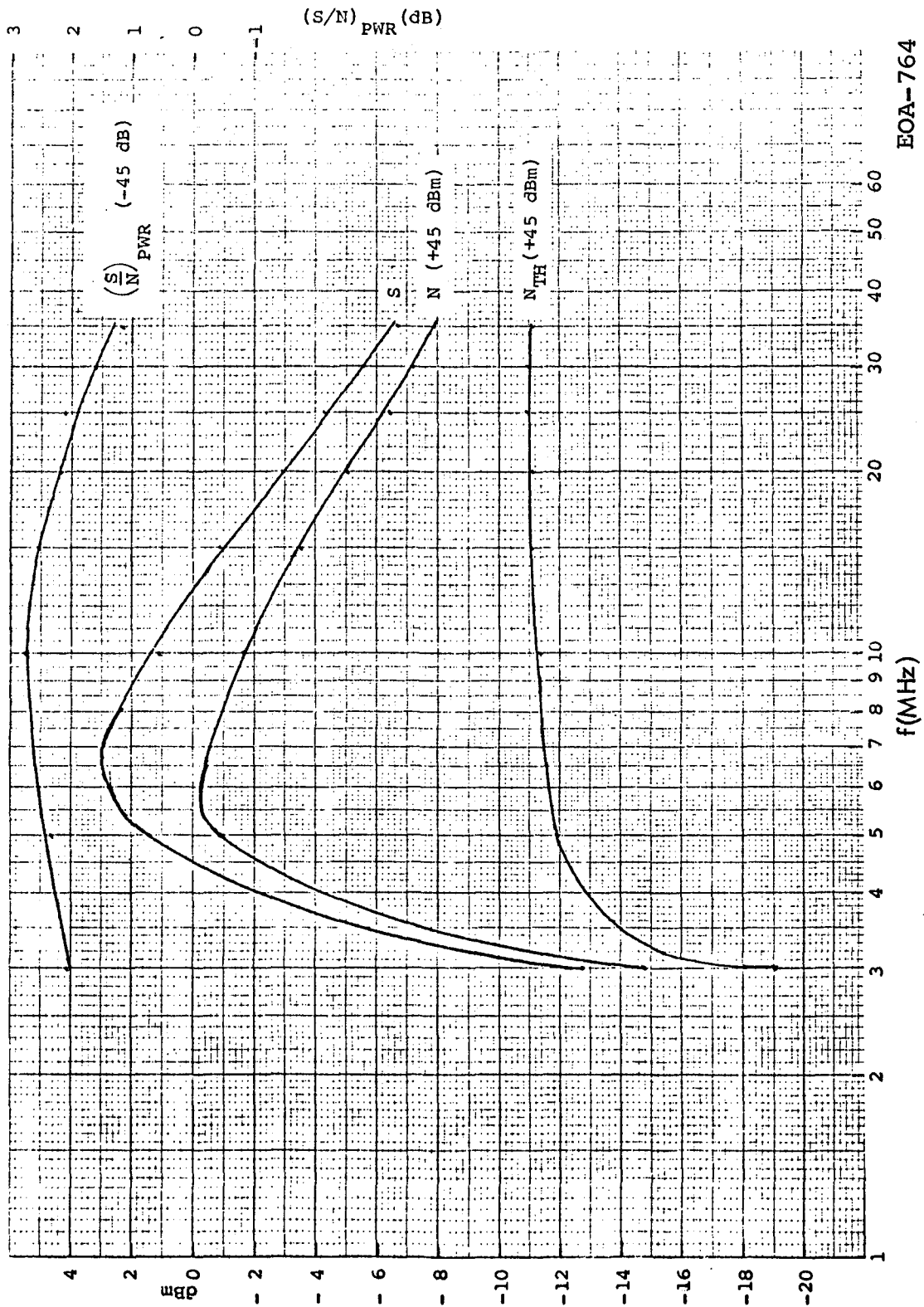
Figure 3-10. CAT Detector & Preamp Characteristics

3-14

3.2.6 SYSTEM HETERODYNE EFFICIENCY MEASUREMENTS

Far field system heterodyne efficiency measurements were made using the arrangement and relationship in Figure 3-11. This measurement combined the coherence losses of the transmitter beam, the signal beam and the local oscillator beam. The method is dependent upon the values of the calibrated Doppler target backscatter coefficient and the responsivity of the calibrated CuGe detector.

The measurement is a far-field measurement by virtue of being performed in the focal plane of the focusing lens. These measurements have consistently yielded a value for η_{op} of -17 dB with the amplifier off, and -22 to -23 dB with the amplifier on, when suitable efforts were made to prevent spontaneous oscillation of the amplifier. The electronic arrangement shown in the block diagram of Figure 3-12 was used for the pulsed measurements.

In order to separate the transmitter efficiency from the receiver efficiency, separate measurements were made of the receiver efficiency utilizing a second laser as a signal source as shown in Figure 3-13. These measurements, which included an _in situ_ detector responsivity and resistance measurement, showed the system loss due to the transmitter alone.

Losses associated with the transmitter are assumed to arise from the annular structure indicated by the output beam profile shown earlier. The primary cause of this structure is the reflection of the "wings" of the beam by the amplifier tube walls. Clipping this oblique radiation to clear up the output and increase the gain of the amplifier is discussed in Section 3.

3.2.7 BEAM EXPANDER ALIGNMENT

The beam expander geometry was examined to determine the reason for beam degradation. It was found that the entrance bore in the expander body was not placed correctly; its diameter and the diameter of the exit bore were clipping the beam at their $1/e^2$ points and the secondary mirror was slightly undersized for full accommodation of the unexpanded beam. By directing the beam through the expander
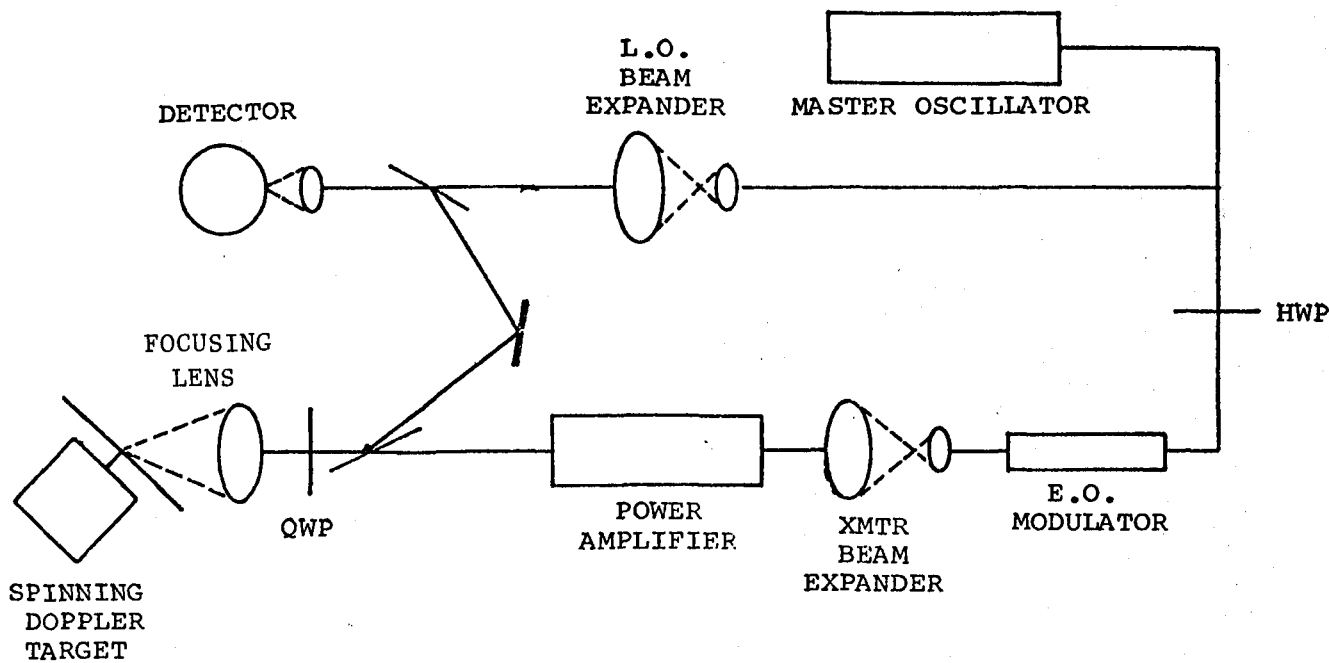
$$\eta_{op} = \frac{2 \, R^2 \, \eta_{SA} \, V_{sig}^2}{\pi \, P_T \, P_{LO} \, \rho_i^2 \, \rho(\pi) \, R_L^2 \, D^2}$$

R = FOCAL LENGTH OF FOCUSING LENS

η_{SA} = FACTOR FOR RESPONSE OF SPECTRUM ANALYZER TO RAYLEIGH SIGNALS

V_{sig} = MEASURED SIGNAL VOLTAGE

P_T = TRANSMITTER OUTPUT POWER

ρ_i = DETECTOR DYNAMIC CURRENT RESPONSIVITY

$\rho(\pi)$ = TARGET MATERIAL BACKSCATTER COEFFICIENT

R_L = DETECTOR LOAD RESISTANCE

D = LOCAL OSCILLATOR $1/e^2$ DIAMETER

EOA-765

Figure 3-11.   Far Field System Heterodyne Efficiency
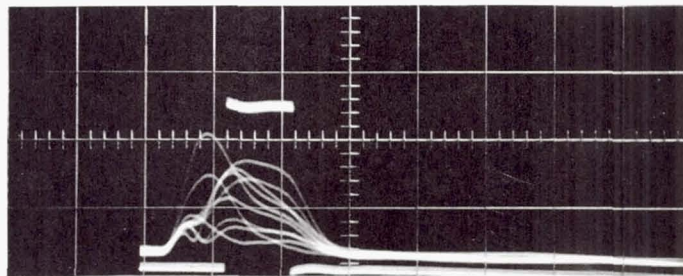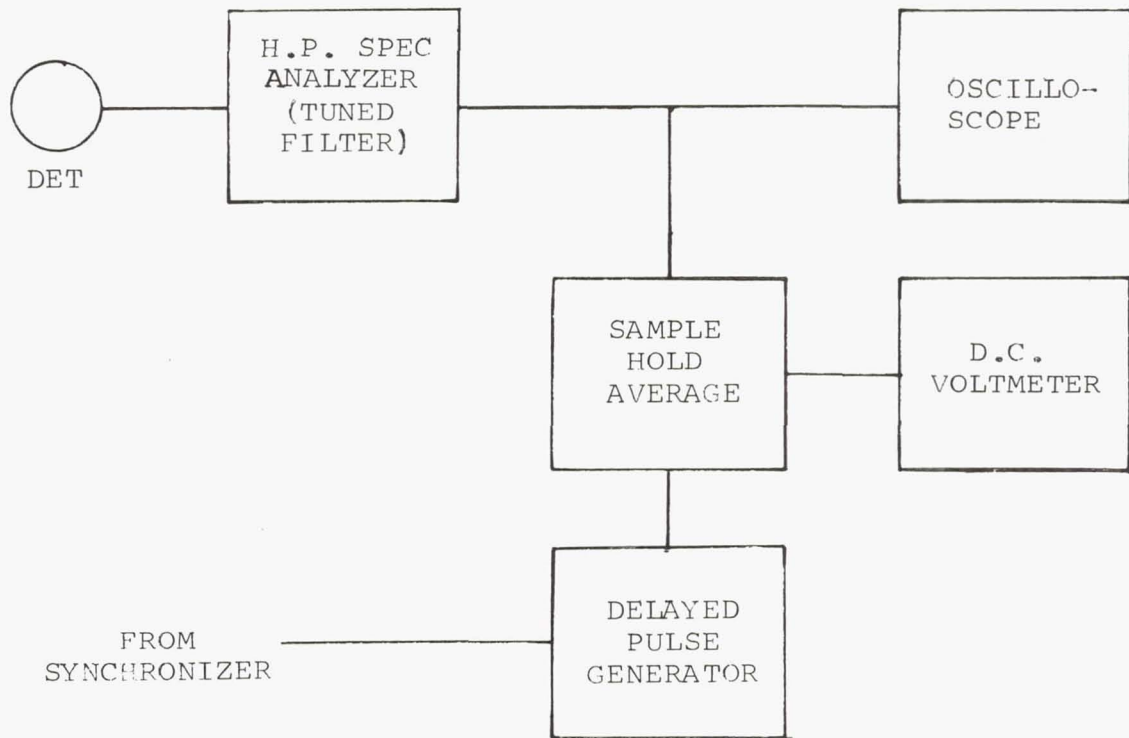
Photograph of Detected Signal
and Sampling Pulse (10 μsec/div)

EOA-766

Figure 3-12. Pulsed Signal Measurements

SIGNAL
LASER

BEAM
EXPANDER

SYSTEM UNDER
TEST
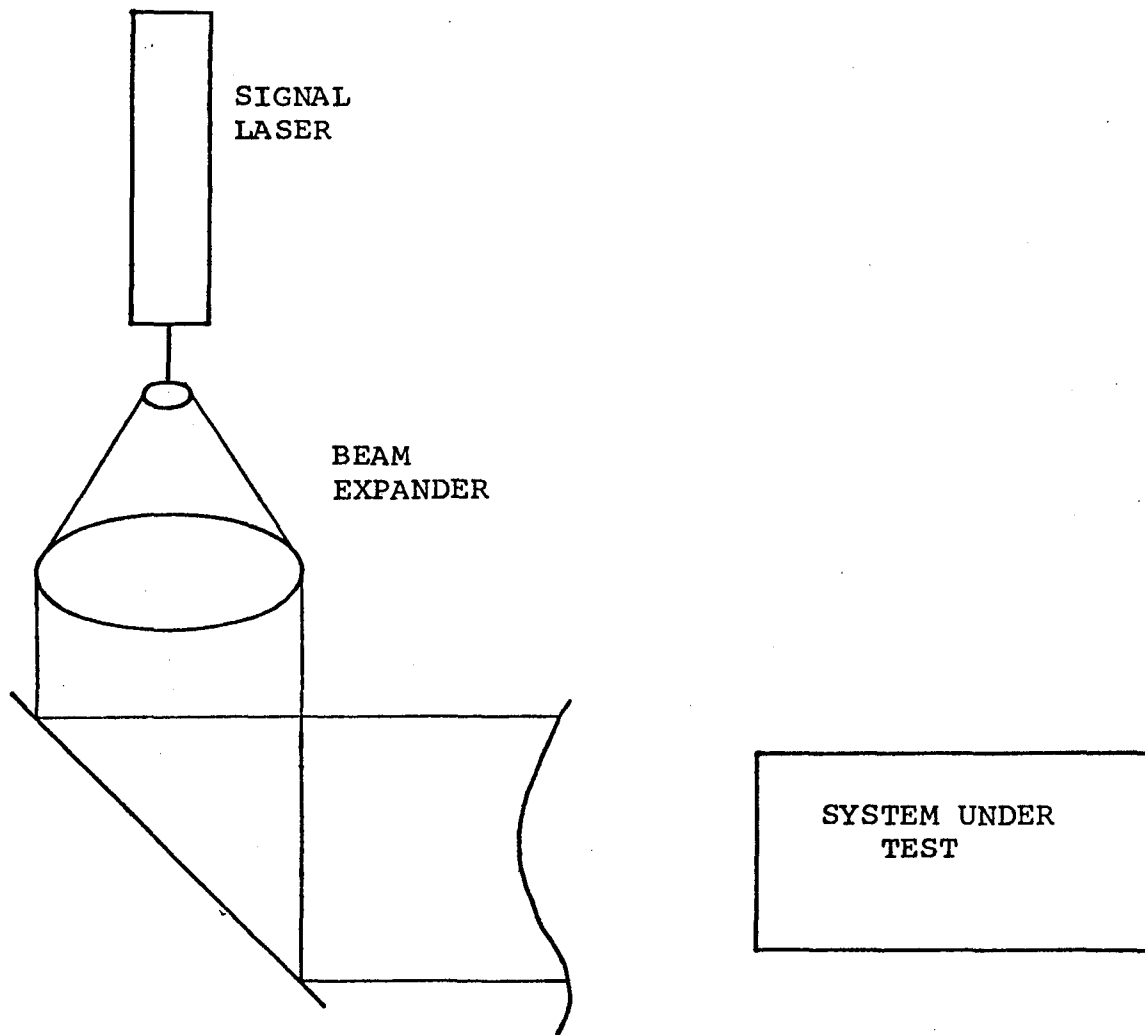
$$\eta_{OP} = \frac{\overline{V}_{sig}^2}{\pi D^2 \rho_i^2 P_{REF} P_{sig} R_L^2} \left[1 - e^{-d^2/D^2} \right]^2$$

V_{sig} = signal voltage

D = Gaussian local oscillator beam diameter

P_{REF} = local oscillator beam power

P_{sig} = signal beam power density at receiver

R_L = detector load impedance

d = receiver aperture diameter

ρ_i = detector responsivity

EOA-767

Figure 3-13.   Far Field Receiver Efficiency Test Setup

slightly askew, a reasonable output could be had, but with aberration.

Calculations determined the optimum Gaussian beam waist diameter for the output of the beam expander. The diameter is plotted as a function of W_o in Figure 3-14 for $z = 10$ m, the length of the amplifier, and shows that the present 15 mm output diameter results in a diameter of 17.2 mm at the end of the 19 mm diameter amplifier tubes. To clean up the amplifier output beam, a program was directed toward controlling the expander ratio to produce a 12 mm waist and a 16.4 mm beam at 10 m (see Section 3.3.3).

3.2.8 MEASUREMENTS OF OUTPUT POWER CYCLING

Figure 3-15 shows part of a record made during the power cycling after the system had warmed up and the output pulse shape at peak power output and at minimum output during the cycling. In the upper photo a large part of the power is in a sharp peak with a wide bandwidth making it less suitable for CAT heterodyne measurements than the pulse shape in the lower photo.

Calculations were made to determine the cycling rate which would be expected if the cause were the thermal expansion of a cavity having a length equal to the distance between the amplifier output window and the master oscillator output coupler. The length of this cavity subject to expansion by heating of the aluminum frame is 985 cm. The remainder is Invar which has a much smaller expansion coefficient. Using an expansion coefficient of 24×10^{-6} K^{-1} for aluminum, a 2 K temperature change would cause a length change equal to 89 half wavelengths. The number of power output cycles measured during a 2 K frame temperature rise was 90 ± 10, with the error being due to temperature reading inaccuracies. This strongly supported the theory that the amplifier acted as a resonant cavity with the sources of feedback located at the ends.
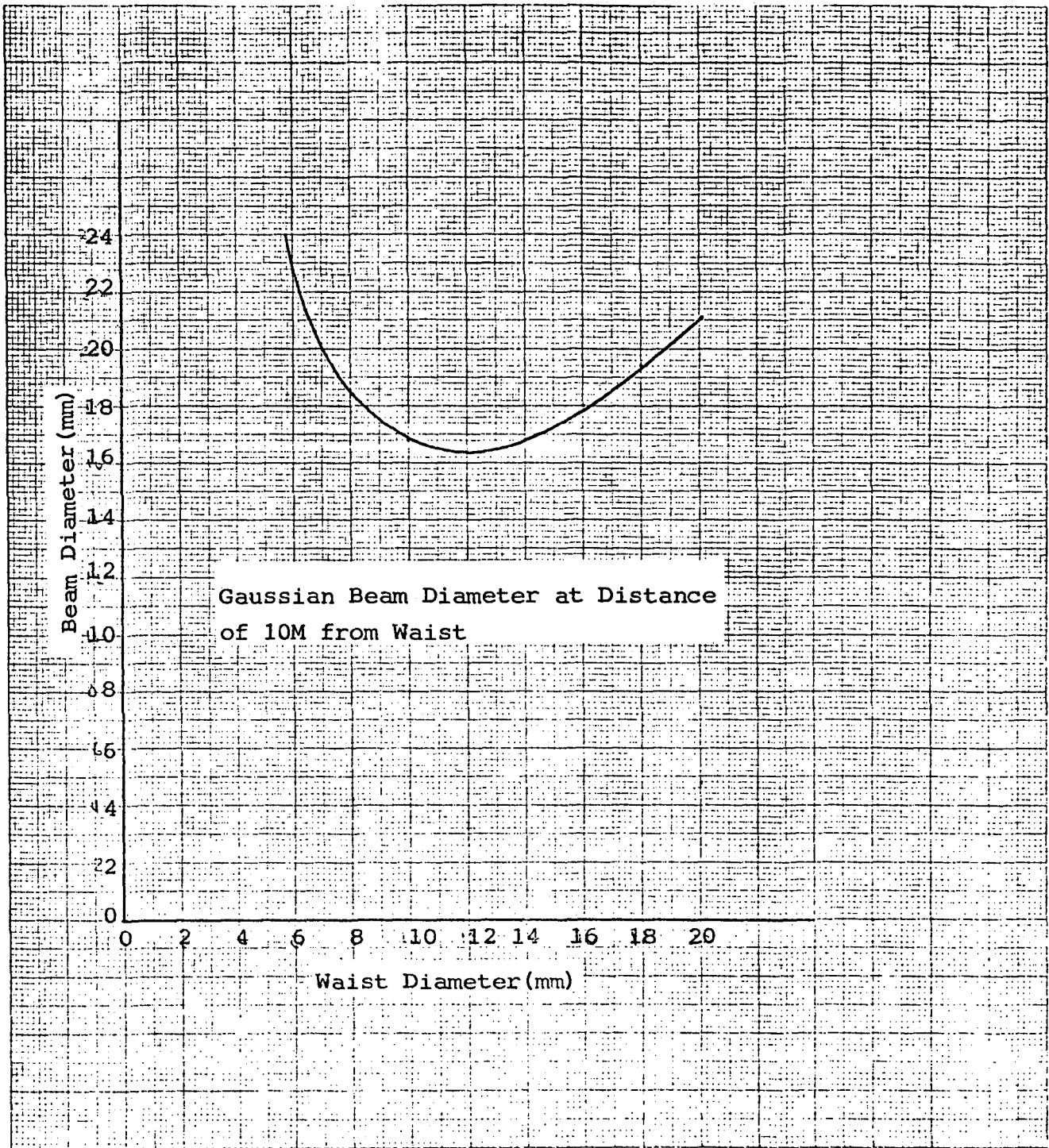
Figure 3-14.   Expanded Beam Diameter

EOA-768
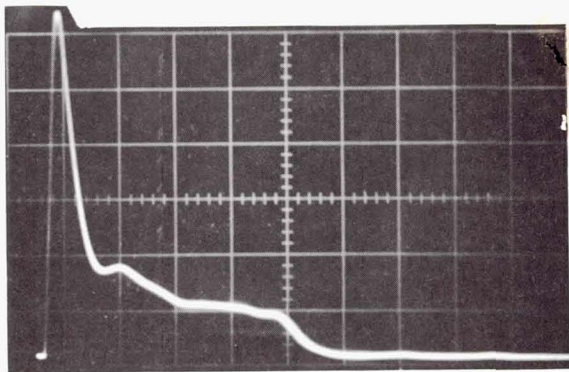
Power Output vs Time
at peak power moment
Time Scale 2 μs/div
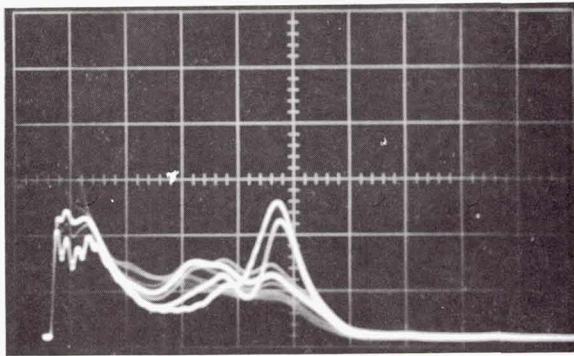
Power Output vs Time
at minimum power moment
2 μs/div
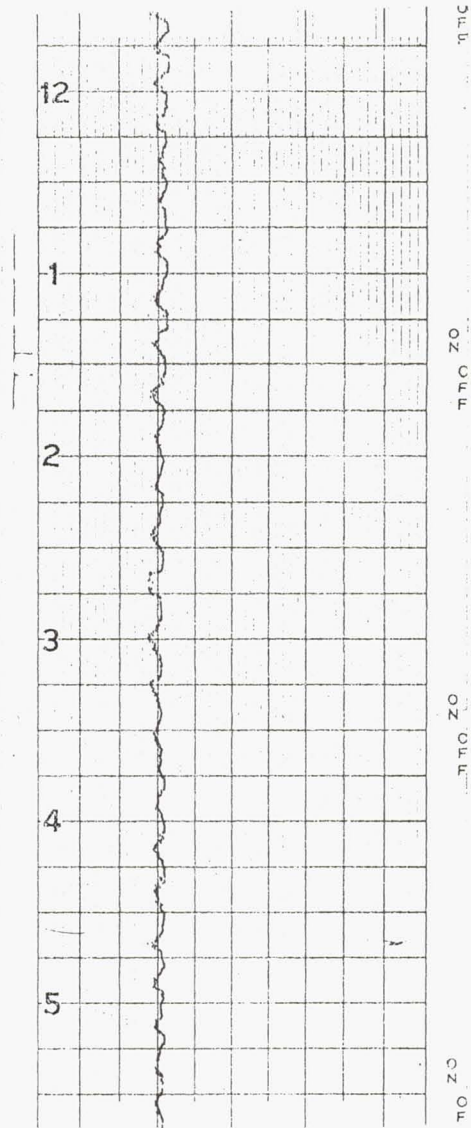
Sample Record of Power Cycling
after System has warmed up
1.5 min/div

EO-452

Figure 3-15. Power Cycling Photographs and Strip Chart Record

3.2.9 FREQUENCY-TIME CHARACTERISTICS

Because of the possible application of the system to nearby, low frequency targets, receiver measurements were made in the 0 - 10 MHz spectral range immediately following the output pulse. It was found that the most severe problem would be that of etalon switching of the modulator. This emphasized the need for low reflectivity AR coatings on the crystals.

The upper trace in Figure 3-16 shows the gated detector signal with modulator ring plus any scattered signals from the receiver optics. The gate passed a signal for 110 μs starting on the falling edge of the synchronizer pulse. This signal is also passed through a spectrum analyzer and displayed below the signal trace (Figure 3-17). The spectrum analyzer is used as a 100 kHz bandpass filter set at frequencies of 0.7, 1 and 1.5 MHz. The downward pulses at the beginning and end of each trace in the five pictures are the result of the switching transients whose characteristics are dependent on the rise and fall times of the switching pulse. In order to make close-range low frequency heterodyne measurements, the transient problem will have to be solved. Efforts are underway to do this by optical means, isolating the modulator, thus removing the need for a switch, as well as reducing the ringing.

3.2.10 RECEIVER SATURATION CHARACTERISTICS

Using an injected signal, measurements were made of the saturation characteristics of the receiver electronics to determine the amplifier dynamic range (40 dB). During these tests, it was found that the modulator caused the master oscillator to shift by 150 kHz, which normally caused no problem; however, when this shift resulted in the oscillator jumping to another P-line, the amplifier fluctuation in the local oscillator would be enough to saturate the amplifier and result in a sensitivity loss of nearly 20 dB as well as the generation of a large number of spurious frequencies in the 0 - 50 MHz band.

(1) f = 0.7 MHz
     Scale = 20 μsec/div
     B.W. = 100 kHz

(2) f = 1 MHz
     Scale = 20 μsec/div
     B.W. = 100 kHz
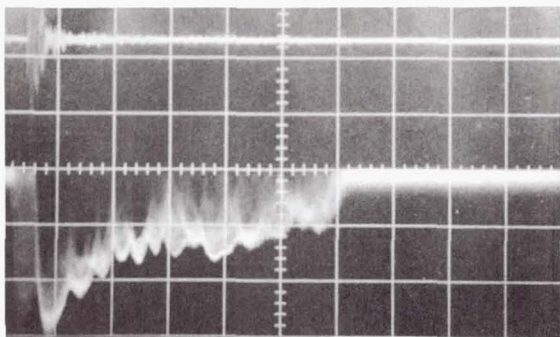
(3) f = 1.5 MHz
     Scale = 20 μsec/div
     B.W. = 100 kHz
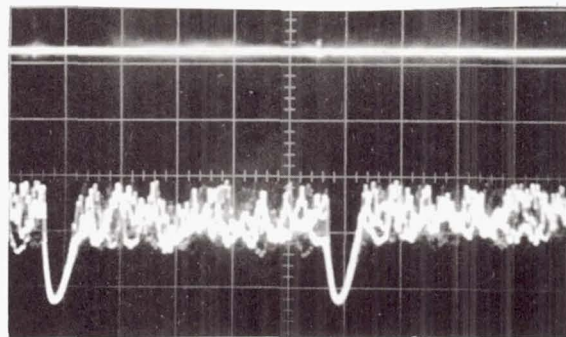
(4) Test Setup Noise
     Bias Off
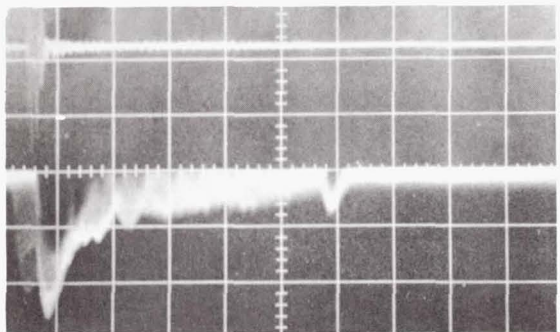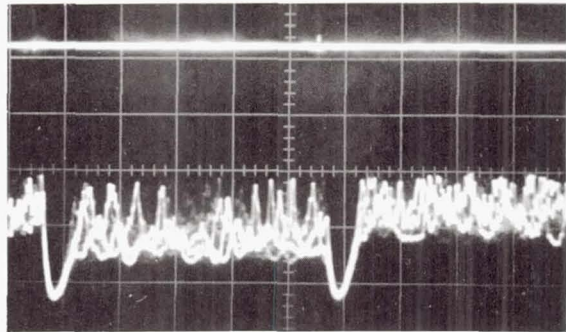
(5) Test Setup Noise
     Plus Detector Noise
     Bias on

     Detector RMS
     Noise = -112 dB
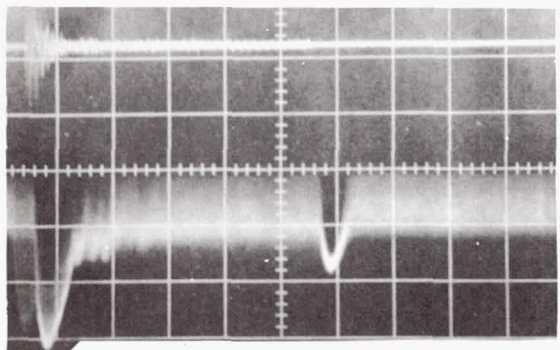
EO-453

Figure 3-16.   Frequency-Time Characteristics of CAT
               System Modulator and Switching Transients
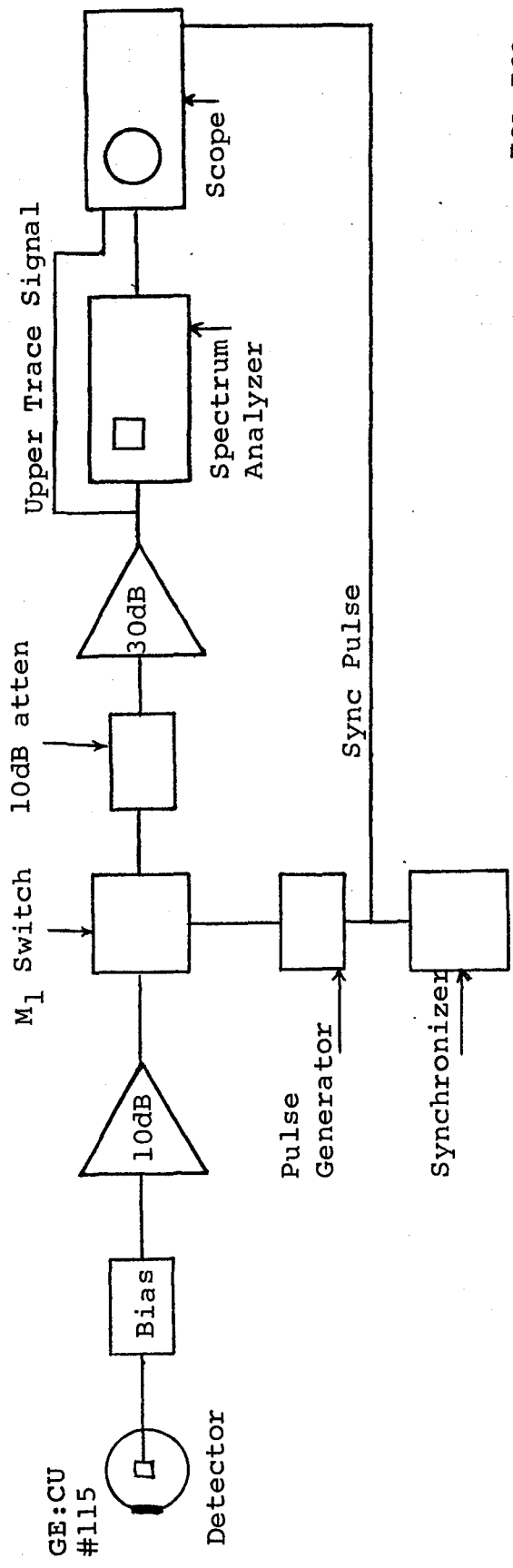
Figure 3-17. Test Setup for Photos of Frequency-Time Characteristics

EOA-769

3.2.11   MEASUREMENT OF SYSTEM BACKSCATTER

Measurements were made at the detector location in order to determine the magnitude of the backscatter and validate the numerical analysis of the telescope in Section 3.3.2.

There are two paths by which backscatter can reach the detector. The first is directly through the optical front end and is the dominant mode. The second is back through the amplifier and along the local oscillator path and includes amplifier gain and polarization considerations.

A series of measurements were made using the chopped local oscillator beam as a calibration source. In the case of pulses arriving via the local oscillator path, the backscattering coefficient is subject to error due to the problem of accurately measuring a pulse with a peak power near that of the local oscillator. The results for the local oscillator path must be reduced by any attenuation used to reduce the detector local oscillator power. In the case of a photo-voltaic detector, this reduction is 10 dB.

Measurements were made with and without the telescope mounted. In both cases, the power amplifier was on and the output beam was directed into a water-filled dump. In the absence of the telescope, it was found that the major contribution was from the quarter-wave plate holder because of the small size of the holder (15 mm diameter) compared to the output beam. This scatter was polarized so that most of it re-entered the amplifier, and even with the attenuation losses in the LO path, it exceeded the power arriving at the detector via the direct, but incorrectly polarized, receiver path.

With the telescope mounted, the secondary becomes the dominant source of scatter. Because the secondary follows the quarter-wave plate, the direct receiver path now dominates slightly. The results of these measurements (made with a 20 mw LO power) are presented in Table 3-1 along with the calculated secondary scatter value obtained in Section 3.13 after being reduced by 30% for beamsplitter losses.

TABLE 3-1

SCATTERING COEFFICIENTS

WITHOUT TELESCOPE		WITH TELESCOPE	
ON LO	ON RECEIVER	ON LO	ON RECEIVER
6.5×10^{-6}	4.4×10^{-7}	3.2×10^{-4}	7.0×10^{-4}
CALCULATED VALUE FOR TELESCOPE SECONDARY ON RECEIVER 7.6×10^{-4}			

Table 3-1 shows that with a 10 kw output pulse, the peak power at the detector may reach 7 W with the present telescope design; whereas, without the telescope, the level would be 65 mW. A planned increase in the wave plate size (to 22 mm) is expected to reduce the scattered pulse peak power to less than 1 mW in the absence of the telescope. These measurements established the importance of telescope design changes directed toward reduction of secondary backscatter. The close agreement between the measured value of 7×10^{-4} and the calculated value of 7.6×10^{-4} for the telescope secondary supported the validity of the analysis in Section 3.2.11.

3.3   REDESIGN AND EVALUATION

3.3.1   FREE CARRIER FARADAY ISOLATOR DESIGN PROGRAM

3.3.1.1   Introduction

A 10.6 μ room temperature optical isolator was designed to prevent backscattered radiation from entering the amplifier sections of the laser transmitter. The optical isolator was based on the free-carrier Faraday effect and consisted of an indium antimonide (InSb) Faraday rotator placed between two linear polarizers whose principal axes were orientated 45° with respect to each other.

A beam of linearly polarized light derived from the master oscillator passed through the front polarizer, was rotated 45° and transmitted through the rear polarizer. Maintaining its original polarization, backscattered radiation from optical components re-entered the isolator through the rear polarizer, was rotated an additional 45° and subsequently blocked by the front polarizer which was at right angles to the plane of polarization. The degree of isolation achieved depended on the material characteristics of InSb, the uniformity of the applied magnetic field, and the extinction ratio of the polarizing elements. Of the three, the material characteristics of the InSb limit the figure of isolation.

3.3.1.2 Material Considerations

The free-carrier Faraday effect exhibited by semiconductor materials, such as InSb, is a function of operating temperature, donor concentration, sample thickness, and magnetic field strength. All these parameters had to be balanced to minimize absorption losses and maximize isolator performance.

W. T. Boord, et al,[1] made a study on the interdependence of these various parameters for isolation applications. Choosing 300 K as our operating temperature, data were extrapolated from their results and replotted to establish the tradeoffs for our design. Figures 3-18 and 3-19 illustrate the tradeoffs involved between field requirements and absorption losses for various donor concentrations (N_D) and sample thicknesses (t). These plots imply that a reasonable room temperature isolator could be designed with InSb wafers 0.02" (0.0508 cm) or 0.03" (0.076 cm) thick having donor concentrations in the range of 1.0 - 2.0 x 10^{17}/cm^3. Ideally, the best compromise of parameters for our application would be a 0.02" (0.0508 cm) wafer with N_D = 1.5 x 10^{17}/cm^3. Under these
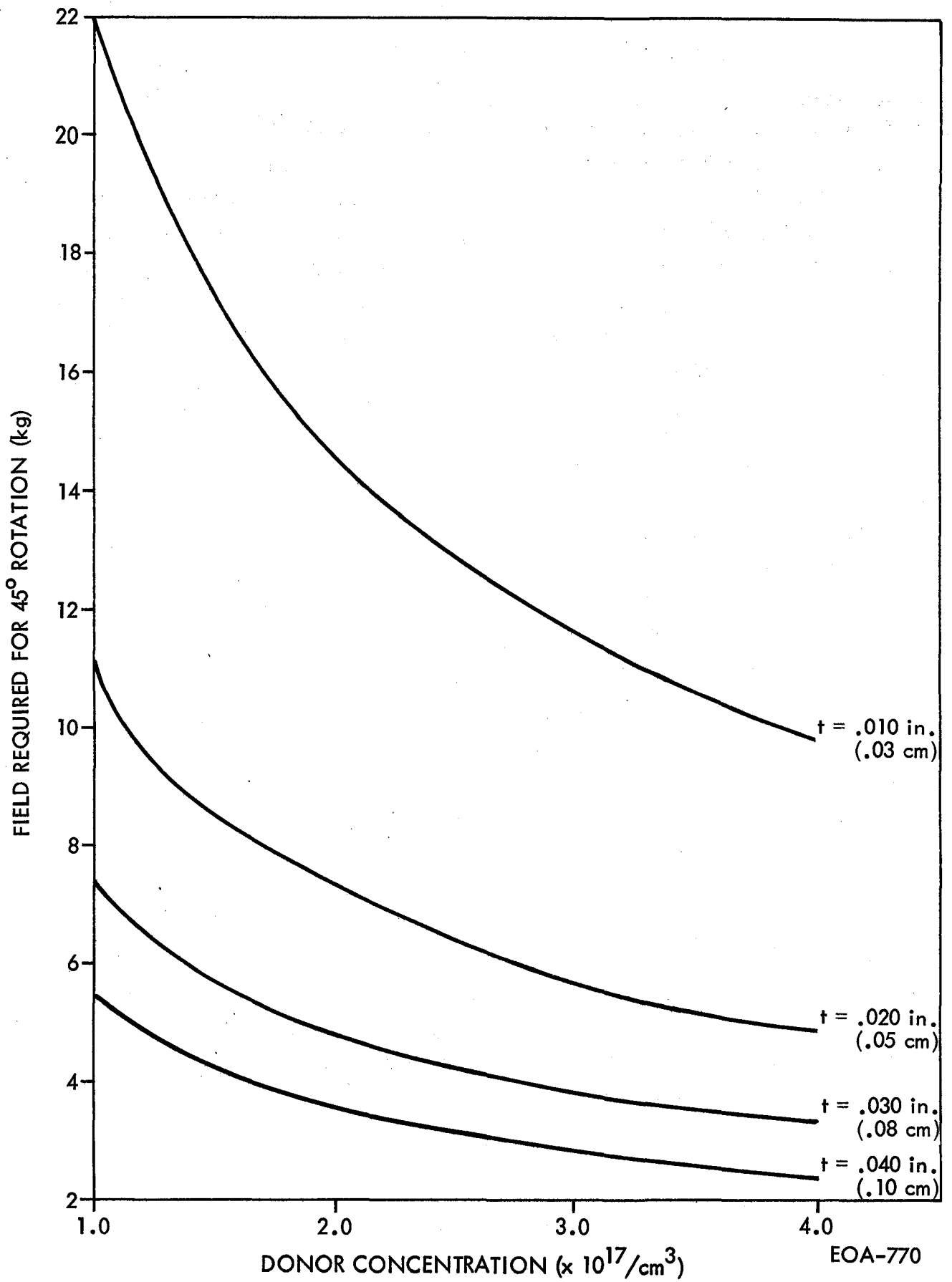
Figure 3-18. Field Requirements for InSb at T = 300 K
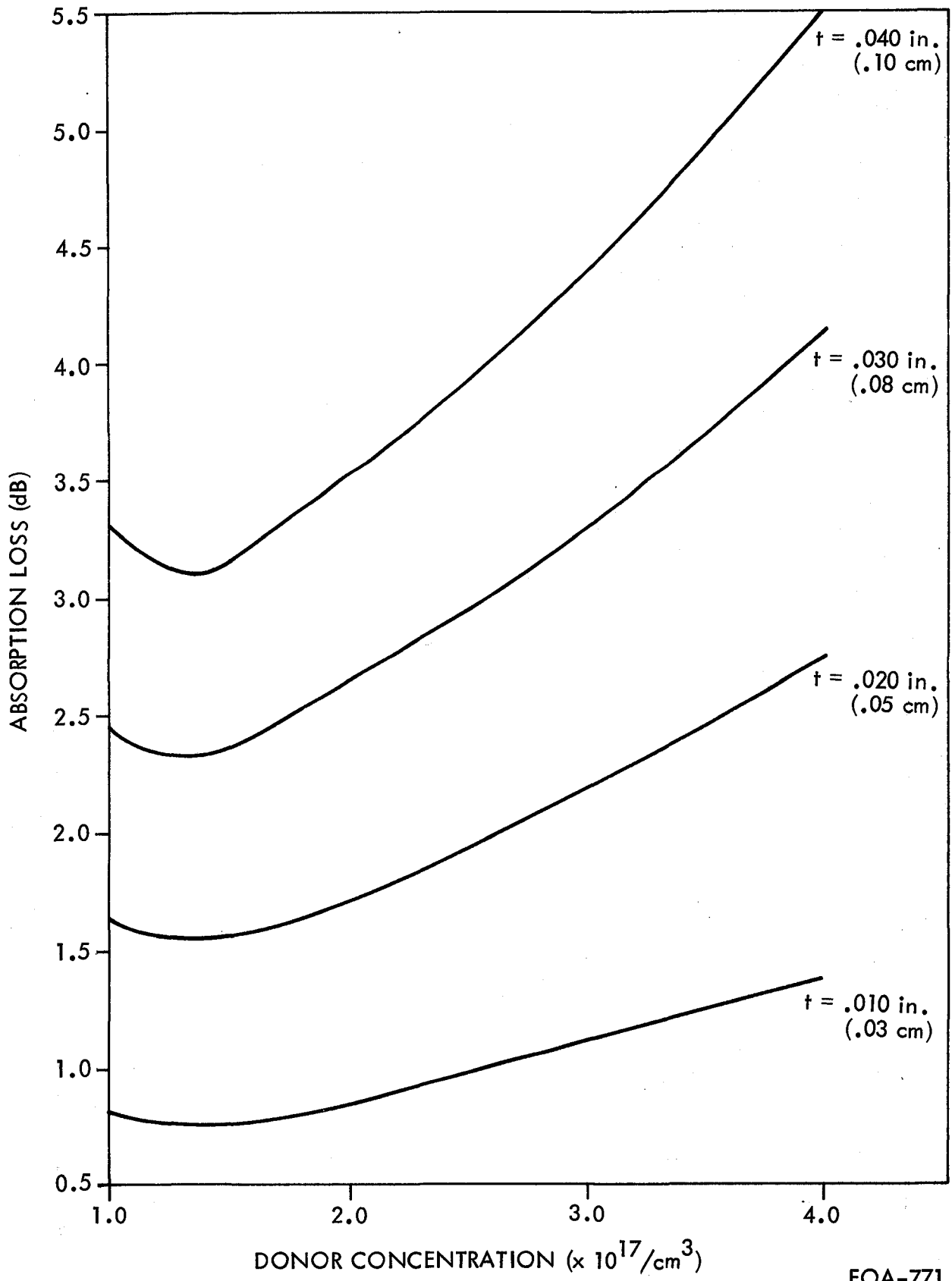
Figure 3-19. Absorption Loss for InSb at T = 300 K

EOA-771

conditions, the absorption losses would be as low as 1.6 dB with a field requirement of 8.5 kG. It has been shown that 10.6 μ isolators employing InSb wafers with these specifications have produced over 30 dB isolation.

Unfortunately, we were limited by the crystal manufacturers' ability to grow wafers. State-of-the-art techniques are still limited to trial and error to achieve donor concentrations within 1.0 x 10^{17}/cm^3 of specified values. Also, manufacturers will not guarantee better than $\pm$ 15% donor doping uniformity across the aperture of a 1 cm wafer. This becomes a problem when high figures of isolation are required since non-uniformities in doping lead to phase variations, non-uniform rotation and differences in free-carrier absorption. Figure 3-20 indicates that a 15% change in doping concentration leads to a 4° change in Faraday rotation. Assuming perfect polarizers, Figure 3-21 further illustrates what effect this has on the isolation figure. We see that a 15% change in doping uniformity leads to a 2% leakage transmission through the polarizers due to the additional rotation of the plane of polarization. It should be pointed out that these numbers represent worst-case values since leakage would not occur over the entire aperture.

3.3.1.3 Magnet Design

In order to accommodate the variety of wafers purchased, a magnet had to be designed capable of supplying a uniform magnetic field over a 1 cm aperture for magnetic field strengths varying between 3.5 kG and 11.0 kG. Due to size limitations in the present CAT system, this magnet must be small and compact. Samarium cobalt, which has high and uniform fields, compact size, and lightweight, was chosen as the magnet material. The magnet design shown conceptually in Figure 3-22 and in detail in Figure 3-23 was done using a computer program developed at Raytheon. Adjustable pole pieces were used to vary the magnetic field strengths across the 1 cm aperture in the center of the magnet. The size of the entire magnet assembly was limited to a 5-inch cube and had virtually no leakage field.
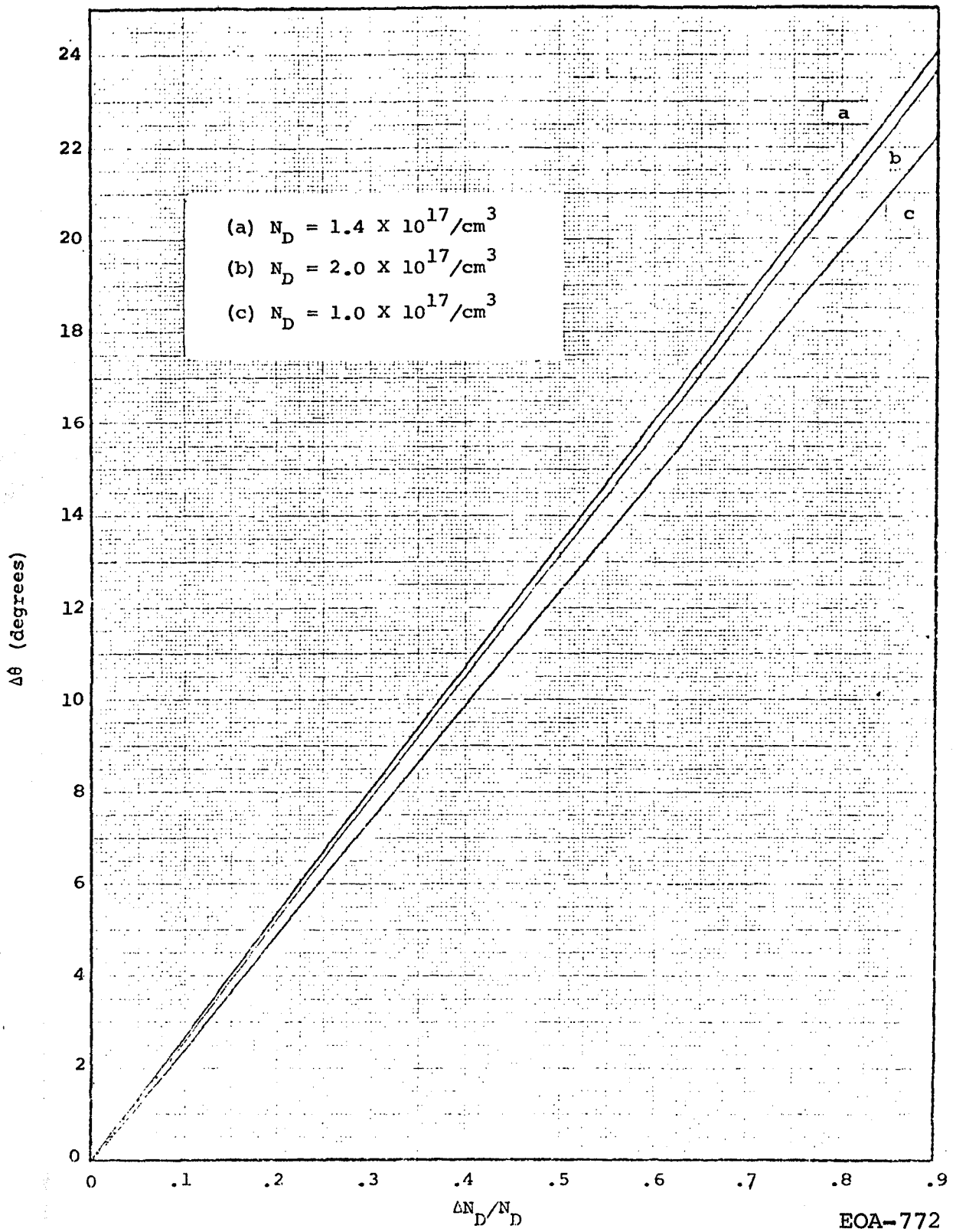
Figure 3-20. The Change in Faraday Rotation Due to a Change in Donor Concentration for InSb at T = 300 K
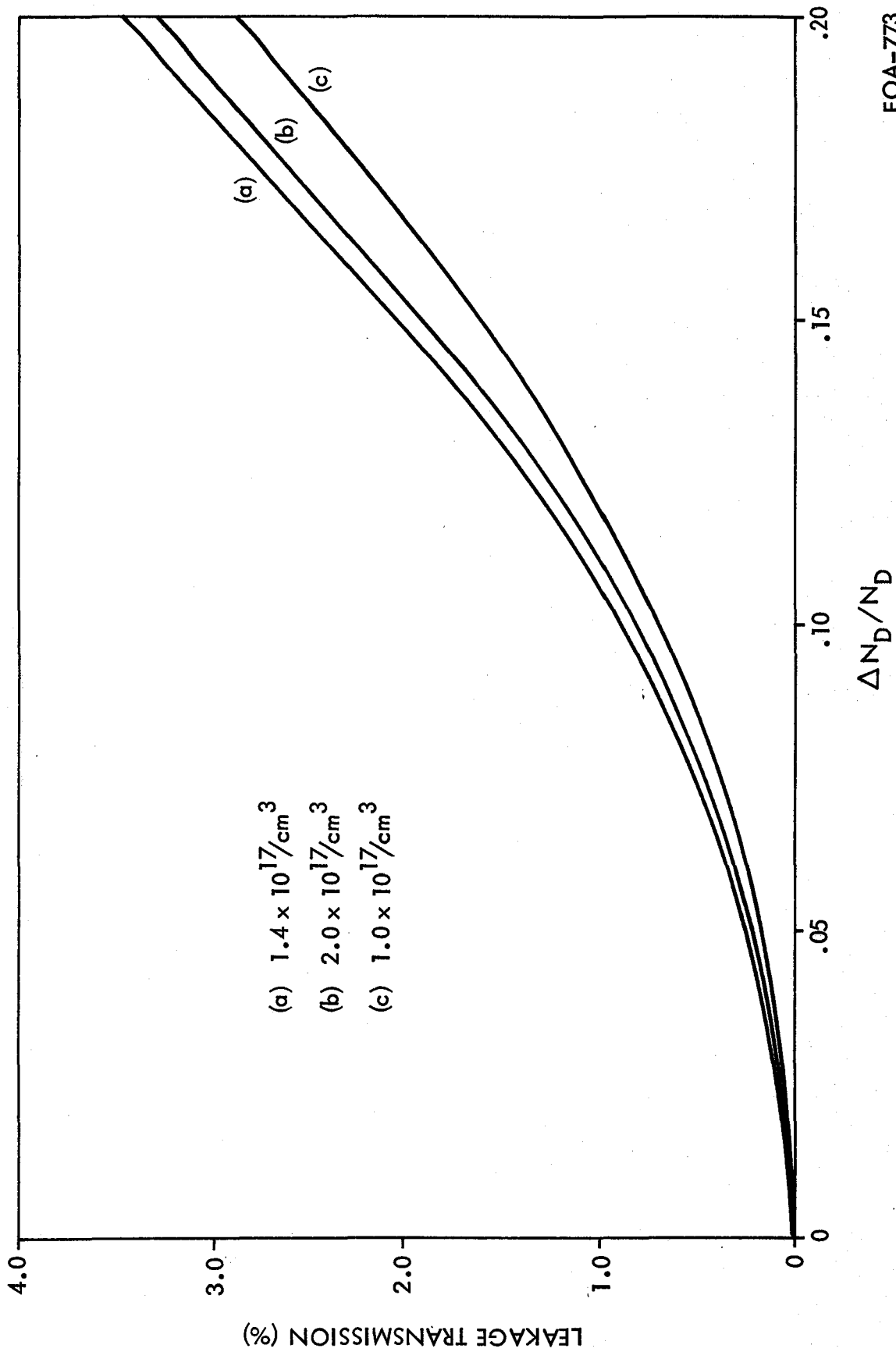
EOA-772

Figure 3-21. Leakage Transmission due to a Change in Donor
Concentration Assuming Perfect Polarizers

EOA-773

PBN-72-105

Hole for
cold finger →
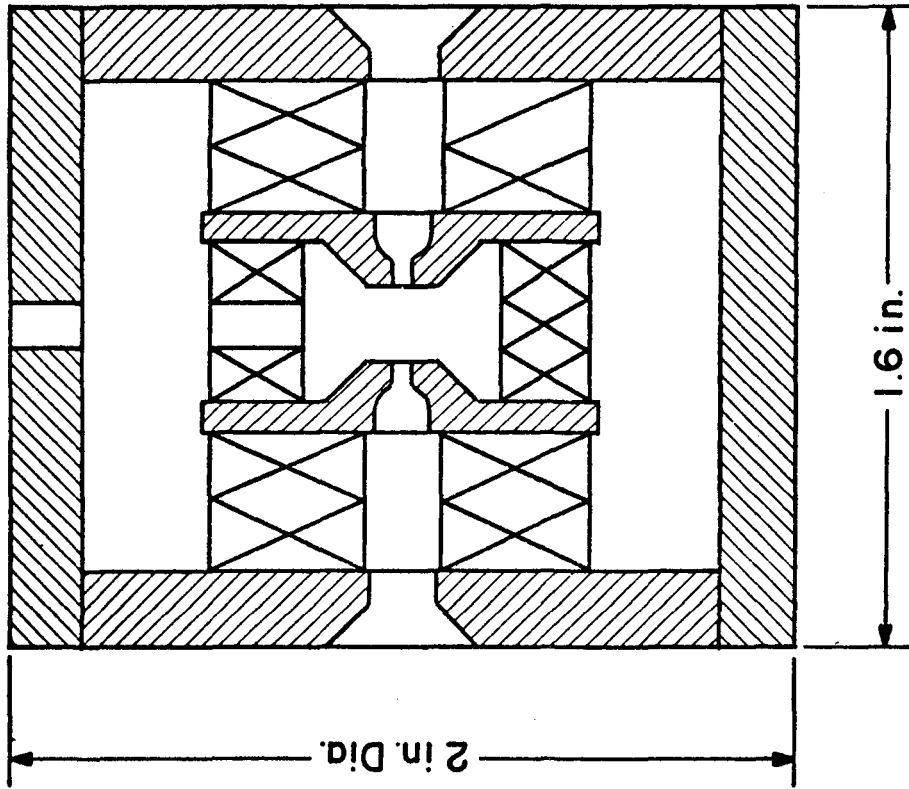
← Laser beam input

Samarium cobalt
magnets

Pole piece

EOA-774

2 in. Dia.

1.6 in.

Figure 3-22. Faraday-Effect Isolator Magnet Assembly

3-33

FLOATING POLE SUPPORT

SHIELD SLEEVE SPACER

CONETIC SHIELD SLEEVE

FLOATING POLE

CONETIC SHIELD COVER

INNER POLE

THREADED SHUNT

POLE SPACER

END SPACER

END POLE

FLUX GUIDE A

InSb WAFER LOCATION

ARC MAGNET

A

A

FLUX GUIDE B
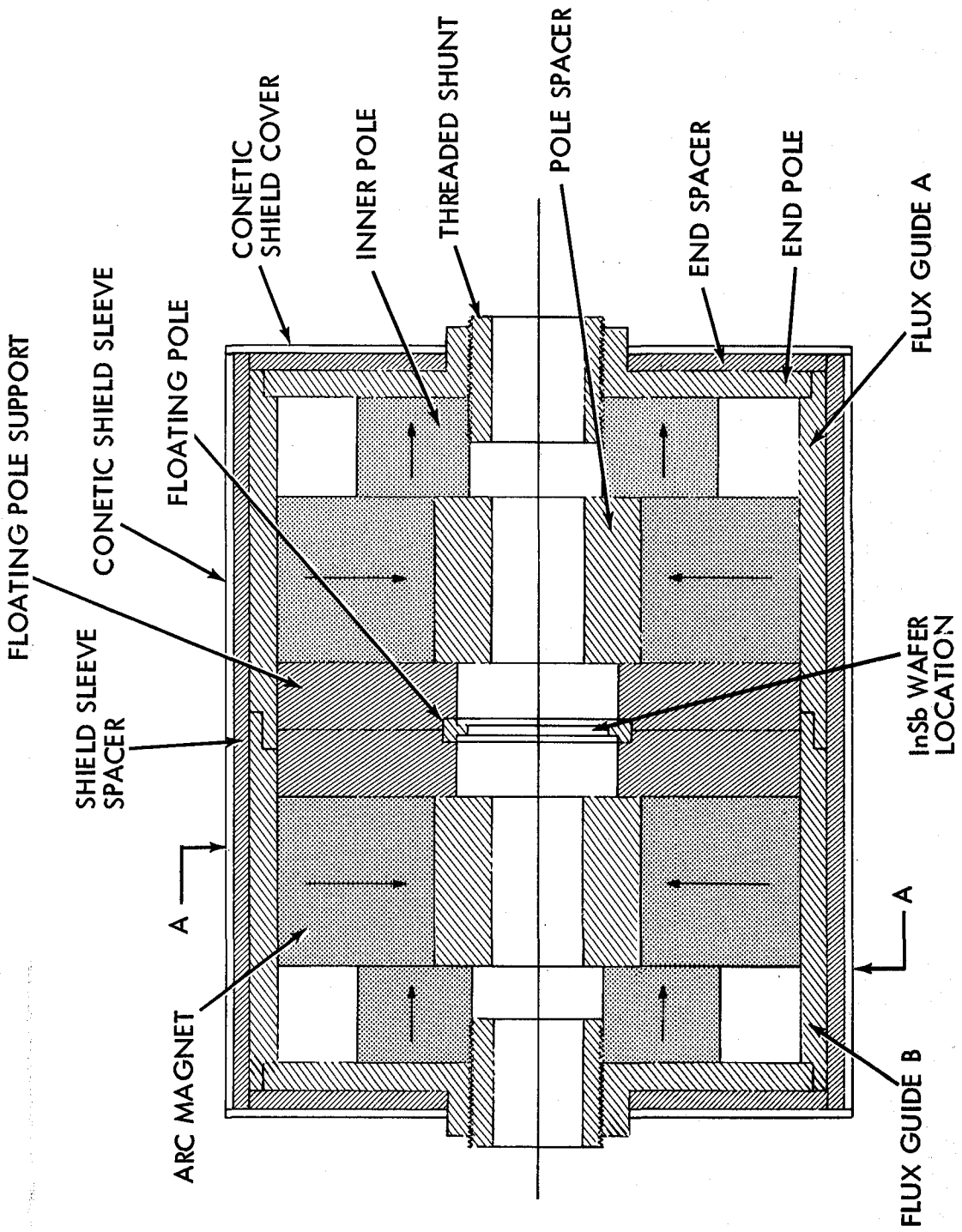
EOA-775

Figure 3-23. Cross-Sectional Views of Isolator Magnet

3.3.1.4 Thermal Characteristics

A thermal analysis was performed of the thermal properties of edge-cooled InSb in a CO_2 laser beam. It was determined that for the CAT master oscillator beam parameters, beam powers in excess of one watt would lead to thermal runaway. This would make the insertion loss of the material exceed 5 dB and induce strong refractive errors in the material. It was concluded that the isolator should be placed at a position between the modulator and beam expander where the average power level is less than 10 mW.

3.3.1.5 Laboratory Tests

Tests were conducted on the two wafers that were polished and anti-reflection coated, when the magnet was assembled and delivered. The field strength of the magnet was less than the computer prediction; however, it was enough to produce $45°$ rotation of the polarization entering wafer 1 when the poles of the magnet were shunted. This means that the thinner wafer, 2, would also be usable in this magnet by unshunting the poles. Measurement of the rejection of the ZnSe tent polarizers yielded 12 dB which is the expected amount. (With the input and output polarizers set at $45°$, wafer 1 installed, and the magnetic field applied, transmission losses of about 2 dB were measured in the correct direction.) Transmission in the reverse direction yielded 12 dB. This gives an actual isolation of 10 dB, which is less than the expected 12 dB.

Examination of the beam quality leaving the isolator shows a strongly divergent ring-shaped beam (see Figure 3-24A). A set-up was constructed to image the wafer on a pyroelectric vidicon to make an examination of material uniformity. At this point, it became obvious that the material had an inclusion causing refraction of the beam. The inclusion appeared to be a region possessing a different index of refraction. The manufacturer would not speculate on the crystal non-uniformity but expressed concern with the Te concentration. An effort was made to determine, by imaging, if the remaining unpolished wafers
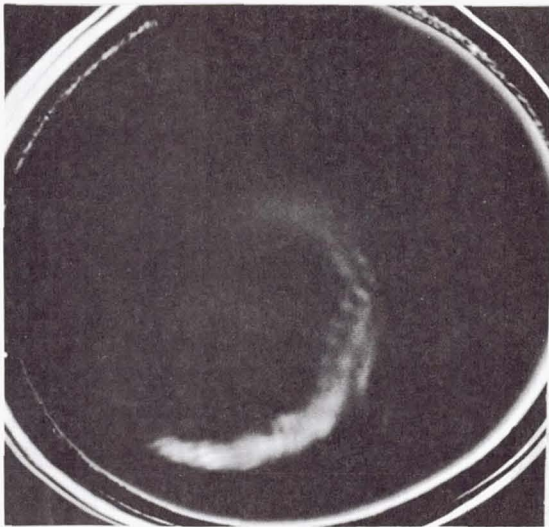
A

Output of isolator projected on surface of pyroelectric vidicon target. Beam is going through the isolator in the low loss direction.
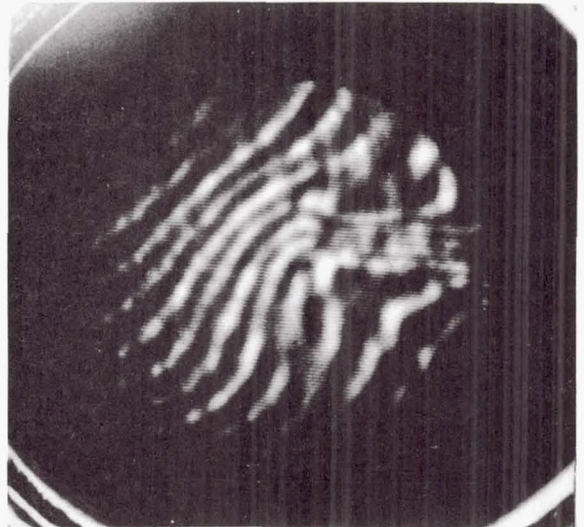
B

Wafer imaged on vidicon target with lens. Note the fringe pattern generated between the two surfaces.
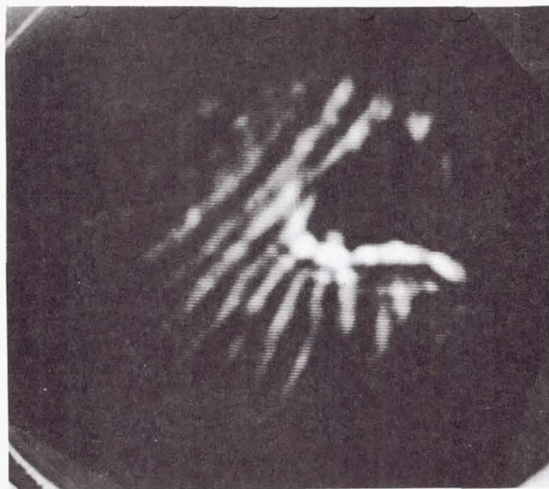
C

Wafer has been moved toward the lens out of the focal plane which images the inclusion. Note that the inclusion position is where the fringe bunching occurred in Photo B.
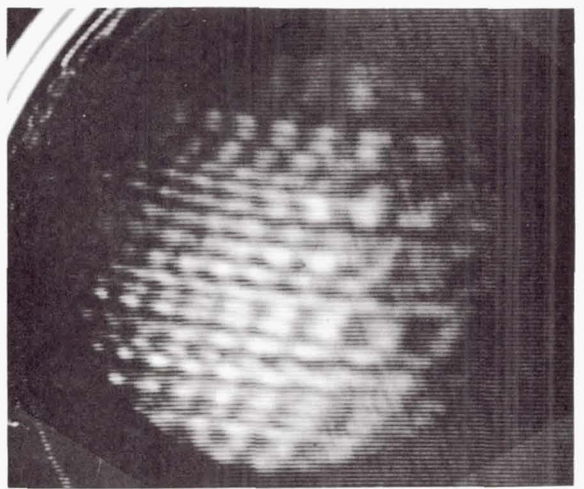
D

Saw line marks in wafer. Wafer imaged at Pyrocon.

EO-454

Figure 3-24. Examination of Beam Quality

had inclusions. In all but 2, inclusions could be seen. Two wafers without inclusions were polished in-house. Polishing proved extemely difficult because of thinness and a tendency to creep after polishing. To achieve flatness, they were polished too thin. Because of the lack of AR coatings on these wafers, fringes were generated between the two surfaces of the wafer (Figure 3-24B) showing the warping of the wafer (they should be straight lines) and in the region of tightest warping and bunching, the location of the inclusion (Figure 3-24C). Based on observations, the difficulty of polishing may be greatly reduced with uniform material.

When the wafer was mounted, there was a small amount of scatter from saw lines as shown in Figure 3-24D, which was not significantly detrimental to the operation of the isolator.

The isolator was assembled with each wafer in turn and measurements made of insertion loss and maximum rejection with the addition of another polarizer. The following are the results of optical tests on the isolator using an external wire grid polarizer (WGP):

	Wafer 1	Wafer 2
Insertion loss	-1.8 dB	-1.7 dB
Isolation	-18.6 dB	-18.3 dB
Rejection of WGP	-19.8 dB	-19.6 dB
Difference between isolator in beam and out	-1.2 dB	-1.3 dB

A test of the totally assembled isolator with Wafer 2 using built-in ZnSe tent polarizers and wave plate guides gave the following results:

Insertion loss	-1.9 dB
Isolation	-12 dB

Since the maximum rejection of a tent polarizer of ZnSe would be -12 dB, the above isolation figure is what would be expected. These tests concluded that the isolator was operating as well as could be expected and that no change to the magnet would be required.

It was also noted that the entrance angle of the beam into the isolator polarizer was important because of the compactness of the polarizer assembly. Internal reflections, despite the inner blackened surfaces, would emerge with the same polarization as the entering beam. This would cause a variation in isolation depending on the angle of the entering beam. For this reason, care is demanded in mounting the isolator in the system.

3.3.1.6 Field Tests

The major problem with backscattered energy in the CAT system was identified as frequency pulling of the master oscillator. This could be viewed as a periodic frequency shift for stationary targets between ± 2 MHz. The periodicity is due to slow changes of the system temperature, which covers the length of the resonant cavity between the master oscillator and the telescopic secondary mirror. This scatter could be minimized but not eliminated by placing a ball obscuration in front of the secondary. The effects of this pulling could be directly observed by viewing the 10 MHz beat frequency between the two offset locked lasers on the spectrum analyzer "A" scope. A frequency shift would cause the 10 MHz signal to move out of the analyzer bandpass filter and could be displayed by viewing the vertical output of the analyzer on a scope triggered by the modulator signal. There was also an effect on the output pulse shape at the time of the frequency pulling which came to be called breakup. The output became very spiked and had no decay tail. This would cause a mismatch of the return pulse shape in the processor filter bank and subsequent loss of detected signal strength.

Before the installation of the isolator, photos of the "A" scope display were taken. Figures 3-25A and 3-25B show the breakup before the system was modified with the isolator. Figure 3-25A is a worst-case photo with the ball removed from in front of the secondary. Figure 3-25B is a tweeked case where the ball has been carefully positioned in front of the secondary. The frequency pulling realized, even in the best case above, was more than the system could tolerate for proper operation.
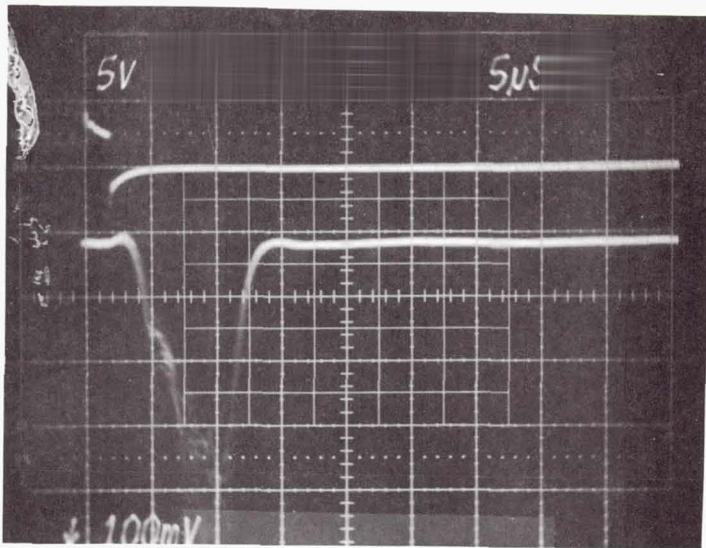
A) "A" Scope display of 10 MHz beat frequency worst case of pulling with ball removed and no isolator.
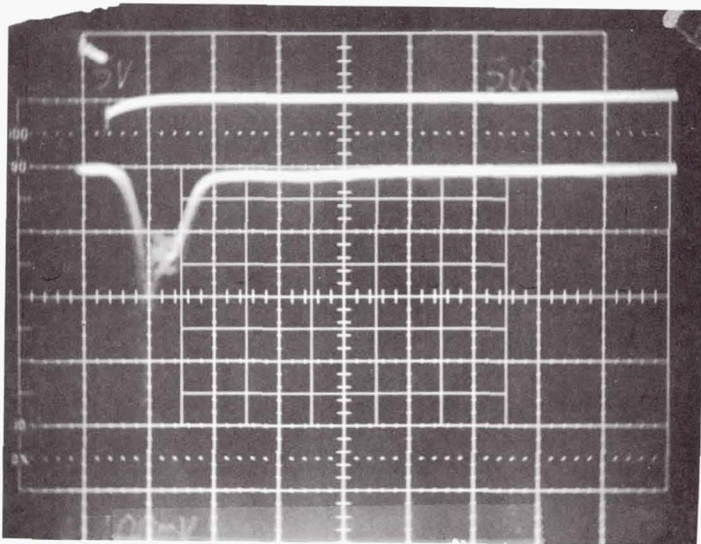
B) Best case of pulling with ball positioned and no isolator.
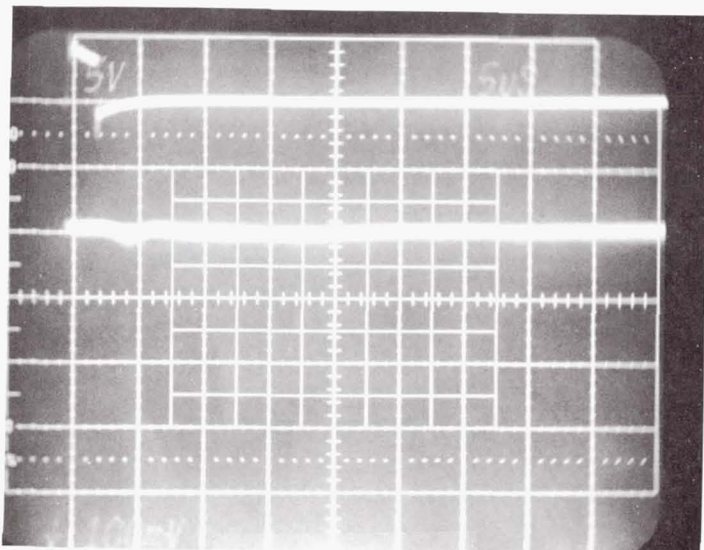
C) Isolator installed and no ball positioned.

EO-455

Figure 3-25. Effect of Isolator on System Stability

The isolator was installed and complete realignment was required of the optical path from the modulator on through to the amplifier output. The side stepping mirrors were moved forward as well to make room. System alignment had to be made with the InSb wafer removed so that visual alignment could be made with the cathetometer. The isolator was mounted against hard stops so that it could be removed and replaced, after wafer replacement, to the exact same alignment. With the isolator installed, there did not appear to be any degradation of the output beam. Power was about 12 mJ at 2 μs pulse length. Figure 3-25C shows the "A" scope display after the isolator was installed with the ball obscuration still in the same location as for Figure 3-25B of the best case with no isolator. The improvement was remarkable.

Several plots were made of the first moment on the computer to determine the frequency stability of the system as the computer and processor saw it. Figure 3-26 is a plot of the first moment with the ball tweeked and all other system adjustment optimum. Frequency deviation was minimal, plotted as meters per second on the vertical axis and elapsed time in seconds on the horizontal axis. The target was the stationary sandpaper target on Madkin mountain.

3.3.2 TELESCOPE INVESTIGATIONS

The first telescope design proved less than optimum because of the large amount of power which was backscattered from the secondary mirror. This backscatter was a leading cause of high power levels at the detector and led to receiver saturation. It also caused premature oscillation of the amplifier and pulse leading edge sharpening, resulting in decreased effective system output. To reduce these problems, an effort was devoted to the evaluation of alternate secondary mirror designs.
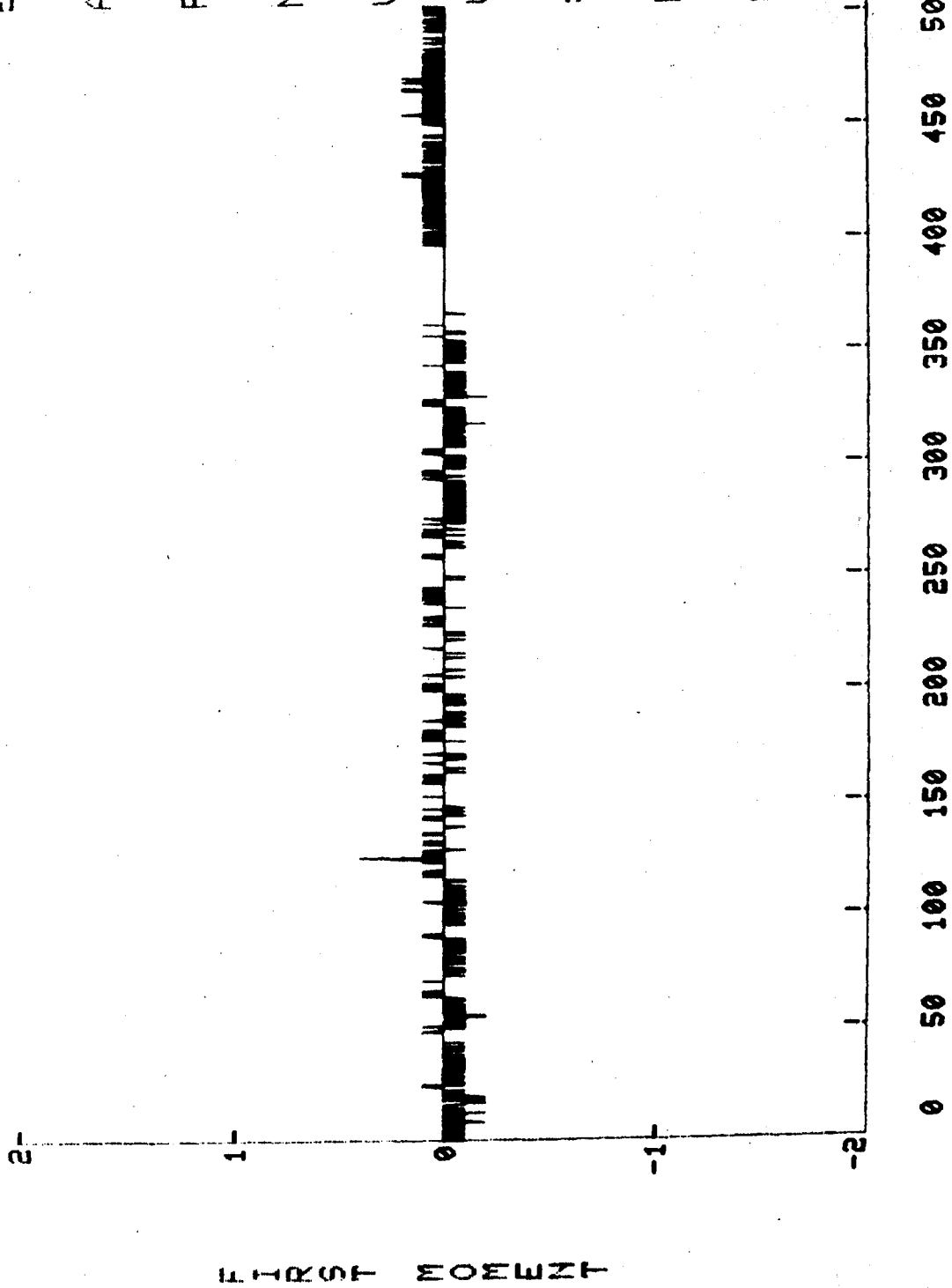
Figure 3-26. Variation In Apparent Velocity of Stationary
Target With Isolator Installed

A computer analysis was performed to determine the backscatter coefficient of both the present design and a Raytheon design which effectively increases the size of the central obscuration whose function it is to reduce the on-axis backscatter power. No obscuration can be totally effective in eliminating the backscatter power because of the tendency of the geometric shadow to fill in due to diffraction. Thus, calculation of the backscatter coefficient for a particular design requires solution of the appropriate diffraction integral. This is a relatively simple task in the case of on-axis diffraction intensities, but requires the use of numerical calculations for the general case.

Following the analysis of Webb[2] the intensity of a diffraction pattern may be written as:

$$I(r_o, Z) = \frac{2P}{\pi w^2} \left(\frac{k}{Z}\right)^2 \left(S^2 + C^2\right) \tag{1}$$

where:

$$S = \int_a^b e^{-\left(\frac{r_1}{w}\right)^2} J_0\left(\frac{kr_1 r_o}{Z}\right) \sin\left(\beta r_1^2\right) r_1 dr_1 \tag{2}$$

$$C = \int_a^b e^{-\left(\frac{r_1}{w}\right)^2} J_0\left(\frac{kr_1 r_o}{Z}\right) \cos\left(\beta r_1^2\right) r_1 dr_1 \tag{3}$$

and

$$\beta = \frac{k}{2}\left(\frac{1}{R} + \frac{1}{Z}\right)$$

with:

a = radius of obscuration

b = radius of truncation

Z = position of plane of observation

r_0 = observation coordinate

r_1 = aperture coordinate

P = laser power

R = radius of curvature of laser beam
(>0 for diverging beams)

w = beam radius

λ = wavelength

k = $2\pi/\lambda$

3.3.2.1 Present Telescope Design

The afocal Newtonian-Cassegrain modified telescope presently
incorporated into the CAT system consists of a parabolic primary (12 in.
or 30.5 cm in diameter) and a parabolic secondary (1 in. or 2.54 cm
in diameter). The beam entering the telescope barrel is directed
towards the secondary via a 45° mirror and is expanded and collimated
by the telescope optics. In this configuration, a portion of the
transmitted laser beam located close to the optical axis will reflect
off the secondary mirror and be backscattered along the incoming path
of the laser beam. To alleviate this problem, a 3/32 in. (.24 cm) hole
was centered on the 45° mirror to obstruct the central portion of the
transmitted beam. In order to make the analysis manageable, the geometry
was modified to place the obscuration on the secondary rather than
the diagonal mirror. Since the secondary is in the near-field of the
obscuration, no significant error should be expected.

For the present system we have:

a = .0468" (1.189 mm) R = 2.25" (5.715 cm)

b = .5" (12.7 mm) w = .295" (.749 cm)

λ = 4.17 x 10^{-4}" (10.59 x 10^{-4} mm) Z = 20" (50.8 cm)

Given these values, the S and C integrals were evaluated using
a numerical analysis computer program. The backscatter intensity
distribution was then calculated and plotted as a function of
position off axis (Figure 3-27). Since the intensity distribution
is circularly symmetric around the optic axis, the intensity
function was weighted and then integrated using a polar planimeter
to determine the backscattered power collected by a 1-inch (2.54 cm)
aperture in the observation plane. It was assumed that all the
power collected in this plane is seen by the detector.

The dimensionless quantity P_{det}/P_{out} is used as a figure of
merit in comparing the various designs. This quantity represents
the ratio of the backscattered power detected in the plane of obser-
vation to the output power supplied by the laser amplifier. By
integrating the backscattered intensity distribution over the 1-inch
(2.54 cm) aperture in the plane of observation, the backscatter
power ratio was found to be:

$$\frac{P_{det}}{P_{out}} = 1.08 \times 10^{-3}$$

To weigh the advantages of the presence of the obscuration,
the intensity distribution in the same observation plane was cal-
culated without the obstruction. This intensity distribution is
simply an expanded Gaussian beam and is given by:

$$I(r_o, Z) = \frac{2P}{\pi w'^2} e^{-2r_o^2/w'^2}$$

where w' is the expanded Gaussian beam radius in the plane of observa-
tion. In the present design, w' = 2.95" (7.49 cm) at Z = 20" (50.8 cm).
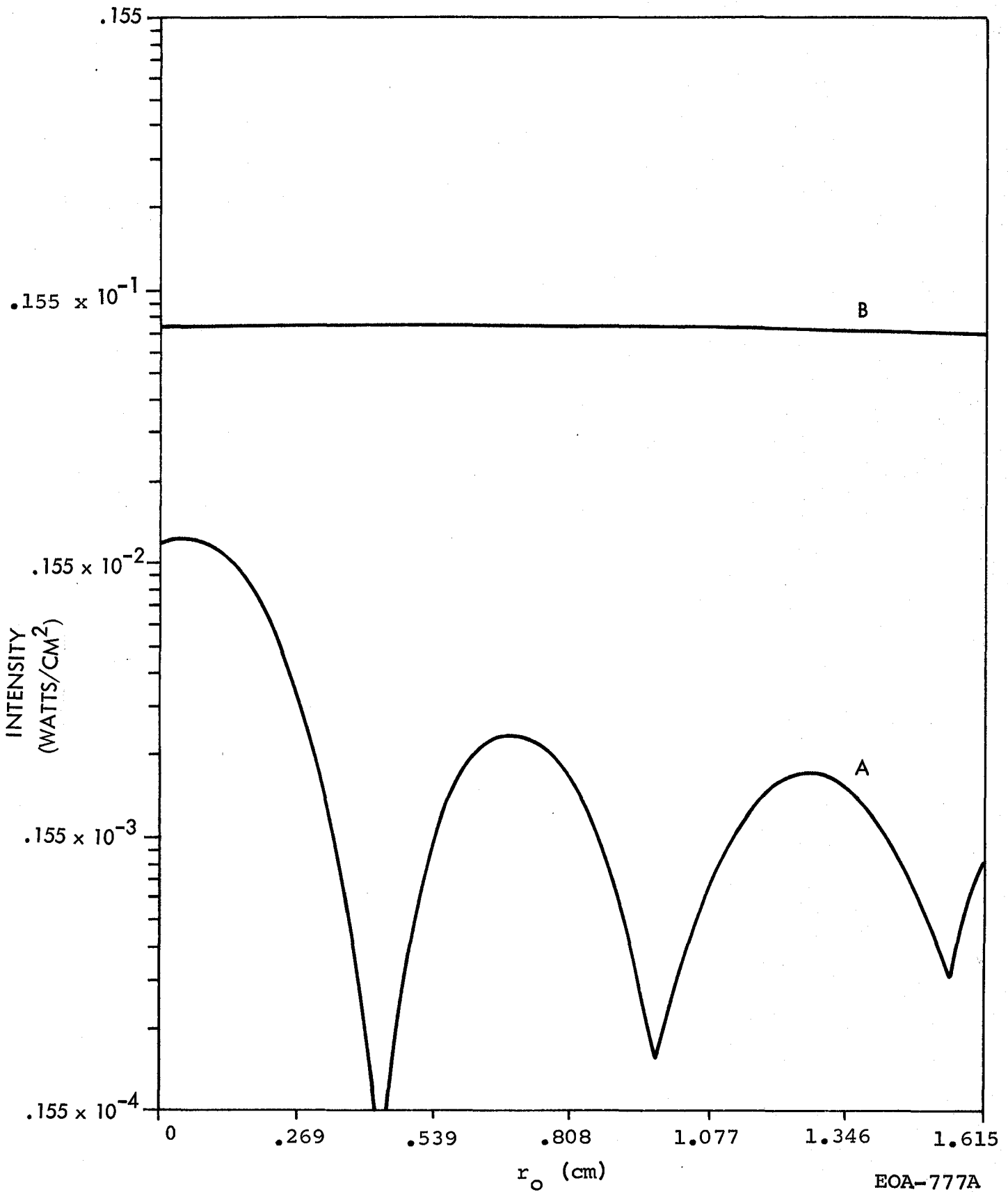
Figure 3-27. Backscatter Intensity Distribution for Present Telescope (A) with Obscuration, (B) without Obscuration

EOA-777A

3-45

This distribution is plotted in Figure 3-27. Integration of this function over the area of the 1-inch aperture produced a backscatter power ratio of:

$$\frac{P_{det}}{P_{out}} = 5.58 \times 10^{-2}$$

Therefore, the backscatter due to the telescope secondary is reduced by approximately 17 dB with the obscuration present.

3.3.2.2 Modified Telescope Design

The intention of the modified design is to expand the Gaussian beam before it strikes the central obscuration in order to reduce the intensity of the beam close to the optic axis, thereby reducing the magnitude of the diffracted light. At the same time, this allows us to use a larger obscuration which brings the detector further into the geometric shadow.

For the modified design, the backscatter coefficient is determined by integrating over a diffraction distribution in a plane near the quarter-wave plate location. This distribution is shown in Figure 3-28. Integrating over the 1-inch diameter of the collecting aperture leads to a backscatter power ratio of

$$\frac{P_{det}}{P_{out}} = 5.66 \times 10^{-4}$$

For comparison, the backscatter intensity distribution for the unobstructed Gaussian beam was also calculated at $Z = 20$ in. (50.8 cm) and is plotted in Figure 3-28. The backscattered power ratio for this distribution is

$$\frac{P_{det}}{P_{out}} = 4.4 \times 10^{-2}$$
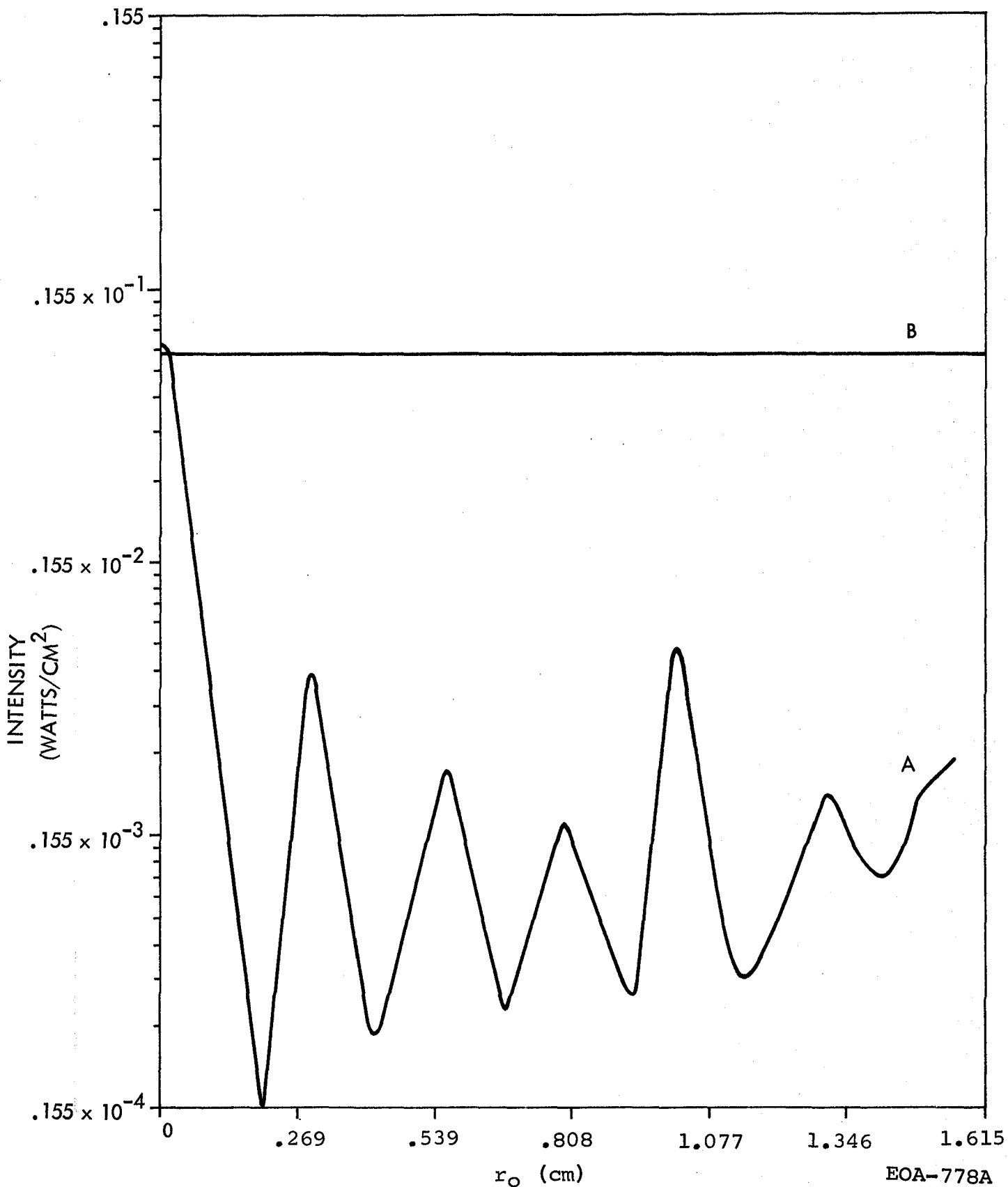
Figure 3-28. Backscatter Intensity Distribution for Modified
Design (A) with Obscuration, (B) without
Obscuration

EOA-778A

3-47

3.3.2.3 Results

Table 3-2 summarizes the backscatter power ratios due to the secondary for each design in units of watts detected/watts output.

TABLE 3-2

BACKSCATTER POWER RATIOS DUE TO SECONDARY MIRROR

	WITHOUT OBSCURATION	WITH OBSCURATION
PRESENT DESIGN	5.58×10^{-2}	10.8×10^{-4}
PROPOSED MODIFIED DESIGN	4.50×10^{-2}	5.66×10^{-4}

We see that in comparing the two designs without their obscurations the backscatter power ratios are essentially equal. This is an expected result since the geometry of the backscattered beam remains constant regardless of the shape or focal length of the telescope secondary. The intention of the modified design was to illuminate the obscuration with an expanded Gaussian beam, thereby reducing the backscattered radiation due to diffraction. In principle this works; but for the present application, the tradeoffs involved did not allow us to take advantage of highly diverging Gaussian beams or large central obscurations. Results show that the modified design would only be capable of reducing the back-scattered power by 2.8 dB over the present design. This slight reduction did not seem sufficient to warrant modification of the existing design.

3.3.3 REDESIGN OF BEAM EXPANDERS

The goals of the beam expander redesign program were to increase the output aperture diameter, remove an off-axis alignment built into the present expander, simplify the focusing adjustment, and consider modifications in the expansion ratio.

3.3.3.1 Beam Expander Analysis

As the transmitter beam propagates through the power amplifier, it expands (due to diffraction) to the point where the wings of the intensity distribution are reflected by the walls of the amplifier tubes and apparently scattered back towards the oscillator by the edges of the various apertures in the system. A smaller beam could be used within the amplifier either with the present collimated beam or by focusing the transmitter beam expander so that a waist occurred within or beyond the amplifier.

The effect of varying the size of the collimated amplifier entrance beam was evaluated and the results are shown in Figure 3-29. It can be seen that with the present entrance beam waist diameter of 16 mm, the amplifier exit beam in the absence of wall reflections or truncations would be 18 mm. This exit diameter could be reduced to 16 mm by using an entrance beam diameter of 12 mm with a change in the beam expansion ratio from 2x to 1.5x. Figure 3-29 suggests that a non-expanded entrance beam diameter of 8 mm would also result in an 18 mm exit beam diameter; however, it does not mean that the expander could be dispensed with. Figure 3-29 assumed that the Gaussian beam waist was located at the amplifier entrance, whereas in the absence of the expander, the waist is located near the output coupler of the local oscillator, 193 cm from the amplifier. In the absence of the beam expander, the exit beam diameter would be approximately twice the diameter of the amplifier tube bore.

A second approach to reducing the exit beam diameter is to focus the beam expander so that the beam waist occurs near the output end of the amplifier. This technique is limited by diffraction to waist locations which are within the amplifier. It can be shown that a Gaussian beam cannot be focused to a waist at a distance greater than half the far field of the focused beam. The far field distance is given by

$$d_{ff} = \frac{\pi D^2}{4\lambda}$$
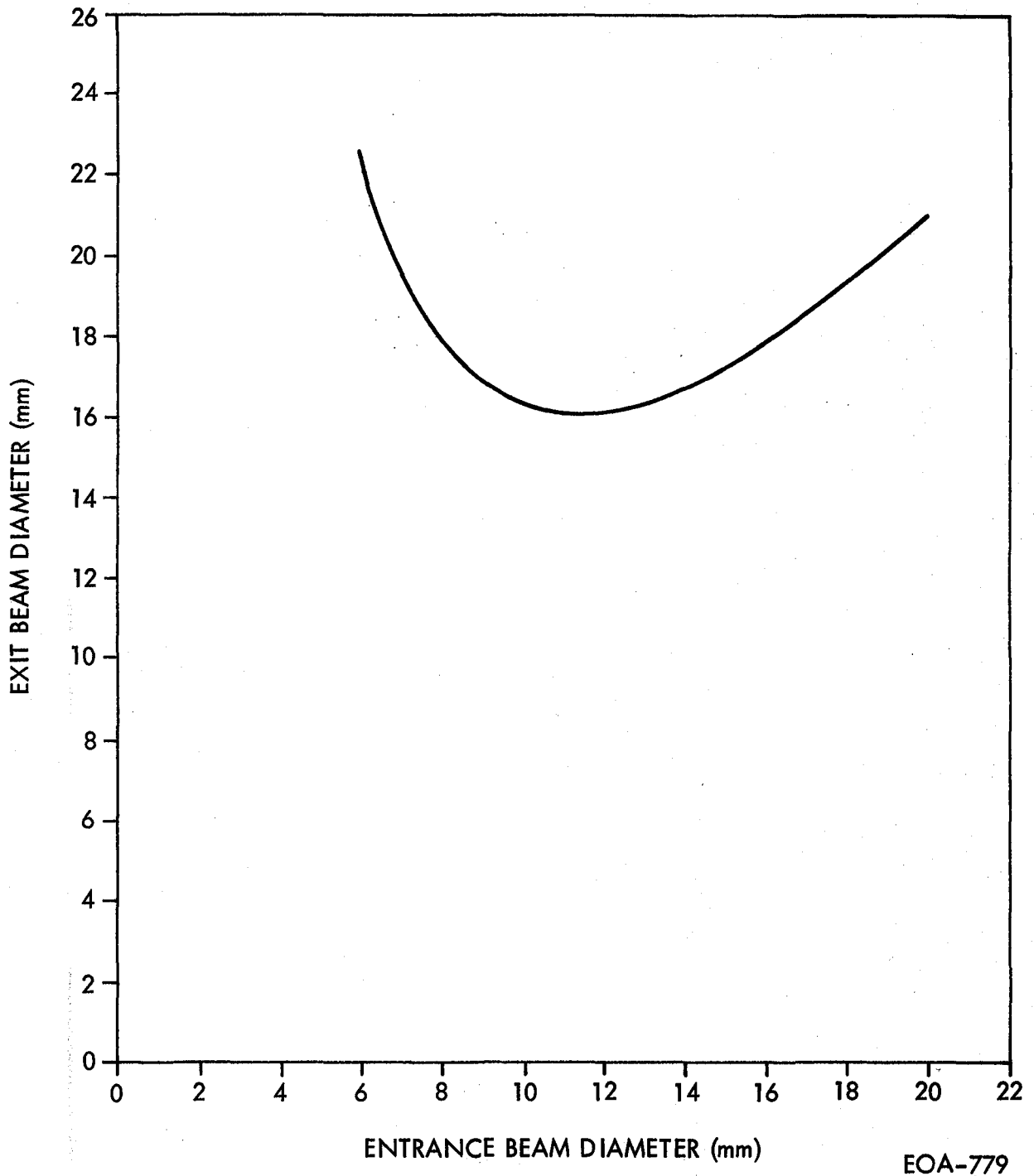
Figure 3-29. Diameter of Amplifier Exit Beam vs.
Entrance Beam (Lamp $\leq$ 953 cm)

where

D = diameter of $1/e^2$ intensity point

λ = wavelength

For the present beam expander, the maximum distance $d_{ff}/2$ is about 8.5 m and the waist diameter at this point is 11 mm. No appreciable expansion occurs between the waist and the amplifier exit window.

The focusing approach offers several advantages:

1) It requires no modification to the present values of the beam expander focal lengths.

2) The amplifier exit beam is a collimated beam which matches the wavefront requirement of the telescope.

3) The exit beam is smaller in diameter and suffers less scattering.

4) The local oscillator beam expander wavefront can be collimated and readily checked by shearing interferometry.

For these reasons the expander design work detailed below has been directed toward a 2X expansion ratio with focusing capability.

3.3.3.2 The Redesigned Beam Expanders

The beam expanders now in system use have the following characteristics:

	Local Oscillator		Transmitter	
	Offset L.O.	MOPA		
Input Aperture	6.5 mm	6.5 mm	15 mm	
Output Aperture	22 mm	22 mm	22 mm	
Expansion Ratio	3.5:1	3.5:1	2:1	
Axis Offset	22.5 mm	22.5 mm	26.5 mm	
Design Inputs ($1/e^2$)	4.4 mm	8 mm	8 mm	
Design Outputs ($1/e^2$)	15.4 mm	28 mm	16 mm	

As described, the transmitter beam expander is designed to be focused so that the beam has a waist diameter of approximately 14 mm at the exit of the last amplifier tube. This reduces the amount of amplifier wall scattering and results in a substantially cleaner output beam. With the 16x expansion of the telescope, this produces an output beam of 176 mm diameter or 64% of the telescope diameter. A shorter focal length secondary would bring this value close to the 80% optimum.

The local oscillator beam expander is designed so that it produces a somewhat larger beam than the transmitter beam when used with the Sylvania local oscillator to permit returning to the non-offset configuration, if desired. Local oscillator diameters less than the transmitter beam size result in rapidly decreasing signals, while larger diameters with truncation do not significantly affect signal levels. If it is desired to return to the collimated amplifier input, the local oscillator will nearly match the transmitter. In any event, the change in diameter will not affect the signal by more than 0.3 dB.

3.3.4 LOCKING LOOP

3.3.4.1 Introduction

The offset system was an analog control system which locked one laser at a fixed offset frequency with respect to another as long as the first laser was on a transition line that the second, or controlled, laser could tune to. A transition line stabilizer was available to hold the first laser on a useful line (usually P20), although it was often found to be unnecessary.

Acquisition of lock was automatic, once the proper line was tuned by the first laser. Control logic in the stabilizer would sweep the controlled laser until the correct frequency was tuned, and lock automatically.

The design used a straightforward frequency locking loop with a discriminator, reference and integrator. While this design was stable with respect to oscillation, a novel discriminator and reference design was required to reduce the effects of thermal drift.

3.3.4.2 Basic Principles

The operating principles of the locking loop were described in Section 2.2.1.4 with a block diagram in Figure 2-4 which is reproduced here as Figure 3-30.

3.3.4.3 Operational Considerations

3.3.4.3.1 Introduction

Although the loop description seems simple, it must be remembered that this unit is really a servo or feedback system. All phase delays and nonlinearities within the loop bandwidth must be known and compensated for if the loop is to be stable. It must be realized, also, that as long as there is to be any suppression of frequency modulation, there must be an open loop gain greater than unity at that frequency and that the suppression is a function of the magnitude of this gain. Furthermore, thermal drift of components may produce variations in the offset frequency.

3.3.4.3.2 Stability

Figure 3-31 shows a linear approximation of the component transfer functions which are significant for stability. The transfer function is:

$$H(s) = \frac{C(s)}{R(s)} = \frac{K(s + a)}{s(s + b) + K(s + a)}$$

It is desirable to have the zero and pole coincided exactly $(a = b)$. This causes the phase and gain effects to precisely cancel. If they are close (say 10% apart), the phase error will be small (5°).

The reason for the compensation mentioned previously is that a phase lag of greater than 180° will cause the servo loop to be unstable. Each R-C frequency cut at f_o produces a phase lag of frequency f as follows:

$$\phi = \text{ARCTAN} \frac{f}{f_o}$$

Two R-C cuts will eventually produce close to 180° phase lag. A phase lag of 180° causes negative feedback to become positive,
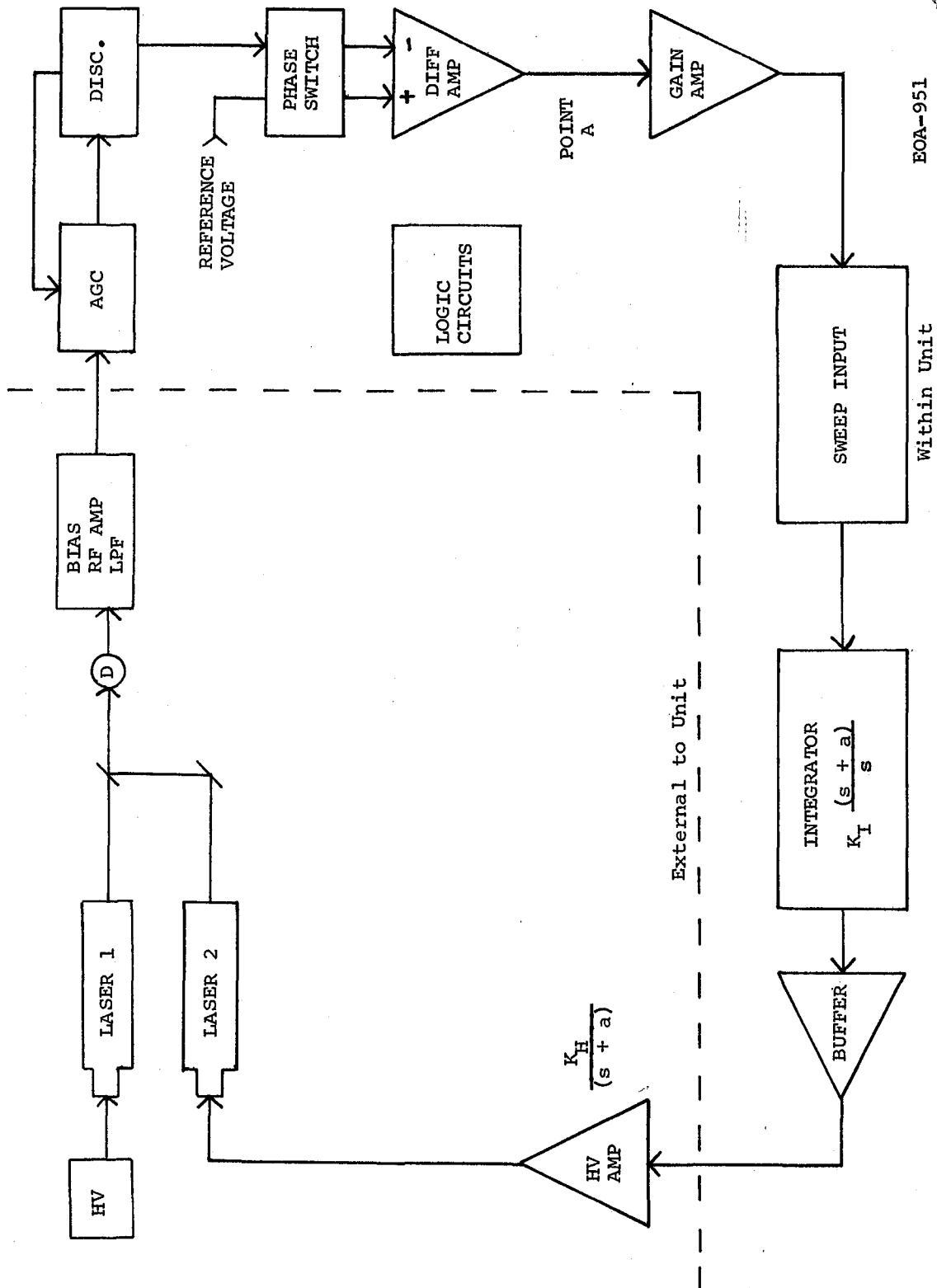
Figure 3-30. Loop Description
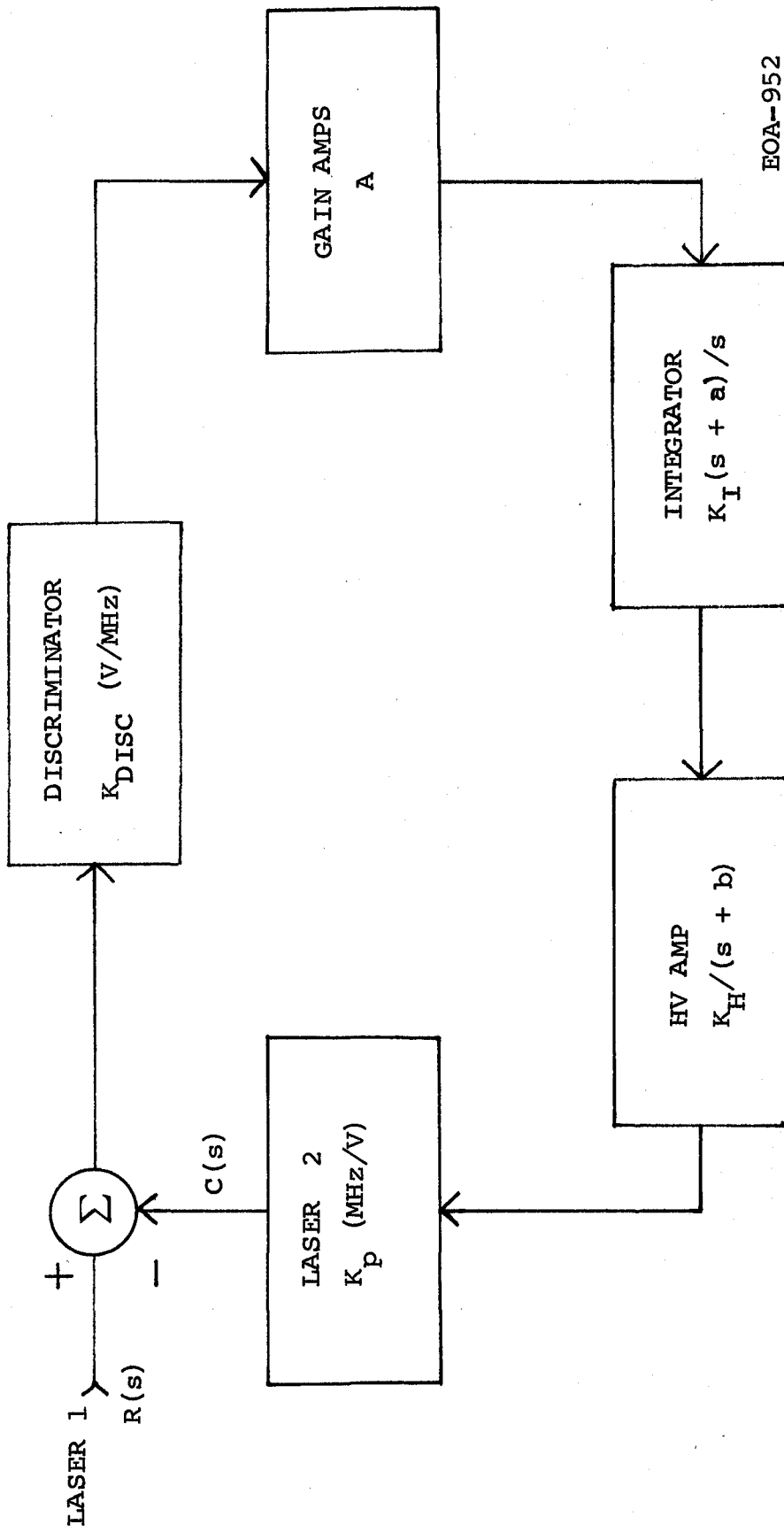
Figure 3-31. Loop Compensation

which causes instability. Any other phase lags in the loop will add to this, so it can be seen that it is desirable to have a single pole roll-off for stabilizing. If all phase shifts are known and fixed, which is not always true in an electro-mechanical system, and are compensatable, it may be desirable to have a two-pole roll-off. In this system, mechanical resonances may be present, so a single pole roll-off has been chosen.

The transfer function becomes:

$$H(s) = K_T \ (S + K_T)$$

$$\text{for } a = b$$

This is unconditionally stable as long as there is less than 90° phase shift due to nonlinearities, mechanical resonances or high frequency roll-offs.

This limit is presently set by the high voltage amplifier which has two R-C frequency roll-offs around 100 Hz. This limits the gain-bandwidth of the system to 100 - 150 Hz before instability occurs.

The next limitation is the mechanical resonance effects in laser 2 or its PZT which may produce high phase shift. This occurs in the 5 - 20 kHz range. The PZT also presents a large capacitance (10 - 60 nf) which must be driven by the high voltage amplifier. The slew rate or maximum number of MHz/second the unit can change is limited by the output current capability of the high voltage amplifier.

3.3.4.3.3 Thermal Drift

The error introduced into the frequency offset loop by thermal drift of a typical discriminator circuit was measured to be between 15 and 18 kHz per Kelvin. This was not considered satisfactory for operation of the CAT system. Analysis of all other components of the loop indicated a thermal drift of 0.55 kHz for a temperature change of 50 K. Thus, a substantial improvement could be realized with an improved discriminator design.

A novel approach using a frequency counter and two 12 bit digital-to-analog converters was adopted. Figure 3-32 shows the discriminator design. The output of the AGC was coupled to the Schmitt trigger. This resulted in a pulse train entering the synchronizer. The synchronizer allowed the pulses into the counter only when the flip-flop was high. The flip-flop was included to ensure pulse width stability in the clock circuitry, since it changed state once for each period of the clock. The counters counted the input train for one clock period. Their outputs were then sampled by the latches and converted to an analog signal. The analog signal was subtracted from a reference D/A to generate an error current, which was averaged by the filter, amplified, and added to the discriminator output, causing a correction to be applied to the integrator.

To prevent sudden pulses from causing the system to unlock, the filter was shorted when the circuit was unlocked.

3.3.5   CAT HYBRID LASER OFFSET LOCKING SYSTEM

3.3.5.1   Program Overview

The CAT Hybrid-TEA Laser Offset Locking System (OLS) stabilizes (via cavity length control) transmitter laser frequency at a 10 MHz offset from the frequency of the local oscillator (LO) laser. It can perform this function under operating conditions peculiar to Hybrid-TEA laser transmitters, mainly brief periodic loss of CW power output. Furthermore, the OLS encompasses certain timing functions which facilitate Hybrid-TEA laser operation.

This task proceeded from specifying design goals, through initial studies, completion of design, fabrication, and evaluation. The design goals settled upon after a discussion of the technology limitations and program needs are as follows:
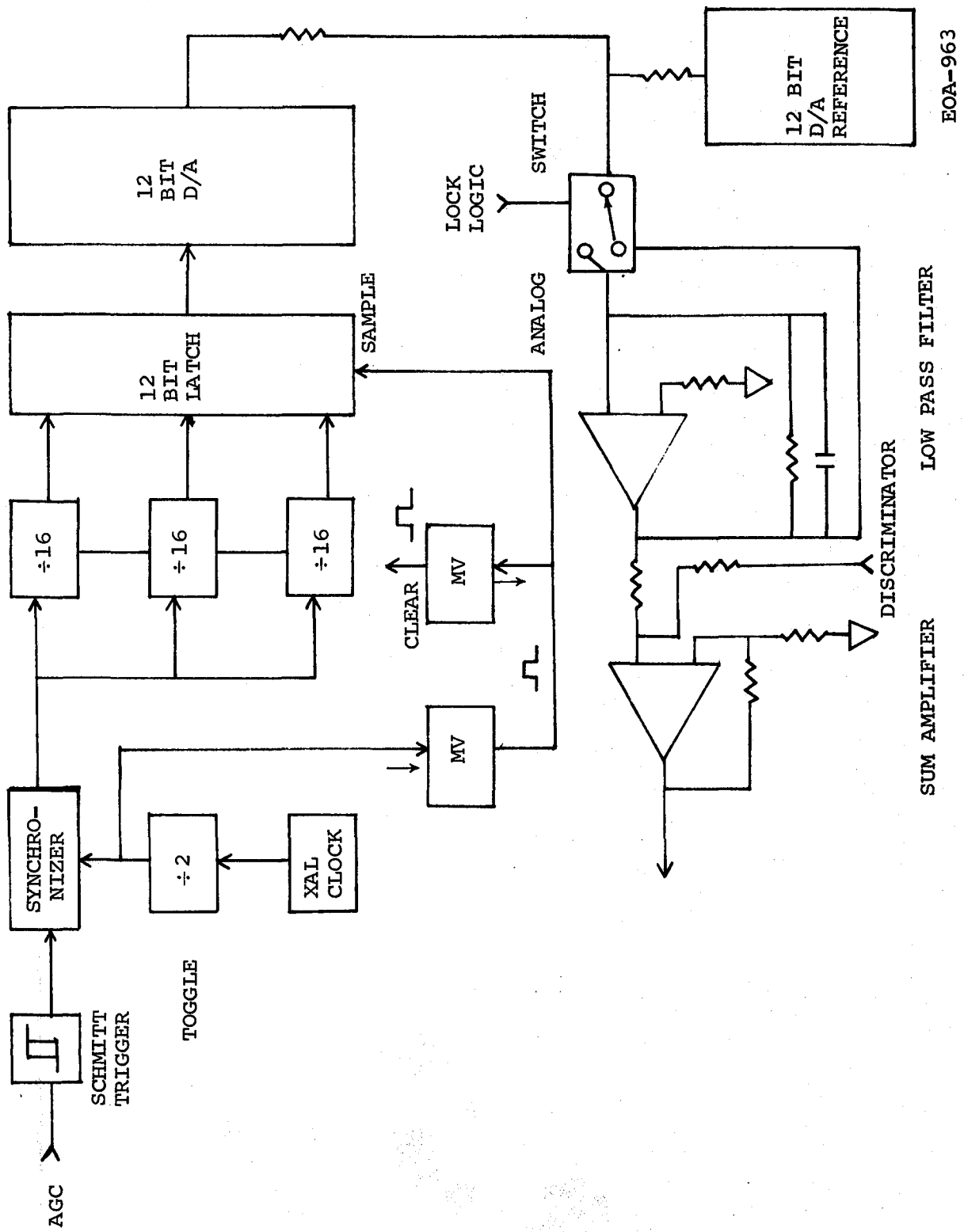
Figure 3-32. Drift Correction Circuit

Center Frequency Range   -   10 MHz to 30 MHz

Hold Time   -   3 to 300 ms

Capture Range   -   5 MHz

Locked System FM Error - $\leq \pm$ 100 kHz

Pull-in Time   - $\leq$ 3 ms

S/N Ratio   - $\geq$ 30 dB

3.3.5.2   Preliminary Technical Studies

Two studies were performed. One investigated the possibility of using a phase detector and phase locking the offset frequency to a stable crystal oscillator reference. The second investigated the possible effects of the TEA laser on a lock-in stabilizer.

3.3.5.2.1   Use of Phase Locked Offset Loop

The question of whether a phase detector should be used in the OLS rather than a frequency detector is discussed here.

3.3.5.2.1.1   Phase Locked Loops (PLL)

A phase locked loop has the general configuration of Figure 3-33. The main components are a phase detector (PD), loop filter and voltage controlled oscillator (VCO). The operation of the loop can be determined by servo theory, because the PLL is a negative feedback system - although nonlinear.

REFERENCE

FREQUENCY

PHASE (PD) DETECTOR

LOOP FILTER

VCO
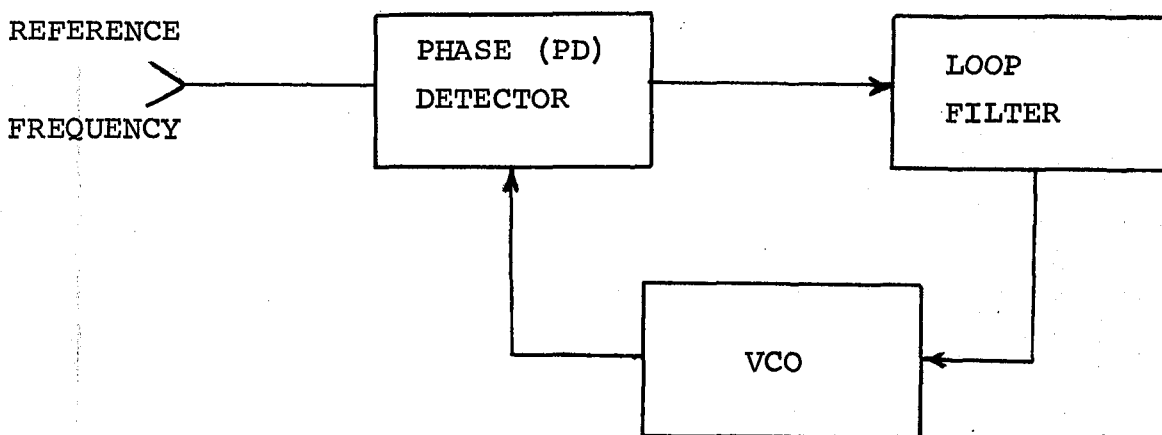
EOA-781

Figure 3-33. General PLL

The reference frequency and phase are compared with that of the VCO. If they are close enough together, an error signal is produced which causes the VCO voltage to change to correct the error. If the loop filter contains a high gain integrator, the steady state error signal will be zero, resulting in perfect phase locking.

The equivalent system utilizing lasers as the VCO is shown in Figure 3-34. The only difference is that the VCO is the frequency difference of the two lasers, and is controlled by the high voltage PZT drive.

The laser version is, like the analog version, a nonlinear approximation to a linear system. The two main sources of non-linearity are the phase detector and the VCO. The VCO may have hysteresis or a nonlinear transfer characteristic which results in changing gain and servo bandwidth.

3.3.5.2.1.2 PLL Lock Acquisition

The characteristics of the PLL are mainly dependent on the phase detector and the loop filter. The loop filter does control most of the loop parameters, other things being fixed.

To acquire lock, a PLL must be in one of two frequency "zones." The first zone is immediately around the reference frequency and is called the "lock-in" frequency ($\Delta\omega_L = \pi\Delta f_L$). If the VCO is closer than this to the reference frequency, acquisition is very rapid. If it is outside this zone, but within the next limit ($\Delta\omega_p$), and the loop is at least a second order or two integrator loop, the frequency will "pull" toward the lock-in point where it will lock. The time necessary for pull-in to occur can be large, but is dependent on the distance from the reference frequency and the servo loop bandwidth (B_L).

There are a number of approximate formulas derived for the time necessary for pull-in and the pull-in and lock-in bandwidths. They depend on the PD used. Here are given equations for a multi-
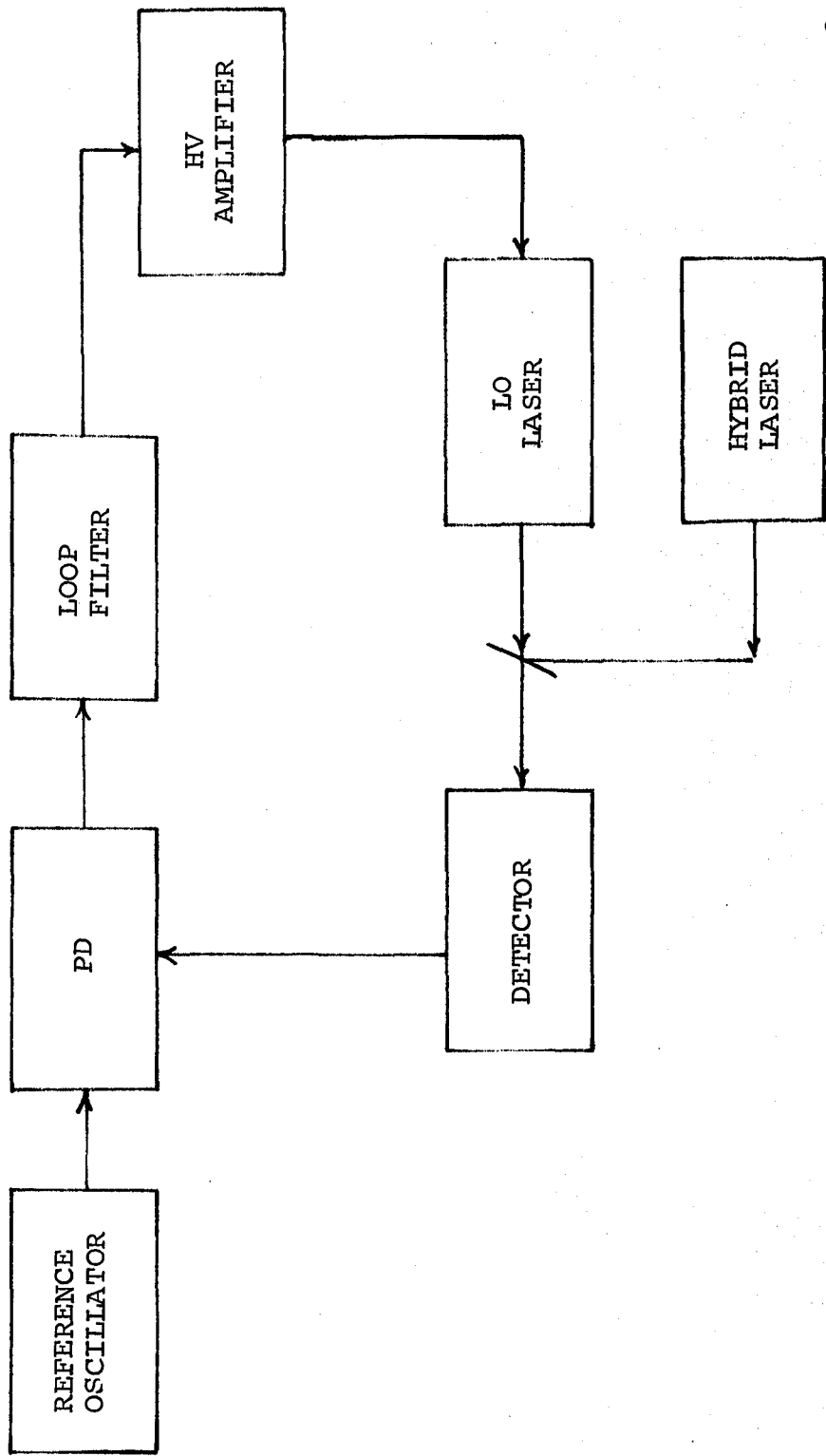
Figure 3-34. Phase Locked Offset Loop for Hybrid TEA Laser

EOA-782

plier type PD. They are also "high gain" second order loops (using operational integrators with very high DC gain).

$$\Delta\omega_P \approx 2\sqrt{\zeta\ \omega_n\ K_v} \tag{1}$$

K_v = DC loop gain

ζ = damping factor

ω_n = natural frequency or loop bandwidth = $2\ \pi B_L$

$$T_P \approx \frac{(\Delta\omega)^2}{2\zeta\omega_n^3} \quad \text{(not accurate for } \Delta\omega \sim \Delta\omega_P \text{ or for } \Delta\omega \sim \Delta\omega_L\text{)} \tag{2}$$

T_P is the pull-in time

$\Delta\omega$ is the difference frequency of the VCO and the reference

$$\Delta\omega_L \approx 2\zeta\omega_n \tag{3}$$

$\Delta\omega_L$ is the "lock-in" frequency

For: $\Delta\omega = 2\pi \times 5$ MHz, $\zeta = 1/\sqrt{2}$, $K_v \approx 10^{11}$, $\omega_n = 2\pi \times 1$ kHz

$\Delta\omega_L \approx 9 \times 10^3$ rad/sec $\Delta\omega_P \approx 40$ MHz

$T_P \approx 2.8 \times 10^3$ sec

For: as above but $\omega_n = 2\pi \times 5$ kHz

$T_P \approx 22$ sec $\Delta\omega_L \approx 44 \times 10^3$ rad/sec

To make $T_P \leq 1$ ms, ω_n must be raised. ζ can be increased some, but ω_n is by far the dominant parameter.

For: $\zeta = 1$, $T_P \leq 1$ ms

$$\omega_n \geq \left[\frac{(\Delta\omega)^2}{2\zeta\ T_P}\right]^{1/3} \approx 800 \text{ kHz}$$

3.3.5.2.1.3 Conclusion

Although a phase locked system will result in less error than the Frequency Discriminator type system described in the previous section, it is too difficult to lock up between pulses in a pulsed system. The servo bandwidth must be very wide, whereas the bandwidth available is presently limited by the PZT response. To increase the speed of response of the system, an electro-optic modulator is required in the laser cavity. This could extend the loop bandwidth to several hundred kilohertz, which would be required by the phase locked system. The S/N ratio also might limit the loop bandwidth because the loop bandwidth would sample more noise.

3.3.5.2.2 Operation of Transition Line Stabilizer in a Hybrid-TEA System

The question of how the transition line stabilizer's phase sensitive detector operates is resolved here. The effects of gating it and rapid short dropouts are also discussed. It may be desirable to use a lock-in amplifier which can operate at other frequencies. This is also discussed.

NOTE: For a better understanding, Section IV of the Lansing Model 80.214 manual may be read before reading this section.

3.3.5.2.2.1 Phase Sensitive Detector

The phase detector used in the Lansing transition line stabilizer as well as most lock-in amplifiers is called a "phase sensitive detector." The operation of this type of phase detector depends on commutation of the input signal polarity, as shown in Figure 3-35.

A phase sensitive detector, abbreviated PSD, may depend on a differential amplifier, as in Figure 3-35. Other methods of signal inversion may be used, such as the signal transformer used in the Lansing unit. The switch may be a diode bridge, FET's or even transistors.

The input signal is chopped by the commutator and either fed directly through to the output or inverted. This performs a
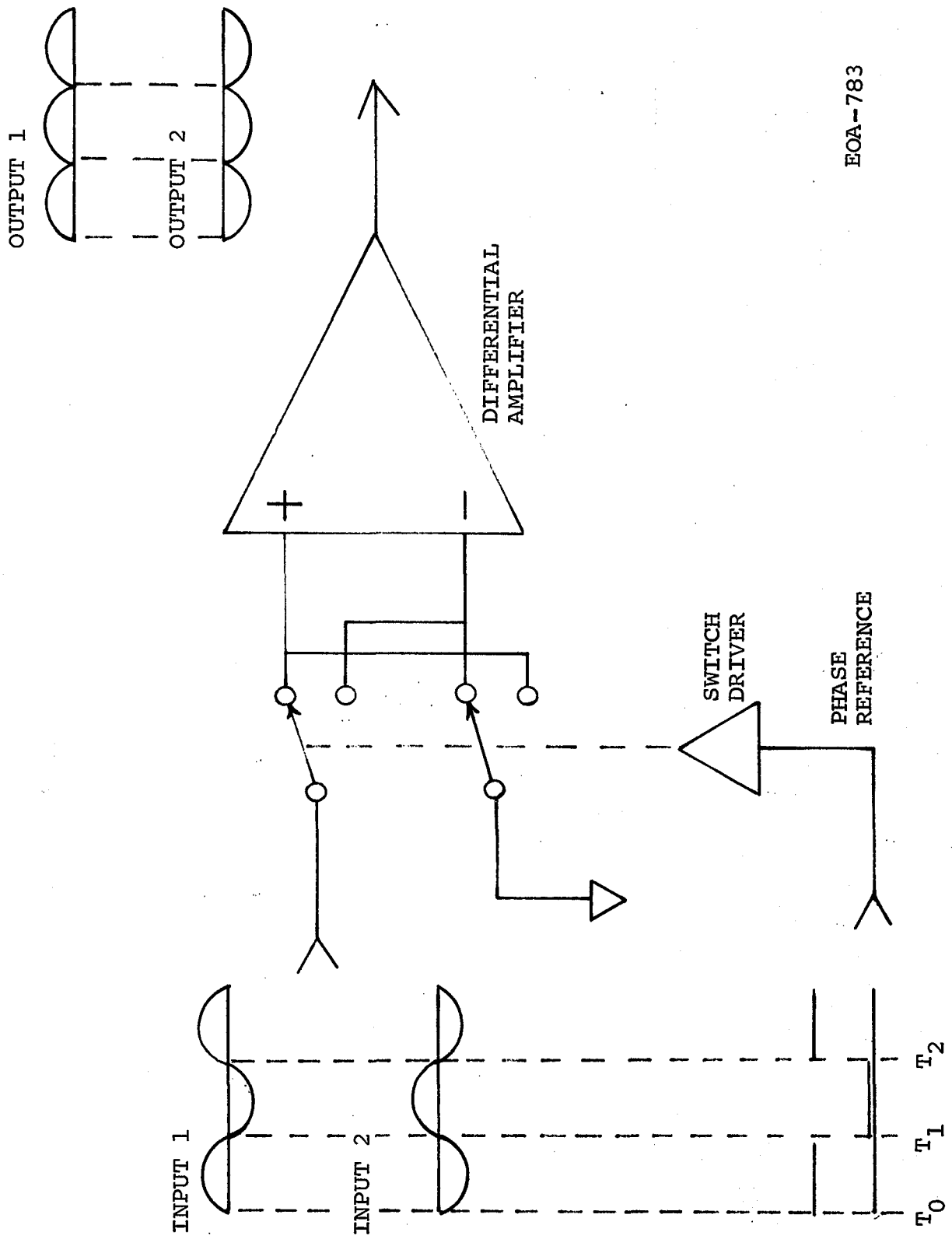
Figure 3-35. Phase Sensitive Detector (PSD)

rectification of the input which is synchronous to the reference. The output components of the input which are synchronous with the reference (including odd harmonics) will produce either positive or negative error signals dependent on the amplitude and phase of the components. The polarity retains the "sense" or phase information.

3.3.5.2.2.2 PSD and Stabilization

The manuals for the Lansing Models 80.210 or 80.214 describe how the reference signal is used to frequency modulate, or dither, the laser on a transition line and encode the resulting laser output power with amplitude modulation.

This modulation has two frequency components. One is at the fundamental reference frequency, ω_o, while the second is at two times this, $2\omega_o$. The first component is zero at line center because of symmetry, while the second is zero when the laser does not hit line center.

The phase sensitive detector output is integrated, so that only the components which have average values other than zero will produce a correction voltage to change the laser frequency. The $2\omega_o$ component will, therefore, have no effect; whereas, if there is a component present at ω_o, a correction voltage will result. This voltage can be used to maximize or minimize this component. In our case, it is minimized. The polarity of the component tells the integrator which way to go to correct for any error present.

It can be shown, by a symmetry argument, that the even harmonic, such as $2\omega_o$ components of the signal can be ignored. Only the odd harmonic components, such as ω_o, are of importance.

3.3.5.2.2.3 Gating and Transition Stabilization

To gate the lock-in system, the integrator input should be opened and the dither removed from the PZT of the controlled laser. Dither should also be removed from any offset loop being used.

The integrator input should be gated to eliminate transient charging or discharging. This is easily done with an FET gate

(analog switch). This is a standard technique. The integrator is tolerant of noise because its bandwidth is very low as is its input impedance. It would take a very large amount of energy to cause significant errors in it.

The dither is removed from the PZT to place the laser on line center for measurements, transmission, etc. This is also done by opening an analog switch, as is the removal of dither from the offset system. The integrator capacitor should be a good quality, low dielectric absorption type, such as polystyrene.

Two gating cases are to be considered. The first is a short high PRF gating pulse. The second is a gating pulse of many cycles and high duty cycle with high dither frequency.

Figure 3-36 shows the first case. Two signals are shown: the input to the discriminator and the output of the discriminator. The output shows that the laser is off line center. If it were on line center, the AC signal would be essentially zero with a symmetric laser transition line curve. The effect of the dropouts is to reduce the rate of change of the integrator output by an amount depending on the duty cycle of the dropouts. It reduces the charge injected into the integrator. This will effectively reduce the loop gain and bandwidth of the servo system and, therefore, the response time. It may require an increase in the FM modulation of the laser to make up for the decreased sensitivity.

In the first case, it is unlikely that the loop will help the recovery time of a TEA laser frequency chirp. It will strive to keep it on line center on the average as long as the TEA laser recovers to the same line during the blanking interval.

If this assumption does hold, then the amplitude of the sine waves will actually be larger immediately after the pulse and decay. The decay time constant will be determined by the frequency recovery time characteristic of the laser as long as the laser frequency recovers before the next time it fires, which must occur for proper laser operation.

FUNDAMENTAL COMPONENT OF
DETECTOR OUTPUT WITH GATING

DISCRIMINATOR OUTPUT
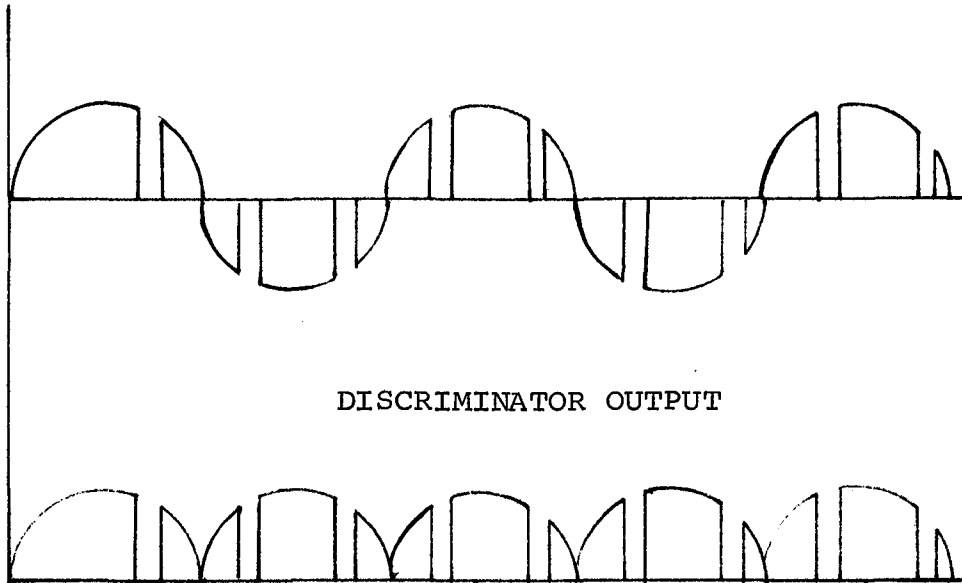
a) High PRF, Short Gate Pulse

FUNDAMENTAL COMPONENT OF
DETECTOR OUTPUT WITH GATING

DISCRIMINATOR OUTPUT
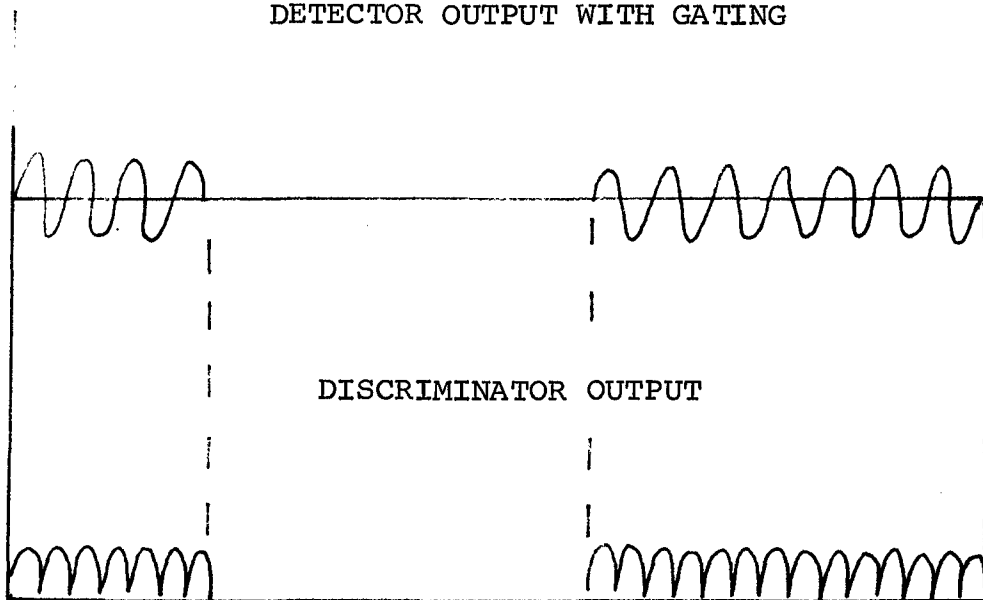
b) High Duty Cycle, Long Gate Pulse, High Dither Rate

EOA-784

Figure 3-36. Modulation Gating

The second case gives the servo loop opportunity to aid the frequency recovery time. This will be limited by the servo loop bandwidth which can be no greater than the Nyquist rate, or half the dither rate. This is an upper bound, and not a realizable bandwidth. The design of the lock-in unit should determine the bandwidth achievable. This will be limited by either signal-to-noise ratio or phase shifts in the lock-in unit due to bandwidth limiting of filters. The signal-to-noise ratio (S/N) should be high enough, for this type system, that the bandwidth should be limited by the filters of the lock-in unit.

3.3.5.2.2.4 Conclusion

Dropout or gate effects on the synchronous detector should result in sensitivity reduction, but should not affect the laser stability significantly as long as they do not produce significant harmonic components at the lock-in frequency.

The high PRF with short blanking pulse situation depicted here should not be a problem if the laser recovers quickly. The high duty cycle, high dither rate system depicted should help recovery of the laser frequency if the bandwidth of the servo is adequate and the S/N ratio is high enough to allow this bandwidth.

3.3.5.3 Design Description

Definitions

The following definitions will clarify succeeding discussions:

DITHER - Intentional frequency modulation of the reference laser which consequently appears in the heterodyne signal. This signal feature is simulated during testing by applying the sine-wave output of the function generator to the FM input of the VCO (see Figure 3-38).

DRIFT - Slow signal frequency changes ($\tilde{<}$ .1 MHz/ms), typically of an aperiodic nature.

DROPOUT - Loss of signal during a TEA laser pulse simulated by
            a "blanking" pulse applied to the AM input of the VCO.

ERROR   - The desired signal frequency of 10 MHz minus the actual
            signal frequency.

FIND   - An action by the OLS in changing from a logic state of
            Search to a logic state of Lock.

FM   - In this discussion, FM will refer to undesired and un-
            expected signal frequency excursions caused by mechanisms
            not under direct control of the OLS (e.g., vibrations).
            This is simulated in a manner similar to Dither.

HOLD   - A substate of Lock during which loss of signal is
            expected and the low-level control voltage is held
            constant by the OLS.

LOCK   - An OLS logic state during which Error is low enough
            to allow closing of the feedback loop and the lock-in
            point is on the desired side of the reference frequency.

MODE   - During actual operation, cavity length, and hence, the
            CW laser frequency, is controlled by voltage applied to
            a piezoelectric transducer (PZT). The Mode is the sign
            of the change in frequency vs. change in voltage response
            of the cavity. Modes will be referred to as A and B
            for + and - response, respectively.

PRF   - Pulse Repetition Frequency.

RECOVERY- The time period following Hold during which Error is
            reduced to less than 100 kHz.

SEARCH   - A logic state of the OLS during which the signal frequency
            (via control voltage) is swept methodically in order to
            locate an operating point that satisfies Lock state
            criteria.

SIDE – The sign of loop gain required to reduce Error. Sides
       will be referred to as 1 and 2 for + and – gains,
       respectively.

SIGNAL – An RF output of a detector resulting from optical
         heterodyne of the transmitter and the LO, which is
         simulated for test purposes by the VCO.

The Signal is applied to the Input Amplifier of the OLS where
it is amplified and digitized. This digitized heterodyne signal is
counted by the Digital Discriminator and Digital-to-Analog converted
to an equivalent voltage level delivered to the Analog Board and
Lock/Sweep Board. The Digital Discriminator also supplies a voltage
equivalent of 10 MHz (the desired offset) to the Analog Board for
nulling the actual signal frequency in Lock state.

The function of Find logic on the Lock/Sweep Board is to ensure
that Lock state is entered only when the loop gain has the proper
polarity, Side, so that Error will be actively reduced during Lock
instead of increased. Side is selectable on the front panel because
changing the side should change the sign of the frequency offset,
that is, whether the CW laser frequency is above or below the
reference, as explained with the aid of Figure 3-37.

During Search, the control voltage produced by the OLS on the
Analog Board is linearly swept periodically in both directions, to broad
limits. But for the sake of circuit simplicity, Find is allowed only
on that portion of the sweep cycle when the control voltage is decreas-
ing. Two scenarios of interest are shown in Figure 3-37. In each,
circumstances pertinent to proper locking are located on a graph of
transmitter frequency as it appears in the signal frequency domain,
that is, unsigned, relative to the LO frequency. In Case 1, as the
sweep progresses, the transmitter frequency perchance moves into the
same P-line as the LO laser. As indicated on the Figure, if the
signal frequency decreases for decreasing voltage, + gain is required
to reduce error if Lock state is entered, since the feedback loop has
the behavior,

Change in Control Voltage $\approx$ Gain X Error.

SIDE 2   SIDE 1

Increasing Signal   Decreasing Signal
   ←———Frequency   ←——— Frequency

     | |
─ Error | + Error   + Error | ─ Error
               | |
─ Gain | ─ Gain   + Gain | + Gain
  Required | Required   Required| Required
───
        10   0   10   Signal Frequency (MHz)

                              ←—— Control Voltage Decrease
                              ←—— Laser Frequency Decrease

        Case 1:   Mode A Cavity Response

═══

SIDE 1   SIDE 2

Decreasing Signal   Increasing Signal
      ·Frequency——→   Frequency———→

     | |
─ Error | + Error   + Error | ─ Error
               | |
+ Gain | + Gain   ─ Gain | ─ Gain
  Required | Required   Required| Required
───
        10   0   10   Signal Frequency (MHz)

Control Voltage Decrease ——→
Laser Frequency Increase ——→

        Case 2:   Mode B Cavity Response

═══

                                          EOA-785

        Figure 3-37. Locking Circumstances

By definition then, Find should be allowed only if SIDE 1 were selected on the front panel. Similarly, by inspection of Figure 3-37, if the signal frequency is increasing, Find should be allowed only if SIDE 2 were selected. Case 2 is interpreted in like manner and the resulting locking criteria are summarized in Table 3-3. Thus, changing the Side selection will move the lock point to the opposite side of the reference laser frequency.

The Injection Board accepts a sine wave of frequency identical to the Dither generated by the Transition-Line Stabilizer of the LO laser (or transmitter laser if that is the one locked to the transition). Using front panel controls, the phase and amplitude of this sine wave can be adjusted and added to the voltage controlling the offset laser, thus dithering that laser in such a fashion as to maintain an undithered 10 MHz offset between the two lasers in LOCK state.

TABLE 3-3

CORRECT LOCKING CRITERIA

Cavity	Signal	Gain Required	Side Selected	Find?
Mode A	Frequency Increasing	−	1	No
			2	Yes
	Frequency Decreasing	+	1	Yes
			2	No
Mode B	Frequency Increasing	−	1	No
			2	Yes
	Frequency Decreasing	+	1	Yes
			2	No

3.3.5.3.1 Input Amplifier

This module consists of an amplifier and buffered outputs to the limit amplifier, the signal detector and the RF monitor. The purpose of this unit is to amplify the low level input from the heterodyne detector module and drive the limit amplifier and signal detector.

The amplifier provides gain of approximately 40 dB. Two transistors buffer the outputs of the amplifier and drive an RF monitor and a high-pass filter network.

Two additional emitter follower buffers drive the limit amplifier module and the signal detector module.

The filter is a high-pass filter with a cut-off frequency of slightly less than 5 MHz. The cut-off is very sharp and deep. This filter is necessary to eliminate harmonics in the signal detector, which would cause the signal detector to react as if a true signal were present.

The amplifier is shielded from the higher level circuitry to prevent oscillation from occurring. The circuit is constructed on a ground plane printed circuit board within a shielded box. The RF inputs and outputs are SMA connectors while the ± 15 volt inputs are through feedthrough chess men.

3.3.5.3.2 Digital Discriminator

The digital discriminator is a frequency-to-voltage conversion circuit. It converts the square wave output of the limit amplifier or LA to a DC voltage level. This is accomplished by counting cycles of the square wave for a preset period and converting the result with a digital-to-analog converter. The counting interval is controlled by a 10 MHz clock oscillator, the output of which is divided to produce a 22.4 μsec counting interval. Also, a preset binary number is converted to an analog voltage for a reference. This voltage is

multiplied by a gain of -1 so that when the loop is locked the sum of the voltages is zero.

3.3.5.3.3 Analog Board

The analog board provides most of the signal processing of the loop. It takes the signal and reference outputs from the discriminator, sums them, and adds them to a reference voltage which is used for frequency trimming, amplifies this voltage, integrates it and drives the high voltage amplifier. This forms the low voltage section of the feedback loop.

A dither signal is fed from the injection board to the analog board. A sample and hold maintains the instantaneous dither value whenever the hold command occurs. Phase and gain adjustments on the dither signal are available.

The high voltage amplifier is a board made by Burleigh Instruments and is identified as Model PZ70.

3.3.5.3.4 Injection Board

The injection board receives a dither signal from a stabilization unit. It adjusts the gain and phase of this signal and feeds it into the analog board. It includes a buffer amplifier and low-pass filter which passes signals lower than approximately 10 kHz. This is to reduce high frequency noise components that may be present. The output voltage is sampled to generate a control signal which forms an AGC.

3.3.5.3.5 Lock/Sweep Circuit

The lock/sweep circuit consists of two circuits, the lock circuit and the sweep circuit.

The lock circuit senses the discriminator output voltage to determine when the discriminator output voltage is greater than one corresponding to one set frequency, and when it is below that corresponding to a second frequency set independently. This information feeds through a latch into a dual flip-flop which senses whether

the frequency is increasing from a low value to a high value or decreasing from a high value to a low value. This information, together with the sweep direction information and the lock side information, provides enough data to determine when to close the servo loop.

3.3.5.4 <u>Evaluation of Performance</u>

An electronic apparatus, diagrammed in Figure 3-38, which simulates the main features of laser operation, was devised to close the feedback loop around the OLS during testing. Its major components are:

1) Voltage Controlled Oscillator (VCO) to provide an RF signal at about -50 dBm which is normally generated in a detector by an optical heterodyne signal. The VCO accepts an FM voltage and is properly adjusted to allow the OLS to vary signal frequency over the range 0 - 50 MHz;

2) Function Generator, whose output added to the control voltage output of the OLS, generates programmed Frequency Modulation of the RF signal;

3) Pulse Generator with output adjusted to the proper amplitude and polarity to "blank" the RF signal when the TEA laser would be fired in actual operation;

4) Noise Generator followed by discrete attenuation for discrete selection of signal-to-noise ratio (SNR);

5) The Offset Locking System (shown in Figure 3-39).

3.3.5.4.1 <u>Lock Stability vs. SNR</u>

In all experiments reported here, signal level is -50 dBm as measured on the HP 141T Spectrum Analyzer with HP 8552 and HP 8553 plug-ins. SNR is varied by varying the noise source attenuation and measured by the Spectrum Analyzer using 100 kHz bandwidth. SNR measurements reported here include the noise level correction indicated in Hewlett Packard's Applications Note #150-4.
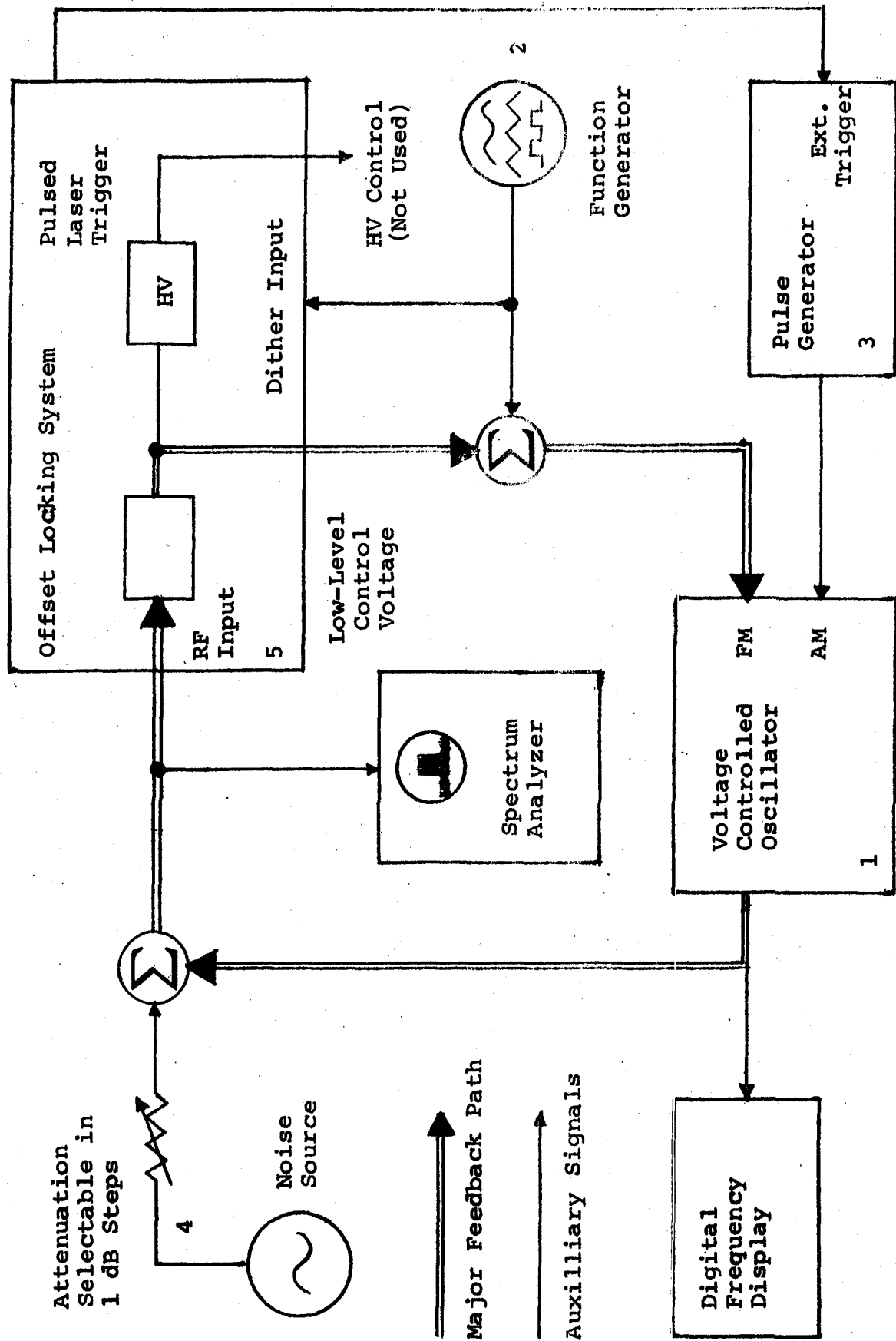
Figure 3-38. Test Equipment Block Diagram

EOA—786

3-76
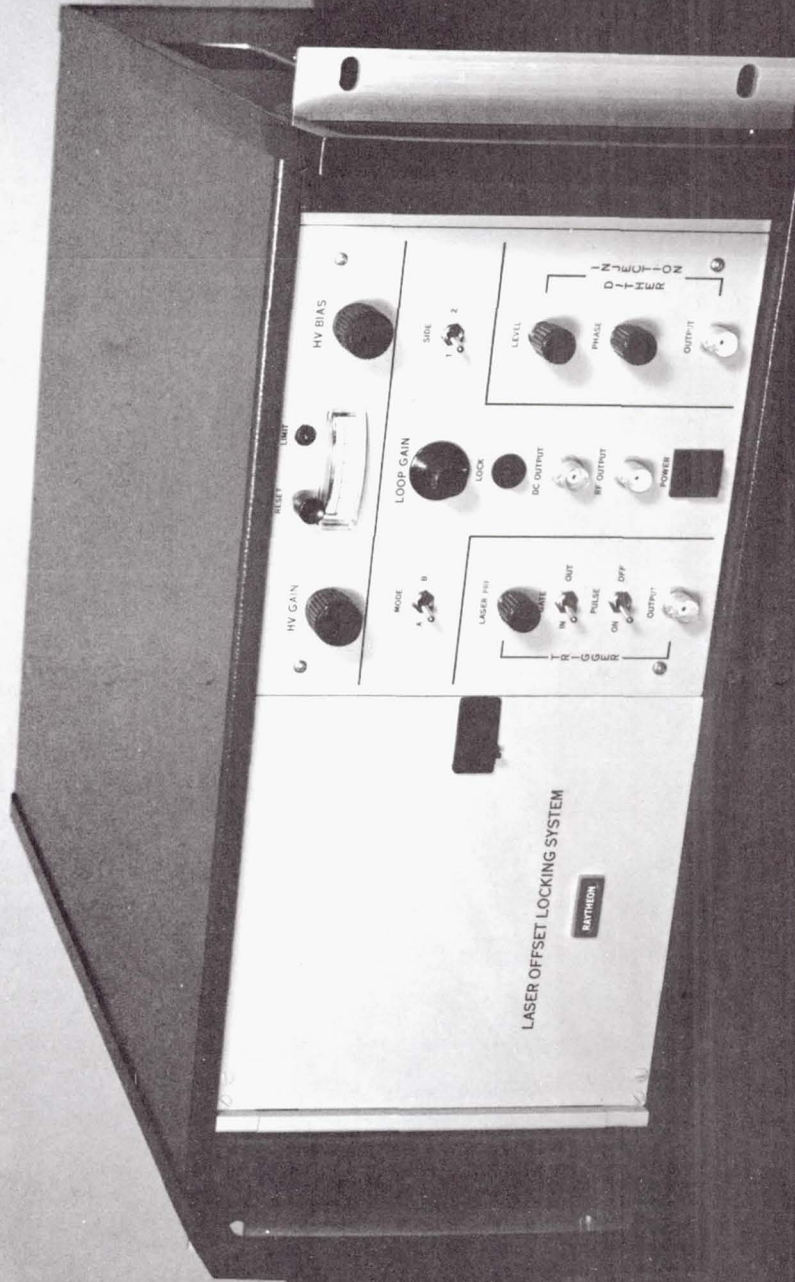
Figure 3-39. Laser Offset Locking System

A. Without FM

Referring to Figure 3-38, the Function and Pulse generators were
not used for this test. In this Section and Section B, gain was
adjusted on the front panel for the smoothest locked signal frequency.
SNR was varied and signal frequency observed in Lock state. These
observations are graphed in Figure 3-40.

Also indicated on the graph are three special SNR limits: the
lowest SNR at which Find happens; the lowest SNR at which Error
remains less than 100 kHz (as long as OLS is not intentionally
removed from Lock state); the lowest SNR at which OLS remains in
Lock state.

B. With FM

In this test, the Function Generator was adjusted to cause FM
at 120 Hz, with 100 kHz amplitude, in the unlocked signal. SNR was
varied and the spectral width of the locked signal was observed on
the Spectrum Analyzer. These observations are graphed in Figure 3-41.
Again, pertinent limits are noted on the graph.

C. FM Suppression

It may be useful in the future to know the maximum FM in the un-
locked signal which can be suffered while still maintaining Error
$\leq \pm$ 100 kHz. As one might expect, this varies with SNR and the
observed values of this parameter are graphed in Figure 3-42. However,
this parameter also depends on the feedback loop gain, adjustable
from the front panel. Gain may be adjusted during normal operation to
some value between a lower limit, below which Error will not be
actively reduced, and an upper limit, above which the loop breaks into
sustained oscillation. In the OLS, the lower limit is also approxi-
mately the value which yields the smoothest signal frequency when no
FM is applied to the unlocked signal. Two curves appear in Figure 3-42,
one for each of these two gain values.
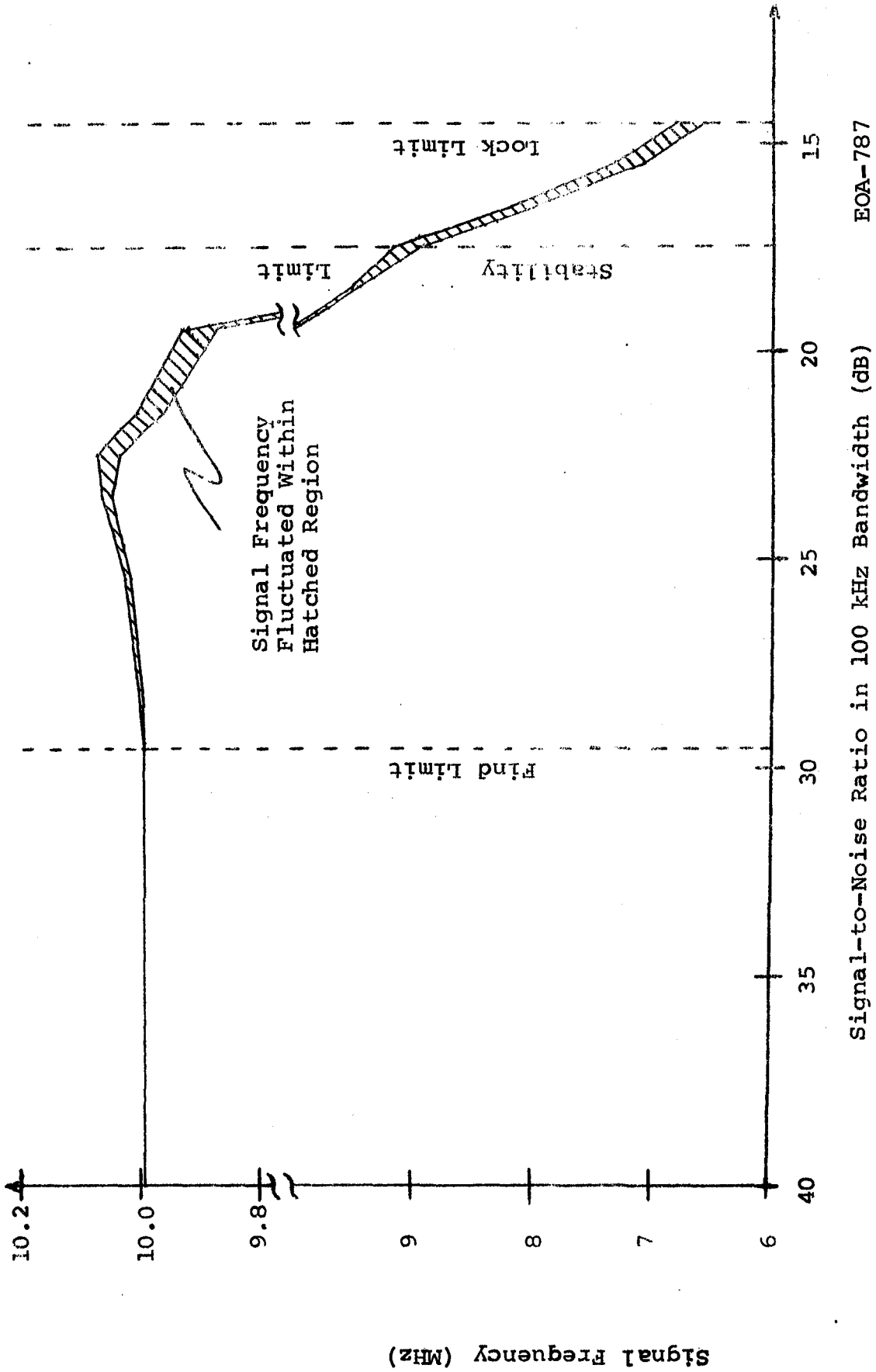
Figure 3-40. Lock Stability Without FM
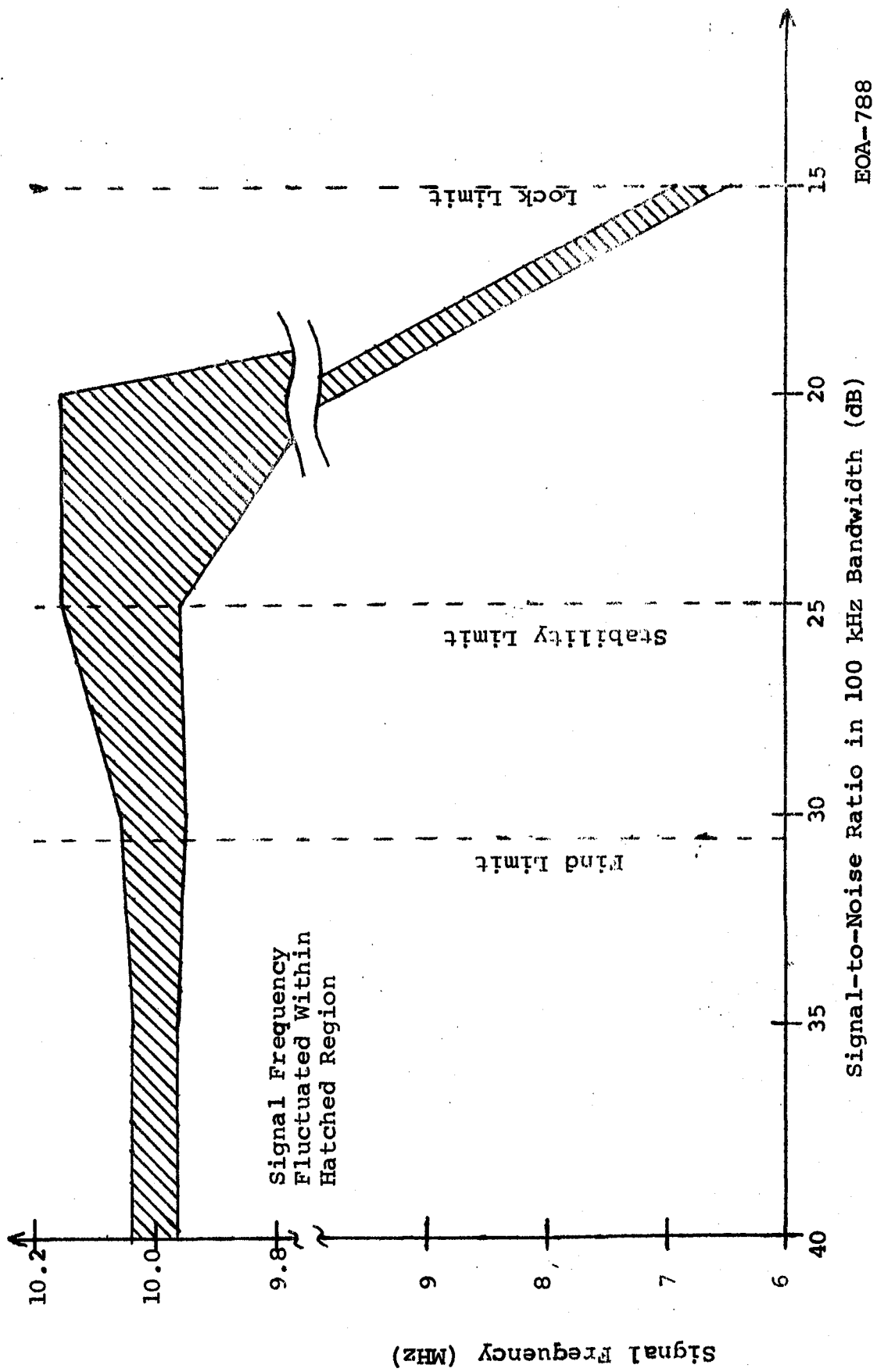
Figure 3-41. Lock Stability with FM

EOA-788

3-80
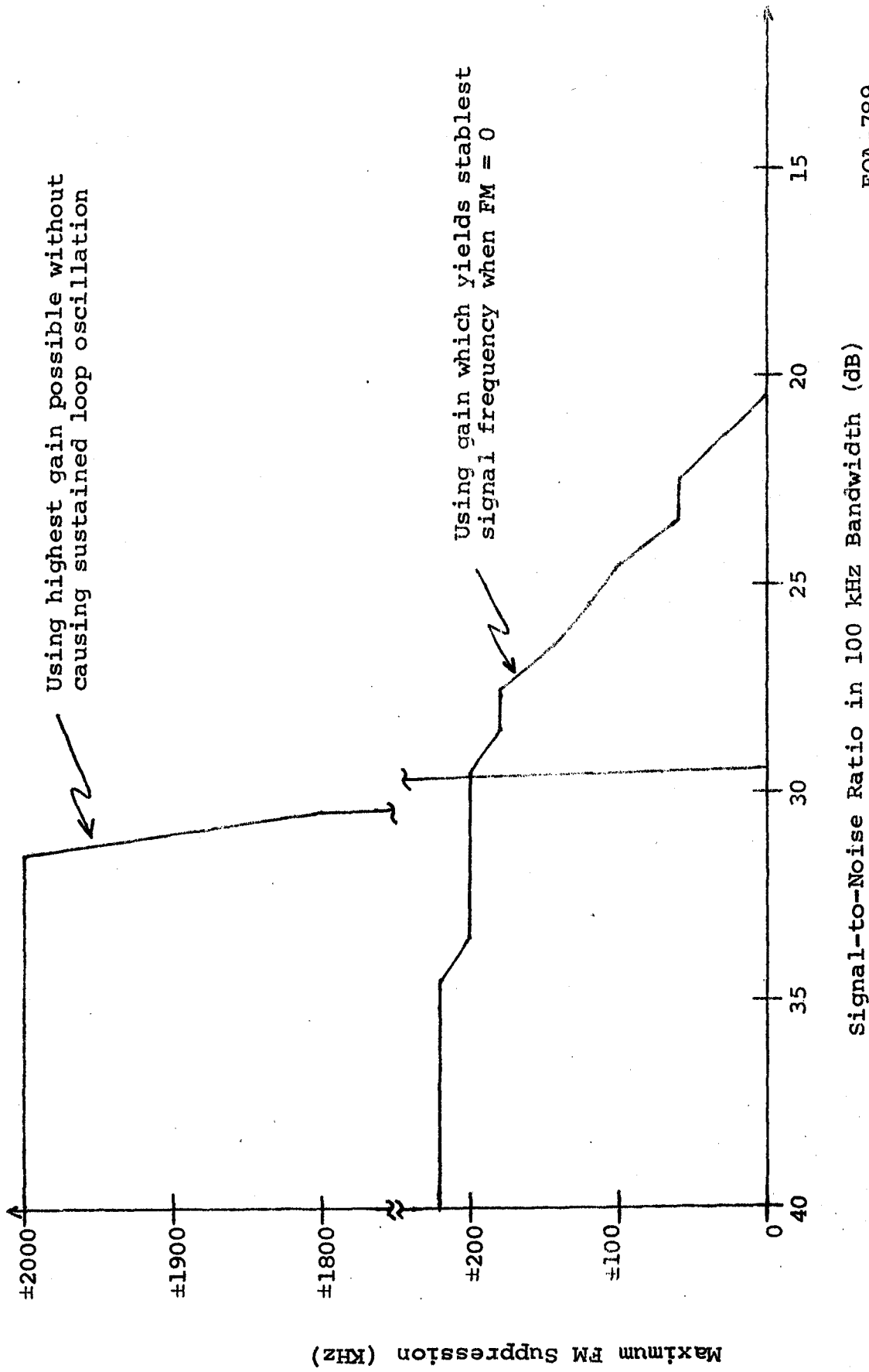
Figure 3-42. 120 Hz FM Suppression

EOA-789
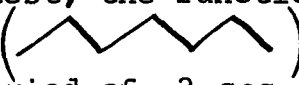
3.3.5.4.2 Recovery Capability

A study of recovery capability requires use of all the simulation equipment to model Hybrid-TEA laser operation. The particular features of interest are:

1) loss of signal during the pulse,

2) possible change in frequency when the signal returns,

3) recovery to a low-Error condition.

The equipment parameters selected for this test are listed below.
Some are adjustments on the simulation equipment, some are on the
OLS front panel, and some internal to the OLS.

Signal level:	-50 dBm
SNR:	35 dB (30 and 40 were also tried with no significant differences)
Hold Time:	18 ms
Signal Dropout Time:	10 ms
PRF:	13 Hz
Gain:	Adjusted for smoothest Signal Frequency
Function Generator:	(Read below)

In this test, the function generator provided a triangular
waveform ($\diagup\diagdown\diagup\diagdown\diagup\diagdown$) with slope variable between 0 and 50 V/sec
with a period of .2 sec; that is, during the 18 ms hold time, the
frequency of the VCO will drift from 10 MHz as much as 4.5 MHz (the
VCO has 5 MHz/Volt FM transfer function). By the nature of the set-up,
the drift is continuous, even through recovery. Hence, recovery
will take longer than if the initial recovery condition were a plain
offset with zero drift. This can be accounted for in determining
recovery time by application of the formula

$$R = \frac{x}{c+d}$$

where

        R = recovery time

        x = initial offset

        c = observed correction rate

        d = selected drift rate

Observations of the time required for the Error analog voltage
(internal to OLS) to return to its steady-state value were used to
determine "c," and then "R." Figure 3-43 graphs the results for
initial offsets of 1/4,1,2,3 and 4 MHz.

3.3.5.4.3 Dither Suppression

The OLS incorporates a circuit which, when supplied with a
sine wave of the same frequency as the dither of the reference, can
be adjusted from the front panel to apply an equal but opposite
modulation to the control voltage, thus nulling the effect of the
dither. To test the extent of this nulling, the function generator
is adjusted to supply dither to both the signal, and the DITHER
INPUT of the OLS. The front panel PHASE and LEVEL controls must be
adjusted to offset the dither applied to the VCO. This adjustment
is correct when the waveform at the FM input to the VCO is as flat
as possible. Any non-linearity in the handling of the dither in
the OLS leads to perturbations in the FM input to the VCO and
consequently to some spectral width in the signal. The handling of
various dither amplitudes as indicated by spectral width is graphed
in Figure 3-44.

3.3.5.4.4 Thermal Drift

During an 8 hour test period beginning with OLS turn-on,
locked signal frequency varied no more than $\pm$ 6 kHz from 10 MHz.
This test was run with no FM, no dither, and no dropouts, at about
40 dB SNR. No adjustments were made during the test period.
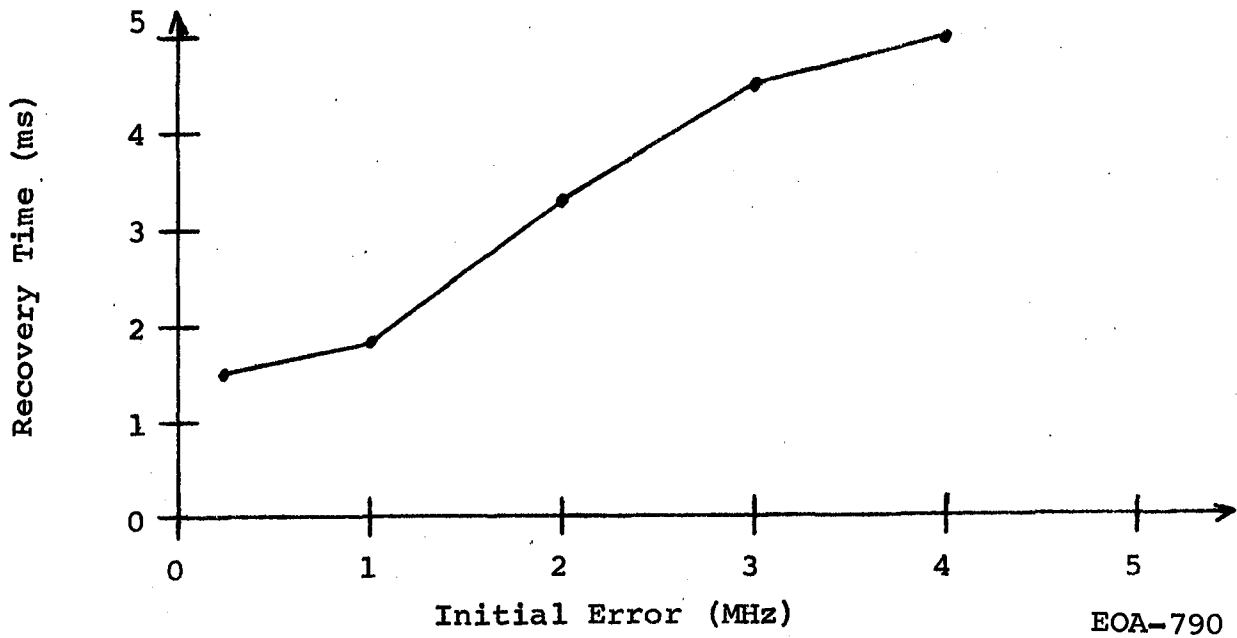
EOA-790

Figure 3-43. Recovery Capability

These 3 points measured with 1 kHz Bandwidth, the rest with 10 kHz
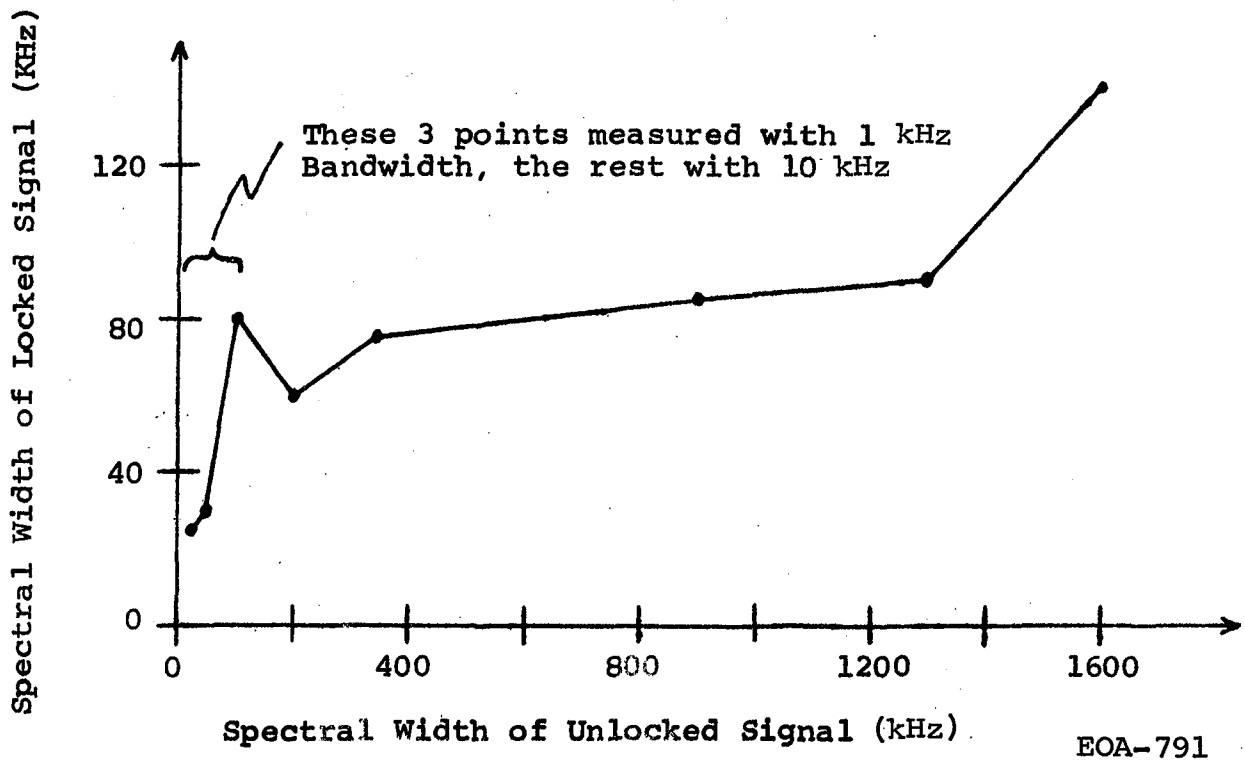
EOA-791

Figure 3-44. Dither Suppression

3.3.5.4.5 Conclusions

The OLS meets performance specifications for normal operating conditions. Following these performance tests, the ability to lock two CW lasers at a 10 MHz offset was verified on an actual Hybrid-TEA laser set-up.

3.3.6 DETECTOR/RECEIVER TESTS

During this program, a number of detectors of various types were evaluated and used in the system. Each of these had to be tested and measured to determine the operating conditions for optimum system performance. Specific tests are presented in the program progress reports. The following description typifies this continuing activity.

HgCdTe Detector No. LK146E9, Serial T-2, was received and tested with the receiver. Detector and receiver measurements were:

Operating Point

Local Oscillator	1 mW
Bias Voltage	50 mV
Bias Current	5.6 mA

Performance

Quantum Efficiency	59%
Frequency Response (-3 dB)	56 MHz
Dynamic Impedance	92 Ω

The I-V characteristics of the detector are shown in Figure 3-45. It can be seen that the detector exhibits a soft breakdown characteristic and a slowly saturating current responsivity. To determine the best operating point, the detector was connected to the receiver and the S/N ratio from a Doppler target was measured as a function of local oscillator power and bias voltage. The results of this measurement, shown in Figure 3-46, indicate an optimum operation point of 0.5 - 1mW
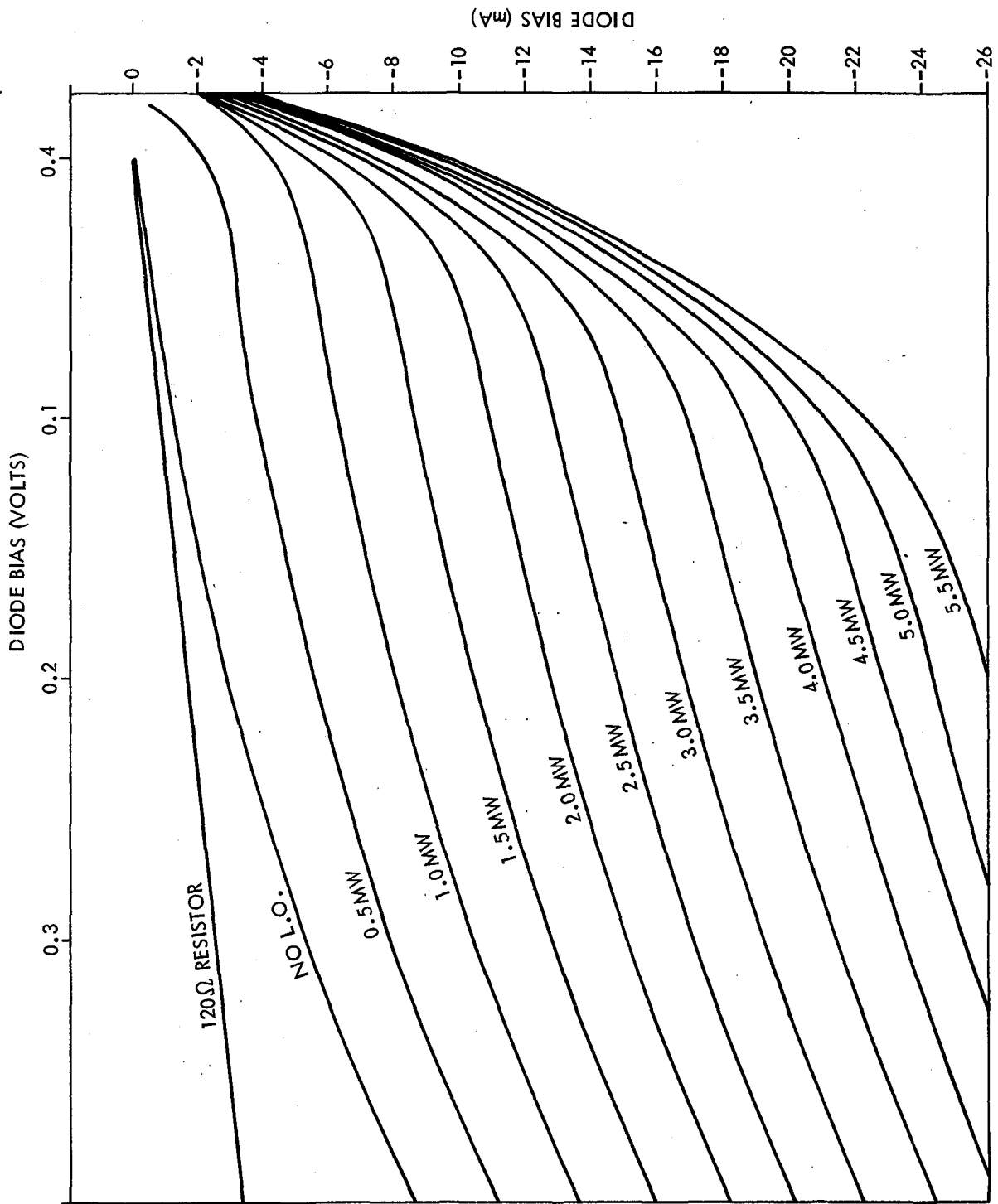
Figure 3-45. I-V Characteristics of CAT PV Detector (LK146E9, S/N T-2)
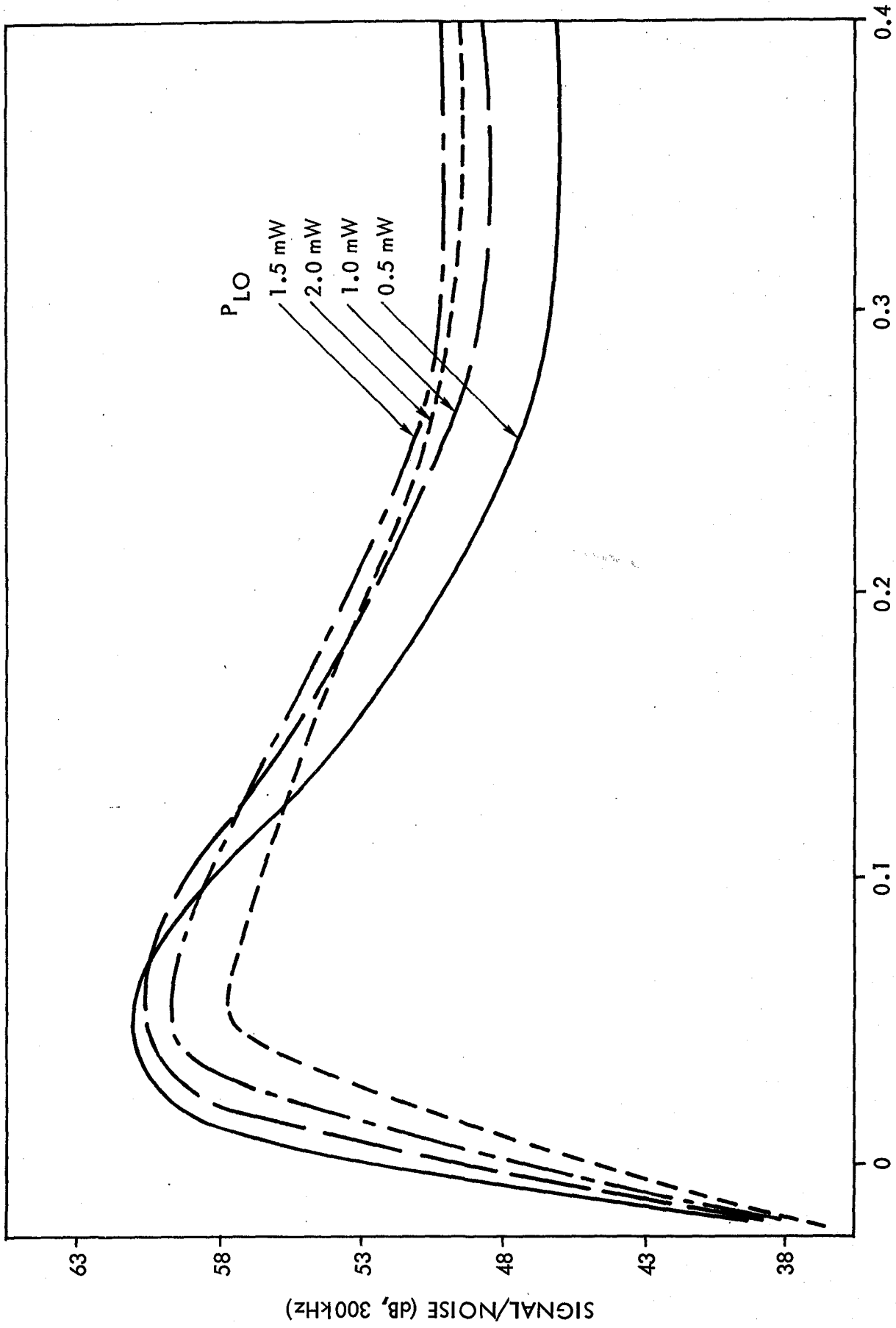
EOA-792

Figure 3-46. Signal/Noise vs. Bias Voltage

EOA-793

at 50 mV bias. The loss in S/N ratio at higher bias voltages is due to excess detector noise associated with the soft breakdown. The output noise spectrum of the receiver and detector is shown in Figure 3-47 and demonstrates that the detector noise exceeds the receiver noise by 5 dB or more at frequencies up to 55 MHz. The response characteristics of the receiver near the notch filter are shown in Figure 3-48 with 1 kHz resolution. The notch is seen to have a depth of 60 dB at 10 MHz and a 3 dB width of $\pm$ 160 kHz.

3.3.7 MASTER OSCILLATOR

The master oscillator used is the original Honeywell CO_2 laser. Because of long term degradation of the laser, it was sent to Honeywell for refurbishment. In the course of this work, the tube was damaged. A completely new laser tube assembly was then built at Raytheon and installed in the original Honeywell frame. This laser has shown good operating characteristics with typical operating times of 200 - 300 hours between gas refills and a maximum output power of 10 watts.

Two significant changes were made in the frequency control of the laser as a result of the implementation of the offset system. It was first necessary to use a stabilization loop to keep the master oscillator on a transition common to the local oscillator. To do this, a commercial stabilization loop was purchased from Lansing Research Corporation. This system places a dither on the laser frequency by driving the laser's PZT with a sine wave. The small amplitude fluctuation which this causes is detected by a pyroelectric detector. The output signal is used by the loop to drive the average laser frequency to the center of whatever transition it is operating on.

A second frequency control modification was necessary to prevent feed-through into the detector at the 10 MHz offset frequency. This feed-through occurs after the pulse when leakage of the modulator allows optical power at the master oscillator frequency to be reflected by the output optics back into the receiver. In the non-offset homodyne
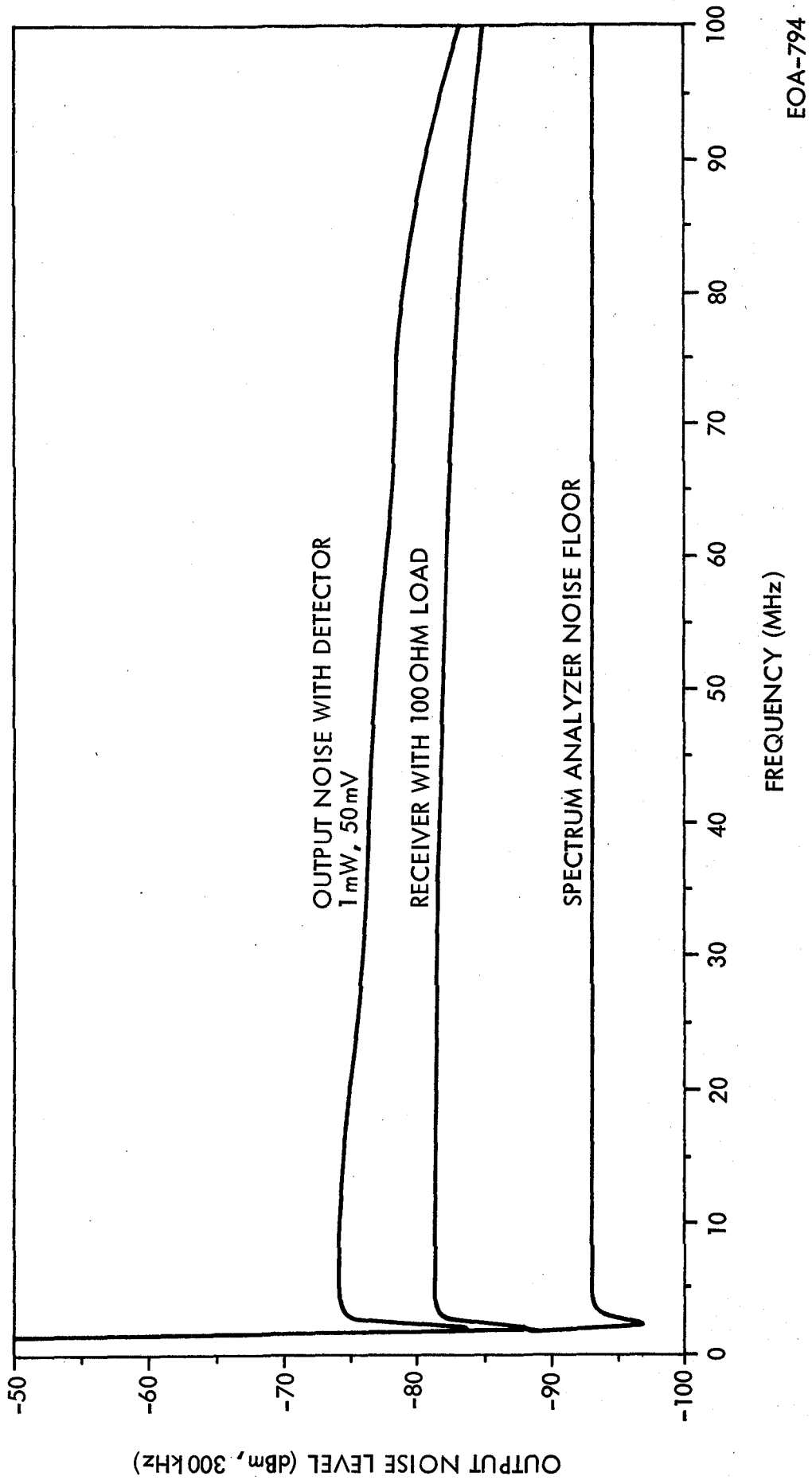
Figure 3-47. Output Noise Spectrum of CAT Receiver and PV Detector (No Notch Filter)

EOA-794
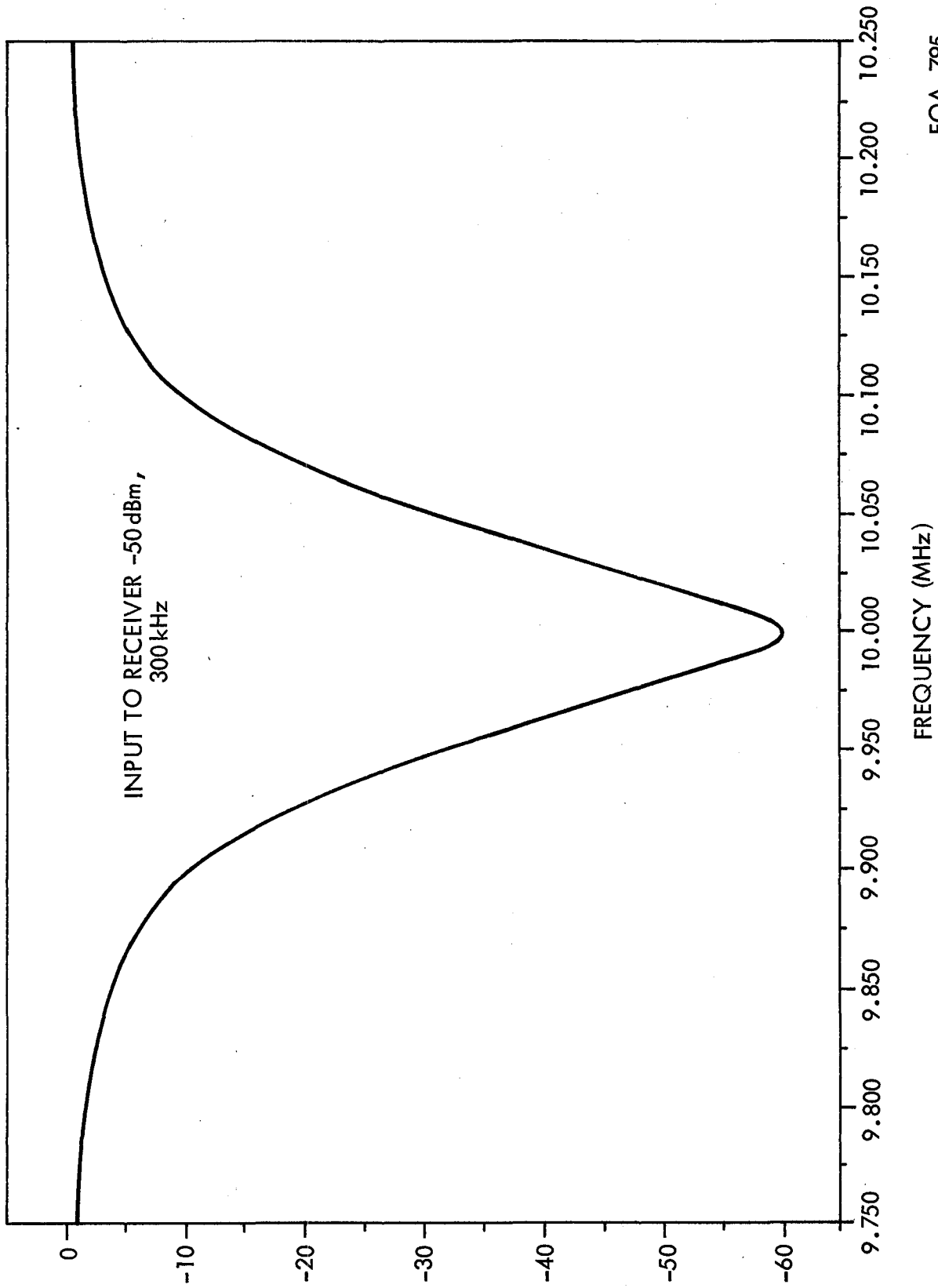
Figure 3-48. Notch Filter Frequency Response

INPUT TO RECEIVER -50 dBm, 300 kHz

FREQUENCY (MHz)

EOA-795

system, this leakage causes a signal to occur at baseband and the variations in the amplitude of this feed-through interferes with the low frequency signals. In the offset configuration, this feed-through occurs at 10 MHz. It was found that it was not possible to adequately remove the modulation sidebands from the frequency regions of interest by normal filtering techniques, and a master oscillator frequency chirping technique was used to solve the problem. In this technique, a large voltage pulse is applied immediately after the output pulse to the PZT of the master oscillator which causes the frequency of the feed-through to change rapidly. In a time of about 18 μseconds, the master oscillator frequency has changed so that the feed-through signal is no longer within the 5 to 15 MHz bandpass of the receiver, and the sensitivity of the system is no longer degraded by modulation effects.

3.3.8   LOCAL OSCILLATOR

The local oscillator used in the system was a Model 941 CO_2 laser with a PZT adjustable cavity. This laser was received in October, 1976, and a series of measurements were made of its characteristics. The results were:

Output Power:	2.2 - 3.1 watts depending upon transition; Maximum power on P(20)
Signature:	$00^{O}1 - 10^{O}0$, R(20) - 10.25 μm R(24) - 10.22 μm R(26) - 10.21 μm P(18) - 10.57 μm P(20) - 10.59 μm P(22) - 10.61 μm
Power Stability:	Better than 3% over one hour after 30 minute warm-up period.
Beam Parameters:	Diameter ($1/e^2$) = 3.8 mm Divergence = 3.8 mrad
Beam Steering:	Not detectable. Estimated to be less than 10% of beam divergence.

Visual examination of the laser showed a faint hazy appearance at the output coupler and a near field beam distribution indicating the laser might be slightly out of alignment. Attempts to remove the haze by clearing with degreasers were not successful. Sylvania representatives told us that the increasing tendency of the laser to operate on transitions other than P(20) was probably due to misalignment as the O-ring takes a set and that realignment should correct this tendency.

Long term operation of the laser has led to the following observations:

1) The alignment of the cavity mirror must be adjusted occasionally as the O-ring takes a set.

2) Inadequate cooling of the laser results in heating of one side of the laser tube which misaligns the cavity. The solution to this problem is better air flow through the laser head.

3) Fluctuations in coolant pressure caused the cavity to change its length with a corresponding change in frequency. Operation on tap water was unsatisfactory with normal pressure regulators. No problem has occurred with the transmitter cooling system.

4) The output power steadily declined to about two watts after 250 hours.

5) Current ripple of the laser power supply was excessive. The laser did not meet its frequency stability specification when run on this supply. When it was controlled by the offset loop, however, the FM deviation was reduced to less than 100 kHz, which is adequate for the system. Two more Sylvania power supplies were tested with the laser with no appreciable improvement in performance.

A number of problems were encountered, and the laser tube was replaced twice. Finally, a new tube produced about 3.1 watts of output power. It was determined that reducing the tube current to 6 ma resulted in little power degradation, but a considerable increase in lifetime. The local oscillator laser was operated successfully in this mode.

3.3.9 CAT MODULATOR RINGING TESTS

When high voltages are applied to a modulator crystal in a pulsed mode of operation, mechanical shock waves are produced which resonate throughout the crystal. These resonance frequencies impose a ringing structure on the tail end of the optical pulse. The amplitude and duration of the ringing is a function of how the modulator crystal is mounted into its housing. Ringing will be minimized if the shock wave can be coupled out of the crystal, i.e., the crystal and its mount are acoustically matched. An initial set of tests were performed on a single modulator crystal to find a suitable conductive adhesive which would bond the modulator crystal to its housing and reduce ringing. Ringing is further reduced by placing a second modulator crystal in series with the first which cuts off the tail end of the optical pulse propagating through the first crystal. The double crystal modulator was installed into the CAT system and a series of tests were made to check the performance of the "tailbiter" in reducing the ringing.

3.3.9.1 Single Crystal Modulator Tests

Tests were made in a laboratory setup using a CO_2 laser source and a Ge:Cu detector. Two Northeast power supplies were connected in series to provide the drive voltage to the modulator. Electrical pulses were provided by an Intercontinental International, Inc. pulse generator. Half-wave voltage could not be achieved due to breakdown in the drive circuitry; therefore, relative measurements were used in comparing ringing performance. In each test, the laser was attenuated to prevent detector saturation. The detected signal was amplified by an ADYU amplifier and displayed on an oscilloscope.

An 8 mm x 8 mm x 52 mm CdTe modulator crystal was cemented into the modulator housing using a rubber caulking cement with silver particles. This silastic bond material grounds the crystal to the housing and is used to dampen the mechanical shock waves. Figure 3-49 illustrates the results of the test made on the modulator crystal. The ringing is characterized by the pulse height to ringing ratio P/R.

CdTe MODULATOR - SILASTIC BOND
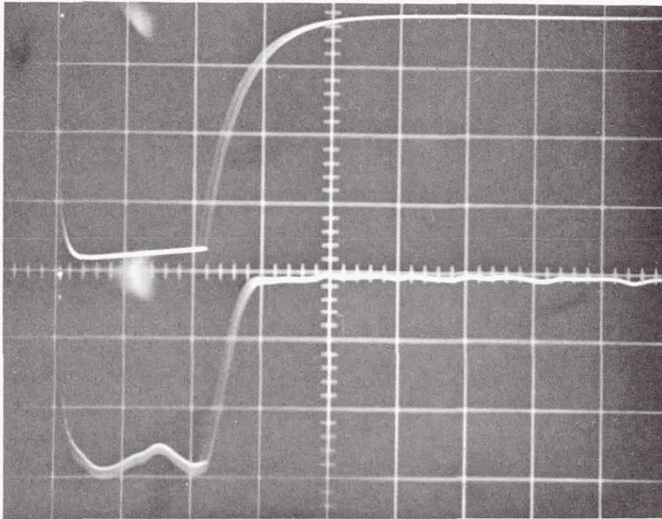
PULSE HEIGHT:

TOP - 2 VOLTS/DIV.

BOT - .5 VOLTS/DIV.

5 μs/DIV.

RINGING AMPLITUDE:

.02 VOLTS/DIV.

10 μs/DIV.
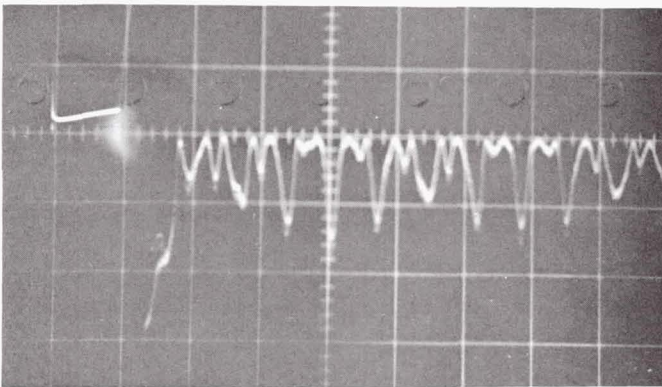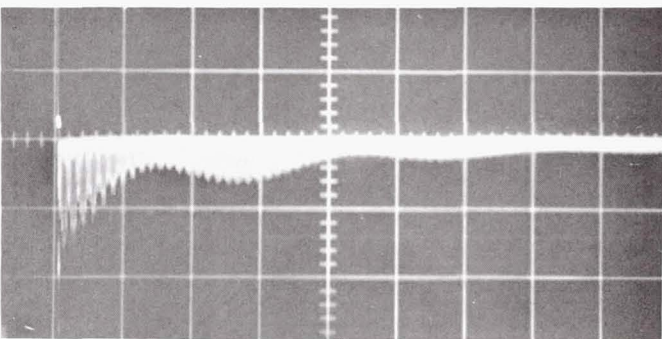
RINGING DURATION:

.02 VOLTS/DIV.

200 μs/DIV.

EO-456

Figure 3-49. Ringing Characteristics Of A
Single Modulator Crystal
(Silastic Bond Material)

From the photos, this is found to be P/R ≈ 47. The magnitude and duration of the ringing was not acceptable since better ratios have been achieved with different materials; therefore, the crystal was removed from the housing and was reinstalled using crystal cement. The cement was allowed to dry over a 24-hour period and similar tests were performed. From Figure 3-50, we find P/R ≈ 59. Crystal cement needs between 48 and 72 hours to dry completely; therefore, the modulator was retested one week later to see if the ringing characteristics would change. Figure 3-51 shows that under identical test conditions the pulse height to ringing ratio is now P/R ≈ 208. This reduction in ringing amplitude is satisfactory for our application; therefore, the second modulator crystal was mounted into the modulator housing using crystal cement.

3.3.9.2 Double Crystal Modulator

The modulator assembly which consists of two CdTe modulator crystals and three Brewster plate polarizers was installed into the CAT system. The drive electronics provided a half-wave voltage of 8.2 kV to each crystal at a pulse repetition rate of 140 pps. Tests were made to measure the ringing on the optical pulse exiting from the modulator. A CO_2 laser beam passes through the modulator and is detected by a Ge:Cu detector. The signal was amplified by a C-COR 3567 amplifier and a Hewlett-Packard 450A amplifier, and then displayed on a Tektronix 453 oscilloscope. A Krohn-Hite 3202 filter was also employed in the circuit as a low pass filter (1 MHz cutoff) to reduce high frequency interference.

The ringing on the optical pulse was measured for two drive conditions: (1) with only the first crystal driven, and (2) with both crystals driven. Figures 3-52 through 3-55 represent measurements taken under these two conditions for 2 μs, 4 μs, and 8 μs pulse lengths. In each case, results show that the ringing on the optical pulse is greatly reduced when the second crystal is turned on. Due to the limited dynamic range of the detector, the amplitude of the ringing could not be measured. In fact, the ringing was so low that it was in the noise

CdTe MODULATOR - CRYSTAL CEMENT (24 Hrs.)
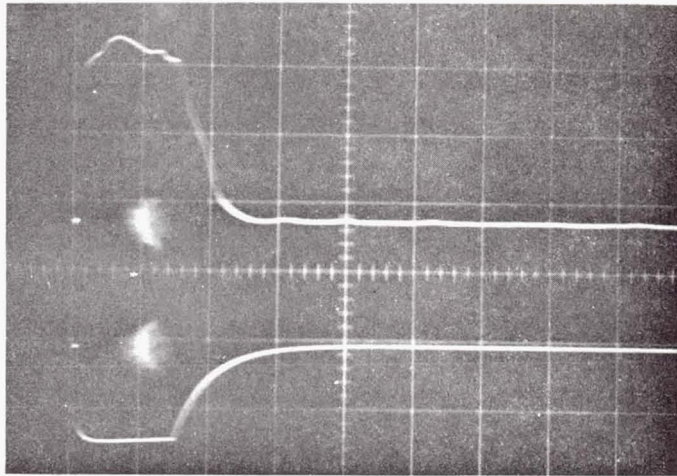
PULSE HEIGHT:

TOP - 1 VOLT/DIV.

BOT. - 5 VOLTS/DIV.

5 µs/DIV.

RINGING AMPLITUDE:

.02 VOLTS/DIV.

10 µs/DIV.
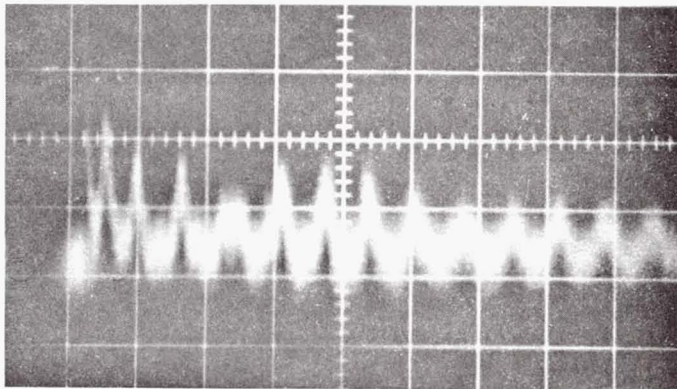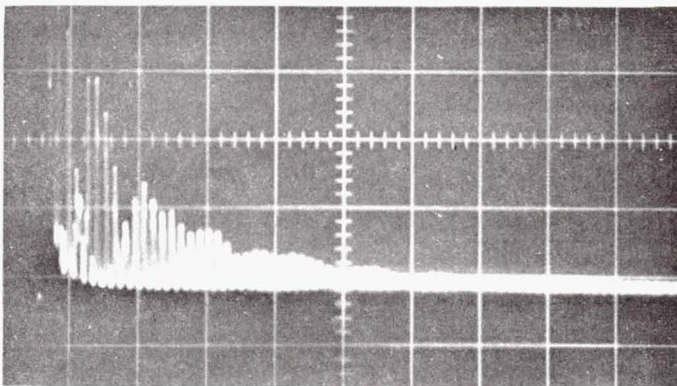
RINGING DURATION:

.02 VOLTS/DIV.

50 µs/DIV.

EO-457

Figure 3-50. Ringing Characteristics Of A
Single Modulator Crystal
(Crystal Cement: 24 hr. dry time)

CdTe MODULATOR - CRYSTAL CEMENT (7 Days)
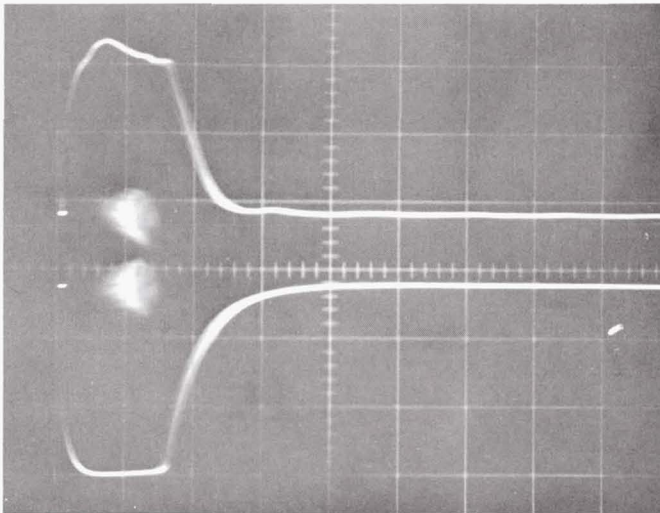
PULSE HEIGHT:

TOP - 2 VOLTS/DIV.

BOT. - 2 VOLTS/DIV.

5 μs/DIV.
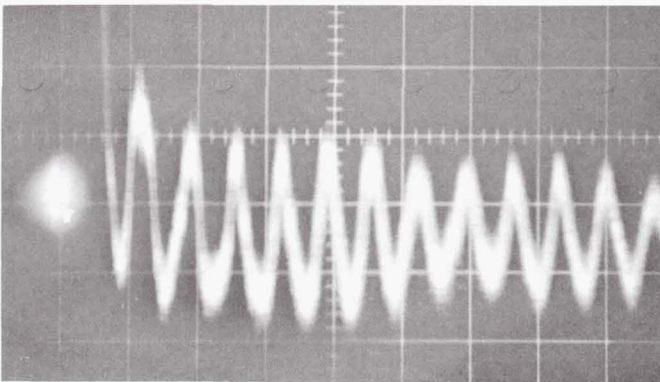
RINGING AMPLITUDE:

.01 VOLT/DIV.

10 μs/DIV.
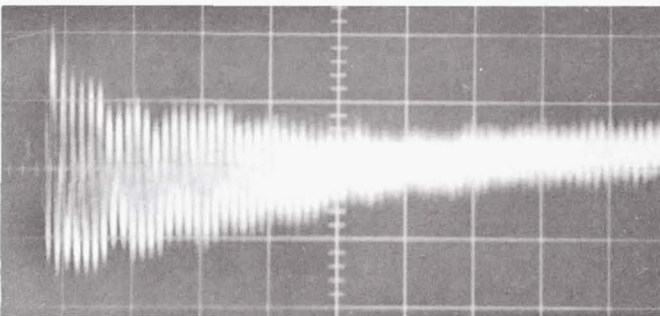
RINGING DURATION:

.01 VOLT/DIV.

50 μs/DIV.

EO-458

Figure 3-51.   Ringing Characteristics Of A
Single Modulator Crystal
(Crystal Cement: 7 day dry time)
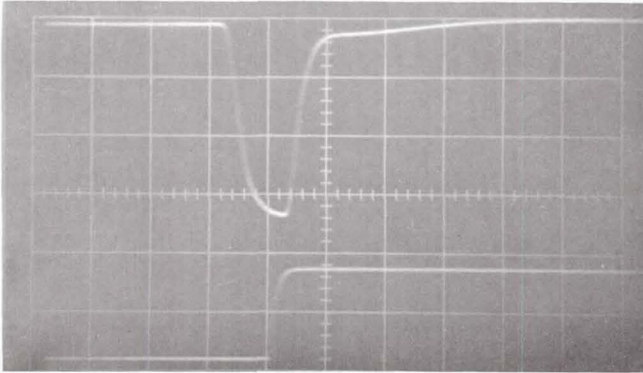
PULSE HEIGHT:

TOP - 2 VOLTS/DIV.

BOT. - 5 VOLTS/DIV.

2 μs/DIV.

RINGING: SINGLE CRYSTAL

.1 VOLT/DIV.

5 μs/DIV.
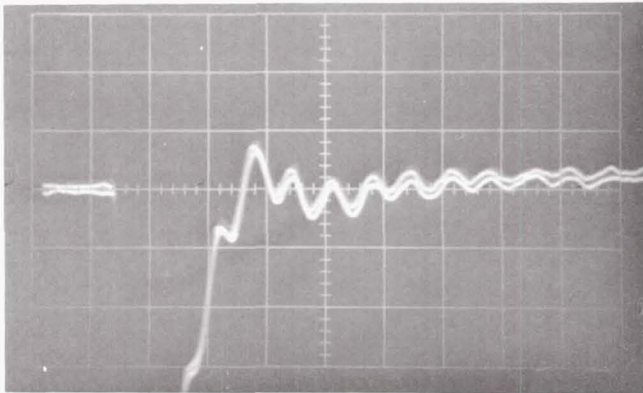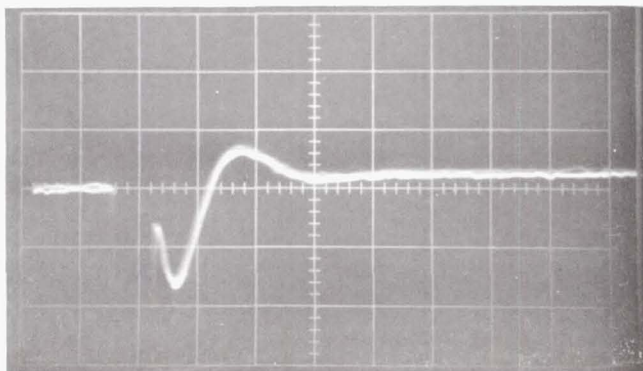
RINGING: DOUBLE CRYSTAL

.1 VOLT/DIV.

5 μs/DIV.

EO-459

Figure 3-52.   Comparison of the Ringing Characteristics
With The Second Crystal Off and Then On.
(2 μs pulse length).
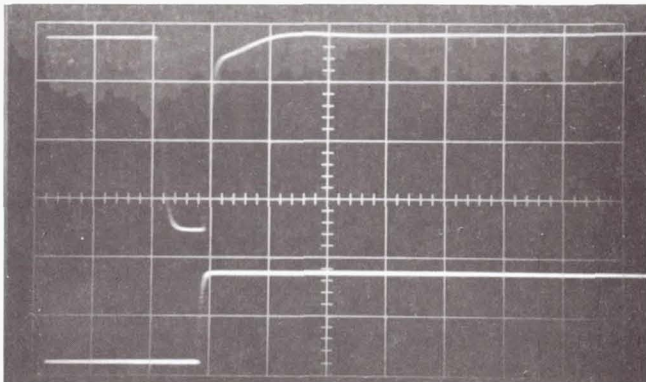
PULSE HEIGHT:

TOP – 2 VOLTS/DIV.

BOT. – 5 VOLTS/DIV.

5 μs/DIV.

RINGING: SINGLE CRYSTAL

.1 VOLT/DIV.

5 μs/DIV.
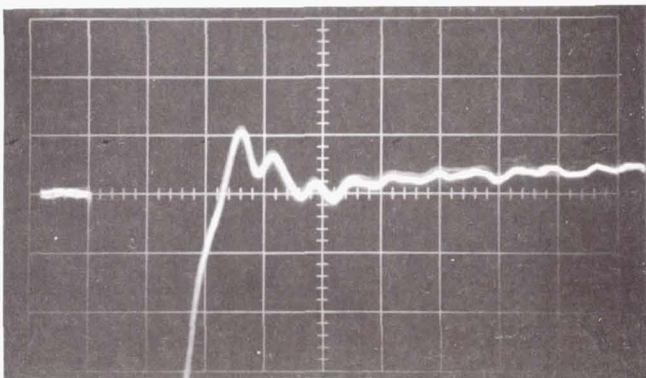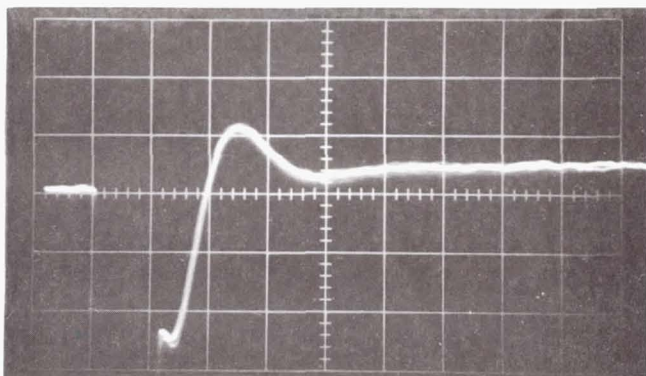
RINGING: DOUBLE CRYSTAL

.1 VOLT/DIV.

5 μs/DIV.

EO-460

Figure 3-53.   Comparison of the Ringing Characteristics
With The Second Crystal Off and Then On.
(4 μs Pulse Length)

CdTe MODULATOR – 8 μs PULSE LENGTH
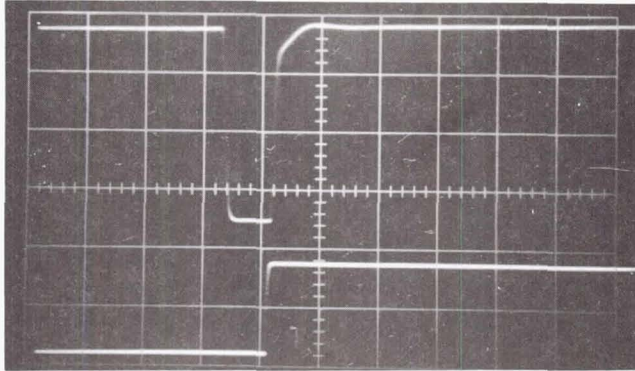
PULSE HEIGHT:

TOP – 2 VOLTS/DIV.

BOT – 5 VOLTS/DIV.

10 μs/DIV.
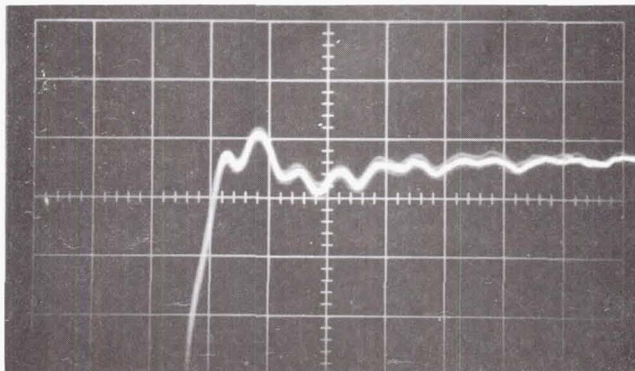
RINGING: SINGLE CRYSTAL

.1 VOLT/DIV.

5 μs/DIV.
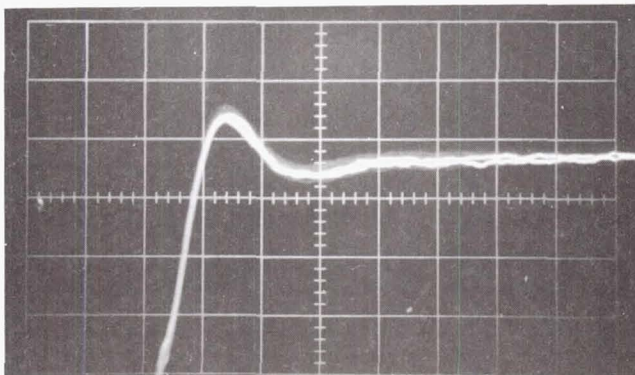
RINGING: DOUBLE CRYSTAL

.1 VOLT/DIV.

5 μs/DIV.

EO-461

Figure 3-54.   Comparison of the Ringing Characteristics
With The Second Crystal Off and Then On.
(8 μs Pulse Length)

CdTe MODULATOR - VARIABLE PULSE LENGTH
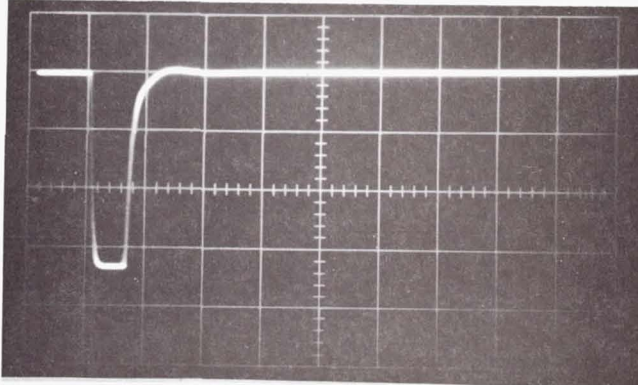
PULSE HEIGHT:

2 VOLTS/DIV.

10 μs/DIV.
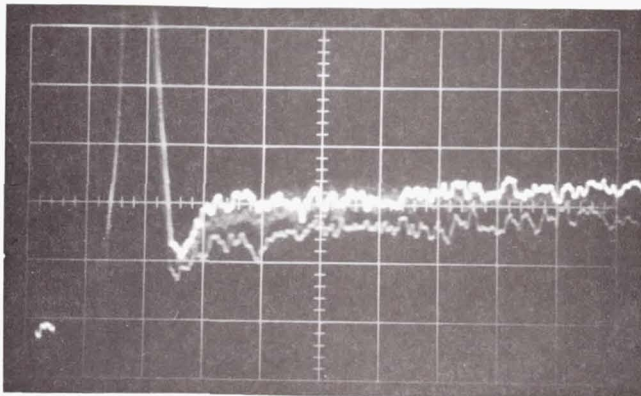
RINGING: SINGLE CRYSTAL

20 MV/DIV.

10 μs/DIV.
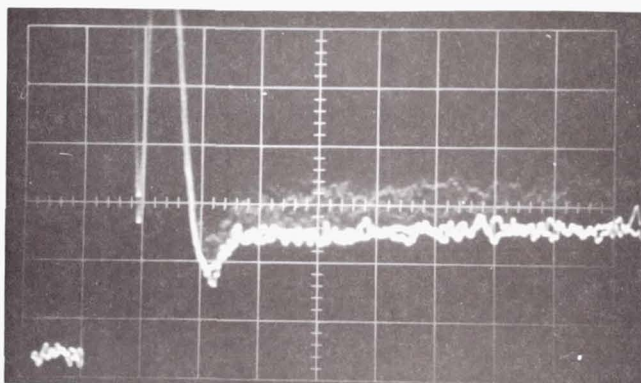
RINGING: DOUBLE CRYSTAL

20 MV/DIV.

10 μs/DIV.

EO-462

Figure 3-55.   Comparison of the Ringing Characteristics
With The Second Crystal Off and Then On.
(Pulse length set to minimize ringing)

of the amplifiers (Figure 3-56) and could not be determined accurately. Under these test conditions, the pulse height to ringing ratio was measured to be $P/R \geq 650$ at all pulse lengths.

In Figure 3-55, the ringing was minimized by varying the pulse length to the point that amplifier noise became predominant; therefore, little change was noticed when the second crystal was turned on.

3.3.9.3 Summary

The results of the ringing tests made on the CAT modulator can be summarized as follows:

(1) Crystal cement was shown to offer a distinct advantage over the silastic bond adhesive in reducing the ringing associated with a single modulator crystal.

(2) The use of a second modulator crystal reduces the ringing on the optical pulse to $P/R \geq 650$.
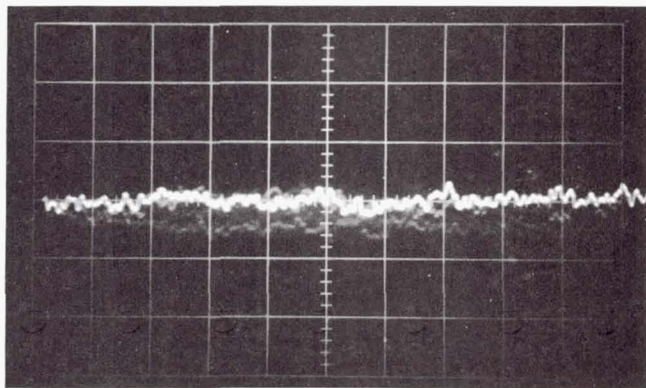
AMPLIFIER NOISE:

20 MV/DIV.

10 µs/DIV.

EO-463

Figure 3-56.   Noise of the Amplifier Used
In Ringing Experiments.

SECTION 4

SIGNAL PROCESSING AND ATMOSPHERIC ANALYSES

4.1 INTRODUCTION

The effects of atmospheric propagation of 10.6 micron radiation on system performance may be divided into three categories:

1. Gaussian beam propagation theory (i.e., vacuum propagation),

2. Atmospheric-turbulence-induced effects on wavefront characteristics, and

3. Absorption of radiation by the atmosphere.

The first effect is described by well-known solutions to Maxwell's equations, resulting in a beam divergence inversely related to the effective output aperture diameter, and leading to an inverse square law for the signal power in a heterodyne system viewing a large diffuse target.

The second and third categories are more complicated because of their variability and complicated effects on SNR. The second effect results in random signal fluctuations over a short time due to variations in the atmosphere, while the third effect results in a more predictable signal variation with temperature and humidity. The signal fluctuations suggest use of processing techniques involving several pulses to enhance the detection probability or reduce the probability of false alarms. Atmospheric attenuation is dependent on the transition line, but this also affects output power, making appropriate line choices more difficult.

Section 4.2 discusses various schemes for using several pulses in detection decisions, while section 4.3 describes the atmospheric attenuation and its dependence on wavelength, temperature and humidity.

4.2 SIGNAL DETECTION PROBABILITY

The probability of detecting a signal depends upon several factors, including signal-to-noise ratio, probability of false alarm, and the statistics of the signal. Signal fluctuations can be caused by the interaction of the radiation with the target or the atmosphere. The case of a Rayleigh-distributed signal has been analyzed in the literature. However, the signals from the CAT detection system appear to be log-normally distributed. An analysis was performed to compare the effects of integrating N returns of a log normal signal or looking for a single return above threshold from N signals.

For N independent pulses, the total probability of a missed detection equals the Nth power of the probability of missing a single pulse:

$$1 - P_{D-T} = (1 - P_{D-P})^N$$

where P_{D-T} = total detection probability

P_{D-P} = individual pulse detection probability

Table 4-1 lists some values of the single pulse detection probability for various values of the total detection probability and the number of pulses observed.

The relationship between detection probability, signal-to-noise ratio, and false alarm rate have been evaluated and are documented in a Raytheon memo by Dr. H. Groginsky wherein signal-to-noise ratios as a function of the number of pulses for various detection probabilities are shown. Curves are drawn both for the case of integration and for detection of one of N pulses. Figures 4-1 through 4-3 correspond to a log-normal distribution whose ratio of mean to median, ρ, equals 2, while Figures 4-4 through 4-6 have ρ = 3.

TABLE 4-1

SINGLE PULSE DETECTION PROBABILITIES

TOTAL DETECTION PROBABILITY	NUMBER OF PULSES	SINGLE PHASE DETECTION PROBABILITY
0.9	10	0.21
0.9	20	0.11
0.9	30	0.074
0.9	50	0.045
0.9	70	0.032
0.9	150	0.023
0.7	10	0.11
0.7	20	0.058
0.7	30	0.039
0.7	50	0.024
0.7	70	0.017
0.7	100	0.012
0.5	10	0.067
0.5	20	0.034
0.5	30	0.023
0.5	50	0.014
0.5	70	0.0099
0.5	100	0.0069

SIGNAL TO NOISE RATIO REQUIRED TO
OBTAIN A PROBABILITY OF DETECTION OF .5

$[P_{fa} = \ln 2/10^4]$

LOG NORMAL RANDOM VARIABLE WITH $\rho = 2$

DETECTION OF ONE OF N

PULSE INTEGRATION

N, NUMBER OF PULSES

SIGNAL TO NOISE RATIO, dB
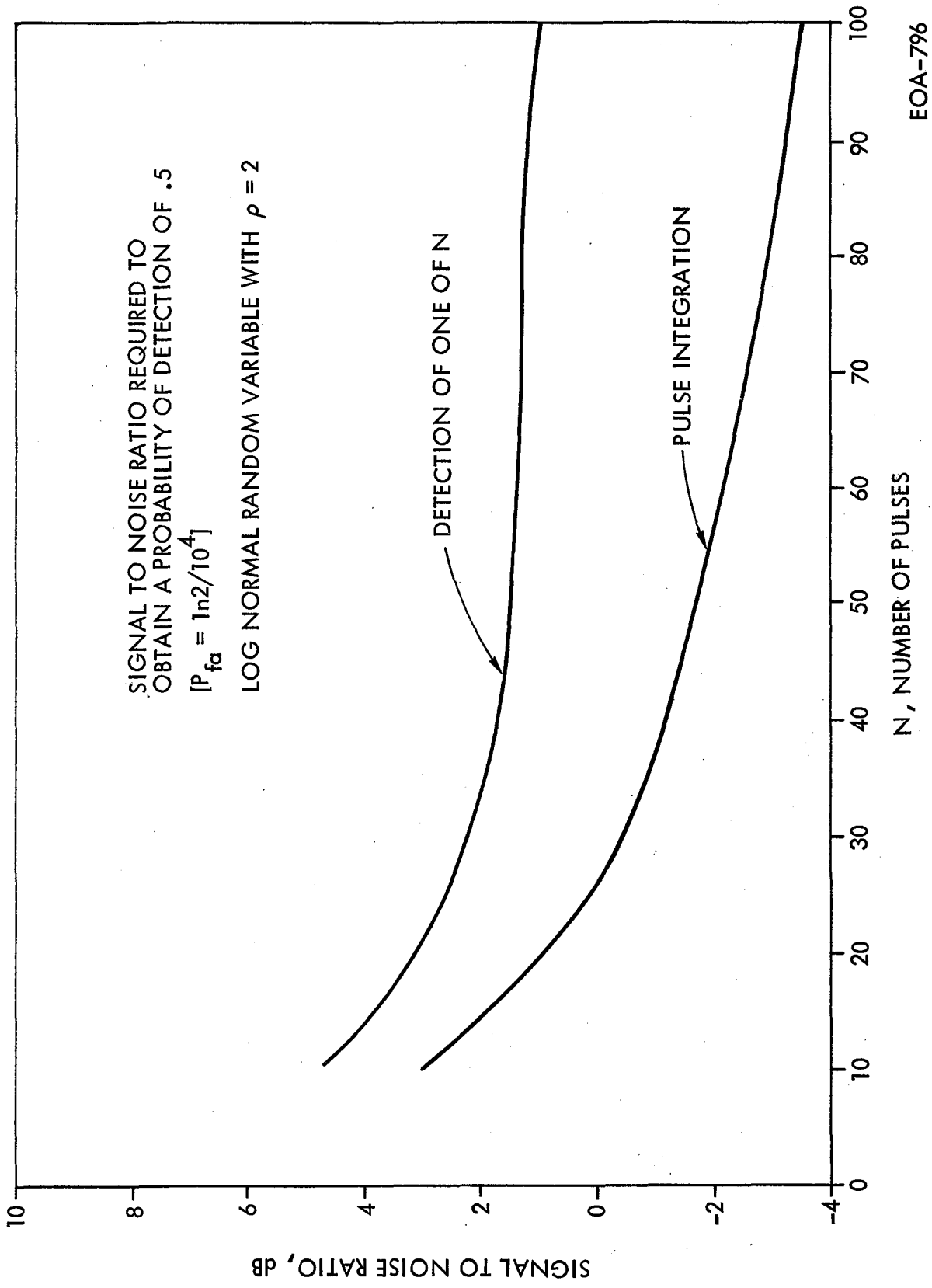
EOA-796

Figure 4-1. S/N Ratio Required to Obtain Probability of
Detection of .5 with P2
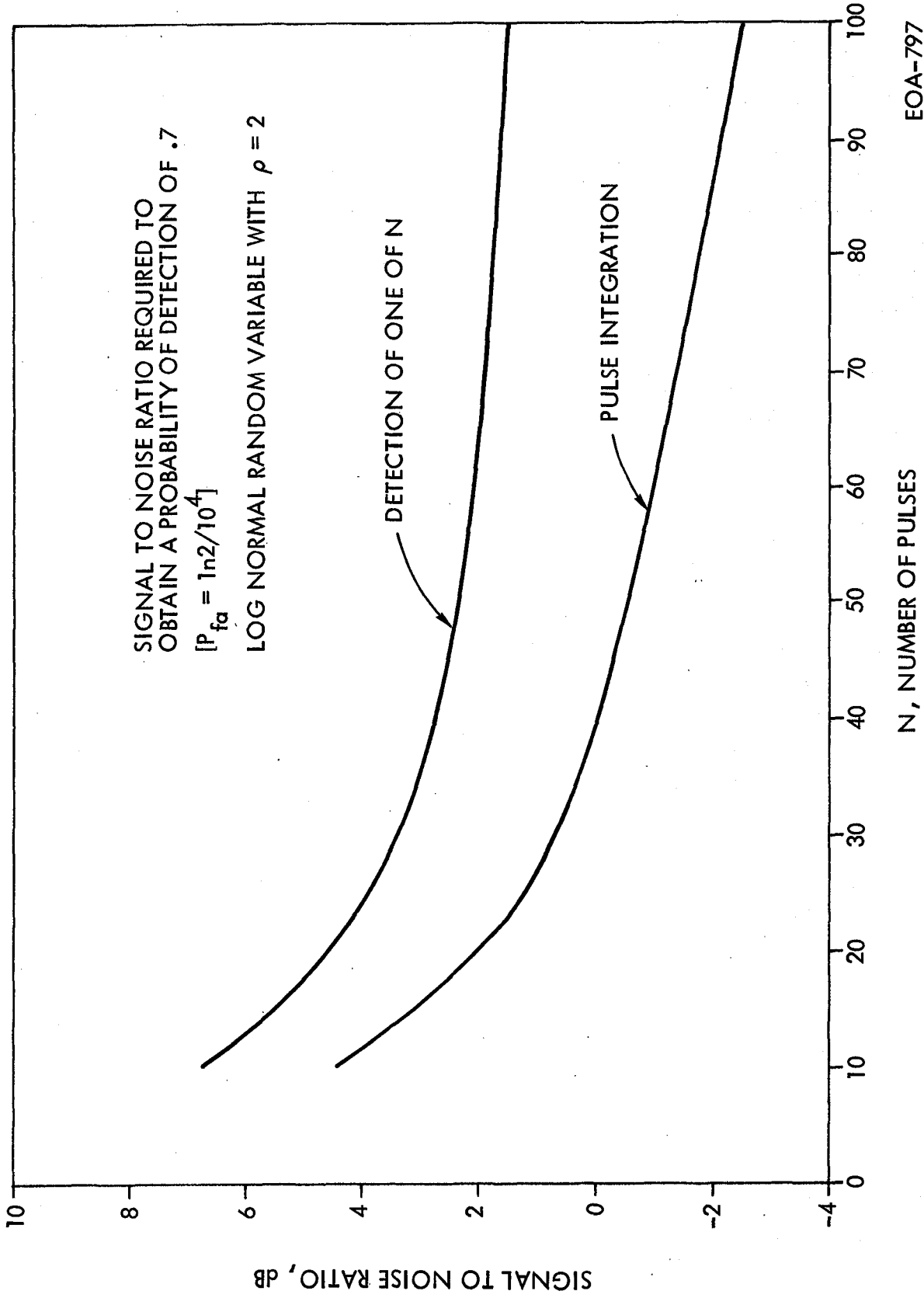
Figure 4-2. S/N Ratio Required to Obtain Probability of Detection of .7 with P2
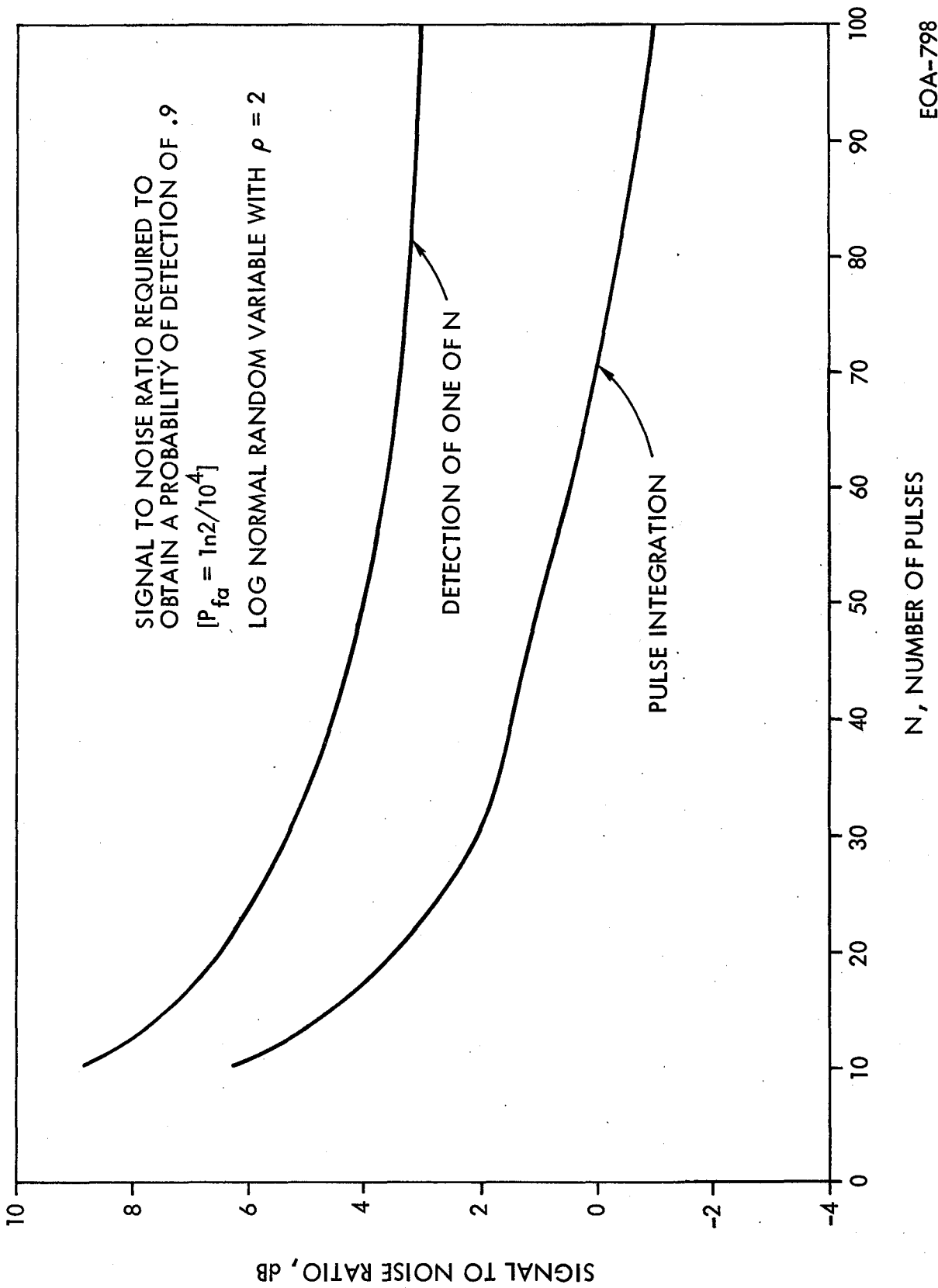
SIGNAL TO NOISE RATIO REQUIRED TO
OBTAIN A PROBABILITY OF DETECTION OF .9
$[P_{fa} = \ln 2/10^4]$

LOG NORMAL RANDOM VARIABLE WITH $\rho = 2$

DETECTION OF ONE OF N

PULSE INTEGRATION

N, NUMBER OF PULSES

SIGNAL TO NOISE RATIO, dB

EOA-798

Figure 4-3. S/N Ratio Required to Obtain Probability of
Detection of .9 with P2

4-6

SIGNAL TO NOISE RATIO REQUIRED TO
OBTAIN A PROBABILITY OF DETECTION OF .5

$[P_{fa} = 1n2/10^4]$

LOG NORMAL RANDOM VARIABLE WITH $\rho = 3$
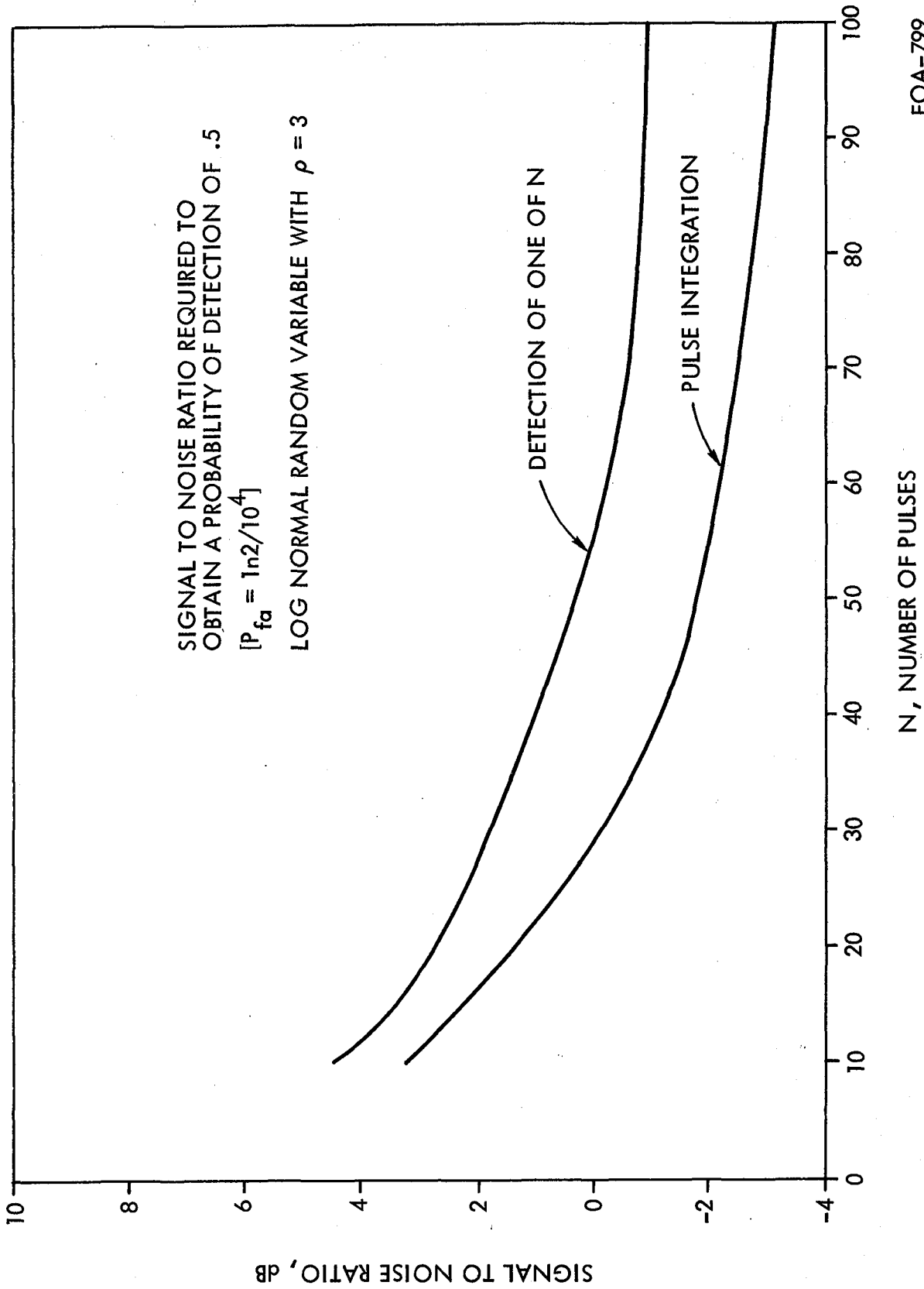
EOA–799

Figure 4–4. S/N Ratio Required to Obtain Probability of
Detection of .5 with P3

SIGNAL TO NOISE RATIO REQUIRED TO
OBTAIN A PROBABILITY OF DETECTION OF .7
$[P_{fa} = \ln2/10^4]$

LOG NORMAL RANDOM VARIABLE WITH $\rho = 3$

DETECTION OF ONE OF N

PULSE INTEGRATION

N, NUMBER OF PULSES

SIGNAL TO NOISE RATIO, dB

EOA-800
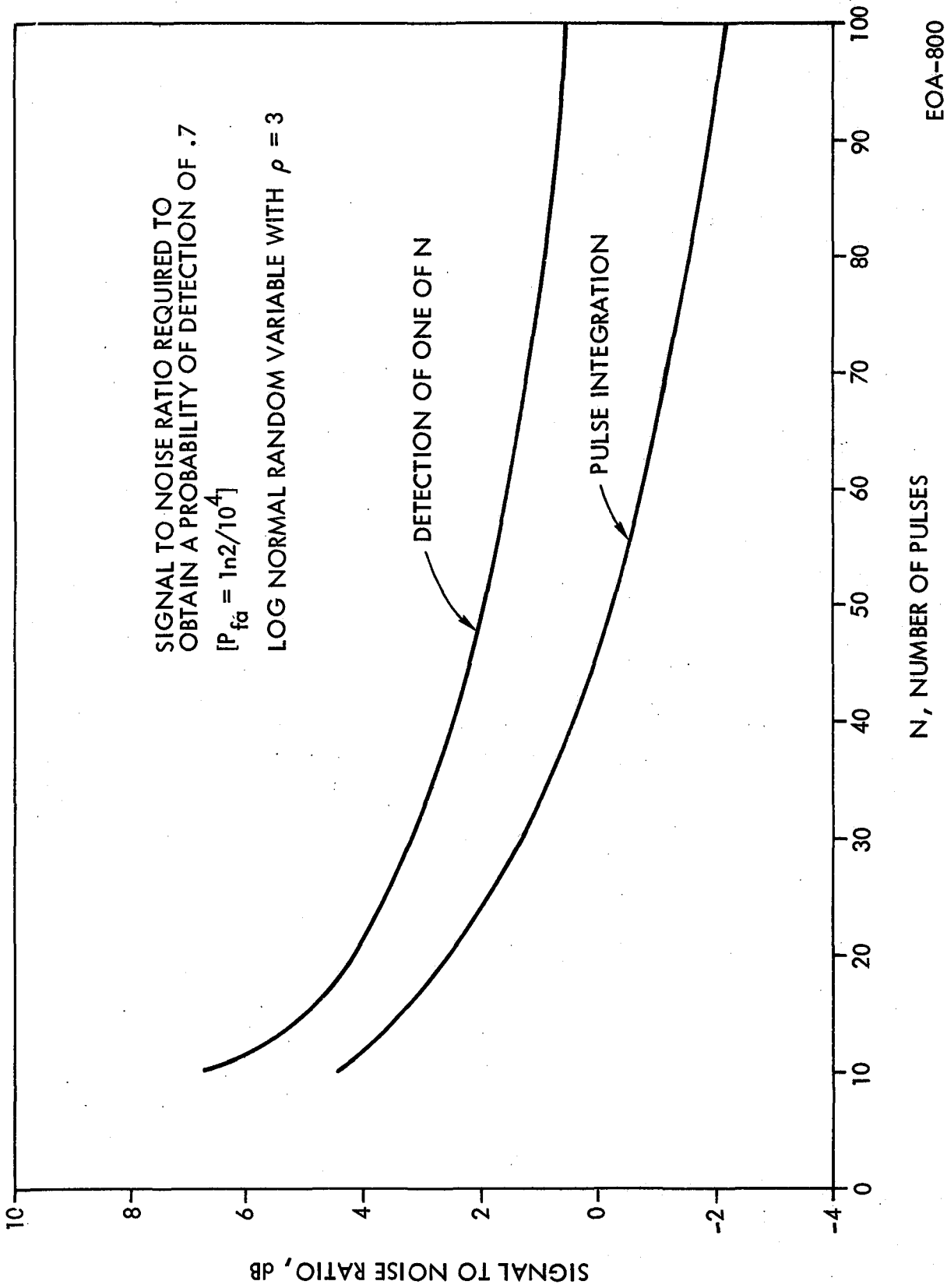
Figure 4-5. S/N Ratio Required to Obtain Probability of
Detection of .7 with P3

SIGNAL TO NOISE RATIO REQUIRED TO
OBTAIN A PROBABILITY OF DETECTION OF .9

$[P_{fa} = \ln2/10^4]$

LOG NORMAL RANDOM VARIABLE WITH $\rho = 3$

DETECTION OF ONE OF N

PULSE INTEGRATION

N, NUMBER OF PULSES

SIGNAL TO NOISE RATIO, dB

EOA-801
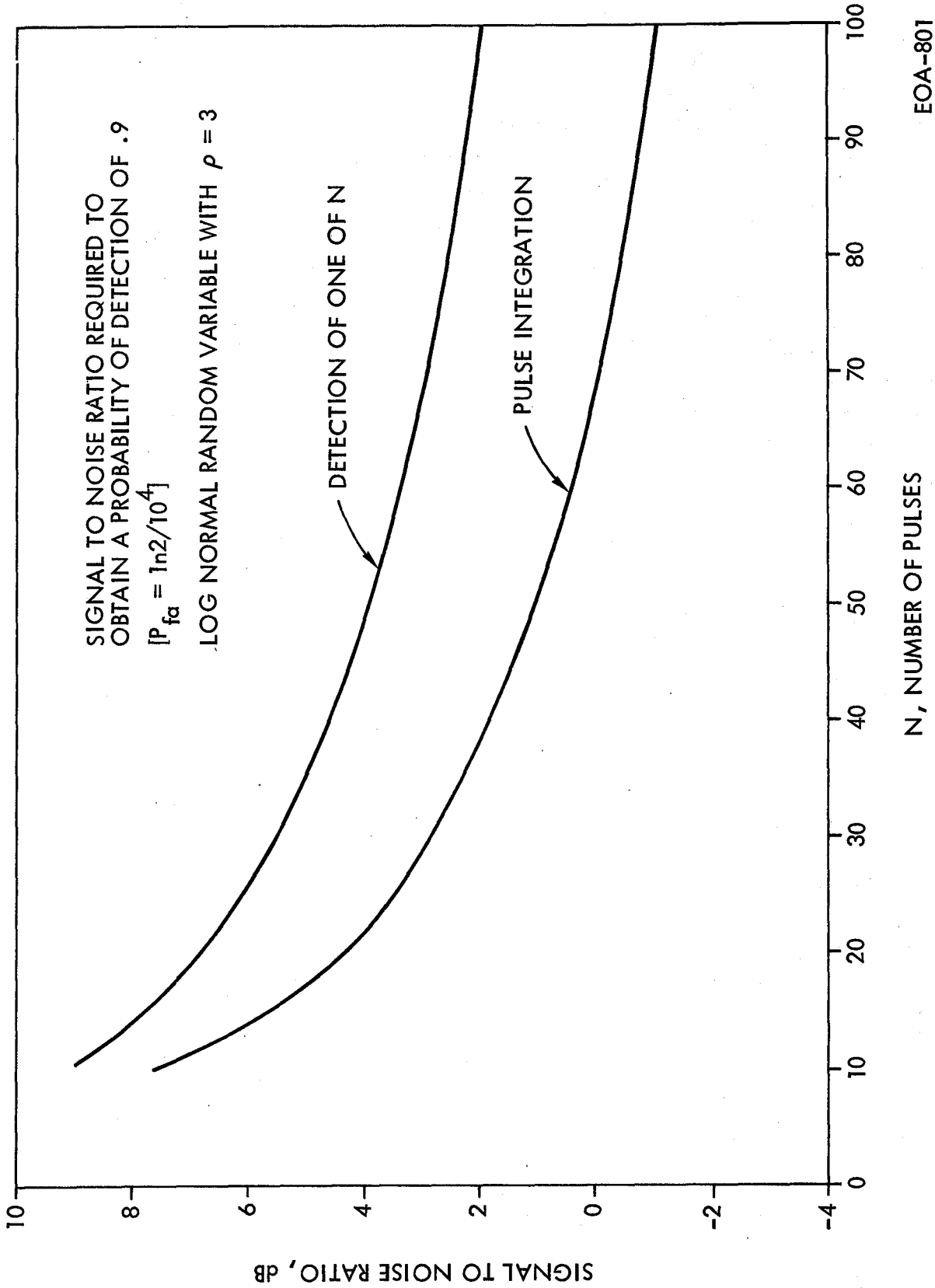
Figure 4-6. S/N Ratio Required to Obtain Probability of
Detection of .9 with P3

4.3 ATMOSPHERIC ATTENUATION

Various researchers have measured the attenuation of CO_2 laser radiation in clear weather. McCoy, Rensch and Long[3] measured specifically the attenuation due to water vapor which is the attenuator of most interest for this analysis, but the measurements of Shumate et al[4] are more recent and appear to have been made under more carefully controlled conditions. Therefore, the data of the latter were used for the attenuation due to water vapor. For the CO_2 attenuation, the values presented by S. Murty[5] based upon the measurements of P. Yin and R. Long[6] were included. Finally, the aerosol attenuation values were taken from McClatchey's data[7] extrapolated to a visibility of 12 km.

The relationship of water vapor pressure to temperature and humidity is shown in Figure 4-7. It is apparent that the water vapor pressure during the summer is often above the highest pressure of the Shumate measurement, which was 15 Torr (20.0 millibars). For example, a temperature of 95°F (35°C) and a relative humidity of 95 percent produces a water vapor pressure of 40 Torr (53.3 millibars). Therefore, the data had to be extrapolated to the pressures of interest; but in order to do it accurately, the relationship between attenuation and pressure must be known. The relationship is assumed to be quadratic.

$$\mu = Ap + Bp^2 \tag{1}$$

where μ is the attenuation coefficient, p is the water vapor partial pressure and the coefficients A and B depend upon the total pressure.

The atmospheric attenuation coefficients were determined for selected emission lines of the CO_2 laser in clear weather as a function of temperature and relative humidity at sea level. The lines of specific interest for this analysis are the P(16), P(18), P(20), P(22), P(24) and P(26) lines of the 10.4 micron branch, but other lines were also briefly examined.

The conclusions of the analysis are:
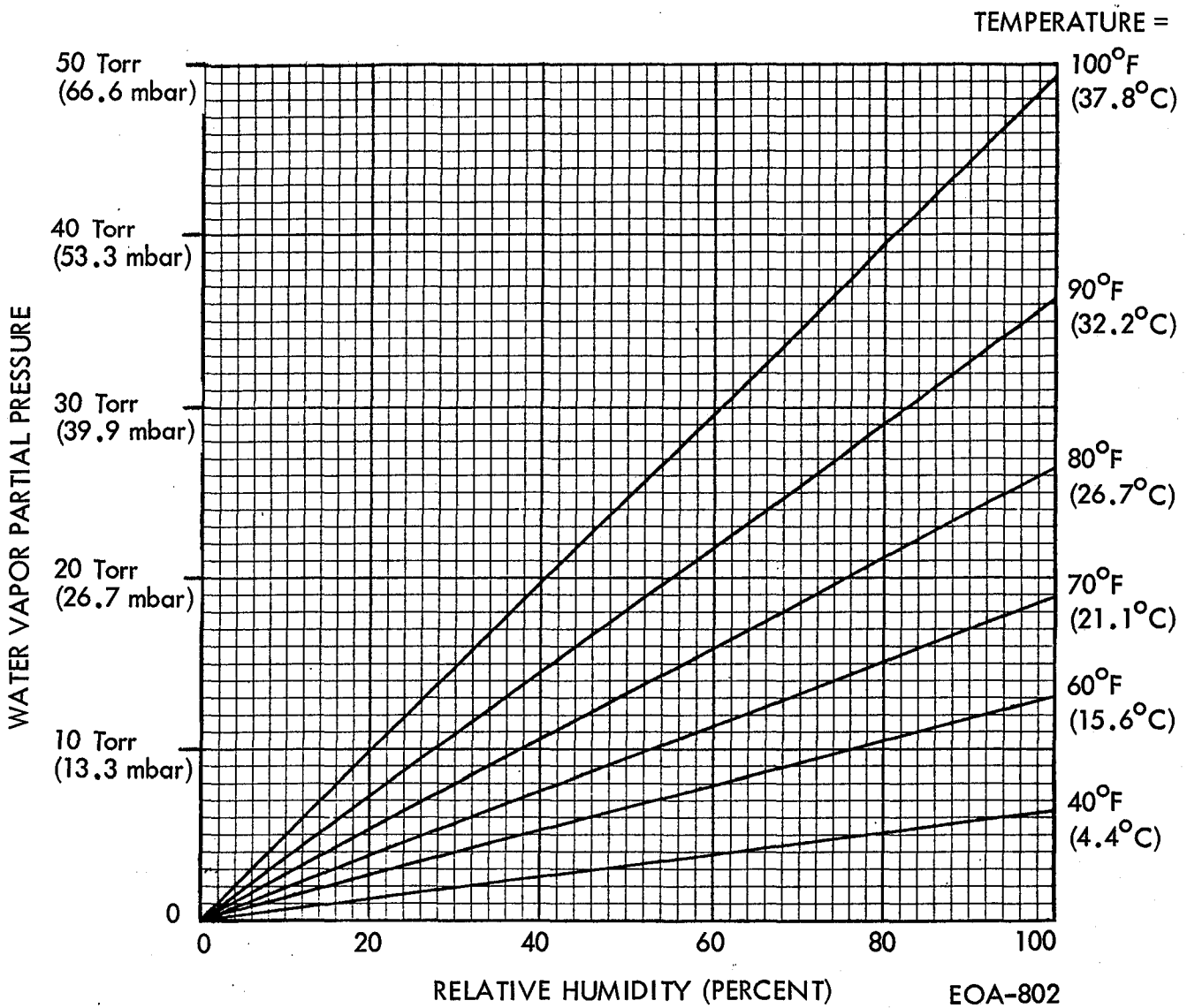
Figure 4-7. Water Vapor Pressure as Function of Temperature and Humidity. One cm of H_2O/km $\approx$ 10 Torr (13.3 mbar)

1. Attenuation coefficients for the P(18), P(20), P(22), P(24) and P(26) lines are generally within 0.5 dB/km (each way) of each other, with the P(20) line the worst and the P(26) line the best of this group. The P(16) line, however, attenuates by a somewhat greater amount - 0.5 to 2 dB/km more depending upon humidity - and should be avoided. Figures 4-8 and 4-9 compare the attenuation for different P-lines.

2. Typical attenuation values vary from 1 dB/km each way in an 11 Torr (14.7 mbar) water vapor pressure atmosphere (e.g., T = 70°F (21°C), R.H. = 60%) to 6 dB/km each way in a 40 Torr (53.3 mbar) atmosphere (e.g., T = 95°F (35°C), R.H. = 95%). For a 5 km path, the corresponding atmospheric losses range from 10 to 60 dB round trip. Figure 4-10 shows the variation of atmospheric attenuation with range. Figures 4-11 and 4-12 show the variation with temperature and humidity for two specific P-lines, P(20) and P(26), which bracket the attenuation for the five lines from P(18) to P(26).

3. Under humid conditions, water vapor is the dominant attenuator. In a clear dry atmosphere, CO_2 is the dominant attenuator. Finally, under foggy conditions, the aerosol scatter becomes dominant, but note that the fog must be fairly dense in order for the aerosol extinction to exceed the water vapor attenuation at warm temperatures. A 40 Torr (53.3 mbar) clear atmosphere (e.g., T = 95°F (35°C) and R.H. = 95%) produces roughly the same attenuation as a 150 meter visibility fog.

4. The 9.4 micron branch and selected R lines of the 10.4 micron branch suffer substantially less attenuation under hot and humid conditions than the P lines of the 10.4 micron branch. Differences may reach 5 to 10 dB/km round trip. Thus, laser operation on these other lines should be considered for hot, humid environments even though the efficiency is lower and the laser is more complex.
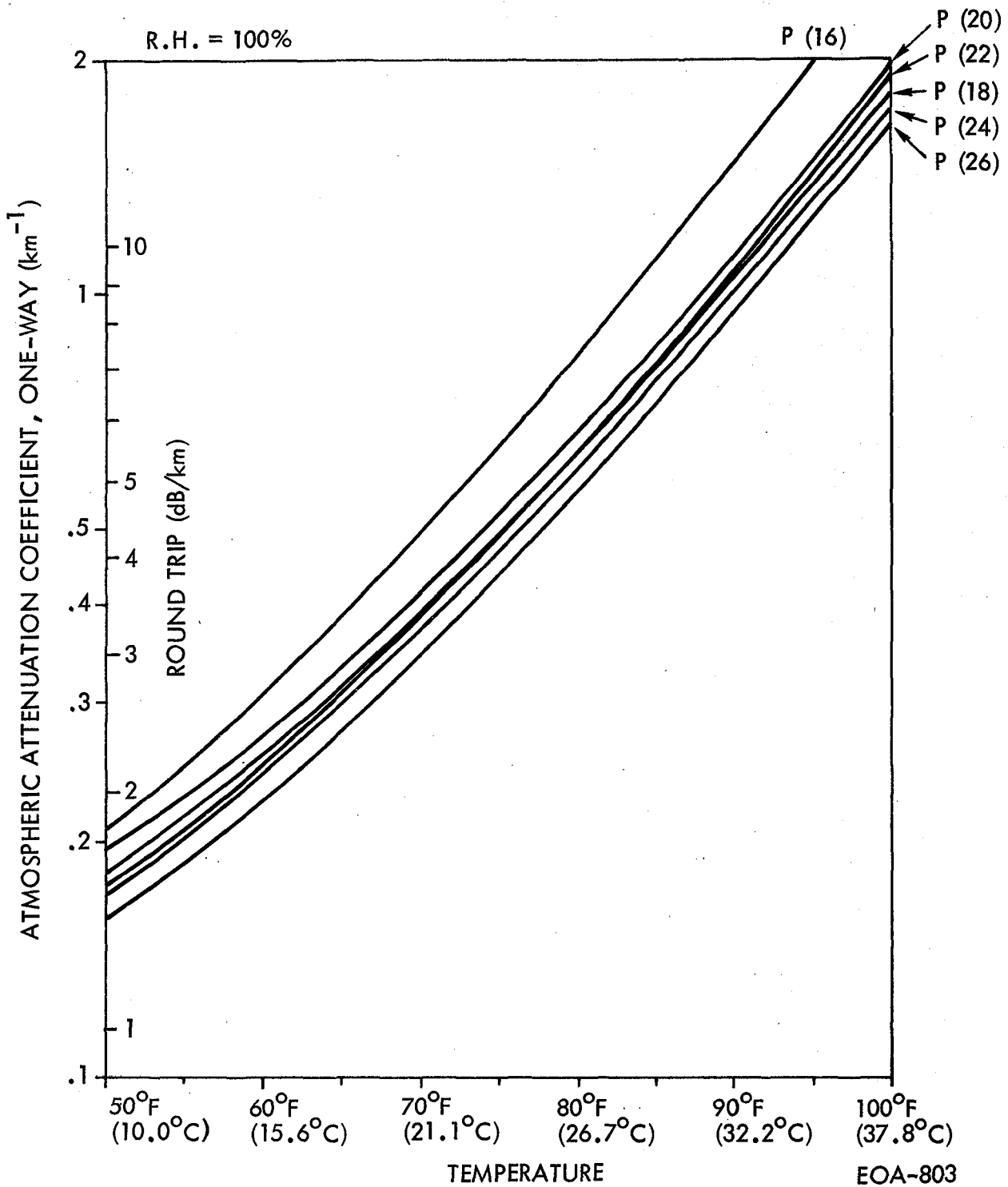
Figure 4-8. Atmospheric Attenuation Coefficient for 10.6 Micron CO_2 Laser Lines at Sea Level, 100% Relative Humidity.
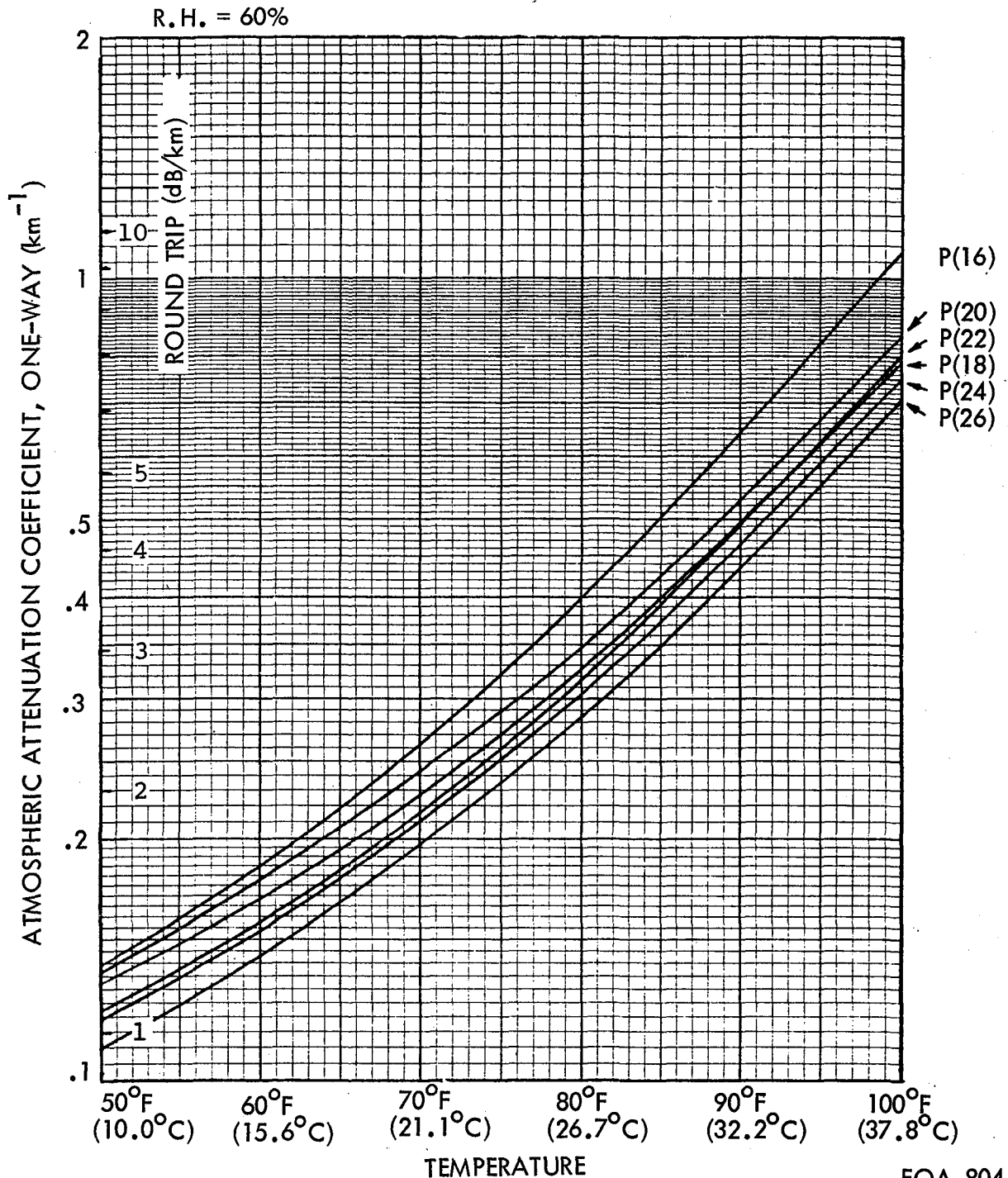
Figure 4-9. Atmospheric Attenuation Coefficient for
10.6 Micron CO$_2$ Laser Lines at Sea Level,
60% Relative Humidity.

EOA-804

4-14
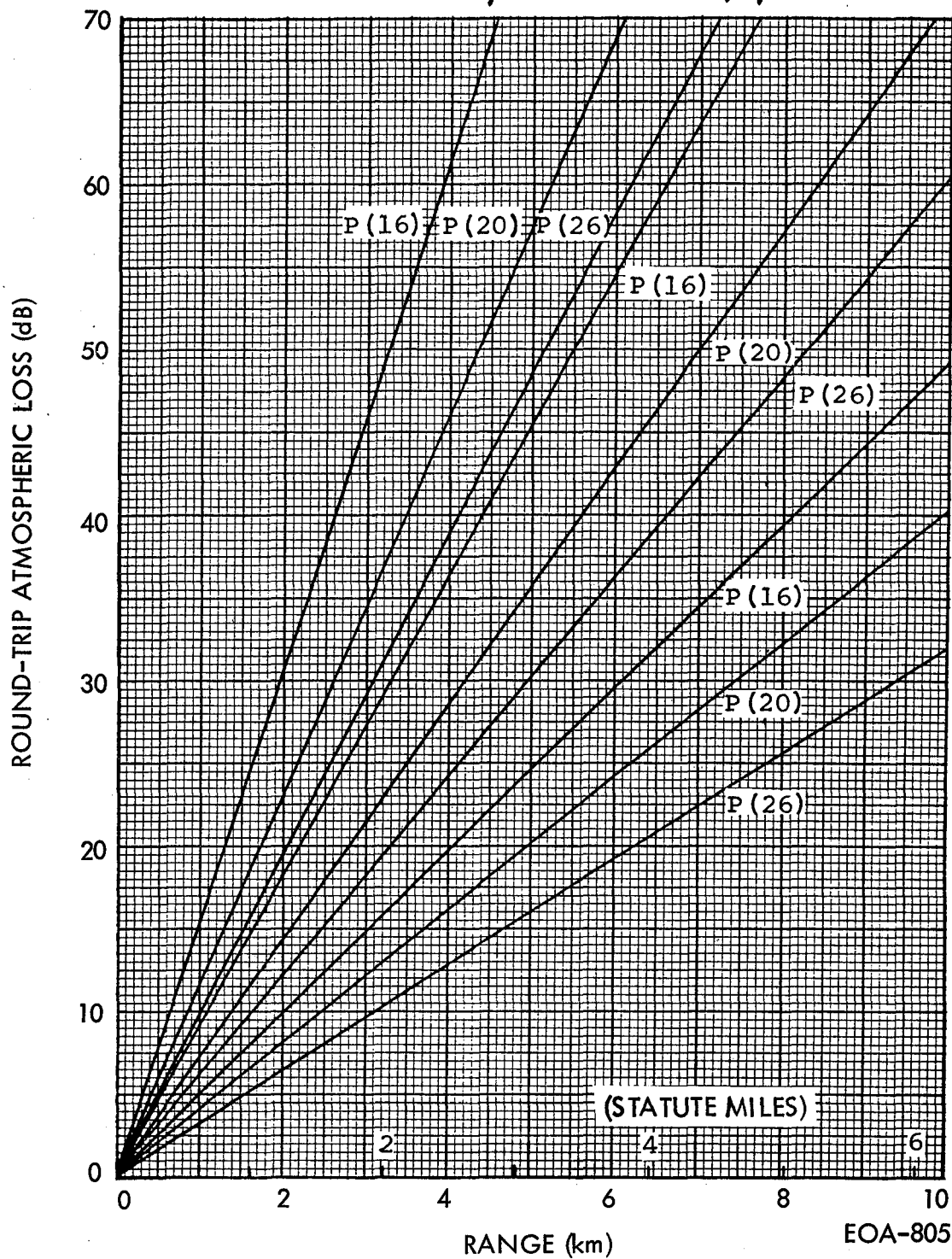
Figure 4-10. Atmospheric Loss for Different
10.6 Micron CO$_2$ Laser Lines as
Function of Range at Sea Level.
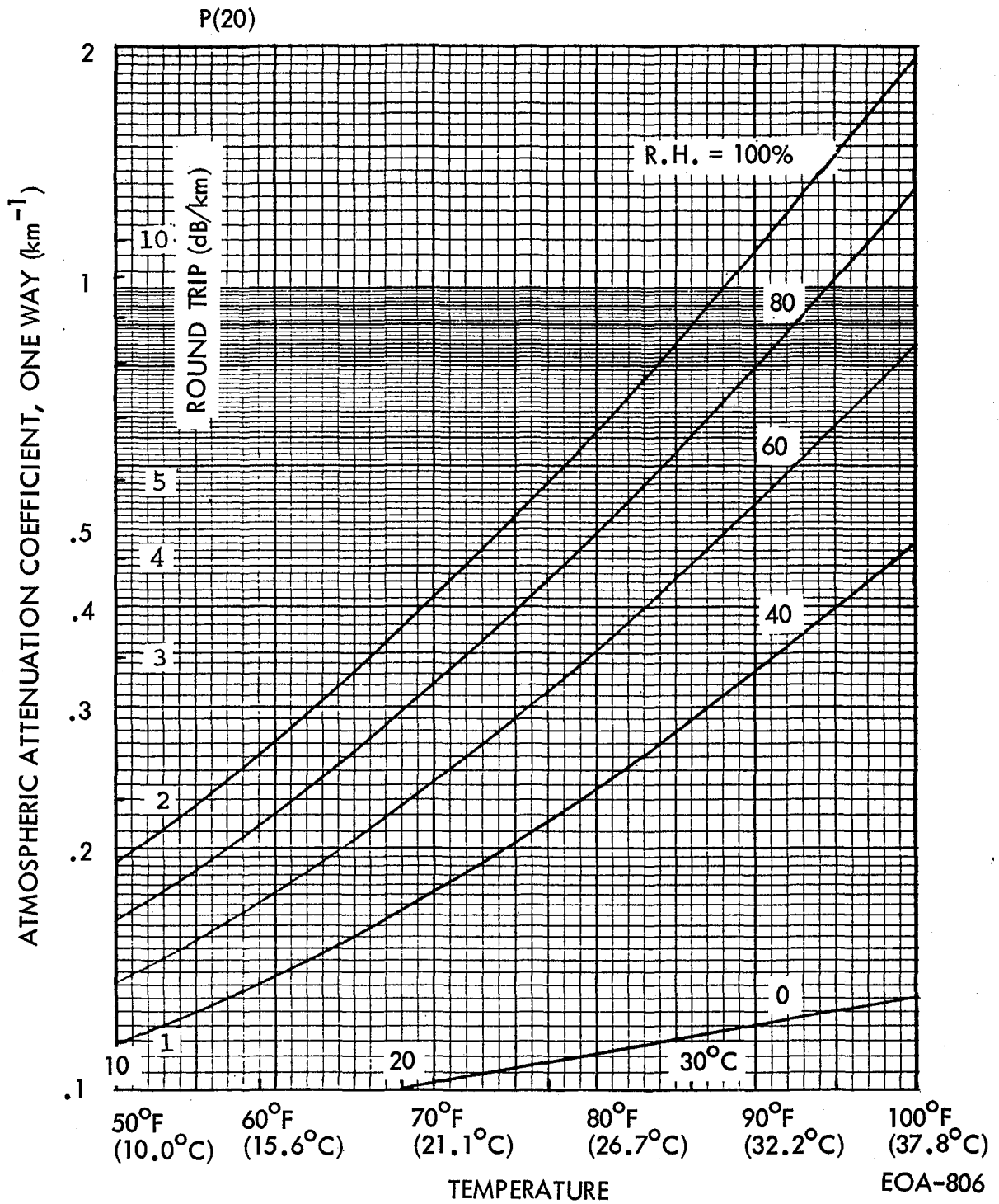
Figure 4-11. Atmospheric Attenuation Coefficient for
P(20) Line of CO_2 Laser at Sea Level
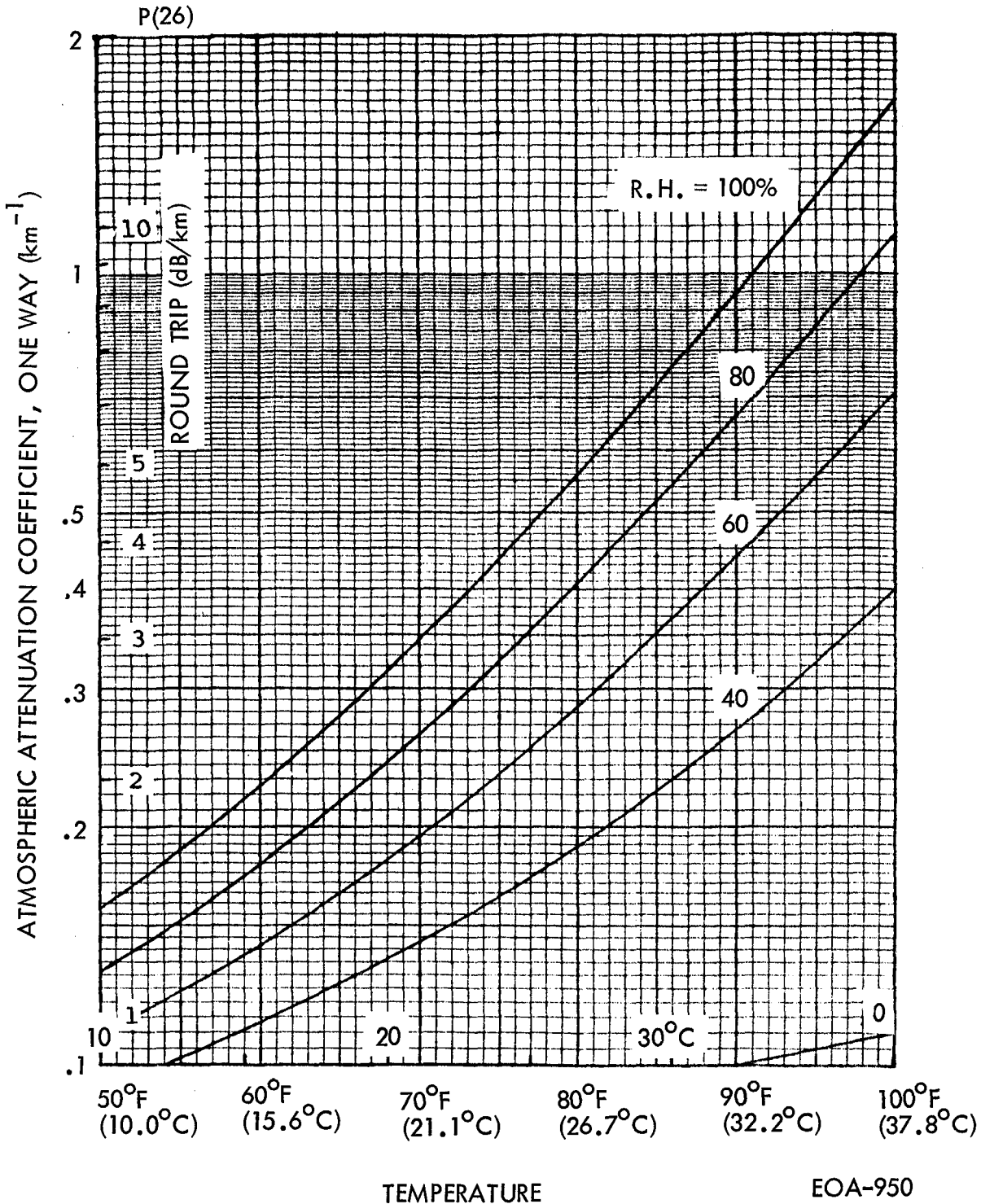
Figure 4-12. Atmospheric Attenuation for P(26)
Line of 10.6 Micron CO$_2$ Laser at
Sea Level

4-17

SECTION 5
AIRCRAFT INTERFACE PROGRAM

5.1 SYSTEM INSTALLATION

To make the CAT system an airborne instrument, a program was defined to investigate aircraft flight parameters and configure the CAT instrumentation for optimum performance with respect to the NASA Convair 990 test aircraft. The Airborne Science Office at the AMES Research Center had indicated that a pod fairing at Station 728 (Figure 5-1) would be required for the optical scanner assembly in order for the signal beam to radiate from a point outside the aircraft's boundary turbulence zone (7-8 inches at Station 728). The system configuration shown in Figure 5-1 was arrived at after flight noise, vibration, shock, and safety analyses were performed. These analyses are presented in Appendices A and B, Volume II of this report. The arrangement within the aircraft, as shown in Figure 5-1, has blocks A and C as "lowboy"-type equipment racks supporting the CAT transmitter assembly. Block D is a standard equipment rack (Figure 5-2) containing the transmitter electronics and system synchronizer, Block G, (Figure 5-3) is the receiver/processor rack, and Block E, (Figure 5-4) contains support and backup instrumentation for the system. Figures 5-5 and 5-6 show the shock-mounted transmitter assembly being installed on its two supporting lowboy racks, and a view of the CAT telescope projecting into the CAT fairing, through what used to be the aircraft port escape hatch.

The CAT fairing (Figure 5-7) was attached to the CV990 in a manner compensating for the nominal 1.5° nose-up flight altitude. Incorporated within the fairing is a pair of motor-driven clamshell doors, shown closed in Figure 5-8, to protect the CAT window from particle damage during takeoffs and landings. A television camera
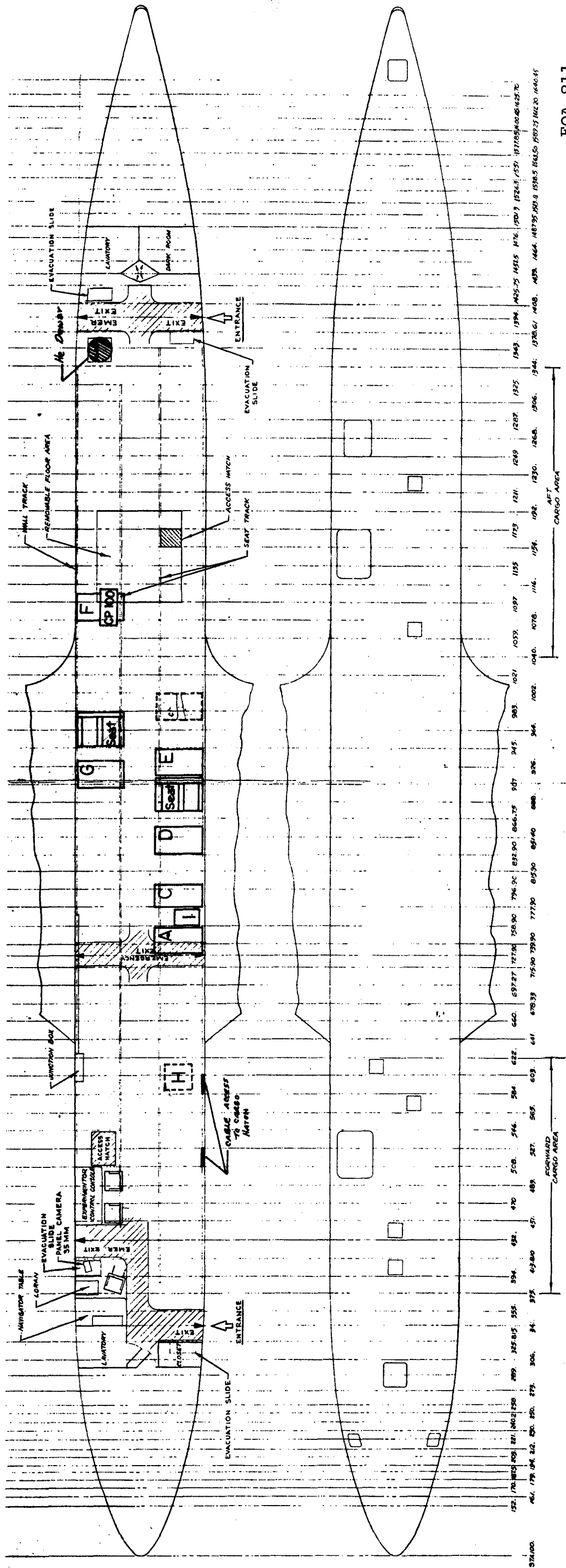
Figure 5-1. CAT Installation
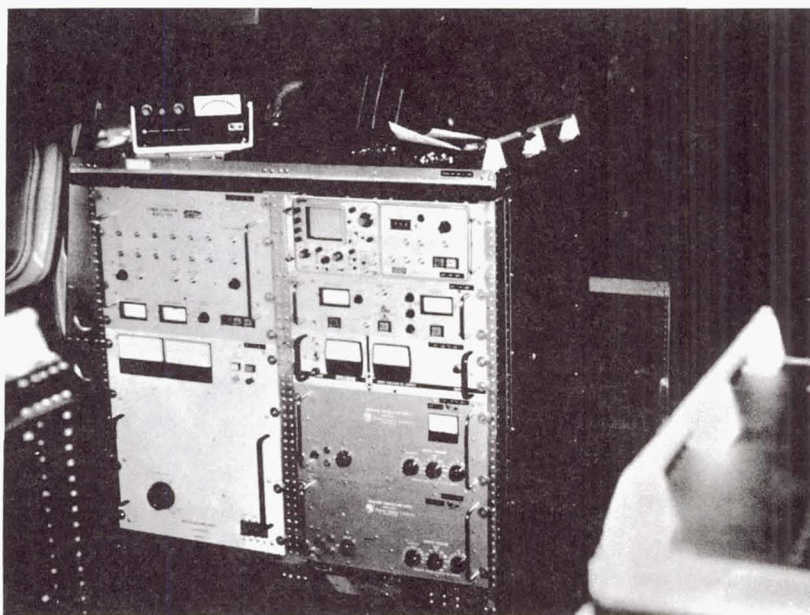
EO-466

Figure 5-2. Transmitter Rack in CV-990
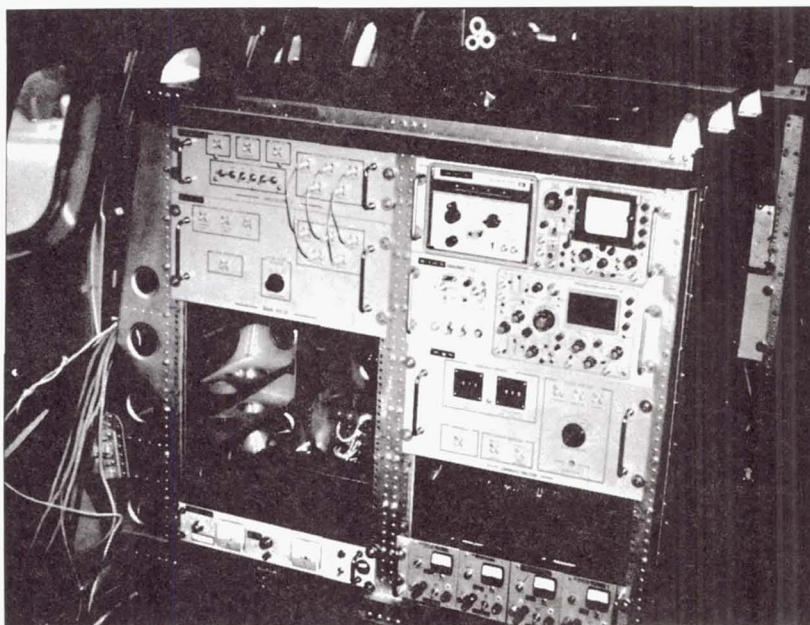
EO-467

Figure 5-3. Receiver Processor in CV-990
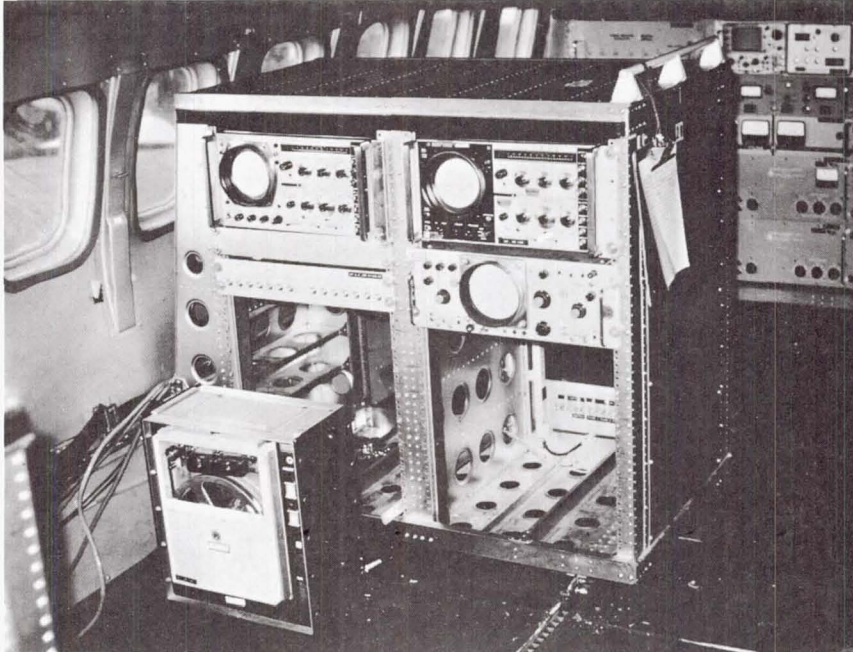
EO-468

Figure 5-4. Backup Instrumentation Rack,
During Installation
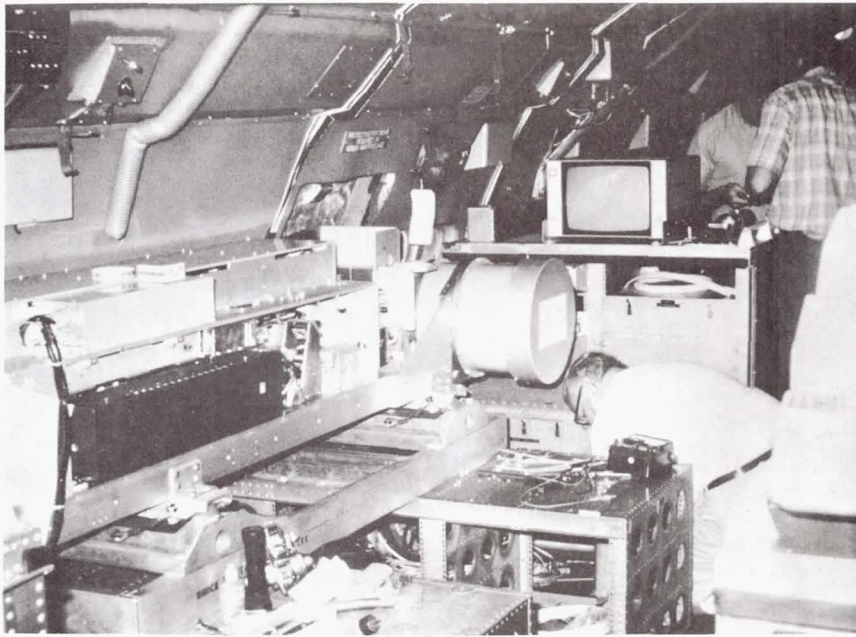
EO-309

Figure 5-5. CAT Transmitter Assembly Being Installed in CV-990
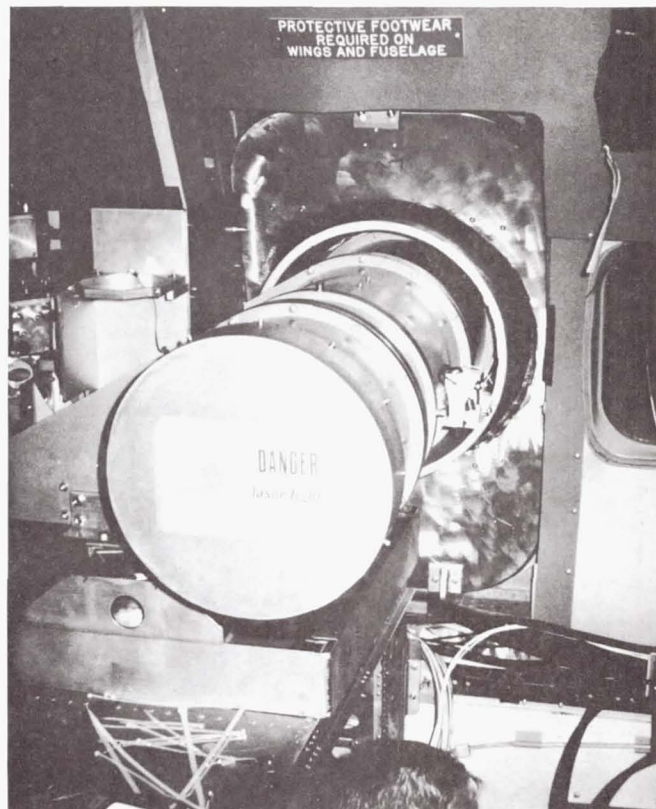
EO-465

Figure 5-6. CAT Telescope, Shown Centered on the CAT
Fairing Input Aperture
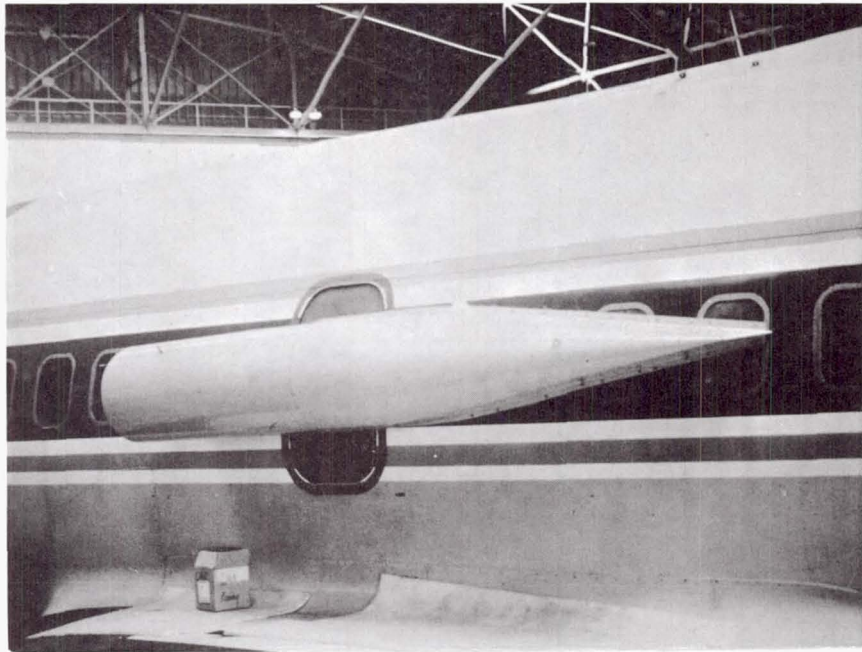
Figure 5-7.   CAT Fairing on CV990
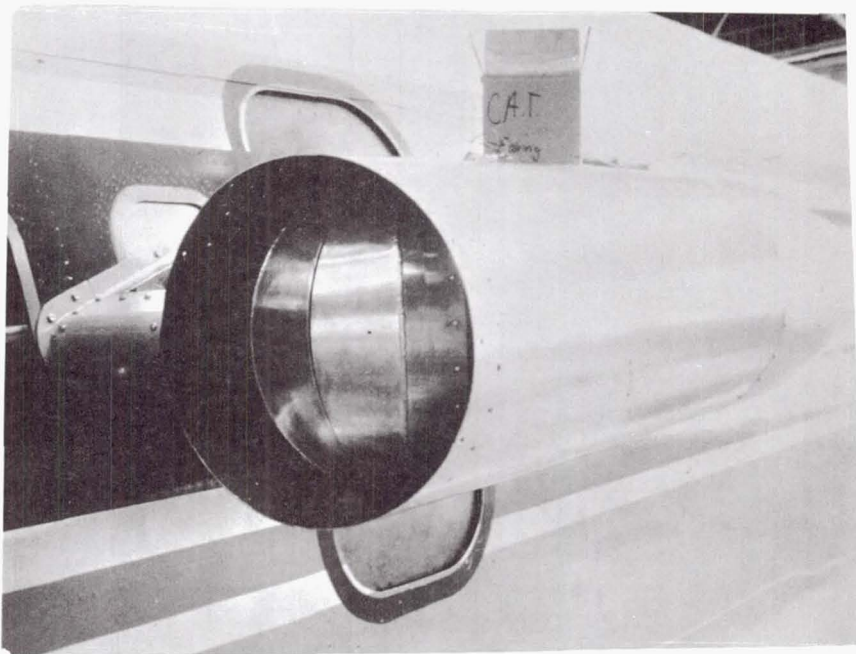
Figure 5-8.   "Clamshell" Doors in CAT Fairing.

installation was planned for follow-on programs to be boresighted with the CAT systems output beam axis for evaluation of system performance against discrete terrain features or clouds. This camera location was planned to be within the CAT pod.

5.2 AIRCRAFT INSTRUMENTATION

The following instrumentation was installed in the aircraft in order to record relevant aircraft performance with respect to CAT instrumentation data for use in the several data analyses programs (see Appendices E and F).

Ampex Model CP-100 14 Channel Recorder	To record the receiver/processor multiplexed PCM format containing synchronization, run and frame numbers, data status, sampling range, and filter bank output data as well as aircraft XYZ accelerometer ouputs, IRIG-B time code, and aircraft intercom, on separate channels.
Precision Instruments Model 7-Channel Recorder	To record the swept HP analyzer display and sweep, WWV time (audio), sequence camera pulses and aircraft intercom.
35-MM Sequence Camera	To photograph the RVI and "A" scope displays, usually at a 1 frame/second rate. Incorporates a data box, containing a WWV synchronized clock, frame counter, and flight information card.
Hewlett Packard Model 197A Oscilloscope Camera	For in-flight sampling of "A" scope displays. Incorporated a clock synchronized with WWV.
Tektronix Model C-30-A Polaroid Backed Oscilloscope Camera	For in-flight sampling of RVI and IVI data at the receiver processor station.

SECTION 6
SITE EXAMINATION AND SELECTION PROGRAM

6.1 GENERAL

As described in Raytheon publication ER72-4243 propagation tests
and experiments are necessary for various system evaluations and
system alignment. These tests required stable transmission platforms
and targets and were considered most desirable if they could be
located near the airfield and the contractor's facilities. Airfield
sites evaluated at the AMES Research Center were:

The Systems Engineering Facility (Bldg N-244)

The Space Sciences Laboratory (Bldg N-245)

The Life Sciences Research Laboratory (Bldg N-279)

with site N-244 being selected.

Test sites evaluated near the contractor's plant were:

Plum Island, Ipswich, Mass.

Springhill Beach, Sandwich, Mass.

South Beach, Martha's Vineyard, Mass.

Coatue Beach, Nantucket, Mass.

Monomoy Island, Chatham, Mass.

Great Island, Wellfleet, Mass.

The evaluations of the latter included examinations of USGS
surveys, local ordinances, property rights, acceptability of local
weather conditions, range availabilities, accessibility of power,
and equipment protection considerations. Specific ground test pro-
grams and results are described in Section 7.

6.2 THE MARTHA'S VINEYARD SITE

Evaluation of the possible contractor test sites led to the selec-
tion of the Martha's Vineyard location (Figure 6-1) for field tests
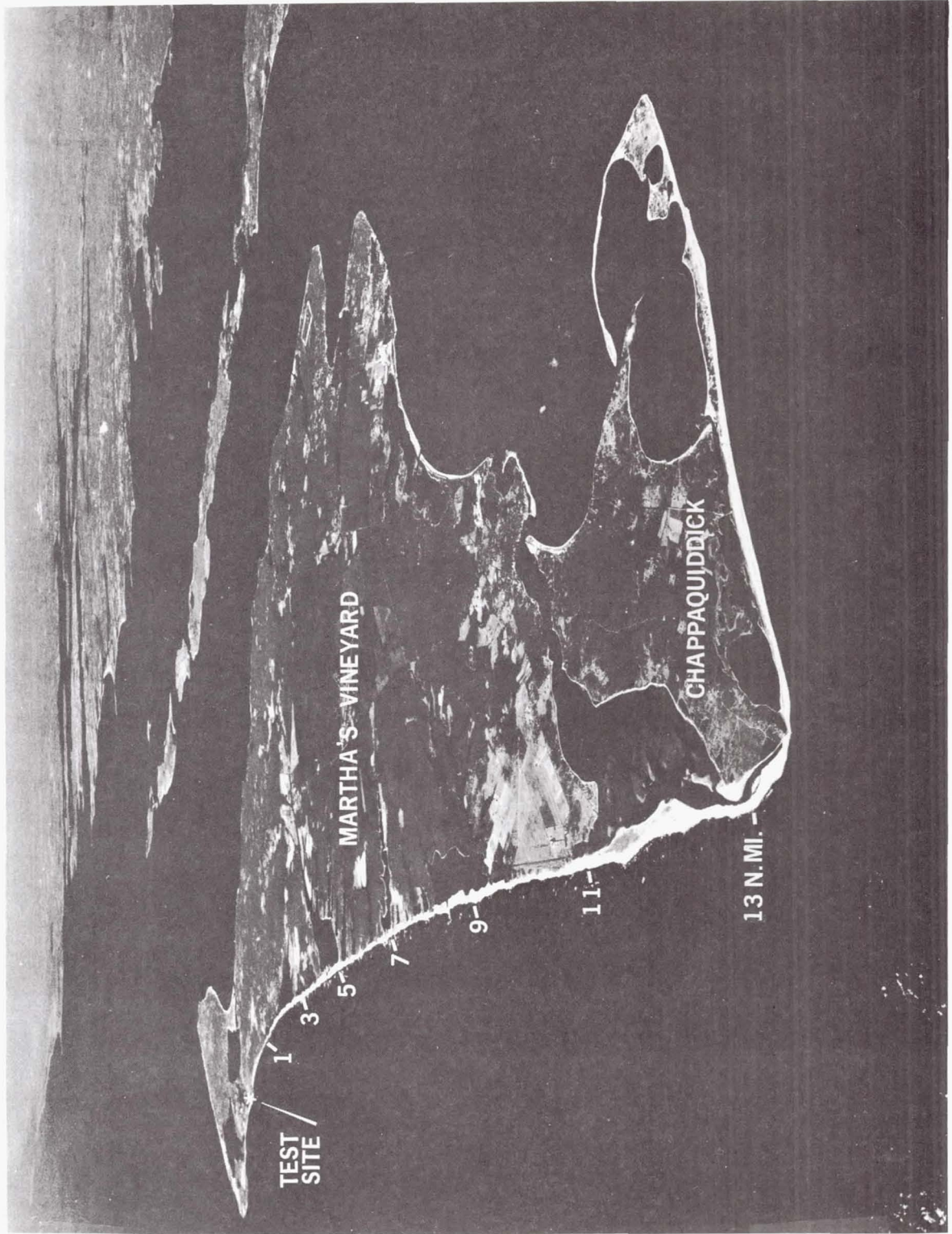
Figure 6-1. Martha's Vineyard Test Site

using a van as a base station after arrangements were worked out for site rental and access rights. The following is the preliminary CAT ground test outline:

1. Reestablish system parameters achieved at Moffett Field: 20 + mJ output at 160 Hz, 8 μsec PW. (P_{avg} under these conditions is ∿3.5 watts.)

2. Set up target at 6800 ft. (2,073 m) (Moffett situation) and perform total system alignment, including the telescope, with a HeNe source.

   a. Take S/N measurements of belt target signals at 6 MHz and higher, if possible.

   b. Take S/N measurements at a variety of ranges along the beach with the "as flown" alignment conditions. At each range, the following data were monitored and recorded:

   Transmitter parameters, i.e., PRF, P_{avg} PW, etc.

   "Ringing" waveforms

   Beam diameter measurements at the target sites

   Weather parameters (temp., RH, wind velocity and wind direction)

   c. Perform steps 2a and b with the 7 x 7 x 100 mm GaAs modulator flown in August-September '72 with both CAT detectors.

3. Focusing Tests - When the beam diameter measurements made in 2b above have established that the transmitter is collimated, the following focusing activities were performed.

   Realign the telescope from a HeNe source at some other range

Realign the telescope at some given range at 10.6 μ to correct for measured discrepancies.

Varying the focus of the internal beam expanders to maximize S/N at discrete ranges and determine what these focusing parameters are.

4. Additional system evaluations:

Master Oscillator tests. Thermal/Acoustical evaluation, P-( ) line characteristics; beam shape, etc.

Modulator Ringing. Comparison of both units-Measurement of backscattered energy on detector.

Avantek Amplifier tests. Response vs. back-scatter level.

Cooling system evaluations.

Receiver/Processor tests. "Ringing" effects on processor - calibration of effect of integration, record system, and IVI. Comparison of "A" Scope; RVI and IVI.

Window Tests.

The feasibility of using a van as a base site and as a long range pointing platform was successfully demonstrated through HeNe laser tests, where the laser/telescope combination was set up in the van and focused on a target screen 6,800 feet (2,073 meters) away. Beamsteering attributable to wind effects on the van were on the order of 12 μradians, ±1.0 inch (2.54 cm) around some central mean. Winds were SW 15 - 22 miles per hour (6.7 to 9.8 m/sec) (broadside to the van) and generally along the beam axis. Personnel moving about within the van had a greater effect on beam motion, with a ±3.0 inches (7.6 cm) vertical displacement at 6,800 feet (2,073 meters) resulting from a single individual walking the full length of the van. Van stability was considered excellent, particularly with regard to wind effects, and

tests of the CAT system against the beltsander target in winds in excess of 30 miles per hour (13.4 m/sec) were conducted with no difficulty (Test Plan - AC-73-16 and Huntsville recommendations AC-73-17).

6.3 THE AMES RESEARCH CENTER SITE - BLDG 244

The CAT system was set in the penthouse of the Systems Engineering Facility building as shown in Figure 6-2. The ground test range was over a nominal 7,000 foot (2,134 m) range, as shown in Figure 6-3, to a tower structure (Figure 6-4) owned by the Lockheed Company in Sunnyvale. The belt sander (Figure 6-5) was located on the platform of this building, and preliminary system alignment to the target was accomplished with the aid of a HeNe laser propagating into the system. The system was operated against the belt sander target to determine that the required optical alignment of the CAT transmitter assembly mated with the telescope assembly as well as optimum S/N ratios were achieved before the system was turned over for aircraft applications.
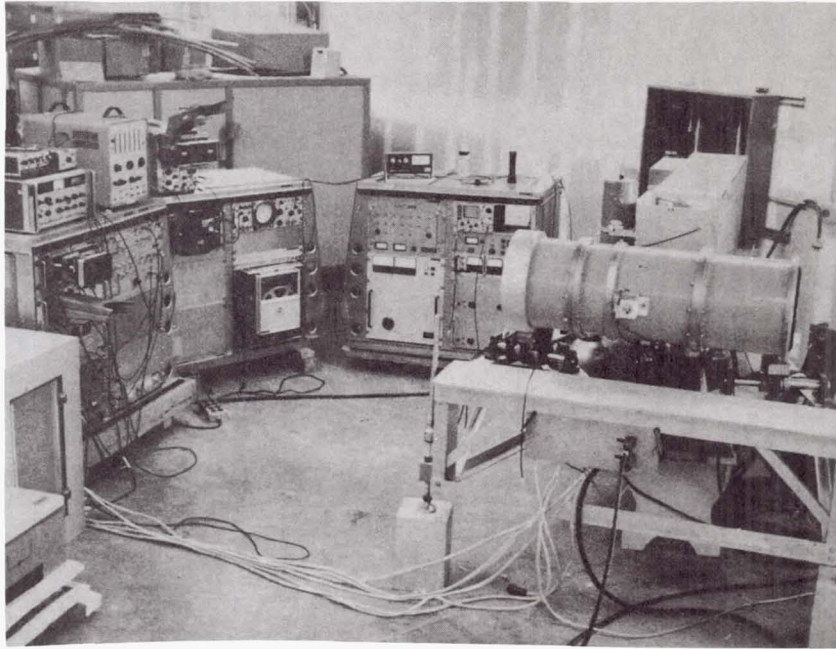
EO-484

Figure 6-2.   CAT System in AMES Test Site
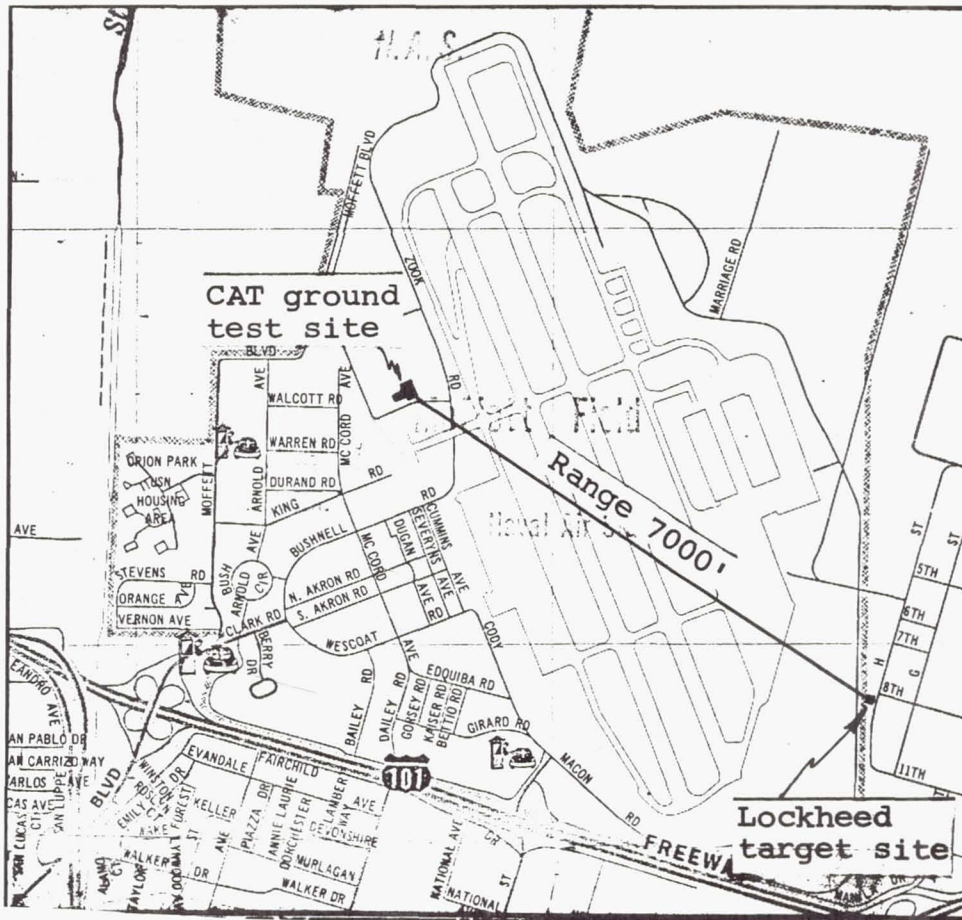
EO-485

Figure 6-3.   CAT Ground Test Range, Moffett Field

Figure 6-4. Lockheed Target Building

EO-486
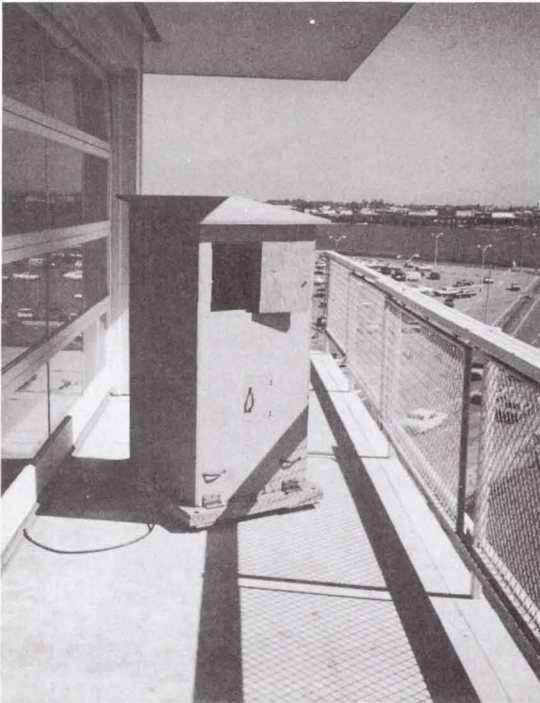
Figure 6-5. Belt Sander Target Enclosure

EO-487

SECTION 7
GROUND TESTS/FIELD TESTS

7.1 BASELINE TESTS

In order to establish a common data base during the ground test phase of this program, identical system parameters were established for the Moffett and Martha's Vineyard site tests. This section describes the Martha's Vineyard test plan.

7.1.1 FOCUSING THE CAT TELESCOPE

The focus variable was tested by means of a HeNe source located 6,875 feet (2,096 m) from the system and aligned with the input aperture of the telescope. The HeNe energy collected by the telescope was coupled out of the telescope and projected to the front of the van, $\sim$ 30 feet (9.15 m) away. By varying the distance between the telescope primary and secondary mirrors, the HeNe beam projected from the telescope was adjusted for minimum divergence or convergence.

7.1.2 OUTPUT BEAM COLLIMATION AT 10.6 μ

The output beam profile, energy distribution, and degree of collimation were probed with a mechanically scanned pyroelectric detector device, fabricated especially for these tests (see Figure 7-1). The test apparatus consisted of a motor-driven carriage having a linear travel of 23.5 inches (60 cm) in $\sim$ 2.5 seconds. Attached to the carriage was a battery powered Harshaw P43 pyroelectric detector, at the focus of a 1.25^{-4} diameter, f/3.5 a lens. The lens was combined with an adjustable iris and could be stopped down to $\sim$ 0.1 inch (2.54 mm).

7.1.3 DOPPLER MEASUREMENTS – S/N VERSUS RANGE TESTS

The target for the data points in these tests was a belt sander producing a Doppler signal in the 9 MHz region. To achieve internal parameters identical to those at Moffett Field the following steps were taken before each test program:
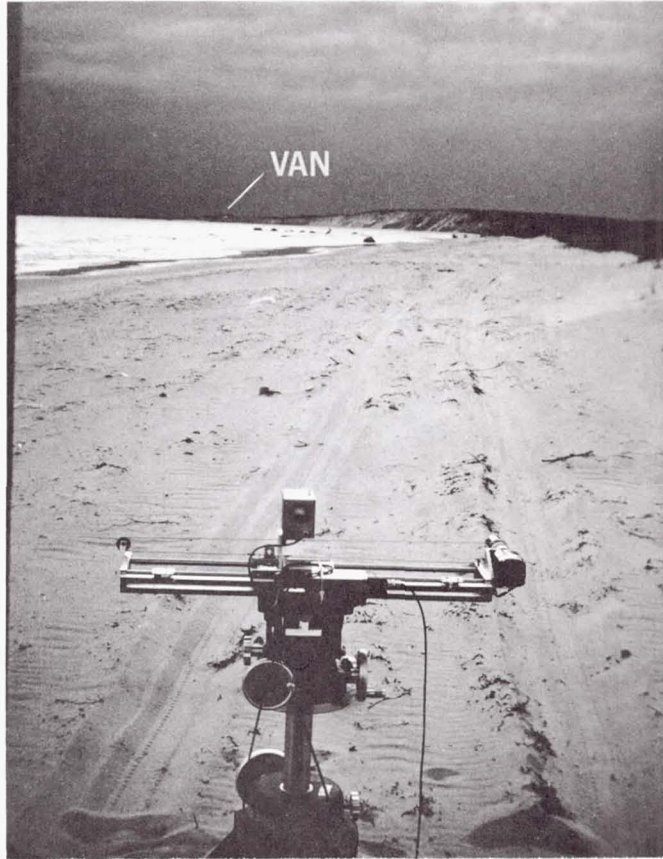
Figure 7-1. Beam Profile Apparatus at 2 nmi. (3.7 km)

Realign the internal beam expanders in exactly the same manner used in all previous tests.

Establish the output power levels achieved at Moffett Field.

Recheck CAT telescope alignment from a HeNe source $\sim$ 6,800 feet (2,073 m) distant, as at Moffett Field.

Recheck electro-optical waveshapes (pulse shapes, ringing levels, etc) to verify the stability of various system elements.

Perform an optical alignment within the transmitter assembly, with particular emphasis on the LO/recombination optics.

Make a sensitivity test of Avantek amplifiers under static and fully operational conditions to insure sensitivity at $\sim$10 MHz was -115 dBm.

Check the output collimation of the CAT telescope directly at 10.6 μ by means of a set of beam profile measurements taken with the mechanically scanned pyroelectric detector.

Weather conditions were then monitored and recorded for each series of S/N tests. Table 7-1 gives a weather summary for a set of tests at Martha's Vineyard and Figure 7-2 is a plot of data from these tests.

All points plotted in Figure 7-2 are from data photographs, with the exception of the 11/6/73 data, which was read off directly from the "A" scope display. Pulse-to-pulse signal amplitude fluctuations were also monitored and recorded as S/N measurements were made. The photographic data were taken by compressing the "A" scope sweep display so that $\sim$80 consecutive signal pulses were recorded on a single photograph. Fluctuations as high as 20 dB were observed on adjacent

Table 7-1. Weather Summary 11/6 – 11/20/73

DATE	TEMPERATURE	WIND	VISIBILITY	SKY CONDITION
11/6/73	40°F (4.4°C)	20 – 40 MPH NW (32.2-64.4 km/hr)	—	Pt. Cloudy (75%) to solid overcast
11/7/73	47 – 50°F (8.3 – 10°C)	8 – 15 MPH NW (12.9-24.1 km/hr)	>15 mi. (>24.1 km)	Pt. Cloudy (35%)
11/8/73	50°F (10°C)	30 MPH W (48.3 km/hr)	—	Pt. Cloudy (60%) to solid overcast
11/15/73 AM	56°F (13.3°C)	13 – 16 MPH SW (20.9-25.7 km/hr)	~3 mi.-surface haze (~4.8 km)	Clear
11/15/73 PM	56°F (13.3°C)	18 – 22 MPH W (29-35.4 km/hr)	~4 mi.-surface haze (~6.4 km)	Clear
11/20/73	43°F (6.1°C)	5 – 12 MPH NE (8-19.3 km/hr)	>10 mi. (>16.1 km)	Pt. Cloudy (75%) to solid overcast
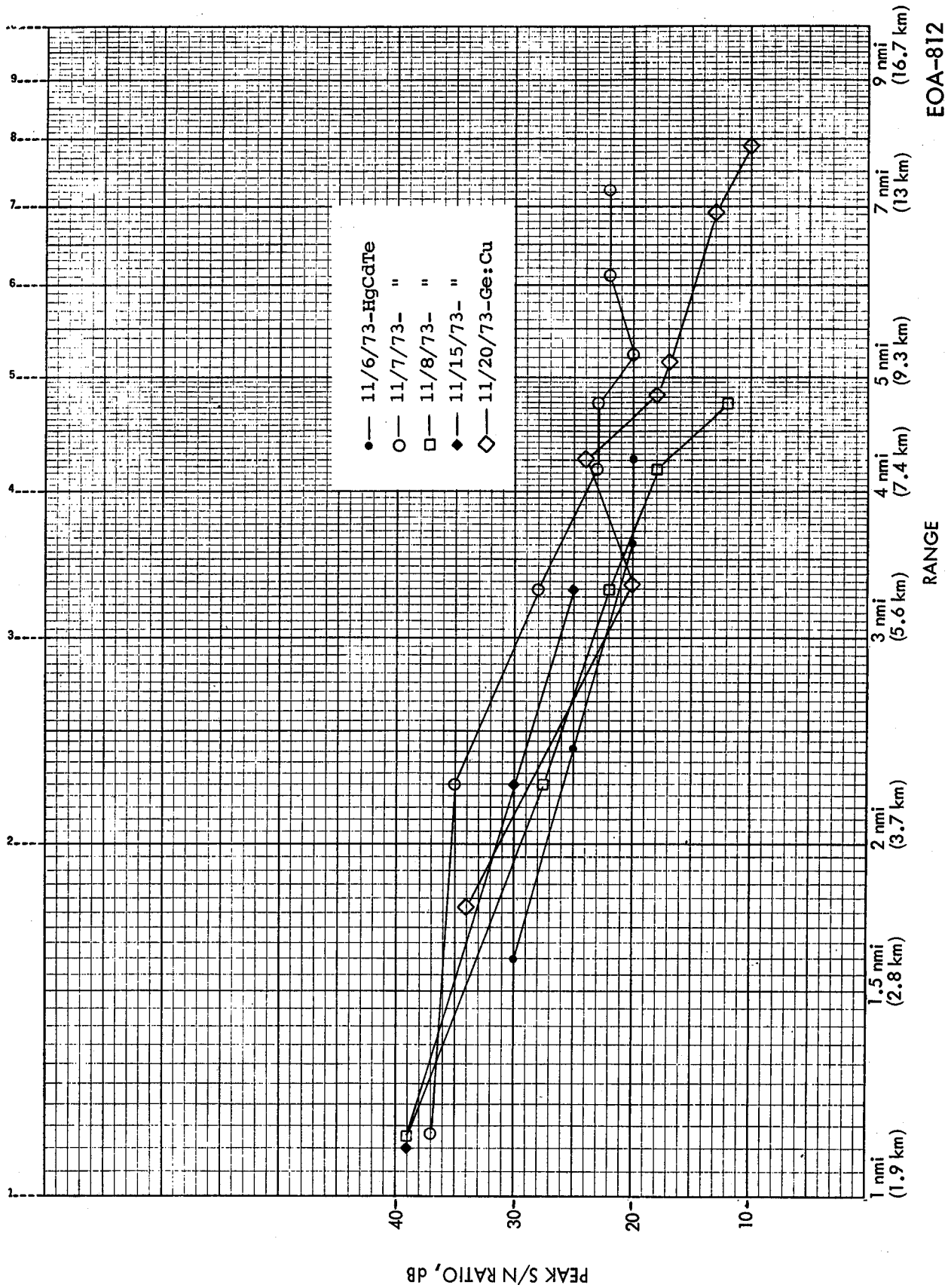
Figure 7-2. Range Dependence of SNR

EOA-812

pulses (∿6.5 ms), although the average was closer to 2 to 4 dB. The overall amplitude fluctuations often exhibited longer term periodicity, in the 100 to 200 ms range, as shown in Figure 7-3.

7.2 SYSTEM GROUND TESTS

System ground tests were performed to determine the optimum means of operating the system. Ground test operating procedures were established - presented as Appendix G of this report - for determining and correcting timing problems in the system's synchronizer, for measuring filter bank frequency responses, and for determining overall system performance before installation in the aircraft.

Representative system performance using the procedures given in Appendix G is illustrated in Figures 7-4 through 7-7 which show the HP spectrum analyzer display (with telescope open and blanked), the RVI display, IVI displays and a "range-gated" display utilizing the HP spectrum analyzer (non-sweeping) as a receiver tuned to the Doppler frequency with selectable IF bandwidths. In this mode of operation, the recovered signal pulse from the belt can be displayed directly as a function of range and direct S/N readings taken. The IVI display of a relatively broad Doppler spectrum (Figure 7-6) can be seen to be indistinguishable from that produced by a pure sine wave input. S/N ratios of 35 dB were commonly noted during the ground test phase, with readings in excess of 40 dB noted under rare solid-overcast, low-humidity weather conditions.

As a means of comparing various system displays with marginal S/N signals, the DC bias on the detector would be reduced almost to zero, with the result that the beltsander S/N ratios were reduced to ∿10 dB, as noted on the HP spectrum analyzer displays (see Figures 7-8 and 7-9). Under these conditions, the receiver processor RVI display would display the beltsander signal (shown circled in Figure 7-10) quite steadily, albeit on a noisy raster. Two consecutive samples of the IVI display under these conditions are shown in Figure 7-11. (Under conditions where one may be varying the LO
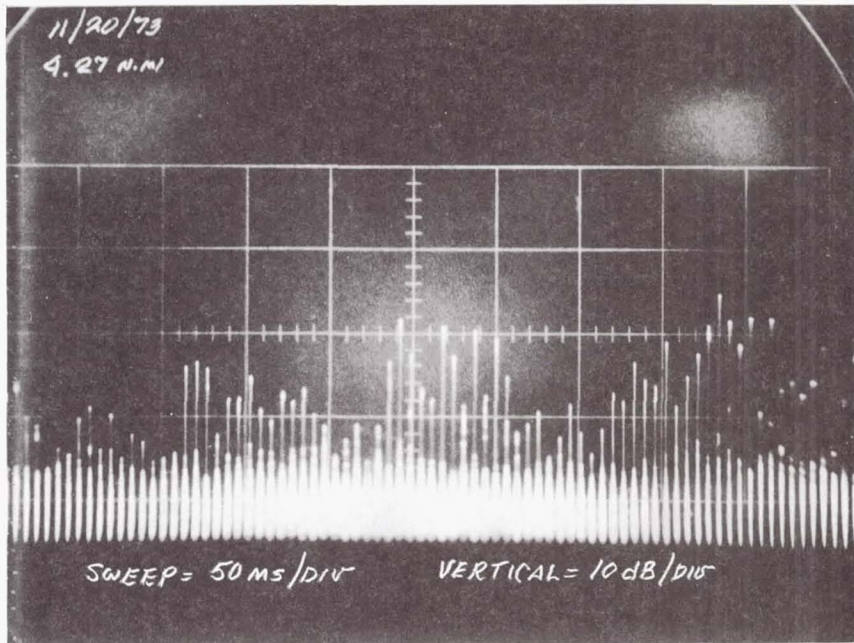
Figure 7-3. An Example of "A" Scope Signal Fluctuations
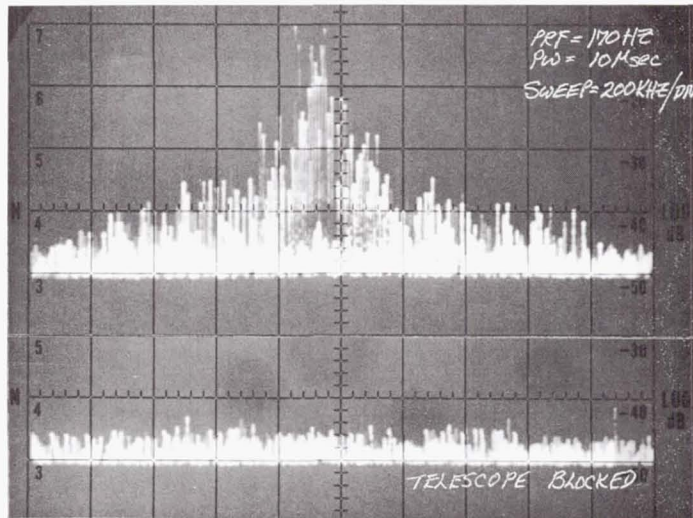
EO-502

Figure 7-4. Belt Sander Display on HP 141 Spectrum Analyzer
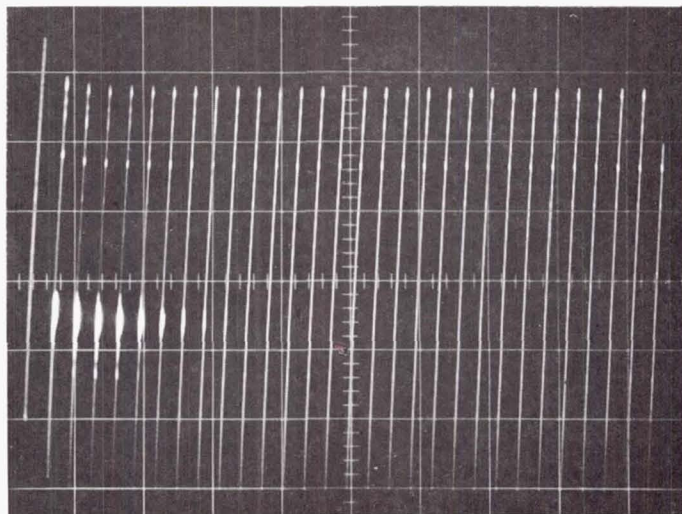
EO-503

Figure 7-5 . RVI Display, 0-10 Mile Range, Showing Belt Sander Signal
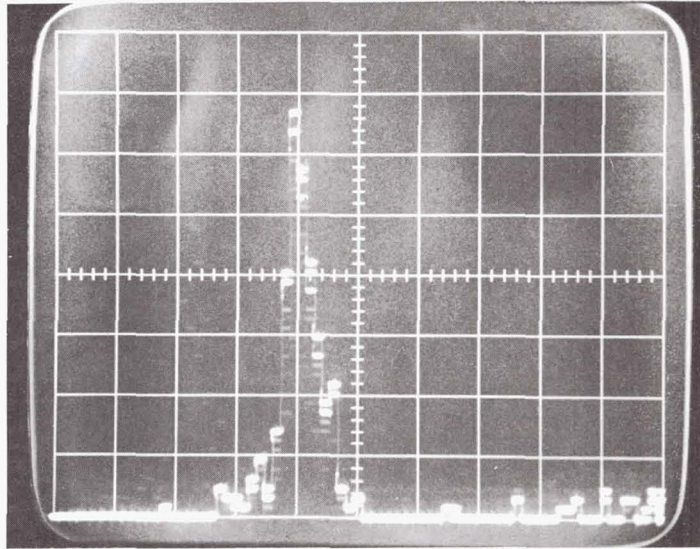
EO-504

Figure 7-6. IVI Display of Belt Sander Signal; S/N >35 dB
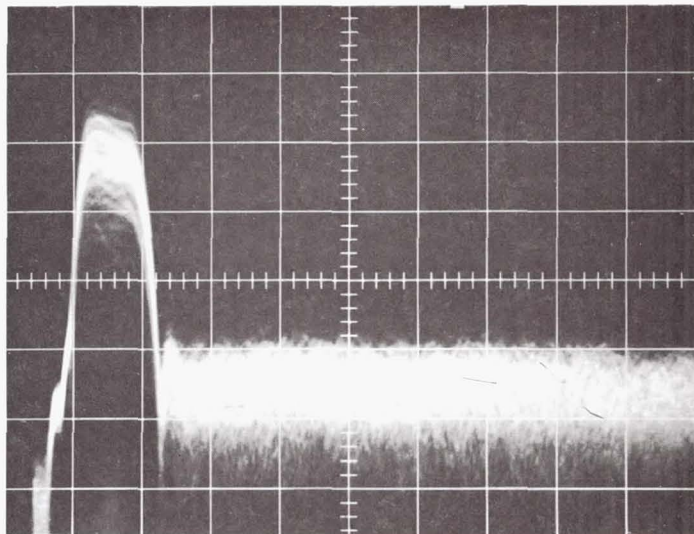
EO-505

Figure 7-7. "Range-Gated" Display -- Sweep:
10 μsec/Div; Vert: 10 dB/Div.
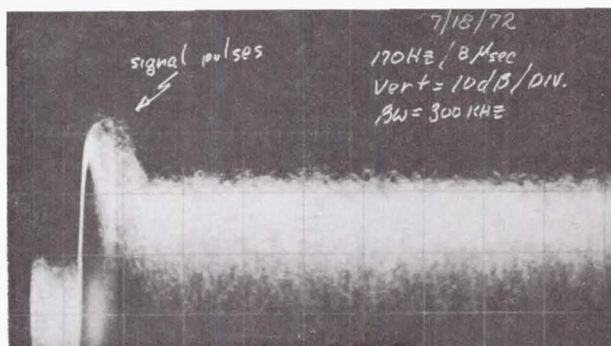
EO-506

Figure 7-8.   Low S/N Ratio Range-
            Gated Display, Belt
            Signal @ 6,600 ft.
            (2 km)

EO-507

Figure 7-9.   Low S/N Ratio Spectral
            Display, Belt Signal @
            6,600 ft. (2 km)
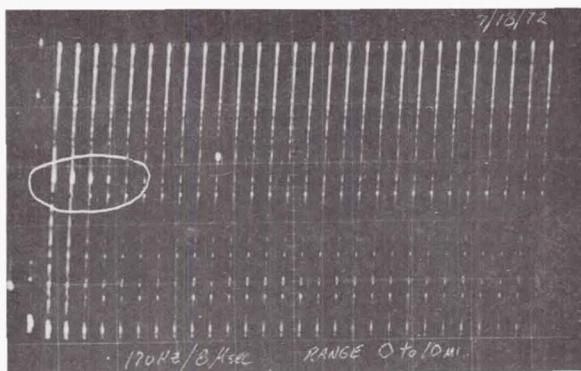
EO-508

Figure 7-10. RVI Display with Low
            S/N Ratio Belt Signal
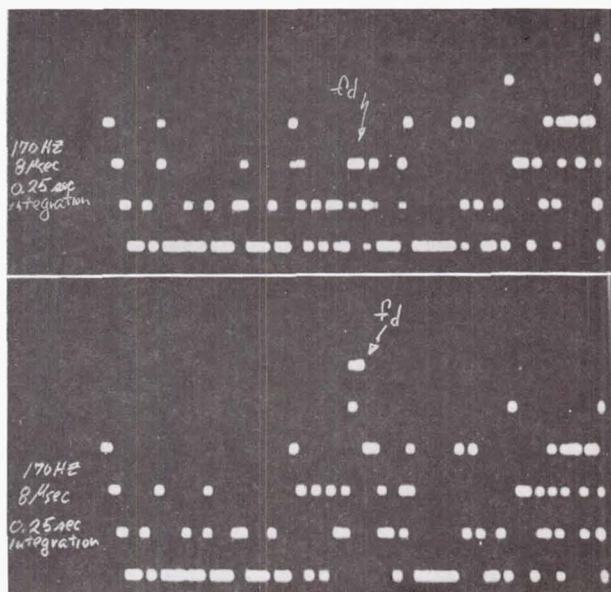
EO-509

Figure 7-11. Two Consecutive IVI
            Photos of 10 dB S/N
            Belt Signals

(mixer) to track the spectrum into the filter bank, or where the Doppler frequency may be changing due to aircraft velocity and/or altitude changes, it would be difficult to identify the desired frequency in such a presentation.) Here again, if it were possible to recalibrate the filter bank response to ± 0.25 dB, one might essentially eliminate many of the extraneous "humps" shown in Figure 7-11 and display the true signal without ambiguity.

It should also be noted that system integration was set at 0.25 seconds for the IVI photos shown in Figure 7-11, and that the display was virtually unchanged for all other integration settings through 4.0 second after allowing each setting to "settle out" for an appropriate period of time.

7.3 AIRCRAFT GROUND TESTS

In order to preflight test the overall system from the CV990, it was necessary to first point the aircraft by "eyeball" in the direction of the beltsander target. The aircraft was then jacked to a nominal 1.5° nose-up attitude because the CAT pod is installed at a -1.5° orientation relative to the aircraft waterline. Fine system steering was accomplished by using a HeNe laser located at the target site and directing its beam into the output aperture of the CAT fairing. The HeNe laser energy thus collected by the CAT telescope was combined with the 10.6 micron LO beam in the usual manner and fine system steering accomplished by X and Y loading of the transmitter system within its shock mount frame.

The aircraft was jacked at the nose only, and essentially rotated on its main landing gear. Aircraft stability with a 5-10 mph (8-16 km/hr) wind and people moving about within the cabin was adequate for optimizing internal system alignment but not stable enough to permit system sensitivity checks.

7.4 FIELD TESTS OF THE CAT SYSTEM WITH THE FREQUENCY OFFSET LOOP

Field tests were performed on the offset system to demonstrate its capability and to gain experience for anticipated flight tests to further demonstrate the capabilities of the CAT system. Several field tests took place during this program; the test at Kennedy Space Center is described here to show the type of activity involved in the several field exercises.

The testing at KSC was designed to coincide with TRIP 77 (Thunderstorm Research International Program) run by KSC with the involvement of a large number of researchers and having a great deal of cooperative instrumentation available (instrumented towers, several types of weather radars, radiosondes, etc.). In fact, the weather proved to be uncooperative and no significant storm activity occurred within the operating range of the system. As a result the measurements performed were limited principally to calibration measurements under high turbulence and humidity conditions, and to atmospheric signal range dependence under moderate humidity conditions.

The calibration measurements were made with the targets located near the instrumented weather tower at UC-16 with the van located at UC-4 near the ocean. These locations are indicated on the map in Figure 7-12. The range between these locations is 3.4 km on a path which is never more than about 10 meters above the ground. The water vapor partial pressure was generally in the range of 20-30 Torr (26.7-39.9 mbar). The high humidity resulted in much greater water vapor attenuation values than had been encountered at the MSFC test and restricted the range of the instrument to a maximum observed value of 5 to 6 km. On many humid days, signals could not be obtained from the 3 km minimum range of the instrument. This was in spite of typical measured values of $\beta(\pi)$ of 10^{-7} to 10^{-6} m^{-1} which match the values obtained at MSFC. Comparison of signal-to-noise ratios after water vapor attenuation and range correction showed that the calibration S/N ratios were approximately 10 dB lower at KSC than at MSFC. Much of this loss could be accounted for by a C_n^2 value of 10^{-12} without considering the losses due to the beam missing the target.

CAT System Site

Calibration Target Site

LEGEND

KASEMIR-NOAA	⌂
KRIDER-U of AZ	▲
R. E. ORVILLE-U of NY	♥
H. D. ORVILLE-S.D M & T	♣
UMAN-U of F	♦
FEW-Rice U	★
BROOK NMIMT	▲
MOORE- NMIMT	●
TAYLOR-NOAA	▬
LHERMITTE-U of M	▬
WRIGHT PATTERSON AFB	♣
VONNEGUET STATE U OF NY	▲
ANDERSON,NRL	#
LEVINE GSFC	◉

NORTH BOUNDARY-CCAFS

SCALE IN FEET

5000   0   5000   10000   15000
1524   0   1524   3048   4572

SCALE IN METERS
3281 FEET 1 KILOMETER

Y=1525,000

EOA-844

Figure 7-12. KSC Site Map

An attempt was made to determine if any lag angle effect could be observed by scanning the laser beam rapidly past the VAB building. The maximum rate of scan was limited by the integration time of the processor. This requires that all the pulses transmitted during the integration period fall on the target. In order to be certain that this is the case, the scan rate must be slow enough so that at least two integration periods are required to complete the scan across the target. With scanning rates up to twenty degrees per second, the variations in signal did not exceed the experimental accuracy. Since the maximum scanning rate corresponded to a lag position error of only 0.1 meter, the theoretically expected loss with the beam diameter of 0.5 meter is 4%, which is in agreement with the experimental results. A range of nearly 25 km would be required to have a 3 dB loss at twenty degrees per second.

Attempts to measure signal loss during rainy weather were inconclusive. Signals from the VAB were observed in a heavy rainstorm during which the building could no longer be seen. The sudden drop out and reappearance of the signal suggests that wetting of the building or wander of the beam off the target due to atmospheric steering was the cause rather than attenuation by the rain itself. Occasional light and localized showers were not observed to increase the losses beyond those due to water vapor.

Work was performed on comparison of the calibrated target signal losses with published water vapor attenuation data (see Appendix C). This work was complicated by the difference in water vapor content between the van and target site and by the loss of much of the tower site humidity data due to a dry wet-bulb. These comparisons are made by doing a best quadratic fit to the calibration signal vs vapor pressure data and by comparison of the signal range dependence of the expected exponential behavior.

A number of system parameters were characterized during the tests and a few problems located and corrected. These included the following: calibration of the zero moment calculation with respect to input power, location and understanding of a register overflow problem in the processor, restoration of a dropped bit in the computer, alignment of the scanner with respect to the compass points, and minor system repairs.

The feedback phenomenon caused more problems at KSC than at MSFC. At MSFC, the feedback from the telescope caused a slow fluctuation in the signal amplitude but the master-oscillator frequency pulling could be eliminated by fine tuning the system's optics. At KSC it was not possible to do this without reducing the amplifier drive power and this resulted in a lower output power and a signal loss of 8 dB. A loss of this magnitude has a severe impact on the performance against the atmosphere. It was found that a 9 dB optical attenuator placed in the future isolator position eliminated the frequency pulling but not the amplitude fluctuations. For the retained polarization which was probably the dominant cause of the pulling, the isolator provided greater than 20 dB reduction in backscatter. This with suppression of the amplitude fluctuations will reduce the sensitivity of the system to alignment with respect to the backscatter problem.

Tables 7-2 through 7-5 present a summary of the calibration and atmospheric data from the MSFC and KSC tests. Except as noted, the atmospheric data is entered as signal-plus-noise with noise noted separately to facilitate data analysis.

7.5 <u>SYSTEM SENSITIVITY ANALYSES AND PERFORMANCE PROJECTIONS</u>

7.5.1 SENSITIVITY ANALYSES

System sensitivity analyses were performed to obtain indications of system performance. These analyses were carried out using the following general procedure:

TABLE 7-2. Calibration Data - 1977 MSFC Tests
(Sheet 1 of 2)

CALIBRATION DATA MSFC

| | | | | | | Madkin Mt | | Martin Rd | | |
DATE	CDT TIME	TGT	SNR	Ep mJ	LINE	T_1	H_1	T_2	H_2	σ_x
5/26	1150	Sander	34	8.85		75°	80%	77°	55%	
"	1150	Cube	64	8.85		75°	80%	77°	55%	
"	1445	Sander	32		P(22)					
"	1445	Sander	29							
"	1458	Sander	35							
"	1458	Sander	35							
"	1515	Sander	39							
"	1530	Cube	63			76°	72%	80°	52%	
"	1530	Sander	39							
5/27	1500	Sander	39	11.5	P(20)	74°	90%	76°	60%	
"	1500	Cube	63	11.5	P(20)	74°	90%			
5/31	1500	Sander	20	-	P(20)	85°	44%	87°	30%	
"	1500	Sander	32	-						
"	1500	Sander	38	-						
6/2	1800	Sander	40		P(20)	78°	46%	82°	28%	.2
"	1920	Sander	40	1.5w				80°	47%	
"		Cube	68							
"	2020	-	-	-	-	74°	48%	72°	60%	.3
6/3	1830	Cube	65		P(20)	82°	32%	85°	18%	
6/7	1720	Cube	73			72°	23%	75°	14%	
"	1720	Sander	39							.3
6/8	1910	Board	36	5.4	P(20)	71°	33%	74°	24%	.125
"		Cube	70	5.4	P(20)	71°	33%			.2
"	1925	Sander	33	5.4	P(20)	71°	33%			
"	1930	Sander	34	8.85	P(20)					.27
"		Board	38							.25
"	2010	Board	35							
"		Cube	70							
6/10	1900	Sander	36			78°	35%	83°	33%	.06
"		Cube	62							
"	1915	Cube	75							
"	1923	Sander	35							
"	1930	Board	38			78°	36%	79°	40%	
"	1940	Board	40							
"	1945	Board	42							.15
"	1956	Cube	75							
"	2000	Sander	37							
"	2010	Sander	38	10	P(20)	76°	36%	74°	56%	.23

TABLE 7-2. Calibration Data - 1977 MSFC Tests
(Sheet 2 of 2)

CALIBRATION DATA MSFC

DATE	CDT TIME	TGT	SNR	Ep mJ	TRAN	Madkin Mt T_1	H_1	Martin Rd. T_2	H_2	σ_x
6/13	1355	Board	36			94°	40%	90°	36%	.725
"	1402	Board	38			960	38%			.8
"	1408	Board	39							
"	1413	Cube	69							
"	1415	Cube	69							
"	1420	Cube	69							
"	1426	Sander	38			100°	32%	80°	40%	
"	1431	Sander	38	7.1	P(26)					.575
6/15	1440	Board	37	13	P(20)	73°	100%	74°	100%	
"		Board	37							
"	1502	Sander	29	12	P(20)					
"	1528	Sander	38	–		74°	100%	76°	90%	
6/17	1430	Cube	68	12.1	P(20)	84°	60%	84°	54%	.425
"	1440	Board	30							
"	1445	Sander	28							
"	1454	Board	32							.13
"	1500	Board	29							
"	1515	Sander	28							
"	1530	Sander	30			80°	91%	82°	70%	
6/21	1428	Cube	67	14.3	P(20)	86°	50%			
"	1505	Cube	70	14.3	P(20)	87°	49%	90°	38%	
"	1532	Sander	33			87°	50%			
"	1540	Sander	34							
"	1545	Board	35							
"	1812	Cube	78							
"	1815	Board	35							
"	1823	Sander	34			85°	51%	89°	46%	

TABLE 7-3. Atmospheric Signal Data – 1977 MSFC Tests

Martin Rd

Signal Plus Noise @ Range

DATE	TIME	POLL COUNT	18μs	20μs	22μs	25μs	30μs	35μs	40μs	45μs	50μs	60μs	70μs	80μs	MAX μs RANGE	NOISE	NOTE	TEMP	HUMIDITY
6/3	630	75											5		70	3	1,6		
6/6	730	97										5 @ 62			62	3	6		
6/7	500	109		20					14			7		2 @ 82	82	2	1,6		
6/8	2010	72													66	2	2,6		
6/10	2030	105		25					20			13		6	90	3	6		
6/13	1558	72			16											2	3,6		
6/14	1840	41	14			11	9	6							35	3		74°	100%
	1850	41	15			11	8	7	6 @ 38						38	3		74°	100%
6/17	1535	72		12	10		7	5	4						40	2			
6/21	1230		16	15	14	10	9	7	5	4 @ 42					42	2	4,6		
	1251		17	14		11	10	8	7	6	4 @ 51				51	2	5,6		
	1600		14	13		11	10	8	6	5	4 @ 48				48	2	6	87°	48%

NOTES:

1. Max. Range (dB @ μs) - 5 dB taken as minimum detectable signal Plus Noise (3 dB).

2. Erratic signal due to break-up.

3. RFI Noise prevented more data.

4. Through Scanner, plastic window in place.

5. Through Scanner, plastic window removed.

6. Cut trailer window.

7. No receiver tweak.

8. Tower wet bulb dry.

9. System down.

10. System down

11. Dry wet bulb fixed.

TABLE 7-4. Calibration Target Data - 1977 KSC Tests
(Sheet 1 of 3)

CALIBRATION DATA - KSC Van (USC4) 150M Tower

DATE	EDT TIME	TGT	SNR	Ep mJ	Transition	T_1	H_1	T_2	H_2	
6/30	1136	Cube	67	13	P(20)			92°	72%	
	1349	Sander	23	13	P(20)	86°	74%			
		Board	30	13	P(20)					
7/5	1237	Cube	60		P(20)					
	1257	Board	25		P(20)					
	1312	Board	30		P(20)	89°	90%	86°	44%	
	1705	Dewar	35(27µs)		P(20)	92°	69%			
	1720	Dewar	32							
	1724	Dewar	42							
		VAB	33(44µs)							
	1740		32							
	1741		32							
	1744		35							
	1815	-	-	-	-	96°	52%			
7/6	1224	Cube	71	13		93°	60%	86°	(23%)	
	1244	Board	24	13						
	1246	Board	30	13						
	1258	Board	28	13						
	1311	Sander	20	13						
	1317		22	13						
	1400					93°	60%	86°	(23%)	
	1425			13	P(20)					
		VAB	26							
	1440									
	1510				P(20)	86°	30%			
7/7	1100				P(20)	87°	75%			
	1117							89°	(25%)	
	1129	Cube	74		P(20)					
		Cube	72		P(20)					
	1141	Board	24		P(20)					
			23							
	1146	Board	29							
	1147	Board	29							
	1153	Cube	72							
	1222	Board	34							
	1226	Board	32							
	1245	Cube	75							
	1340	Cube	72							
7/8	1501	Board	30			84°	100%			
	1502		30							
	1516	Sander	26							
			26							
	1527	Cube	74							
	1528		75			88°	84%	92°	(22%)	
	1607									
7/11	1208	Board	26			72°	71%	88°	(29%)	
		Cube	71							
		Sander	18							

TABLE 7-4.   Calibration Target Data - 1977 KSC Tests
(Sheet 2 of 3)

CALIBRATION TARGET DATA - KSC

DATE	EDT TIME	TARGET	SNR	Ep mJ	TRANSI- TION	Van		Tower	
						T_1	H_1	T_2	H_2
7/13	1200	VAB	12		P(20)	86°	100%	83°	72%
7/14	1130	VAB	20		P(20)	90°	84%		
		VAB	23		P(20)				
		VAB	20		P(20)				
	1145	VAB	23		P(20)	92°	80%		
7/15		VAB	22	12	P(20)	88°	83%		
		VAB	22	12	P(20)	87°	98%		
	1416	Cube	70	2	P(20)	87°	98%		
		Board	15	2	P(20)				
		Belt	12	2	P(20)				
7/18	1210	Board	29	13	P(20)	88°	80%		
	1230	Cube	72	13	P(20)	88°	78%	85°	71%
		Sander	23	13	P(20)				
7/19	1214	VAB	22	17	P(20)	90°	82%		
	1555	Cube	70	17	P(20)				
	1621	Board	30	17	P(20)				
	1633	Sander	19	17	P(20)	90°	70%		
7/20	1238	Board	30	17	P(20)	89°	80%		
		Cube	73	17	P(20)				
	1253	Sander	25	17	P(20)	88°	78%		
7/21		Cube	75	17	P(20)	89°	80%	91°	65%
	1243	Board	33	17	P(20)				
		Sander	29	17	P(20)				
7/22	1600	Board	30	16	P(20)				
	1607	Cube	72	16	P(20)	96°	54%		
		Sander	26	16	P(20)				
7/23	1030	Cube	73	19	P(20)	76°	100%		
		Board	30	19	P(20)	76°	100%		
		Sander	27	19	P(20)	76°	100%		
7/25	1309	Cube	70		P(20)	89°	85%	89°	73%
		Board	33		P(20)				
		Sander	24		P(20)				
7/26	1155	Board	31		P(20)	92°	58%	86°	72%
		Cube	72		P(20)	92°	58%	86°	72%
		Sander	24		P(20)	92°	58%	86°	72%
		VAB	21	7	P(20)	92°	58%	86°	72%
		VAB	24	12	P(20)	92°	58%	86°	72%
7/27	1200	Cube	70	16	P(20)	90°	80%	90°	73%
		Cube	71	16	P(20)	90°	80%	90°	73%
		Board	34	16	P(20)	90°	80%	90°	73%
		Board	30	7.5	P(20)	90°	80%	90°	73%
		Sander	24	7.5	P(20)	90°	80%	90°	73%
7/28	1330	Cube	73	16	P(20)	88°	98%	90°	71%
		Board	29	16	P(20)	91°	75%		
		Board	31	16	P(20)				
		Sander	27		P(20)				
7/29	1410	Cube	74	15	P(20)	91°	77%	89°	69%
		Board	34	15	P(20)				
		Sander	29	15	P(20				

TABLE 7-4. Calibration Target Data - 1977 KSC Tests
(Sheet 3 of 3)

CALIBRATION TARGET DATA - KSC						Van		Tower	
DATE	EDT TIME	TARGET	SNR	Ep mJ	TRANSI-TION	T_1	H_1	T_2	H_2
8/1	1140	Cube	70		P(20)			88°	72%
		Board	33		P(20)				
		Belt	31		P(20)				
	120					92°	70%	89°	70%

TABLE 7-5. Atmospheric Signal Data – 1977 KSC Tests

DATE	TIME	POLL COUNT	Signal Plus Noise @ Range											MAX μs RANGE	NOISE	NOTE	Van (UCS-4)		Tower	
			18μs	20μs	22μs	25μs	30μs	35μs	40μs	45μs	50μs	60μs	70μs				TEMP	HUMIDITY	TEMP	HUMIDITY
6/29	1732			17	16	14	12	8		4 @43				43	1	7	81°	88%		
6/30	1349		15	17	15	12	9	6	5					40	2	6				
7/1	1425		15	14	12	10	8	5	4					39	3	6				
7/5			18	15		10								30	3	6.2				
7/6	1440		17	14		9	6	5	5					40	4	6	95°	55%	86°	30%
7/7	1340		11	9		8	5	2	1		1			50	2	5				
	1340		12	12		8	4	2			1			50	2	5.2	90°	65%		
	1800		12	11		7	6	3			1			50	2	5.2	90°	65%		
	1800		13	9		8	5	4						40	2	5.2	94°	72%	92°	42%
7/8	1607		13	9		8	6	5	4	3	3			50	2	6.8	89°	84%	92°	20%
7/11	1403															9.8	94°	72%	89°	
7/12																10				
7/13	1200		4													9,11	86°	100%	83°	72%
7/14	1130		6		5						3			25	3	6	92°	84%		
7/15	1632				5	5								25	3	6	90°	84%		
7/19	1027		12	10	6	4								26	2	6	87°	95%		
	1638		12	12	9	7	3							30	2	6	90°	70%	89°	67%
7/20	1300		13		11	9	6							30	3	6	88°	75%	89°	70%
7/21	1300		17	15	13	12	8	5						36	3	6	89°	80%	91°	65%
7/22	1620		10	8	6	6	3 @ 26	2						32	0	6	84°	60%	92°	62%
7/23	1130			7	4	3	2 @ 26							26	2	6	70°	100%		
7/25	1337		12	10	9	7	4	4						32	3	6	89°	84%	88°	71%
7/26	1211		15	12	10	8	9 @ 26							26	2	6	91°	72%	93°	60%
	1232		12	11	10	10	6							32	3	6				
7/28	1418		11	10	9	7	4							30	2	6	89°	92%	85°	70%
	1430		11	9	7	4	1							30	0	6	89°	92%		
7/29	1400		15	13	13	11	7	6	5					38	2	6	91°	80%		
8/1	1320		10	8	6	4	3	2 @ 32						32	0	6	92°	70%	89°	70%
8/2			10	8	7	5	3 @ 26							26	2	5				

NOTES:

1. Max. Range (dB @ μs) - 5 dB taken as minimum detectable signal Plus Noise (3 dB).
2. Erratic signal due to break-up.
3. RFI Noise prevented more data.
4. Through Scanner, plastic window in place.
5. Through Scanner, plastic window removed.
6. Out trailer window.
7. No receiver tweak.
8. Tower wet bulb dry.
9. System down.
10. System down
11. Dry wet bulb fixed.

Expressing the S/N equation as

$$S/N = \frac{\eta_o \, \eta_{SYS} \eta_{ATM} \, P_T \, D^2 \, \sigma}{32 \, h\nu B \left[R^2 + \left(\frac{\pi D^2}{4\lambda} \right)^2 \right] A_B}$$

where:

η_o = detector quantum efficiency

η_{SYS} = system efficiency

η_{ATM} = atmospheric transmission efficiency

σ = target cross section

h = Planck's Constant

ν = transmitter frequency

B = bandwidth matched to pulse length

λ = system wavelength

A_B = beam area at target

And determining transmitter pulse energy by

$$E_T = \frac{P_T}{KB}$$

where:

E_T = transmitter pulse energy

P_T = transmitter power

B = $1/\tau$

K = ratio of signal bandwidth filter to B

And substituting,

$$S/N = \frac{\eta_o \, \eta_{SYS} \eta_{ATM} \, E_T \, D^2 \, \sigma}{32 \, h\nu K \left[R^2 + \left(\frac{\pi D^2}{4\lambda} \right)^2 \right] A_B}$$

We could determine using gathered measurements (see, for example, Figure 7-13) the system theoretical S/N Figure.
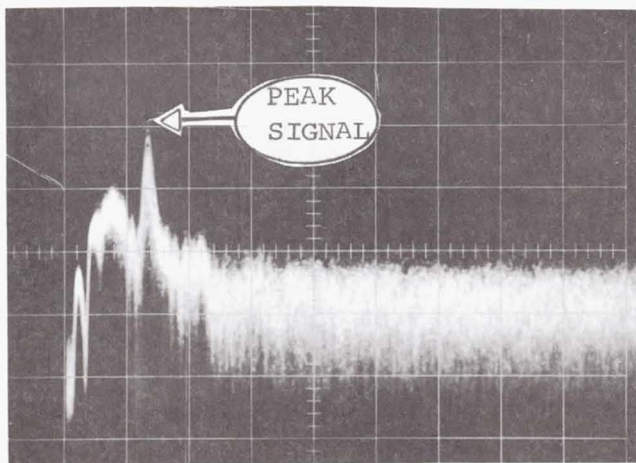
BEDFORD TEST DATA 5/23/72

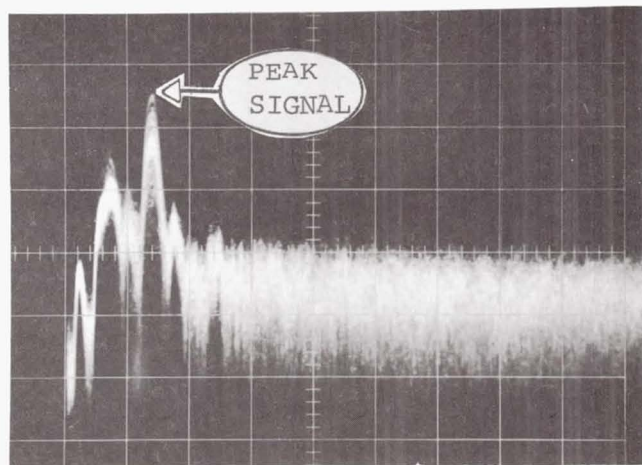TEMPERATURE 71° HUMIDITY 30°

DEW POINT 41%   WINDS @ 220° - 6 KNOTS

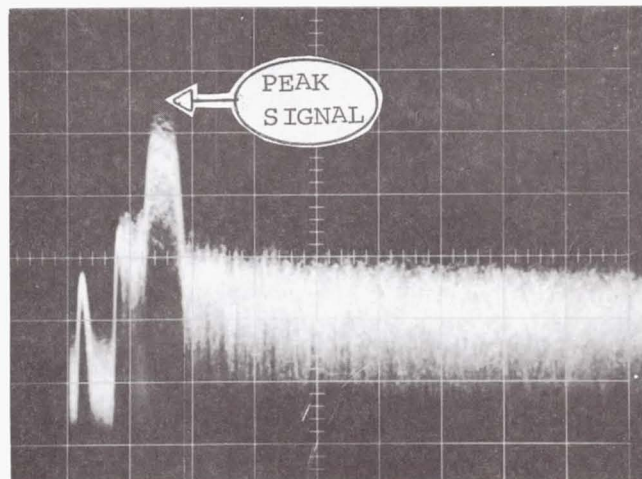| PULSE ENERGY	AVG. P_{OUT}	τ	PRF	S/N (PEAK)	BANDWIDTH
4.2 mj	0.8 W	10µs	190	25 dB	300 kHz
8.2 mj	1.15W	10µs	140	26 dB	300 kHz
4.3 mj	0.6 W	4µs	140	25 dB	300 kHz
3.2 mj	0.45W	2µs	140	20 dB	300 kHz

DETECTOR CURRENT   31.5 MA

L. O. POWER   20 MW

LASER POWER   5 WATTS
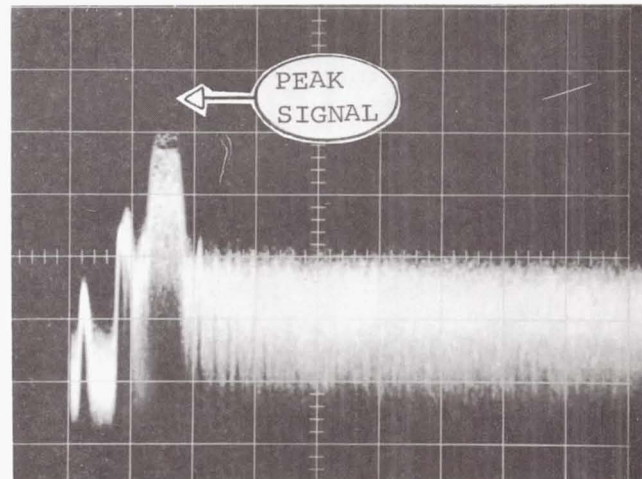

2µs PULSE   140 PPS
20µs/cm

4µs PULSE   140 PPS
20µs/cm

10µs PULSE   140 PPS
20 µs/cm

10µs PULSE   190 PPS
20µs/cm

EO-539

Figure 7-13. Pulse Test Data Management

$$E_T = 4.3 \text{ mj} \quad \text{(measured)}$$

$$\eta_o = 0.15 \quad \text{(measured)}$$

$$\eta_{ATM} = 0.45 \quad \text{(evaluated)}$$

$$D = 1 \text{ Ft.}(30.5 \text{ cm}) \quad \text{(measured)}$$

$$\sigma = 0.54 \text{ } A_T \quad \text{(measured)}$$

$$A_T = 1/4 \text{ sq. ft.}(1.61 \text{ cm}^2) \quad \text{(measured)}$$

$$h\nu = 1.9 \times 10^{-20} \quad \text{(constant)}$$

$$K \quad K = \text{electronic bandwidth mismatch} = 1 \text{ (evaluated)}$$

$$R = 10,400 \text{ Ft.}(3.17 \text{ km}) \text{ (measured)}$$

$$A_B = 18" = 1.8 \text{ sq. ft. } (17 \text{ m}^2) \text{ (measured)}$$

$$\eta_{SYS} = 0.2 \text{ (optics, 2 dB; target depolarization, 2 dB;}$$
$$\text{heterodyne eff., 3 dB; Net: -7 dB) (estimated)}$$

$$S/N = \qquad 39.5 \text{ dB}$$

Actual measured   25 dB

Unaccounted loss 14.5 dB

7.5.2   SYSTEM PERFORMANCE PROJECTIONS

When CAT system efficiency losses were determined by the analyses and examinations described above, system evaluation graphs were compiled to summarize system performance and give an indication of what factors should be considered for CAT system improvement. Figure 7-14 is an example showing overall system improvement factors. In Figure 7-14 the flight test results on the lower curve assume the transmitter to be focused to infinity, the receiver focused to 6,000 feet, (1.8 km), and at 10,000 foot (3.0 km) altitude, and a signal-to-noise ratio of a few decibels. Additionally, the system is assumed to have a system loss of approximately 18 dB with 11 dB of the system losses basically unaccounted for. The curve above the flight test curve is that expected from a system focused to infinity and a total system loss
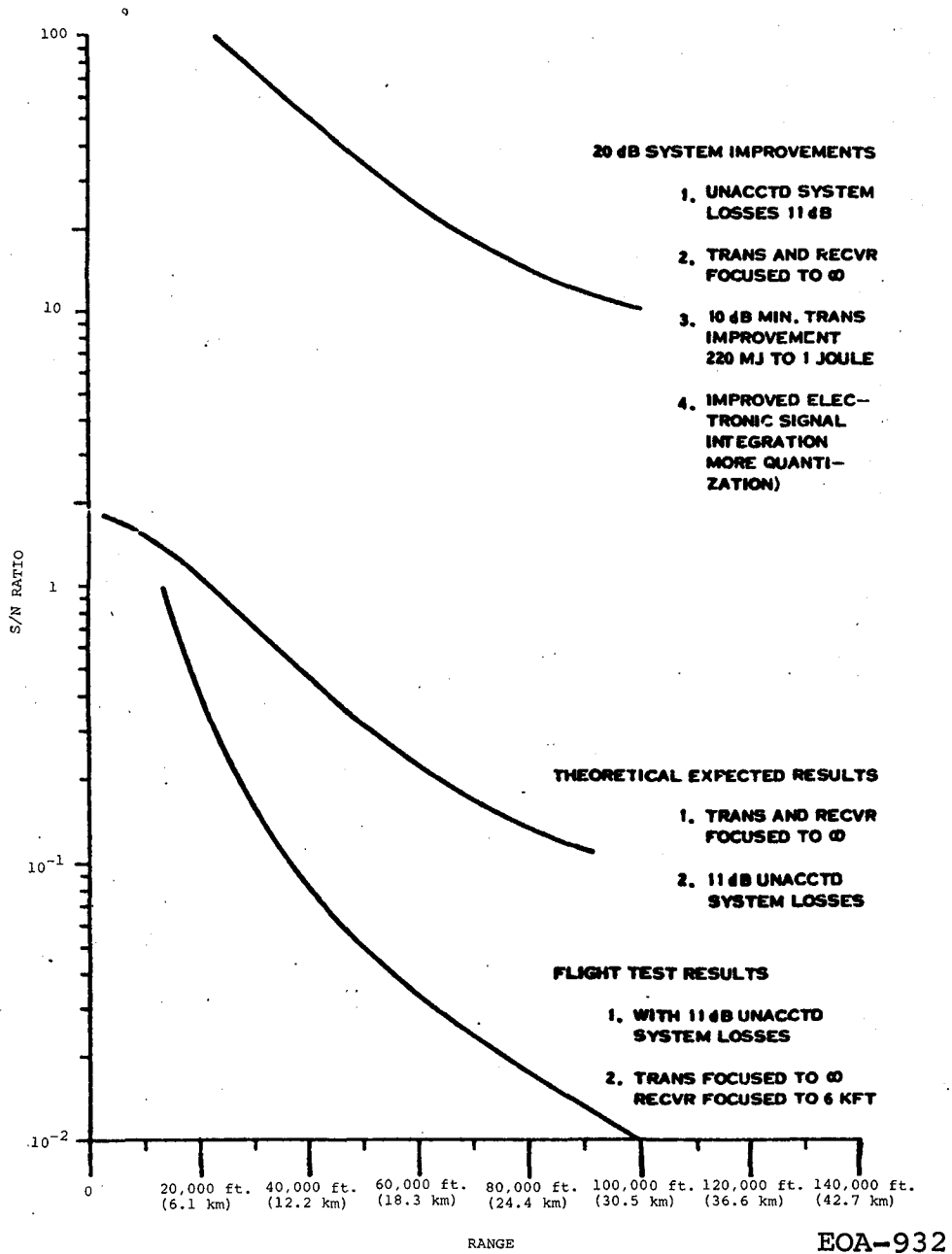
S/N RATIO

100
10
1
10⁻¹
.10⁻²

20 dB SYSTEM IMPROVEMENTS

1. UNACCTD SYSTEM LOSSES 11 dB
2. TRANS AND RECVR FOCUSED TO ∞
3. 10 dB MIN. TRANS IMPROVEMENT 220 MJ TO 1 JOULE
4. IMPROVED ELECTRONIC SIGNAL INTEGRATION MORE QUANTIZATION)

THEORETICAL EXPECTED RESULTS

1. TRANS AND RECVR FOCUSED TO ∞
2. 11 dB UNACCTD SYSTEM LOSSES

FLIGHT TEST RESULTS

1. WITH 11 dB UNACCTD SYSTEM LOSSES
2. TRANS FOCUSED TO ∞ RECVR FOCUSED TO 6 KFT

0   20,000 ft.   40,000 ft.   60,000 ft.   80,000 ft.   100,000 ft. 120,000 ft. 140,000 ft.
      (6.1 km)   (12.2 km)   (18.3 km)   (24.4 km)   (30.5 km)   (36.6 km)   (42.7 km)

RANGE

EOA-932

Figure 7-14. System Improvement Factors

of 18 dB. The top curve indicates that with 20 dB improvements, the system would have a S/N ratio of 10 at a range of 100,000 feet (30 km). Under optimum conditions, this would indicate a system range in excess of 15 nautical miles (27.8 km) at all altitudes.

SECTION 8
FLIGHT TESTS

8.1 GENERAL

Two series of flight tests were conducted: the A flights in
August and September of 1972 and the B flights in January of 1973.
Detailed analyses of each of these tests are presented in Appendices
E and F. Both tests demonstrated that the CAT system operated con-
sistently and reliably under all types of flight conditions within
2 dB of theoretical system performance and that the system detected
and measured turbulence in front of the aircraft. Conclusions from
examination of flight test data (see Section 9.3) indicated how and
to what degree the system should be improved.

8.2 FLIGHT A TESTS (See Appendix E for a detailed analysis of flight A data)

This series of flights was conducted out of the NASA Flight
Research Center at Edwards Air Force Base. The CV990 was at Edwards
for a series of flights to evaluate the Space Shuttle Guidance and
Control System (SSG+C) and operation of the CAT system during these
flights was allowed. The basic SSG+C flight profiles consisted of
a series of steep (6-8° nose-down), power-off glide approaches from
17,000 (5,183 m) and 39,000 feet (11,890 m) to touchdown. A total
of 23 descents in 4 separate flights was made from 17,000 ft. (5,182 m)
and one from 39,000 feet (11,890 m) during the SSG+C flight phases.
This phase of the flight test program proved extremely useful both
as a means of gaining operator training in the flight environment
and as a means of establishing operational constraints on the
system hardware over a range of operational conditions. The system
operated reliably over the whole flight profile which included high
noise/vibration descents, hard landings, takeoffs, etc. High voltage

arc-overs were noted in the GaAs modulator and in the PA driver chassis whenever cabin altitude reached 8,000 to 9,500 feet (2.44 km to 2.90 km), but reducing B+ voltages slightly eliminated the problem.

A number of data runs were taken at a series of altitudes in the San Joaquin Valley and over the Carson Sink, Nevada, area. Some of the data are presented in Tables 8-1 and 8-2. The total volume of data are analyzed in Appendix E. Figures 8-1 through 8-4 are representative examples of in-flight data and the displays utilized. Most of the engineering data were taken using the "A-Scope" display.

The CAT System proved to be extremely reliable under virtually all flight conditions including the full altitude capability of the CV990. The following log from the monthly progress reports supporting this program is of CAT Flight 13, 6 September 1972, and is typical of the reporting conducted during this program.

> Flown under control of the CAT program. Consisted of a series of five runs over the Carson Sink, Nevada, area at a range of altitudes between 4,000 ft. (1.2 km) and 10,000 ft. (3 km) AGL (above ground level). Weak clear air signals were detected to 8,500 ft. (2.6 km) during this series. This was followed by a series of five steep ($6°$ N.D.) descents from 20,000 ft. (6 km) to approximately 200 ft. (60 m) AGL to determine system sensitivity using the ground as a target. During these runs, the ground was repeatedly detected at a range of 14 plus n. miles (26 plus km). Peak power during this series was 450 watts (3.6 mJ) with 8 μsec pulses at 140 Hz PRF.

> Figure 8-5 shows two consecutive camera frames taken during Run 9. The RVI (A) display shows both air and ground targets, the latter at 2.8 n miles (5.19 km), (14 n. miles or 26 km full scale). The two signals are separated by approximately 350 kHz. The lower "A" scope trace is centered on the ground signal, and shows the pulse return at ~35 μsec, the horizontal

Table 8-1. San Joaquin Valley Area-Runs

PRF = 150 Hz ALL RUNS

FLIGHT	RUN	P.W.	APPROX. PEAK S/N (dB)	ABOVE GROUND ALTITUDE	APPROX. MAX. RANGE INTO NOISE
7	1	8	~ 10	1500 ft. (.5 km)	2.2 nmi (4.1 km)
		4	~ 9	1500 ft. (.5 km)	1.25 nmi (2.3 km)
		2	9	1500 ft. (.5 km)	1.1 nmi (2.0 km)
	2	8	10-11	2000 ft. (.6 km)	3.5 nmi (6.5 km)
		4	12	2000 ft. (.6 km)	4.0 nmi (7.4 km)
		2	11-12	2000 ft. (.6 km)	3.0 nmi (5.6 km)
	3	8	10	2500 ft. (.8 km)	2.4 nmi (4.4 km)
		4	10	2500 ft. (.8 km)	3.0 nmi (5.6 km)
		2	10	2500 ft. (.8 km)	2.0 nmi (3.7 km)
	4	8	10	3000 ft. (.9 km)	2.0 nmi (3.7 km)
		4	8	3000 ft. (.9 km)	2.0 nmi (3.7 km)
		2	8	3000 ft. (.9 km)	1.5 nmi (2.8 km)
	5	8	9	3500 ft. (1.1 km)	2.2 nmi (4.1 km)
		4	6	3500 ft. (1.1 km)	1.4 nmi (2.6 km)
		2	7	3500 ft. (1.1 km)	1.6 nmi (2.9 km)
	6	8	5	4000 ft. (1.2 km)	1.5 nmi (2.8 km)
		4	4	4000 ft. (1.2 km)	1.3 nmi (2.4 km)
		2	2	4000 ft. (1.2 km)	0.9 nmi (1.7 km)
	7	8	—	4500 ft. (1.4 km)	—
		4	—	4500 ft. (1.4 km)	—
		2	—	4500 ft. (1.4 km)	—

Table 8-2. Carson Sink, Nevada - Runs

PRF = 150 Hz ALL RUNS

| FLIGHT	RUN	P.W.	APPROX. PEAK S/N (dB)	ABOVE GROUND ALTITUDE	APPROX. MAX. RANGE INTO NOISE
7	16	8	5	500 ft. (.2 km)	2.0 nmi (3.7 km)
		4	7	500 ft. (.2 km)	1.6 nmi (3.0 km)
		2	4	500 ft. (.2 km)	1.0 nmi (1.9 km)
	17	8	7	1000 ft. (.3 km)	1.6 nmi (3.0 km)
		4	7	1000 ft. (.3 km)	1.3 nmi (2.4 km)
		2	5	1000 ft. (.3 km)	0.9 nmi (1.7 km)
	18	8	7	1500 ft. (.5 km)	2.0 nmi (3.7 km)
		4	6	1500 ft. (.5 km)	1.6 nmi (3.0 km)
		2	3	1500 ft. (.5 km)	0.8 nmi (1.5 km)
	19	8	7	2000 ft. (.6 km)	1.6 nmi (3.0 km)
		4	7	2000 ft. (.6 km)	1.5 nmi (2.8 km)
		2	6	2000 ft. (.6 km)	1.0 nmi (1.9 km)
	20	8	7	2500 ft. (.8 km)	1.5 nmi (2.8 km)
		4	5	2500 ft. (.8 km)	1.5 nmi (2.8 km)
		2	5	2500 ft. (.8 km)	1.0 nmi (1.9 km)
	21	8	3	3000 ft. (.9 km)	1.6 nmi (3.0 km)
		4	6	3000 ft. (.9 km)	1.5 nmi (2.8 km)
		2	7	3000 ft. (.9 km)	1.3 nmi (2.4 km)
	22	8	6-7	3500 ft. (1.1 km)	1.6 nmi (3.0 km)
		4	7	3500 ft. (1.1 km)	1.8 nmi (1.5 km)
		2	7	3500 ft. (1.1 km)	1.3 nmi (2.4 km)
	23	8	5	4000 ft. (1.2 km)	1.5 nmi (2.8 km)
		4	6	4000 ft. (1.2 km)	1.2 nmi (2.2 km)
		2	4	4000 ft. (1.2 km)	0.9 nmi (1.7 km)
	24	8	6	4500 ft. (1.4 km)	1.5 nmi (2.8 km)
		4	5-6	4500 ft. (1.4 km)	1.3 nmi (2.4 km)
		2	5-6	4500 ft. (1.4 km)	1.0 nmi (1.9 km)
	25	8	6	5000 ft. (1.5 km)	1.6 nmi (3.0 km)
		4	5	5000 ft. (1.5 km)	1.3 nmi (2.4 km)
		2	2	5000 ft. (1.5 km)	0.7 nmi (1.3 km)
	26	8	5	6000 ft. (1.8 km)	2.0 nmi (3.7 km)
		4	3	6000 ft. (1.8 km)	1.2 nmi (2.2 km)
		2	4	6000 ft. (1.8 km)	0.9 nmi (1.7 km)
	27	8	—	7000 ft. (2.1 km)	—
		4	—	7000 ft. (2.1 km)	—
		2	—	7000 ft. (2.1 km)	—
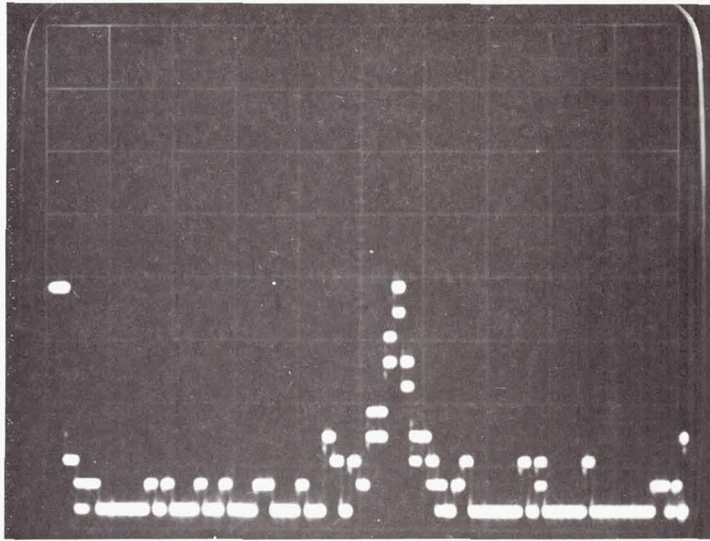
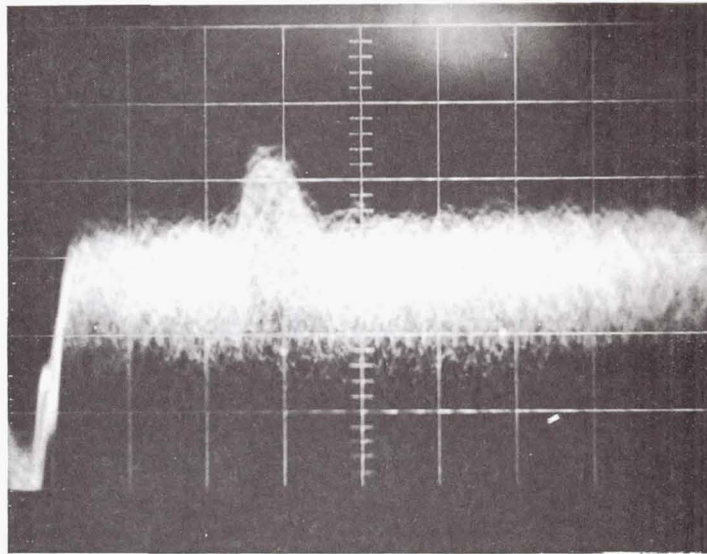IVI Display, 15 μsec Delay
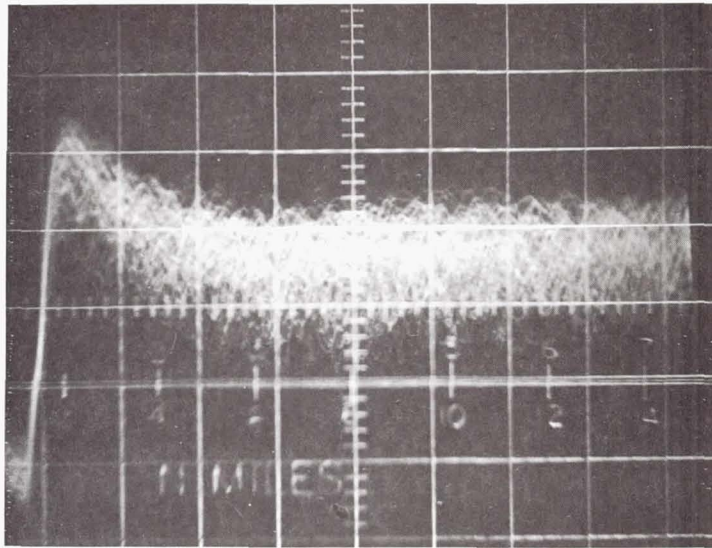
"A" Scope Display Vert. = 10 dB/Div.

EO-540

Figure 8-1. Clear Air Returns, 8,000 ft. (2.4 km) Altitude
Flight 8, Run 20
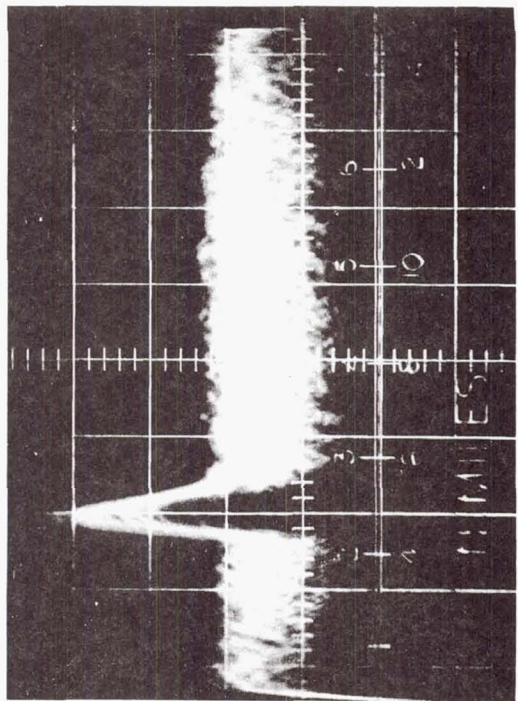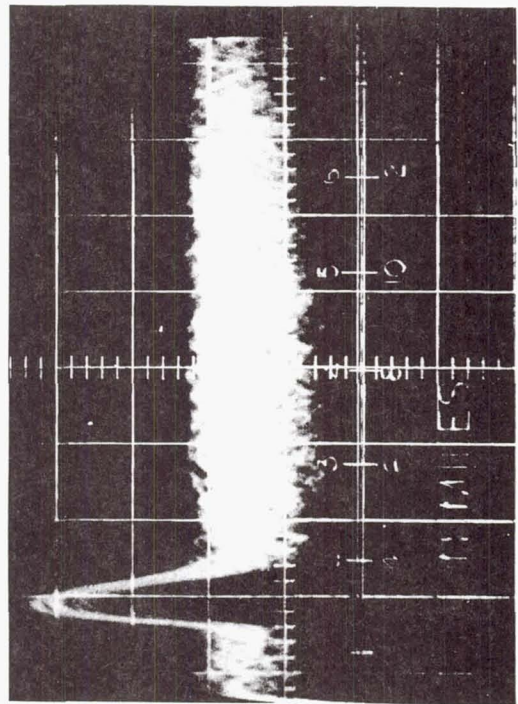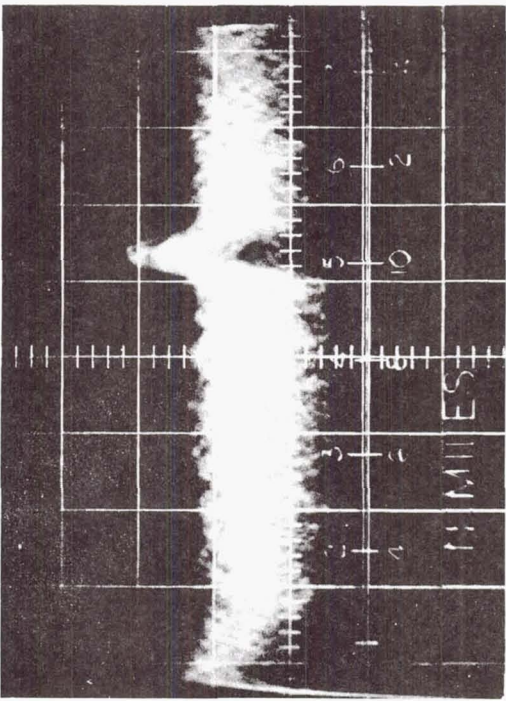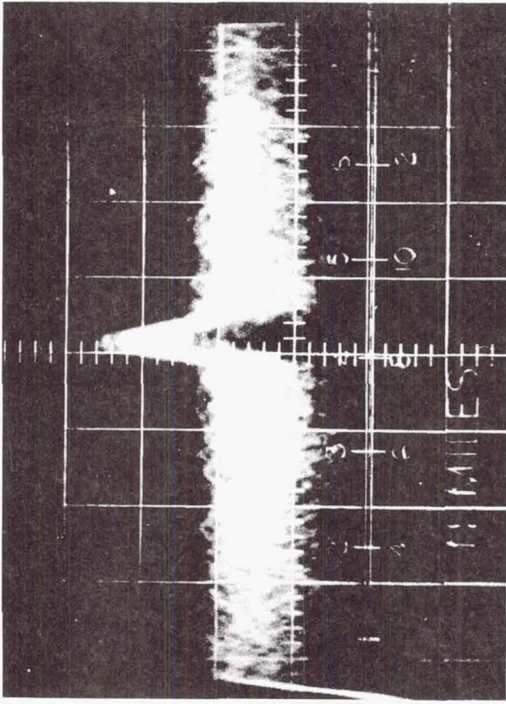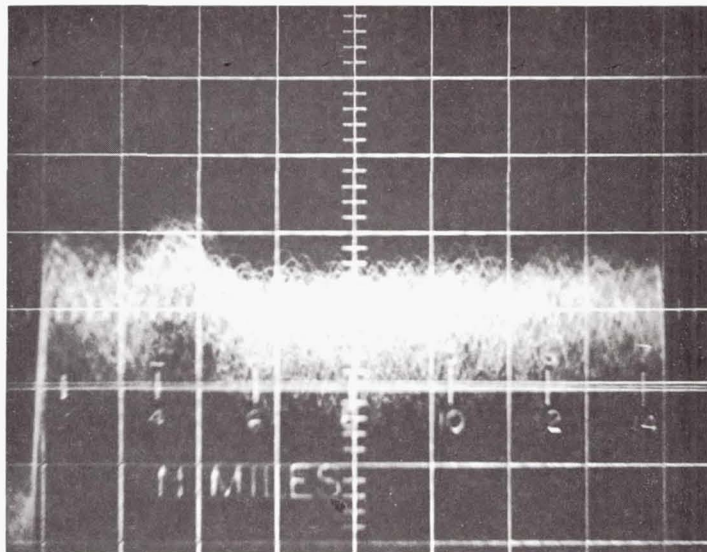
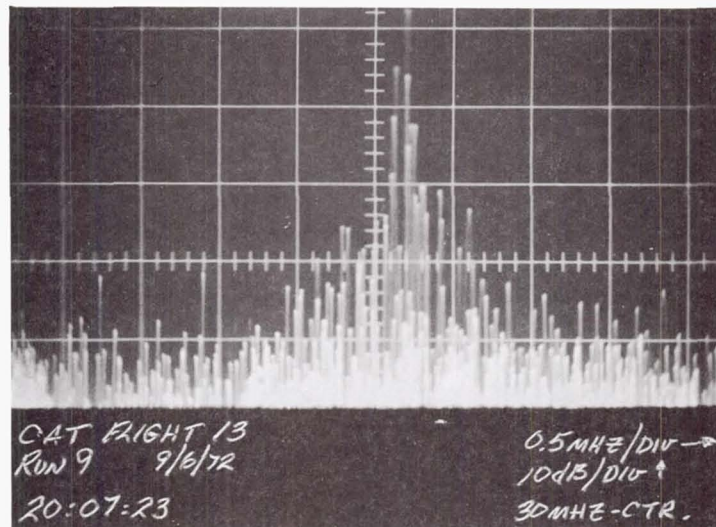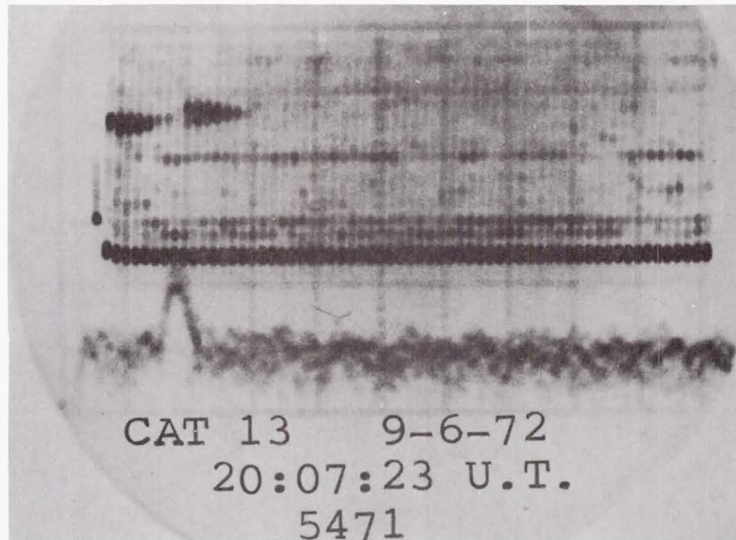Figure 8-2. Ground Signals, CAT Flight 8, Run 4; Mt. Shasta Series

EO-541

EO-542

Figure 8-3.   Cumulus Cloud Signal at 15,000 ft. (4.6 km)

EO-543

Figure 8-4.   Cirrus Cloud Signal at 36,200 ft. (11 km)

CAT 13   9-6-72
20:07:23 U.T.
5471

EO-544

Figure 8-5. Signal Returns from Steep Descent -
Carson Sink, Nevada

scale factor here being 20 μsec. The vertical scale factor for the "A" scope display is 10 dB/div. The passband for the "A" scope display is only 300 kHz; therefore, the clear air signals at 1 mile (1.6 km) are not in evidence in this display. The lower figure shows the composite spectrum for both targets. A peak reading of 42 dB is in evidence, presumably from the ground signal.

Figure 8-6 has the same previous data, except that they occur 1.0 second later. The peak reading on the swept analyzer is approximately 30 dB, with a very broad envelope ~ 1.0 MHz wide at ~ 15 dB, presumably due to the clear air returns.

Figure 8-7 is an example from the same run. In this instance, the ground return is 7.6 n. miles (14.1 km) and both air and ground signals are at the same frequency; therefore, both signals appear (at 10 - 12 dB) S/N on the "A" scope as well.

The aircraft was then directed to the southern California area at a nominal cruise altitude of 15,000 ft. (4.57 km), where a number of cumulus cloud penetrations were made. Acquisition on these targets was made as far as 8 miles (12.9 km). The aircraft then proceeded into the northwest corner of Arizona, where a reasonable probability of encountering blowing dust existed. We were fortunate in encountering just such an area in the Kingman region (see Figure 8-8).
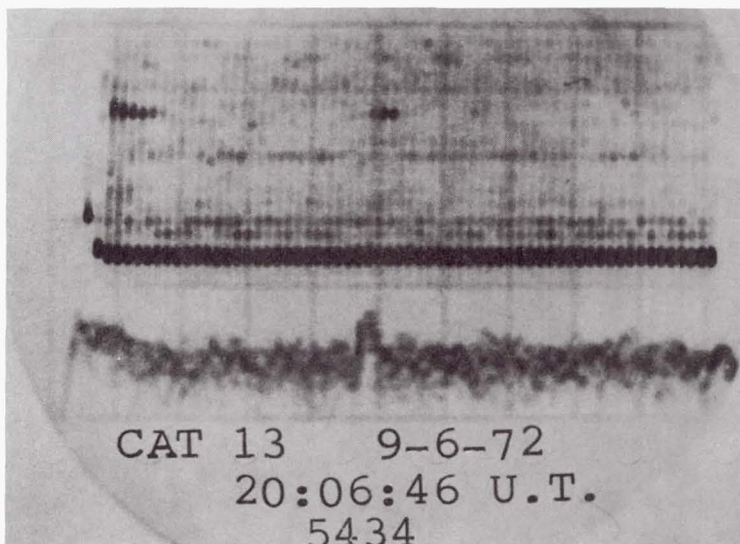
Figure 8-9 is sampling of data photos taken on the 35 mm sequence camera as the aircraft approached the dust storm. Calibration of this sequence is as follows:

Upper display is RVI, with range displayed 0 to 7.0 miles (11.3 km). Vertical raster indicated frequency, ± 5 MHz from raster center, equivalent to ± 50 knots (25 m/sec) of aircraft speed.

CAT 13   9-6-72
20:07:24
5472

CAT FLIGHT 13
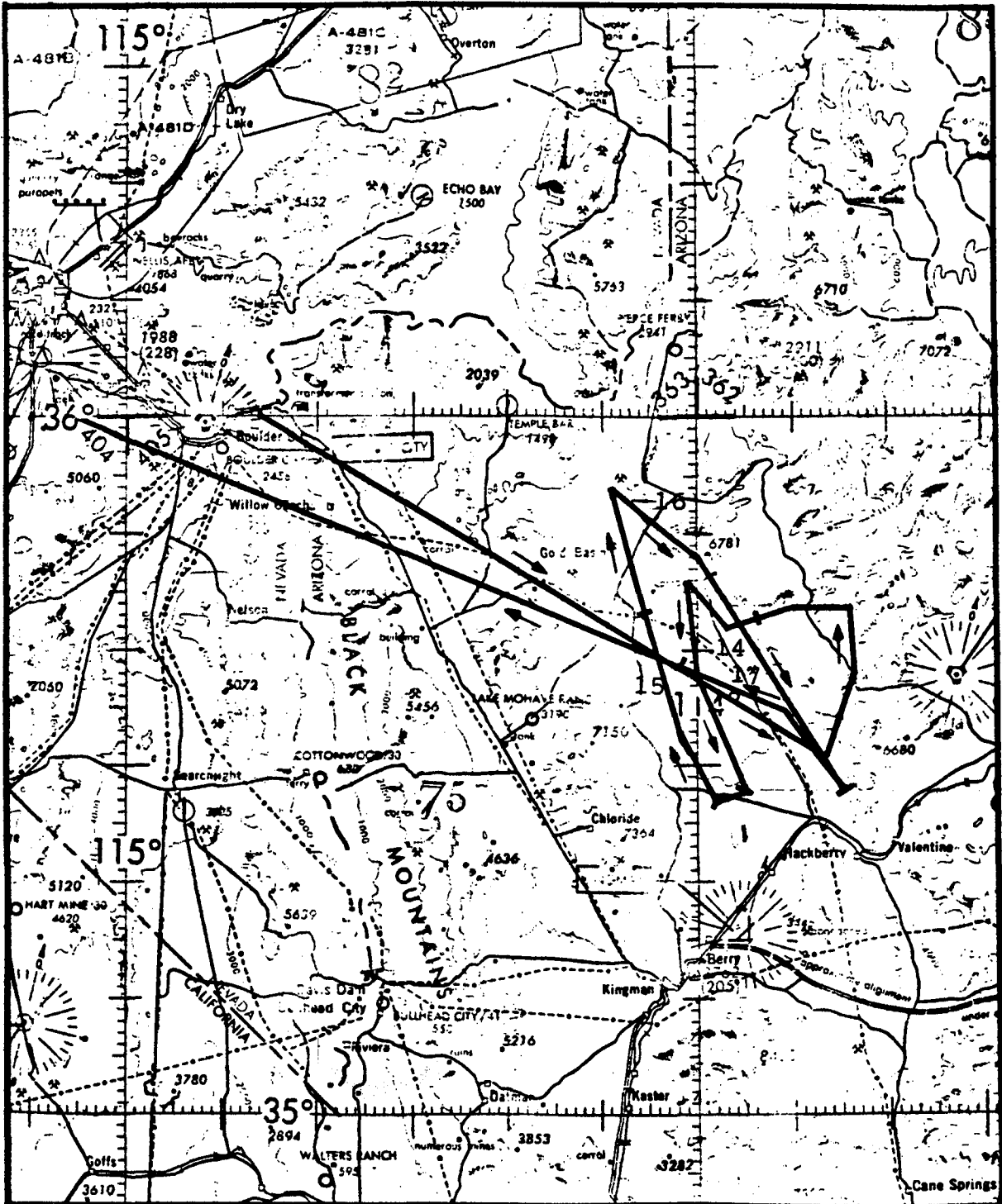RUN 9   9/6/72
20:07:24
0.5 MHZ/DIV →
10 dB/DIV ↑
30 MHZ-CTR.
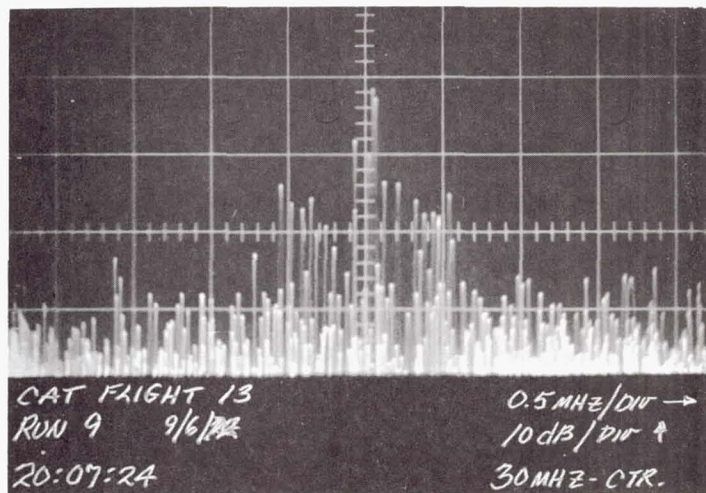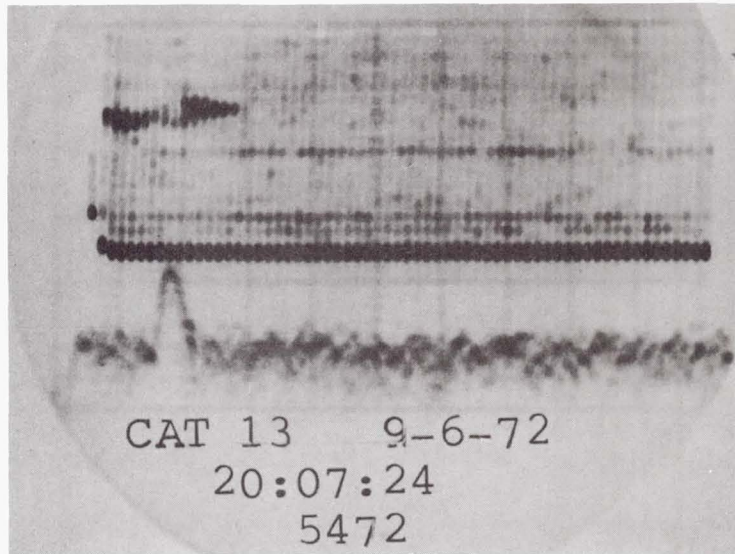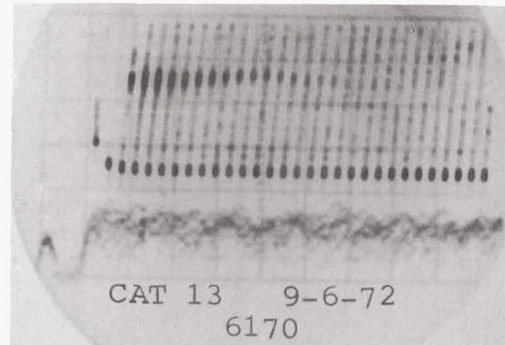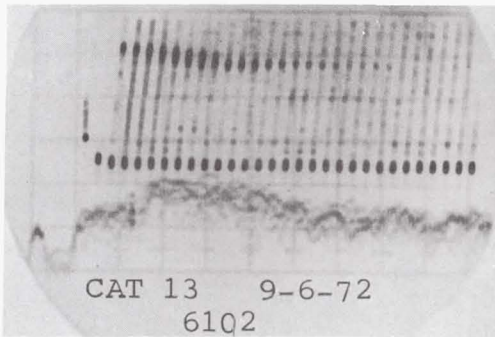
EO-545

Figure 8-6.   Steep Descent Signals - Carson Sink, Nevada
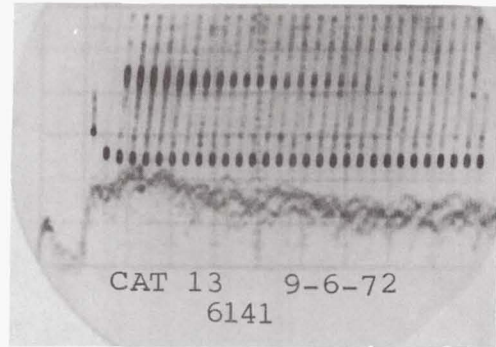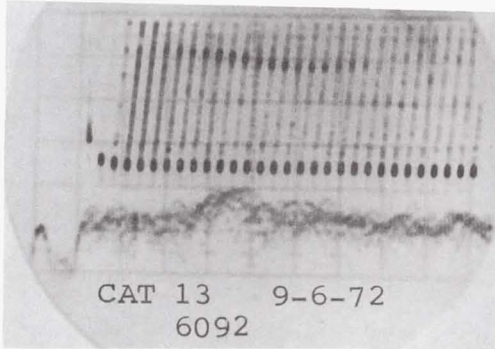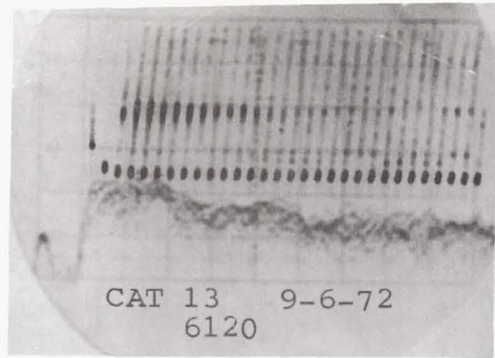
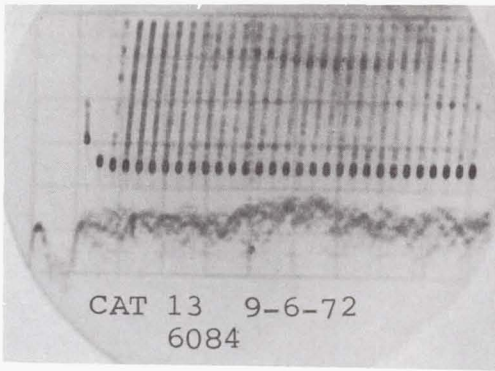CAT 13   9-6-72
20:06:46 U.T.
5434

EO-546

Figure 8-7.   Clear Air and Ground Signals
at Same Doppler Frequency

EOA-933

Figure 8-8. Flight Pattern in the Kingman, Arizona Area -
Flight 13

CAT 13   9-6-72
6084

CAT 13   9-6-72
6120

CAT 13   9-6-72
6092

CAT 13   9-6-72
6141

CAT 13   9-6-72
6102

CAT 13   9-6-72
6170

CAT 13   9-6-72
6113

CAT 13   9-6-72
6205
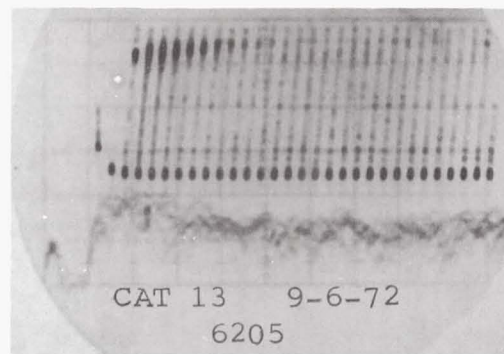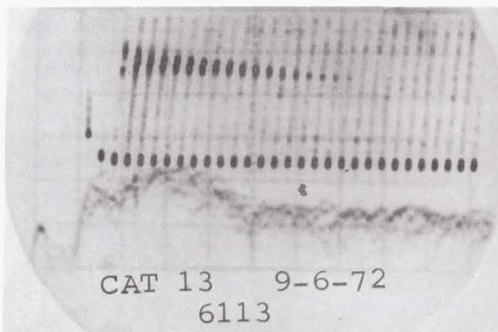
EO-547

Figure 8-9.   Sequence Camera Series - Kingman,
Arizona Dust Storm

Lower display is "A" scope, Horizontal calibration is
10 μsec/Div.

Vertical calibration is 20 dB/Div.

The sequence shows the approach of the dusty area, with the RVI scans clearly indicating the wind velocity along the beam axis at the various ranges. Most of the sequence photos show a distribution of at least 2.5 MHz, equivalent to ∿40 ft./sec velocity changes or 25 knots.

During this series of runs, S/N ratios in excess of 40 dB were detected on the "A" scope.

Figures 8-10, 8-11 and 8-12 are from a later run, and are consecutive frames from a run over the dust storm. Signals are traceable to 6 nmi (11.1 km), with S/N ratios in the 20 dB range. Figure 7-10 shows a discontinuity at ~3.5 nmi (~6.5 km) (circled) presumably due to a minor wind shear at that range.

8.3 FLIGHT B TESTS (See Appendix F for a detailed analysis of flight B data)

The eight B flights of January 1973 utilized both GeCu and HgCdTe detectors with excellent performance from the HgCdTe detectors (see, especially Flight B-2, 12 January, Appendix F) where marginal CAT events were clearly resolved. Flight B corroborated evaluations by A. V. Jelalian (Raytheon memo EM73-1115) of flight A data that 20 dB of system improvement would be desirable. Flight B analysis determined that improvements should be:

∿11 dB for a detection range of 5 nmi. (9.3 km)
∿18 dB for a detection range of 10 nmi. (18.5 km)
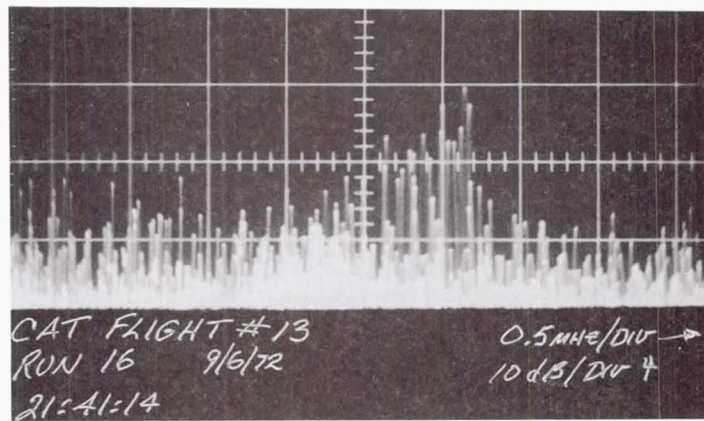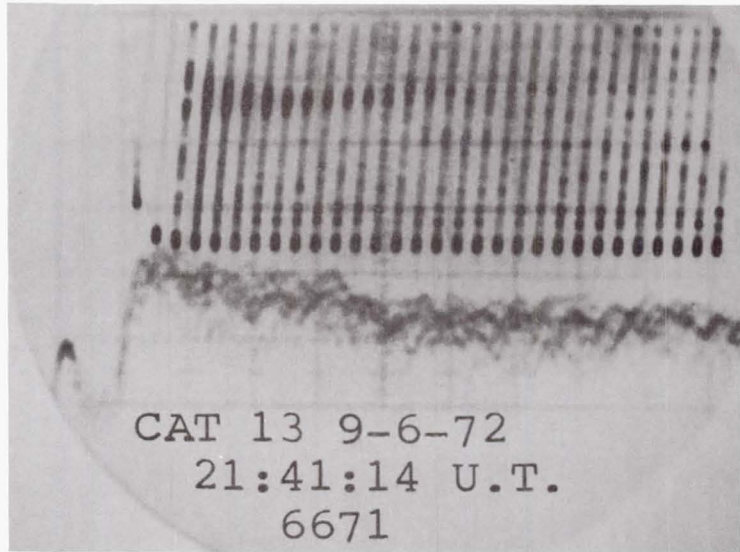∿26 dB for a detection range of 20 nmi. (37.1 km)

at an altitude of 40,000 feet (12.2 km). Since the desired detection range is 10 to 20 nmi. (18.5 to 37.1 km), the required improvement in S/N ratio is roughly 20 dB.

The determination of required improvement is outlined in Table 8-3 and plotted against range and altitude in Figure 8-13. These analyses assumed:

CAT 13   9-6-72
21:41:13 U.T.
6670

CAT FLIGHT 13
RUN 16   9/6/72
21:41:13

0.5MHZ/DIV →
10dB/DIV ↑
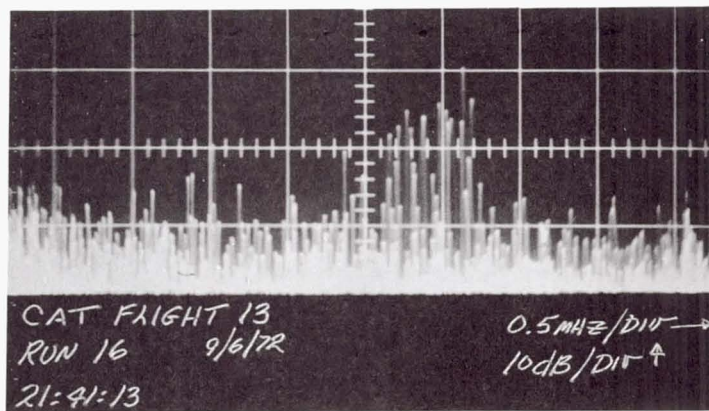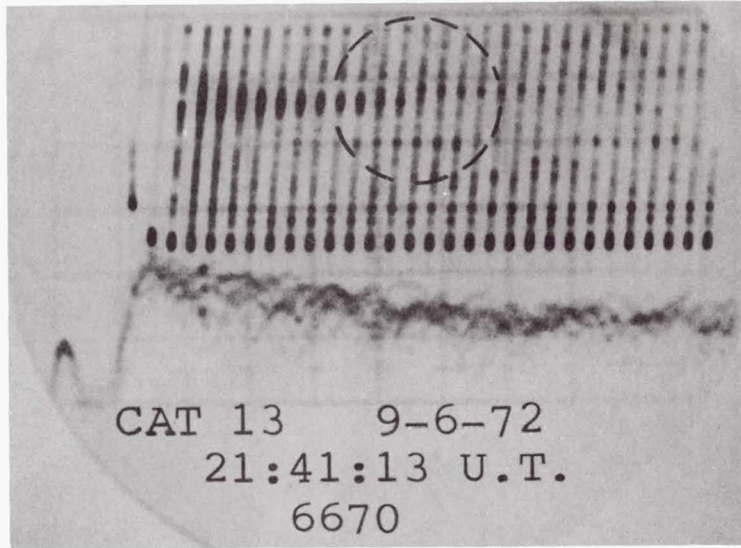
EO-548

Figure 8-10. Doppler Returns - Dust Storm - RVI Shows Abrupt
Wind Shear at ~3.5 nmi. (~6.5 km)

CAT 13 9-6-72
21:41:14 U.T.
6671

CAT FLIGHT #13
RUN 16   9/6/72
21:41:14

0.5 MHz/DIV →
10 dB/DIV ↓

EO-549

Figure 8-11.   Doppler Returns in Dust Storm -
Kingman, Arizona

CAT 13   9-6-72
21:41:15 U.T.
6672

CAT FLIGHT 13
RUN 16   9/6/72
21: 41:15

0.5 MHz/DIV →
10 dB/DIV
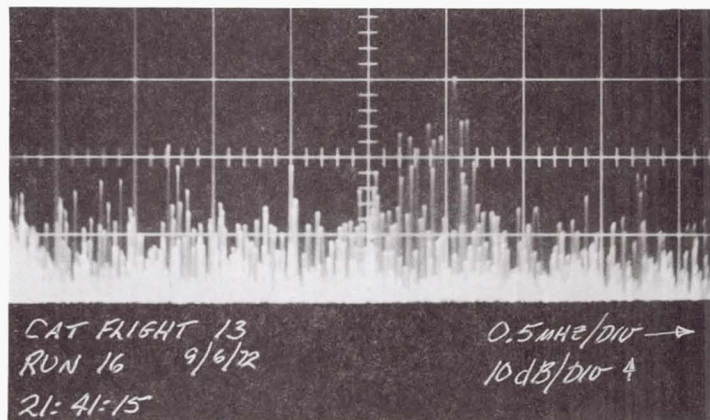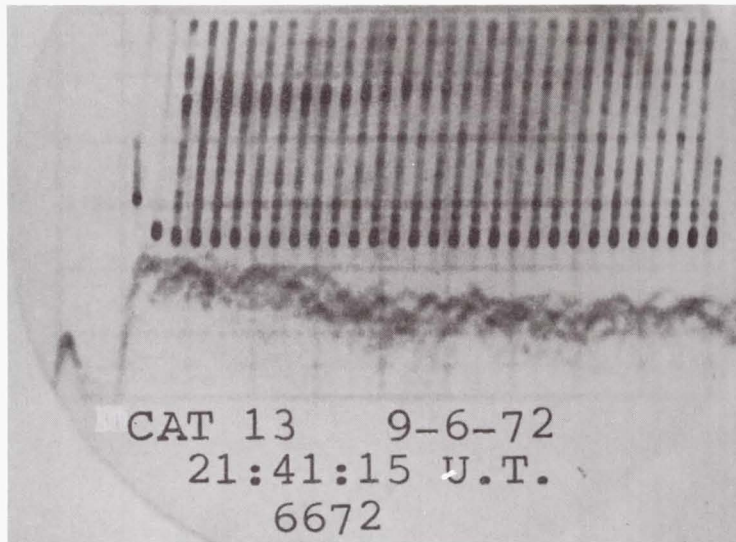
EO-550

Figure 8-12. Doppler Returns - Dust Storm -
Kingman, Arizona
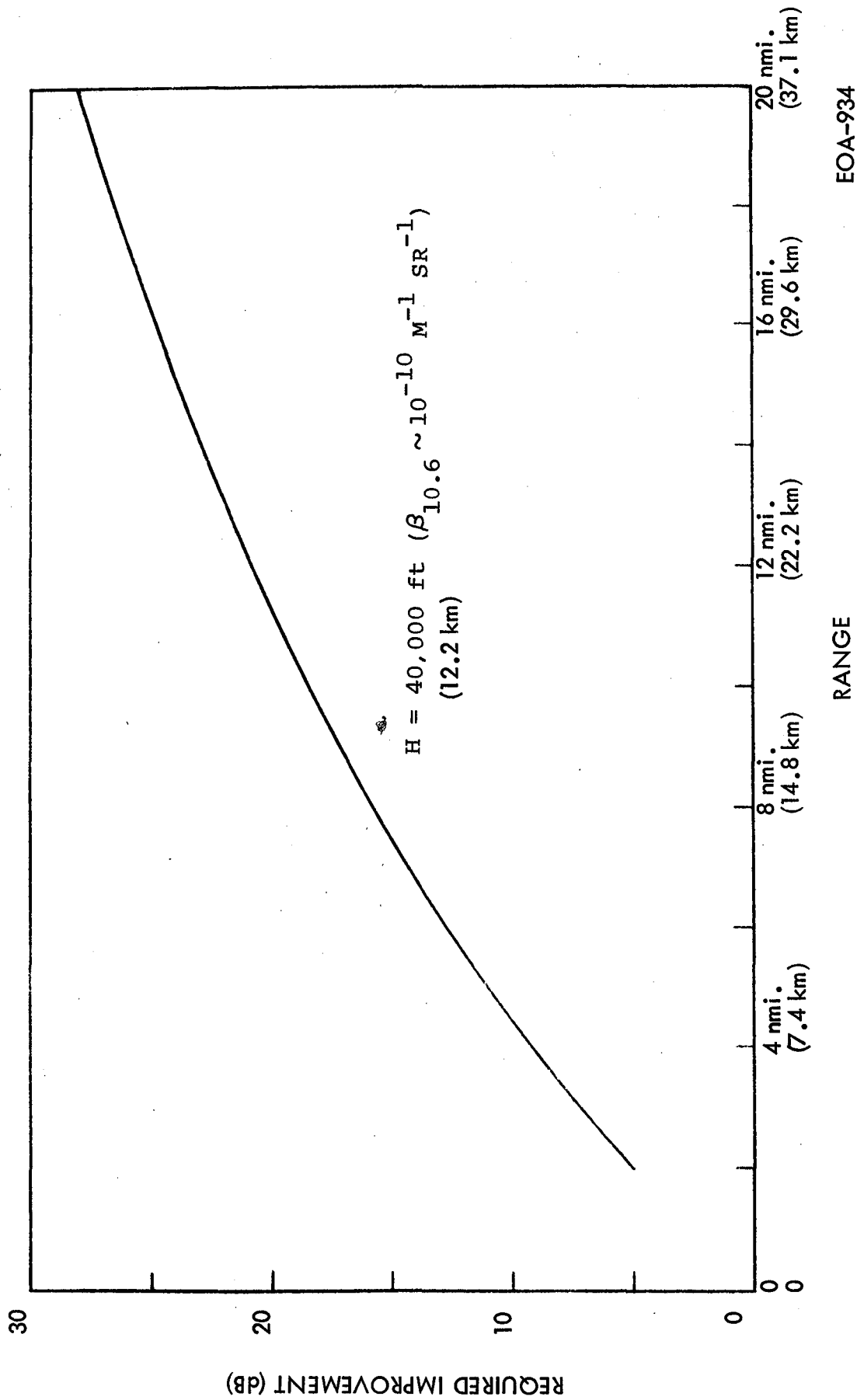
Figure 8-13. Required Improvement in S/N Ratio for Operational CAT Laser Radar

$H = 40,000$ ft $(\beta_{10.6} \sim 10^{-10}$ M^{-1} SR$^{-1})$
(12.2 km)

RANGE

EOA-934

REQUIRED IMPROVEMENT (dB)

Table 8-3. Required S/N Improvement for Operational CAT System

		Required Increase in CAT System	
		Each	Cumulative
1.	Measured SNR from air was roughly 15 dB at low altitude (~3 Kft) for a range of 2 miles in winter		
2.	A SNR of 8 dB is probably sufficient in an operational system, judging by the SC A-scope returns	-7 dB	-7 dB
3.	Improvement from focusing receiver at infinity rather that at 1 mile is 0 dB at a range of 2 miles	0	-7
4.	For operation at 40,000 feet altitude, the backscatter coefficient is estimated to be roughly 12 dB lower.*	+12	+5
5.	a. For operational range of 2 mi. (3.2 km), need 0 dB more	0	5
	b. For operational range of 5 mi. (8.1 km), need 6 dB more**	+6	or 11
	c. For operational range of 10 mi. (16.1 km), need 13 dB more**	+13	or 18
	d. For operational range of 20 mi. (32.2 km), need 23 dB more**	+23	or 28

*Extrapolated from data in Figure 15 of Memo 73:AJ:039

**Assuming an atmospheric attenuation coefficient of 0.1 dB/km at 40,000 feet (12.2 km) in winter

a. The receiver was focused at 6,000 ft. (1.8 km) during the January tests and the receiver can be properly collimated in future systems.

b. The backscatter coefficient is a factor of 16 lower at 40,000 ft. (12.2 km) ($\beta \sim 10^{-10}$ per meter-ster) and a factor of 5 lower at 20,000 ft. (6.1 km) ($\beta \sim 4 \times 10^{-10}$ per meter-ster), compared with ground level.

c. The atmospheric attenuation coefficient is 0.1 dB/km each way at 40,000 ft. (12.2 km) and 0.15 dB/km at 20,000 ft. (6.1 km).

d. A S/N ratio of 8 dB is sufficient for detection, and any reduction caused by frequency broadening of the signal beyond the bandwidth due to turbulence is not detrimental.

The S/N ratio improvement can come from a variety of sources; the logical steps for improvement are:

1. Reduce the losses. The observed loss exclusive of the detector is 15 dB which is detailed as follows:

Optics (beamsplitter, Ge window, lenses)	3 dB
Extended diffuse target, Gaussian beam	5 dB
Target depolarization	1 dB
Receiver electronics	4 dB
Unexplained	2 dB

Up to 5 dB of these losses can be eliminated.

2. Pulse integration. The S/N ratio can be improved by increasing the number of pulses if integration is perfect and signal amplitude remains constant. However, signal amplitude varies widely, and analytical integration of the Edwards returns shows that there was virtually no improvement in the integrating 50 pulses. At higher altitudes air turbulence, the primary cause of the signal variation, is less severe; hence, substantial improvement could be obtained from integration.

3. Increase the laser output. This step should be considered only as a last measure.

4. Other system improvements. Examine the possibilities of improving the detector and the aperture. Because the quantum efficiency of the HgCdTe detector in the test was approximately 0.25, little room for improvement was suggested there. Enlarging the effective aperture from 10 - 15 in. (25.4 - 38.1 cm) would theoretically increase the signal-to-noise ratio at 10 mi. (16.1 km) by 3 dB.

Analyses of the data from the flight tests were conducted under the data analysis section of this contract (see Section 1) and are the bases for the suggestions for systems modification and improvements described in Raytheon proposal ER76-4063, Proposed Modifications to CAT Detection Instrumentation System, 2 March 1976, and in the Offset CAT System component description given in Section 3.

SECTION 9
FLIGHT DATA ANALYSES

9.1 GENERAL

The performance of the CAT system was evaluated by examining the system performance against known targets - ground, clouds, clear air, etc., in order to estimate system efficiency, focusing, and the backscatter coefficients of atmospheric targets. If the ground target is a smooth area, the backscatter coefficient can be determined using samples in the laboratory or data from previous tests. Sand covered ground (Rogers Dry Lake at Edwards Air Force Base) provided such a target. When a sufficient amount of data was consecutively collected, statistics of the signal were measured to determine the effects of backscatter fluctuations, system energy and efficiency fluctuations, and atmospheric turbulence on system performance. The backscatter and system fluctuations were separable from the turbulence fluctuations by a study of range dependence and temporal behavior of the fluctuations. These then were separated from each other using temporal behavior and measurements from ground tests under controlled conditions.

Two atmospheric phenomena were also known to have significant effects on the system: attenuation due to absorption, and scattering and atmospheric turbulence, which causes fluctuation in the signal and a degradation of average signal value. Each of these has a unique range dependence detectable from the amplitude behavior of single and multiple pulses in periods of straight, level flight.

The benefits of pulse integration were also evaluated.

Basically the tests fall into three groups:

1. Returns from the ground to check out and calibrate the laser system. A flat area (Rogers Dry Lake at Edwards AFB) was selected and dives made at it.

2. Returns from clouds to detect turbulence. A mountainous area was selected. Where feasible, the flight was continued through the clouds to correlate actual turbulence with the laser return.

3. Returns from air.

4. Returns from miscellaneous targets.

The data analysis indicated good results from all four categories. The 1973 ground tests showed a signal smoothly varying with range, consistent from run to run on different days, and nearly two orders of magnitude larger than returns measured during flight tests in 1972 at the same location.

The runs against clouds clearly showed the ability of the system to detect turbulence and predict the time it will be encountered. During one flight over the mountains bordering the Owens Valley, a total of 23 clouds was detected. From an examination of the sequence camera record of the A-scope (amplitude vs. range) and RVI (velocity vs. range) plots, the length, range signal-to-noise ratio, and Doppler width of the clouds were measured and tabulated. Although the plane usually avoided the clouds for safety reasons, there were some instances in which a correlation between the sighting and the encountering of turbulence could be made.

Signals were also received from clear air and are correlated in the complete data analysis given in Appendices E and F.

Evaluations were also made of CAT flight data with area of Doppler broadening as a function of pulse width, and from air returns in a steady state, which indicated air speed. Data were taken from sequence camera photos, magnetic tapes, and the on-board computer print-out of flight parameters, and voice commentary.

Three sets of tests were conducted. The first two were in the winter of 1972 and 1973 before the modifications and the third test series was in the first quarter of 1979.

9.2 DATA HIGHLIGHTS

The correlation between CAT instrument returns from a cloud and aircraft response at cloud penetration is shown in Figure 9-1 where the wide IVI trace at 23:53:10 with range gate at 27 μsec is the processed return from a turbulent cumulus cloud. Flying at 350 knots (175 m/sec), the aircraft penetrated the cloud 22 seconds later with the aircraft vertical accelerometer recording a strong impulse 24 seconds afterwards, showing the correlation between turbulence as predicted by the CAT instrument, and as experienced later by the aircraft.

Returns from thin cirrus clouds are shown by the series of RVI and A-Scope photos (Figures 9-2 (a) through (j)). Several examples show two clouds, one seen through the other. (The clouds can appear at different frequencies or different velocities.) The A-Scope filter is sometimes tuned on the near cloud while rejecting the far cloud; or conversely when both clouds are at the same frequency, the A-Scope shows clearly two returns separated in range.

A steep descent at Edwards AFB is recorded by RVI and A-Scope series photos (Figure 9-3 (a) through (h)). The A-Scope sweep is changed at the shorter ranges. Notice that the range to the ground is measured independently by the two displays. The strong returns at close range saturate the receiver which is set at maximum sensitivity, so that a signal appears across the entire RVI range display. The STC would adjust sensitivity with range to prevent this effect.

Another steep descent at Edwards AFB is shown via the IVI presentations shown in Figure 9-4 (a) through (d). The range gate is manually tracked in from 192 μsec to 34 μsec during the descent. Figure 9-4 (a) shows a very strong ground return and a wind return.

Figure 9-5 (a) through (d) shows various returns from dust clouds and ground targets in the Imperial Valley and Owens Valley.
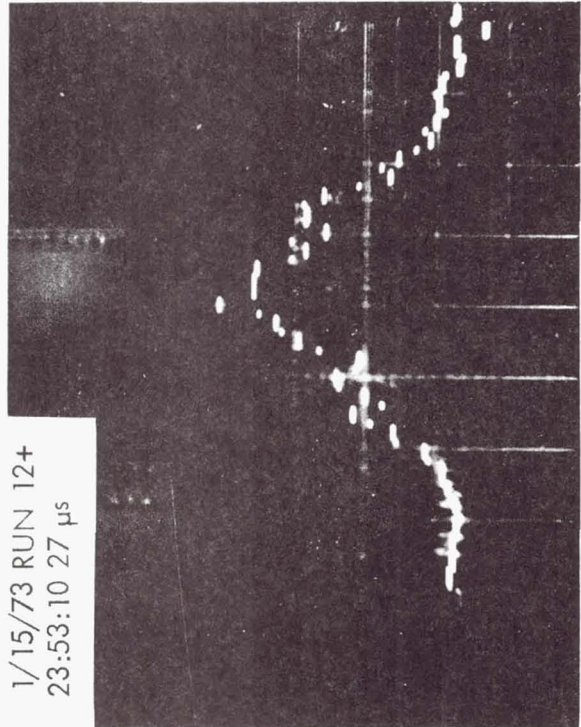
Figure 9-1. CAT Flight Test - Cloud Turbulence Correlation
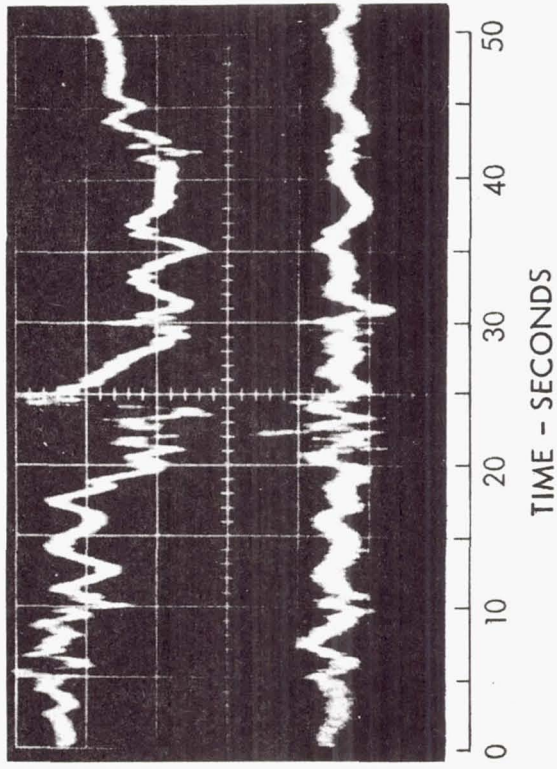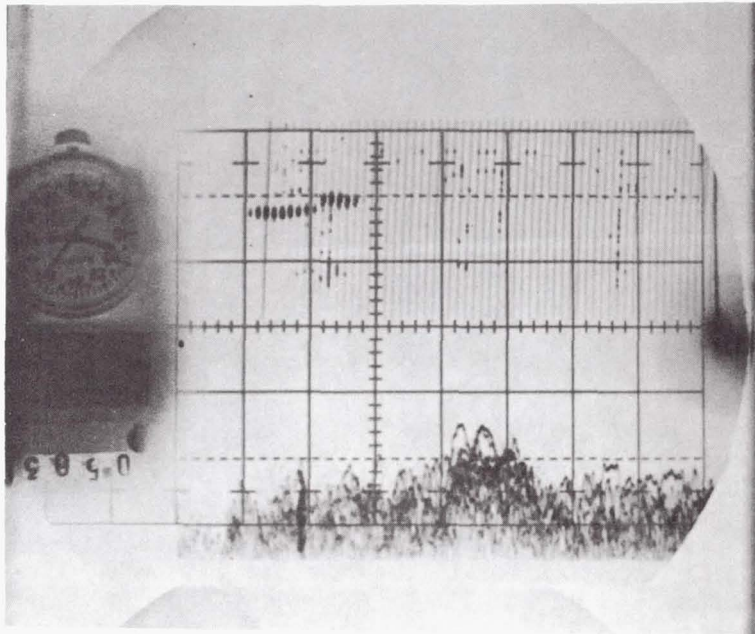
EO-551
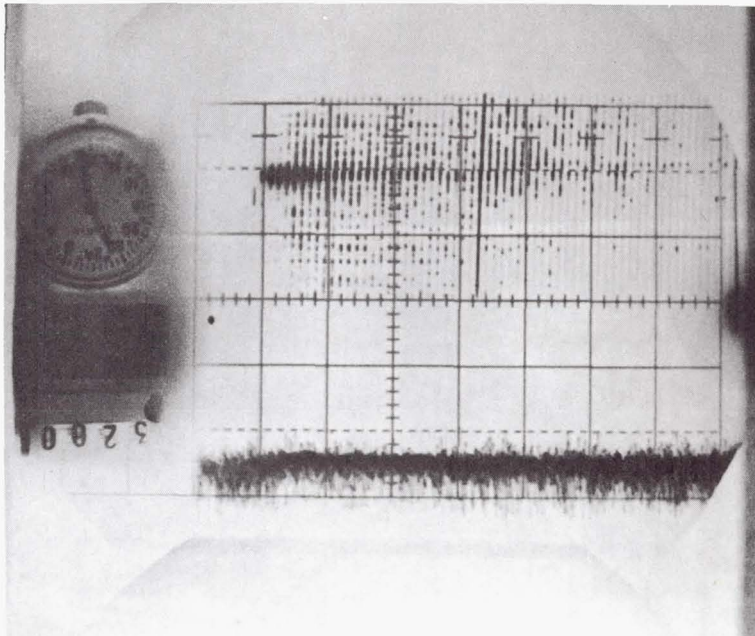
(a)

RVI

Vert. 3.33 MHz/div.

Horiz. 2 nmi/div.
(3.7 km/div.)

A SCOPE

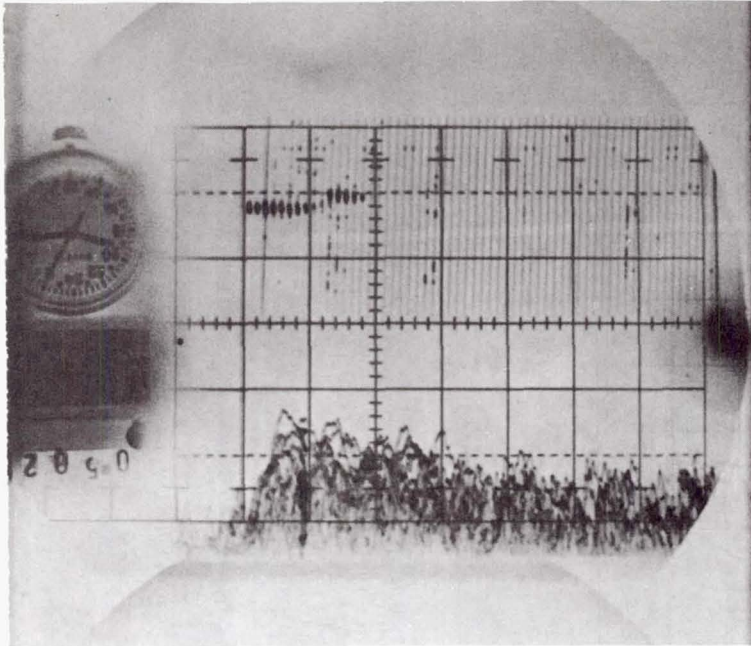Vert. 10 dB/div.

Horiz. 1 nmi/div.
(1.9 km/div.)

(b)

ALTITUDE 33,000 FT. (10 km)   AT START OF SERIES: LATITUDE (DEG. MIN.)
CIRRUS CLOUDS   40.17.0 N
                                                   LONGITUDE (DEG. MIN.)
TRUE HEADING: 79.2°   106.57.5 W
TRUE AIR SPEED: 480 KNOTS (240 m/sec)

                                                   EO-552

Figure 9-2.   Thin Cirrus Clouds Returns
              (Sheet 1 of 5)

(c)

RVI
Vert. 3.33 MHz/div.
Horiz. 2 nmi/div.
   (3.7 km/div.)

A SCOPE
Vert. 10 dB/div.
Horiz. 1 nmi/div.
   (1.9 km/div.)

(d)

ALTITUDE 33,000 FT. (10 km) AT START OF SERIES: LATITUDE (DEG. MIN.)
CIRRUS CLOUDS   40.17.0 N
                                               LONGITUDE (DEG. MIN.)
TRUE HEADING: 79.2°   106.57.5 W
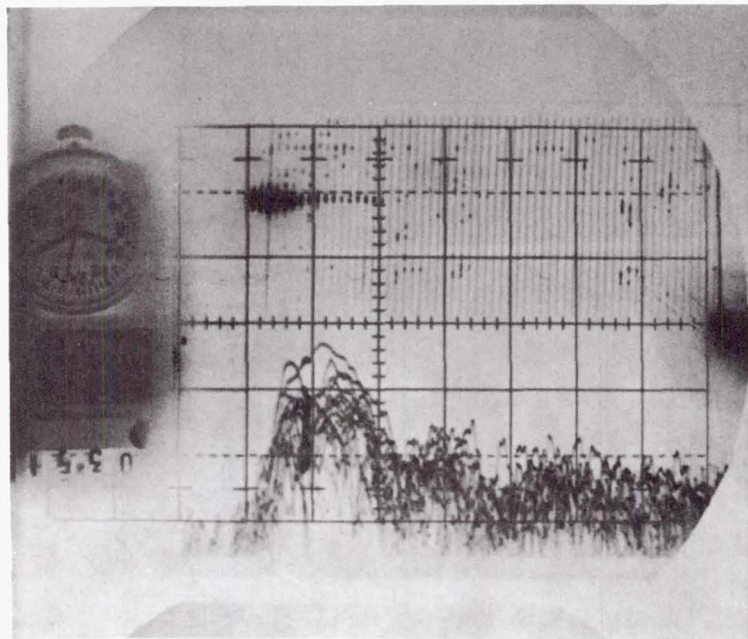TRUE AIR SPEED: 480 KNOTS (240 m/sec)

EO-553

Figure 9-2. Thin Cirrus Clouds Returns
(Sheet 2 of 5)

(e)

RVI

Vert. 3.33 MHz/div.

Horiz. 2 nmi/div.
   (3.7 km/div.)

A SCOPE
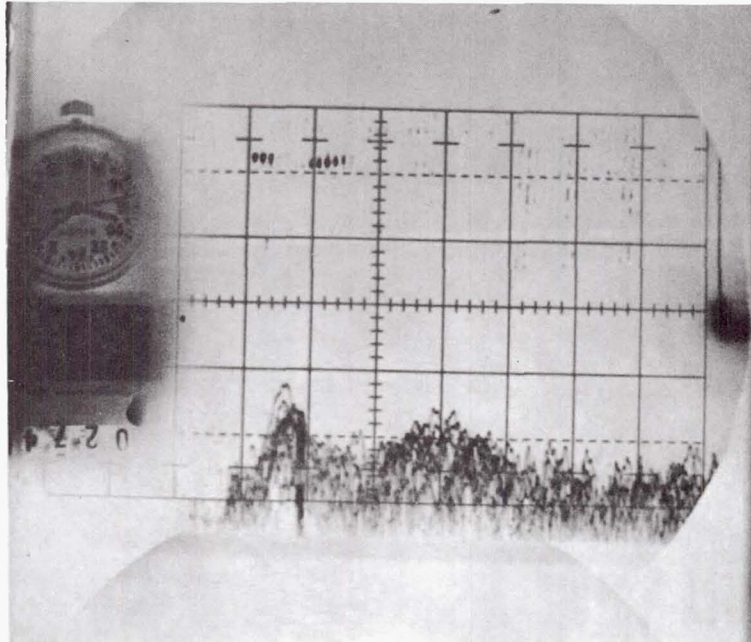
Vert. 10 dB/div.

Horiz. 1 nmi/div.
   (1.9 km/div.)

(f)

ALTITUDE 33,000 FT. (10 km)   AT START OF SERIES: LATITUDE (DEG. MIN.)
CIRRUS CLOUDS   40.17.0 N
                                                   LONGITUDE (DEG. MIN.)
TRUE HEADING: 79.2°   106.57.5 W
TRUE AIR SPEED: 480 KNOTS (240 m/sec)

                                                   EO-554

        Figure 9-2. Thin Cirrus Clouds Returns
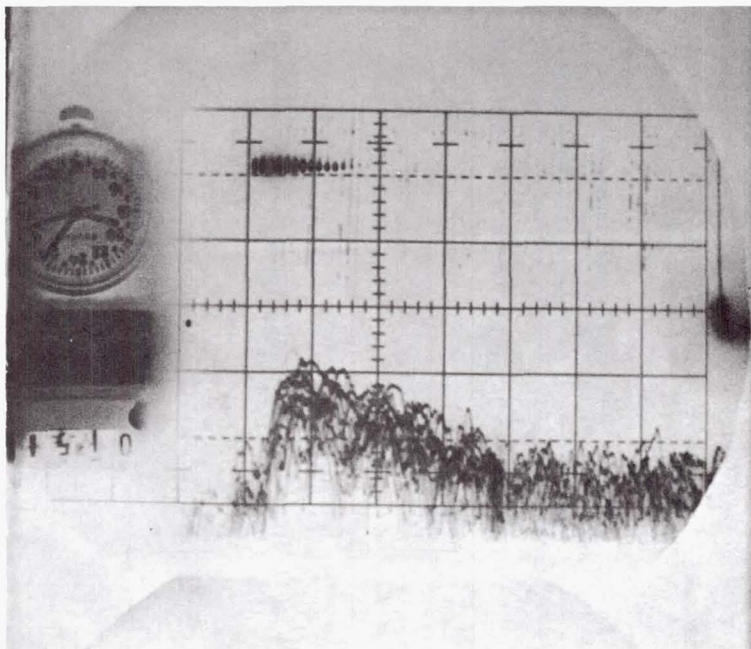   (Sheet 3 of 5)

(g)

RVI

Vert. 3.33 MHz/div

Horiz. 2 nmi/div.
(3.7 km/div

A SCOPE

Vert. 10 dB/div.

Horiz. 1 nmi/div.
(1.9 km/div

(h)

ALTITUDE 33,000 FT. (10 km)   AT START OF SERIES: LATITUDE (DEG. MIN.
CIRRUS CLOUDS   40.17.0 N
                                                     LONGITUDE (DEG. MIN
TRUE HEADING: 79.2°   106.57.5 W
TRUE AIR SPEED: 480 KNOTS (240 m/sec)

                                                     EO-555

        Figure 9-2.   Thin Cirrus Clouds Returns
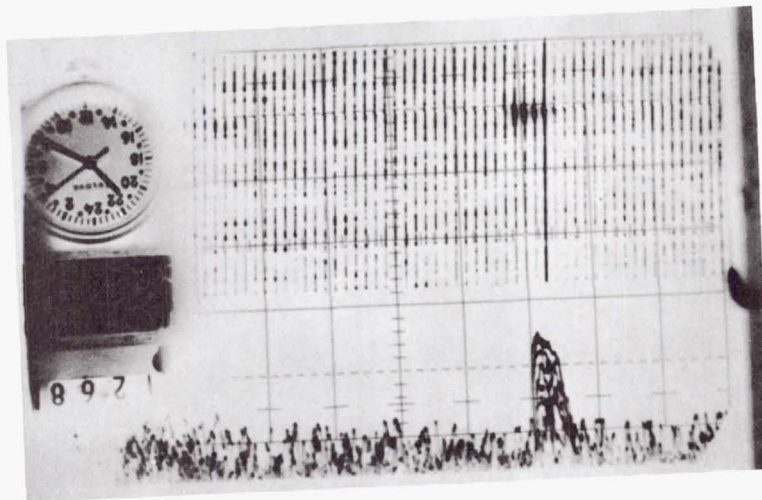   (Sheet 4 of 5)

(i)

RVI

Vert. 3.33 MHz/div.

Horiz. 2 nmi/div.
  (3.7 km/div.)

A SCOPE

Vert. 10 dB/div.

Horiz. 1 nmi/div.
  (1.9 km/div.)

(j)

ALTITUDE 33,000 FT. (10 km)   AT START OF SERIES: LATITUDE (DEG. MIN.)
CIRRUS CLOUDS   40.17.0 N
                                                    LONGITUDE (DEG. MIN.)
TRUE HEADING: 79.2°   106.57.5 W
TRUE AIR SPEED: 480 KNOTS (240 m/sec)

                                                    EO-556

Figure 9-2. Thin Cirrus Clouds Returns
             (Sheet 5 of 5)

(a)

RVI: 2.64 MHz/DIV
20 µsec/DIV

A-SCOPE 10 dB/DIV

(b) PHOTOS 1233--1327
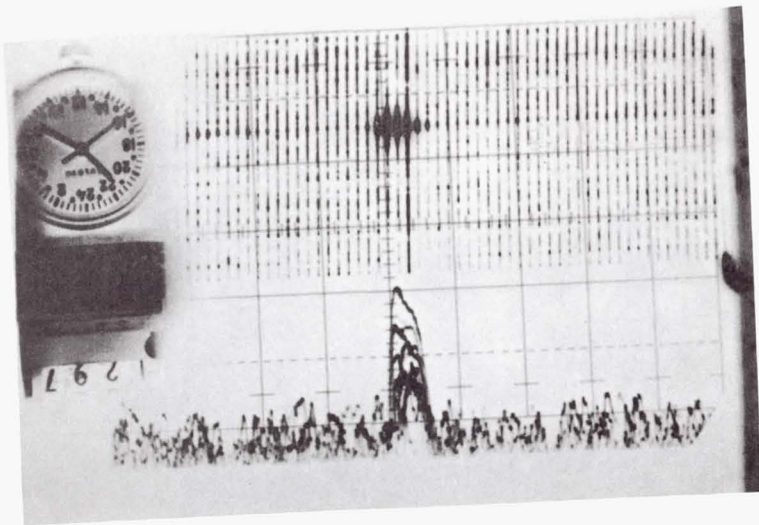20 µsec/DIV
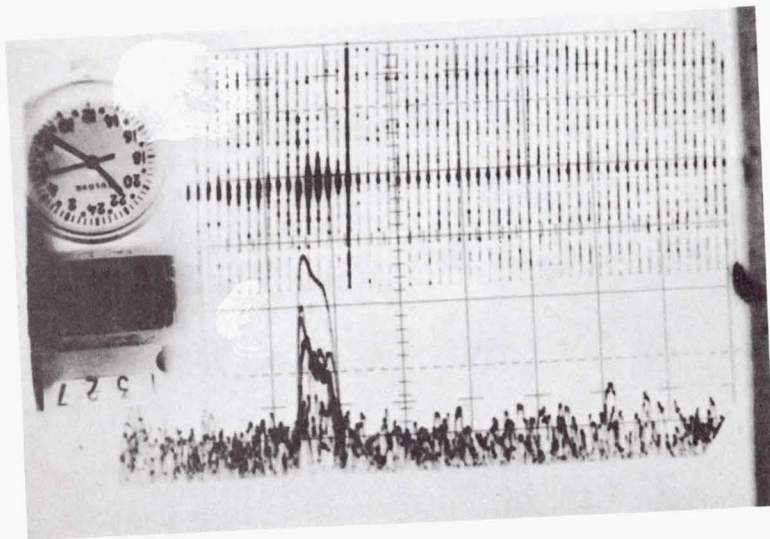
PHOTOS 1339--1368
10 µsec/DIV

(c)

EO-557

CAT FLIGHT 15 - JANUARY 12, 1973 - RUN 9 -- HgCdTe DETECTOR

Figure 9-3. Steep Descent at Edwards AFB (Sheet 1 of 3)
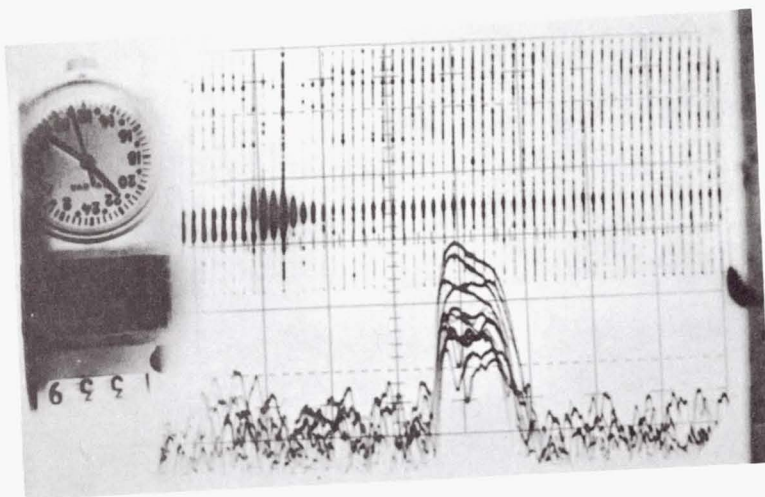
(d)

RVI: 2.64 MHz/DIV
      20 µsec/DIV

A-SCOPE 10 dB/DIV

(e)

PHOTOS 1233--1327
       20 µsec/DIV
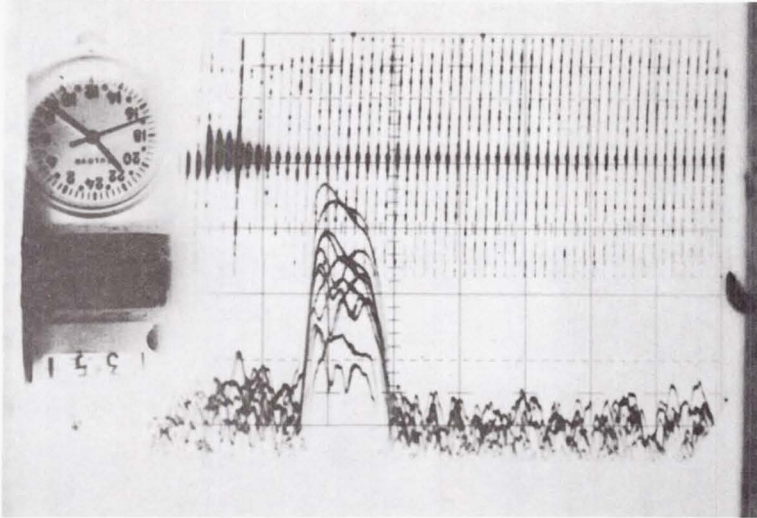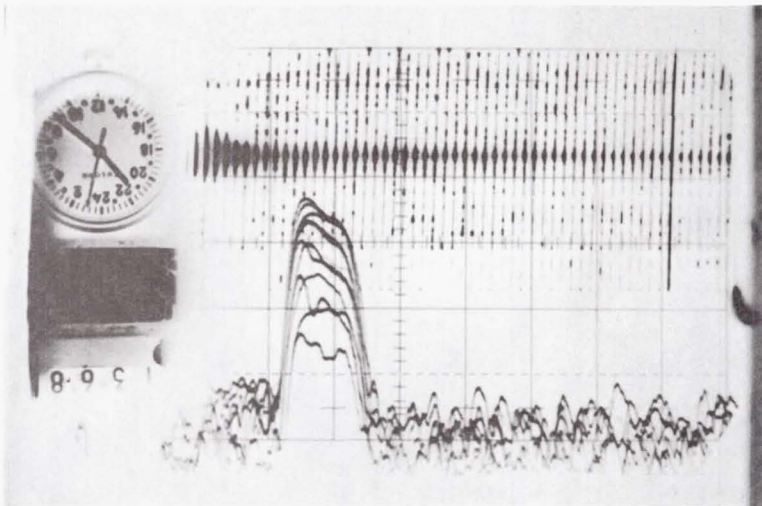
PHOTOS 1339--1368
       10 µsec/DIV

(f)

EO-558

CAT FLIGHT 15 - JANUARY 12, 1973 - RUN 9 -- HgCdTe DETECTOR

Figure 9-3. Steep Descent at Edwards AFB (Sheet 2 of 3)

(g)

RVI: 2.64 MHz/DIV
    20 μsec/DIV

A-SCOPE 10 dB/DIV
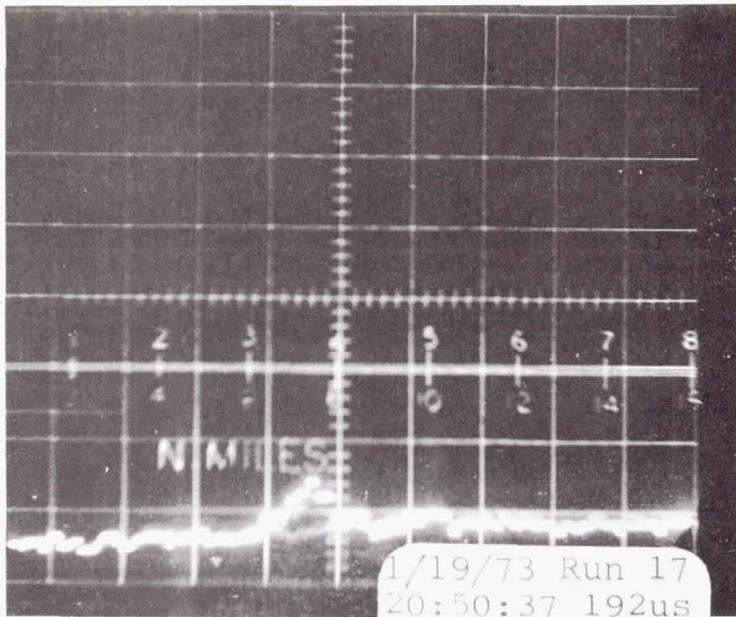
PHOTOS 1233--1327
        20 μsec/DIV

(h)

PHOTOS 1339--1368
        10 μsec/DIV

EO-559

CAT FLIGHT 15 - JANUARY 12, 1973 - RUN 9 -- HgCdTe DETECTOR

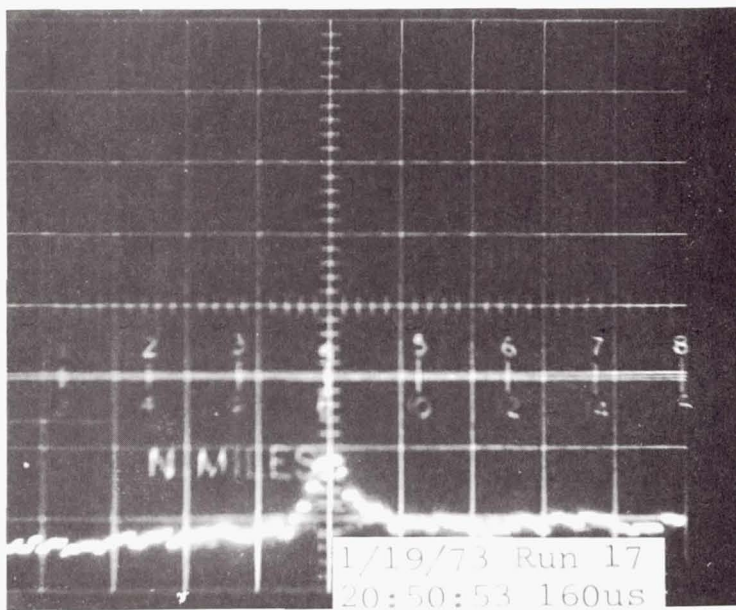Figure 9-3. Steep Descent at Edwards AFB (Sheet 3 of 3)

ADDAS OUTPUT DATA:

WIND SPEED: 33 kn (16.5 m/sec)
WIND DIRECTION: 299°
AIRCRAFT HEADING: 247°
AIRCRAFT DRIFT ANGLE:-5.4°

(a)

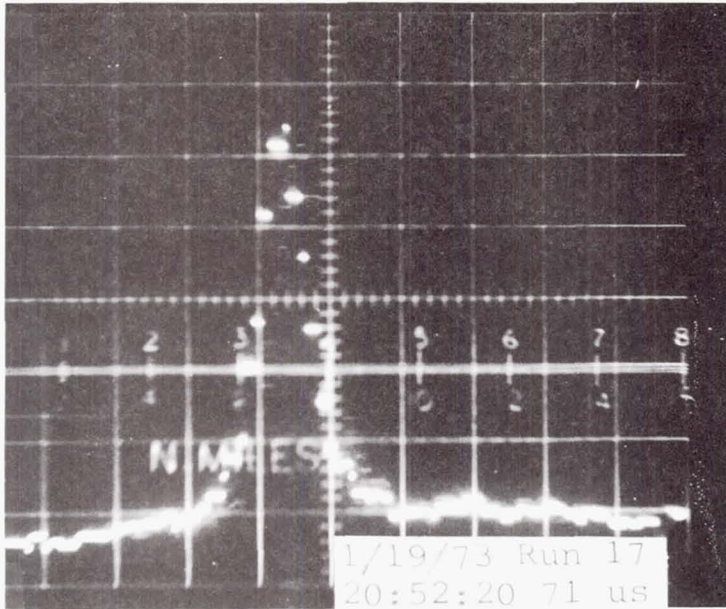IVI DISPLAY PHOTOS
RECONSTRUCTED FROM TAPE.
10 MHz FULL SCALE

IVI MANUALLY TRACKED
ON GROUND RETURN FROM
192 µsec TO 34 µsec
DURING DESCENT

(b)

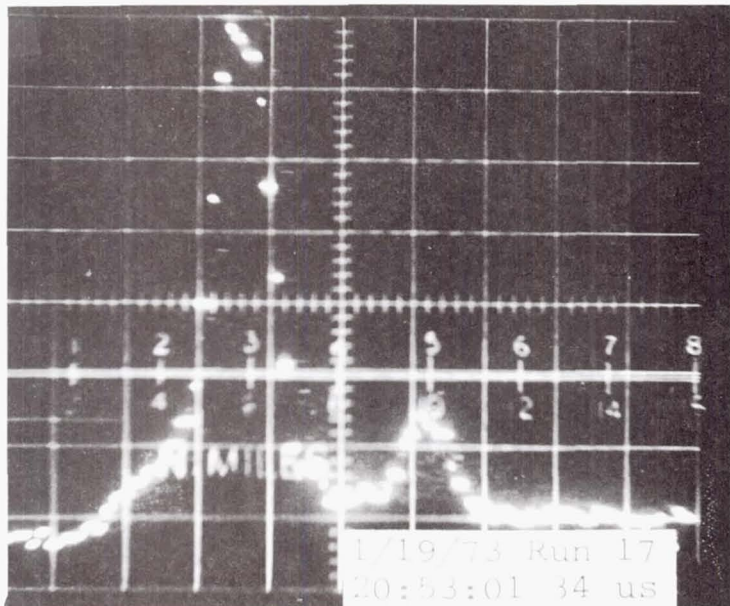EO-560

CAT FLIGHT 21 - JANUARY 19, 1973 - RUN 17

Figure 9-4. Descent at Edwards AFB (Sheet 1 of 2)

(c)

ALTITUDE: 1,500 FT. (457 METERS)
PITCH ANGLE 5.0° DOWN

(d)

SECONDARY RETURN ON
PHOTO 20:53:01 IS
GROUND WIND, CALCULATED
FROM ADDAS DATA AT 2.2 MHz
ABOVE GROUND RETURN

EO-561

CAT FLIGHT 21 - JANUARY 19, 1973 - RUN 17 (continued)

Figure 9-4. Descent At Edwards AFB (Sheet 2 of 2)
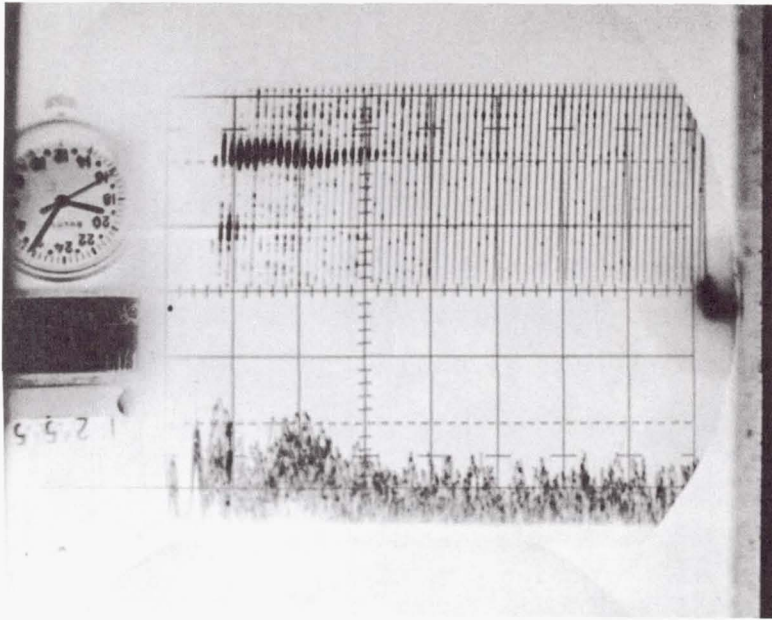
(a)

RUN 9

IMPERIAL VALLEY

DUST CLOUD AT 4,300 FT.
(1,311 METERS)

HORIZ. 2 NMI/DIV.
(3.71 KM/DIV.)

VERT. 10 dB/DIV A-SCOPE
2.64 MHz/DIV RVI
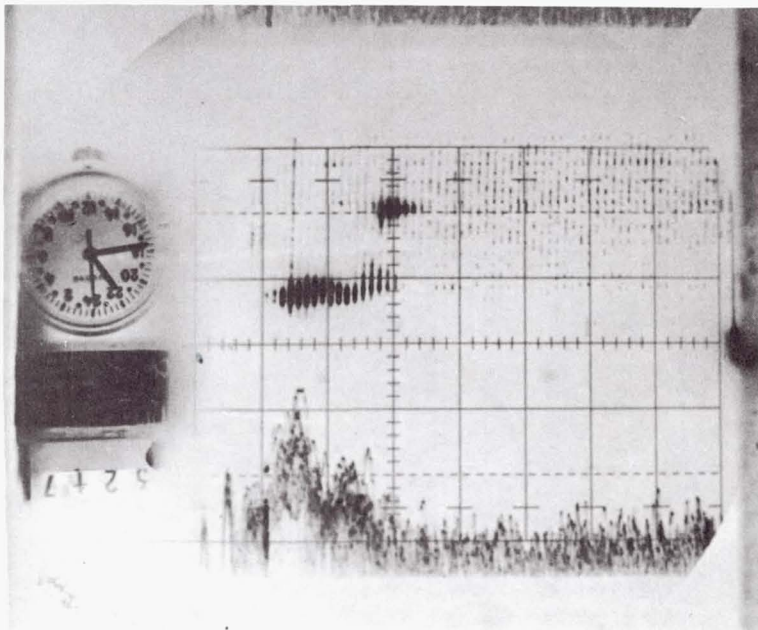
(b)

RUN 20

OWENS VALLEY

DUST CLOUD AND GROUND

CAT FLIGHT 21 -- JANUARY 19, 1973   EO-562

Figure 9-5. Dust Clouds and Ground Targets Returns in Imperial
and Owens Valleys (Sheet 1 of 2)

HORIZONTAL - 2 nmi/DIV (3.71 km/DIV)
VERTICAL - 10 dB/DIV A-SCOPE
2.64 MHz/DIV RVI
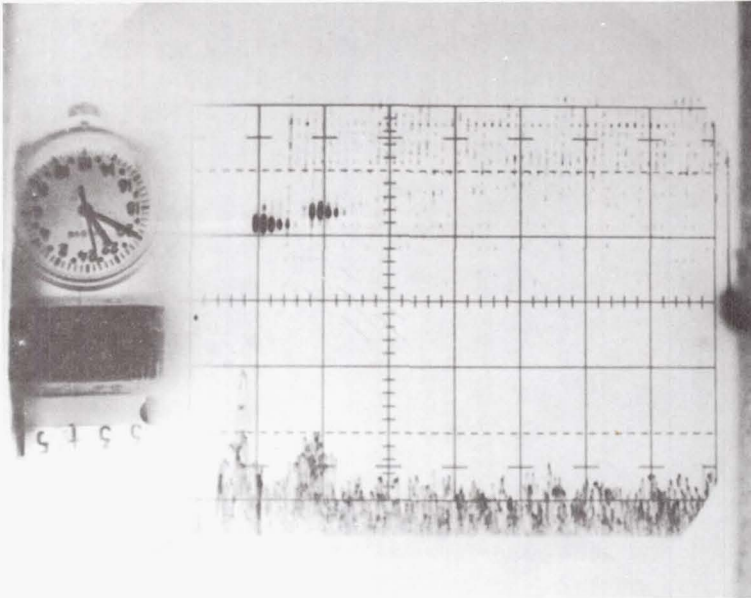
(c)

TWO DUST CLOUDS

(d)

RETURN FROM MOUNTAIN

EO-563

CAT FLIGHT 21 - JANUARY 19, 1973 - RUN 20 -- OWENS VALLEY

Figure 9-5. Dust Clouds and Ground Targets Returns in Imperial
and Owens Valleys (Sheet 2 of 2)

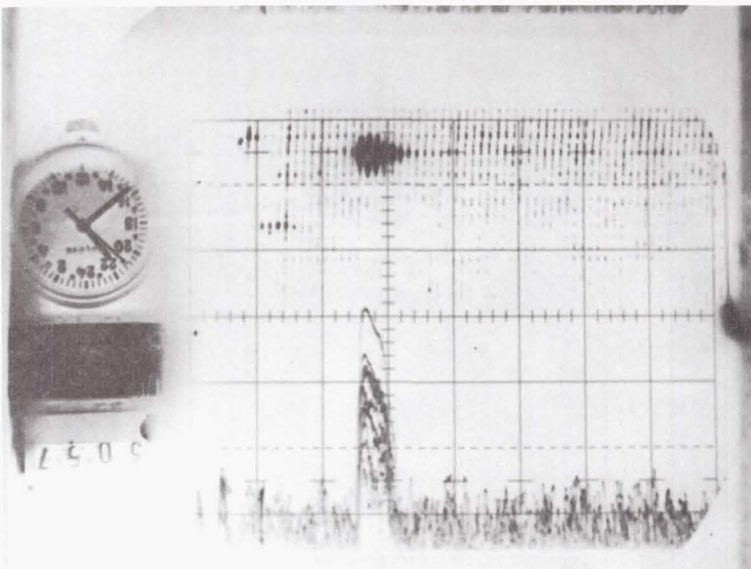A series of clear air returns during a climbout from the Imperial Valley is shown in Figure 9-6 (a) through (h). These IVI photos illustrate signals up to 21,800 feet (6,645 m) altitude. The wind was out of the West, at 280°, and the aircraft heading was approximately 310° from 14,300 feet (4,359 m) to 21,800 feet (6,645 m) altitude. The range gate on the IVI was set at 24 μsec for most of these photos.

Cumulus cloud returns from the Bishop area are shown in Figure 9-7 (a) through (e). The first RVI photo, 9-7 (a) shows three individual clouds at three different ranges and three different frequencies. The A-Scope was tuned on the middle cloud only. The four following photos, 9-7 (b) through (e), show very wide returns from cumulus clouds. The aircraft was maneuvering during this sequence.

9.3   SUMMARY OF 1972 TEST ANALYSIS

9.3.1   INTRODUCTION

The data from the flight tests of the CAT laser radar in August and September 1972 are analyzed in this section. In the first part, the backscatter returns from the ground are compared with theoretically expected values to evaluate the system performance. In the second part, the backscatter returns from the atmosphere are analyzed. The conclusions are presented at the end.

9.3.2   RETURNS FROM GROUND

9.3.2.1   Test Data

Signal-to-noise ratio measurements of ground returns at a nominal pitch angle of 10 degrees were made on runs 6, 7A and 7B of Flight 13 at Carson Sink, Nevada, and on runs 12 and 15 at Edwards. These data are presented in Tables 9-1 and 9-2, and are plotted in Figures 9-8 and 9-9. (Clouds appeared in the beam on some of the measurements at Carson Sink. Their returns were easily identified and rejected.

To compare with the theoretical curves, the atmospheric losses were determined and applied to the measured data. These losses, as calculated by C. Sonnenschein from the altitude, temperature and
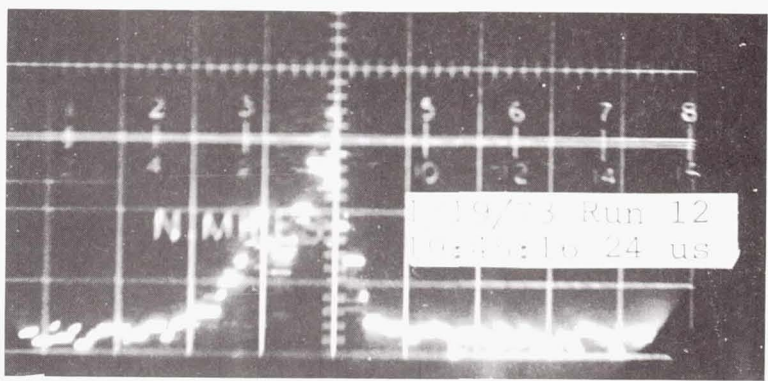
PRESSURE ALTITUDE	TRUE HEADING
(a)	
4,500 ft. (1,371 m)	109°
(b)	
6,250 ft. (1,905 m)	39°
(c)	
14,300 ft. (4,359 m)	304°
(d)	
17,900 ft. (5,456 m)	304°
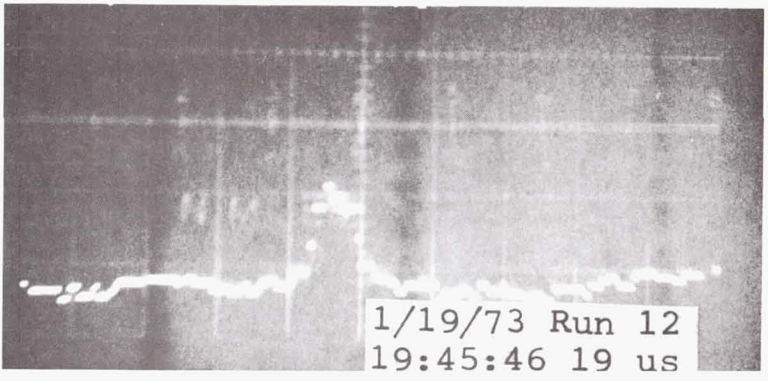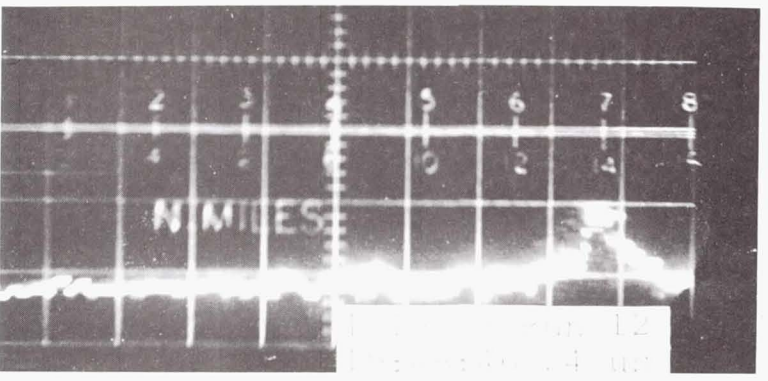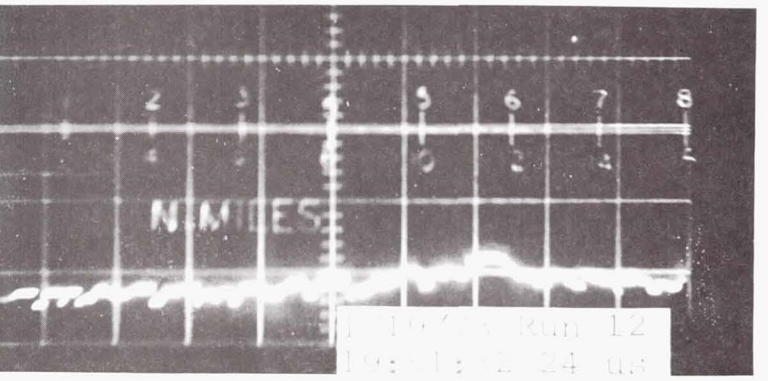
EO-564

Figure 9-6. Climb from Imperial Valley - Clear Air Returns (Sheet 1 of 2)
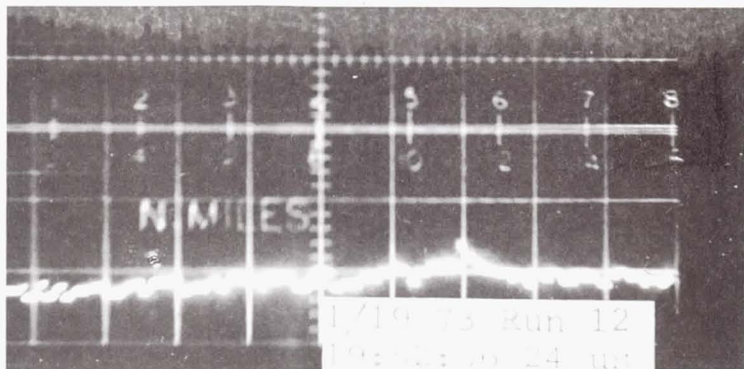
PRESSURE ALTITUDE	TRUE HEADING
(e)	
18,750 ft. (5,700 m)	304°
(f)	
19,800 ft. (5,700 m)	318°
(g)	
20,000 ft. (6,096 m)	318°
(h)	
21,800 ft. (6,645 m)	315°
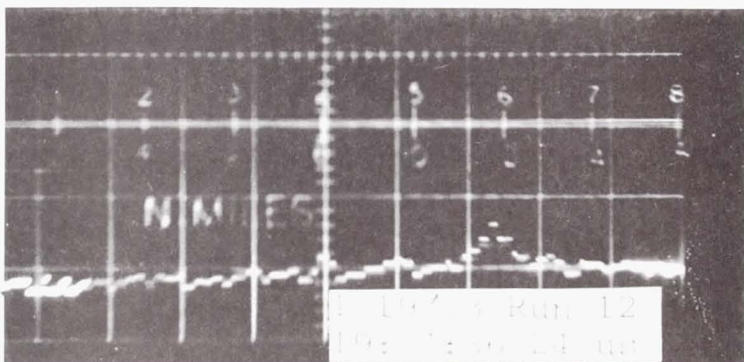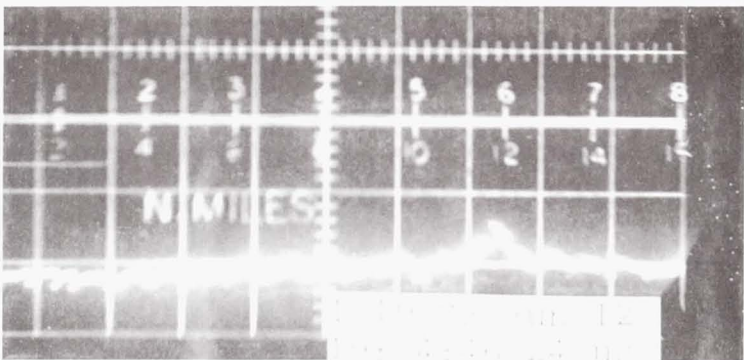
EO-565

Figure 9-6. Climb from Imperial Valley – Clear Air Returns
(Sheet 2 of 2)
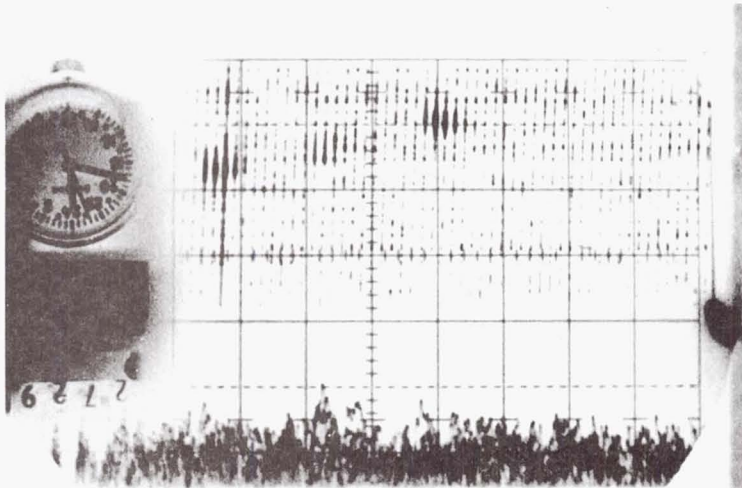
(a)

HORIZONTAL – 2 nmi/Div.
     (3.71 km/Div.)

VERTICAL – 10 $\frac{dB}{Div}$ A-SCOPE

     2.64 $\frac{MHz}{Div}$ RVI

#2729--THREE CLOUDS

#2835 to #2838--
WIDE SPECTRAL RETURNS

(b)
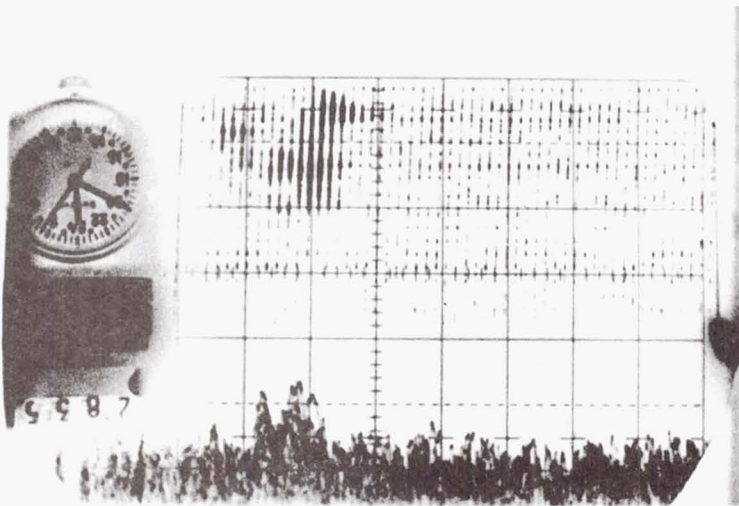
CAT FLIGHT B8 – January 15, 1973 – Run 12

Figure 9-7. Cumulus Clouds in Bishop Area – Altitude: 17,000 ft.
     (5.2 km) (Sheet 1 of 2)
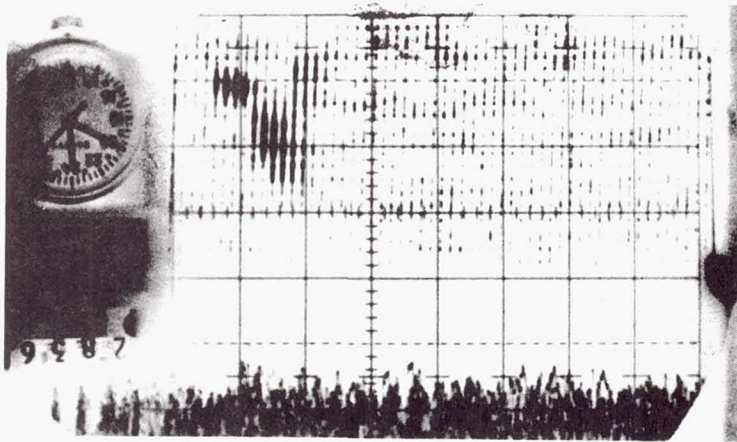
(c)

HORIZONTAL - 2 nmi/Div.
      (3.71 km/Div.)

VERTICAL - 10 $\frac{dB}{Div}$ A-SCOPE

      2.64 $\frac{MHz}{Div}$ RVI

#2729--THREE CLOUDS

(d)

#2835 to #2838--
WIDE SPECTRAL RETURNS
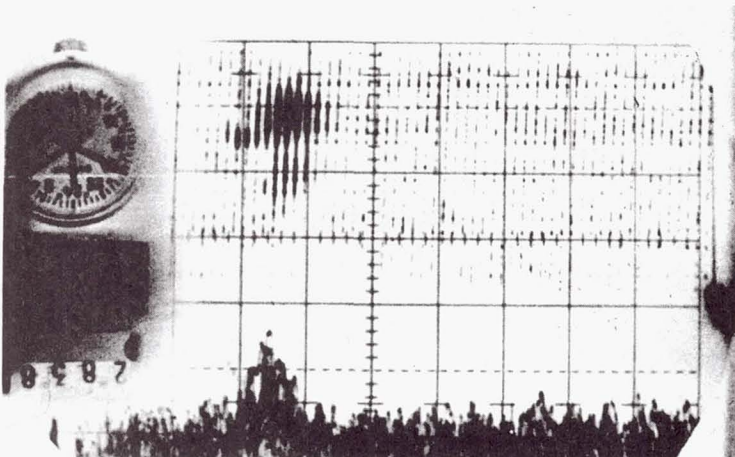
(e)

CAT FLIGHT B8 - January 15, 1973 - Run B8 - (continued)   EO-567

Figure 9-7.   Cumulus Clouds in Bishop Area - Altitude: 17,000 ft.
      (5.2 km) (Sheet 2 of 2)

TABLE 9-1.   CARSON SINK TEST DATA (FLIGHT 13)

Run	Slant Range to Ground	S/N
6	84×10^3 ft	3 dB
	60	6
	18	30
	12	35
7A	84×10^3	1
	48	10
	18	30
	15	33
7B	84×10^3	3
	72	5
	63.2	8
	48	9
	36	16
	12	34

To convert from feet to meters, multiply by .3048.

TABLE 9-2.   EDWARDS TEST DATA (FLIGHT 9)

| | PICTURE DATA | | INFLIGHT | |
Run	Slant Range	S/N(Typ.)	Slant Range	S/N
12	5.8 n. mi.	7 dB	6	7 dB
	5.6	6	4.8	12
	4.8	8	3.8	15
	4.0	11	3.3	20
	3.1	12	2.5	18
	2.5	16	2.0	24
	2.0	18		
	1.6	22		
15	5.5	6	5.5	6
	4.6	8	4.5	10
	3.5	12	3.5	12
	3.2	10	2.5	22
	2.2	20	1.5	25

To convert from nautical miles to kilometers, multiply by 1.853.

CARSON SINK, FLIGHT #13, RUNS 6, 7A and 7B, 9/6/72
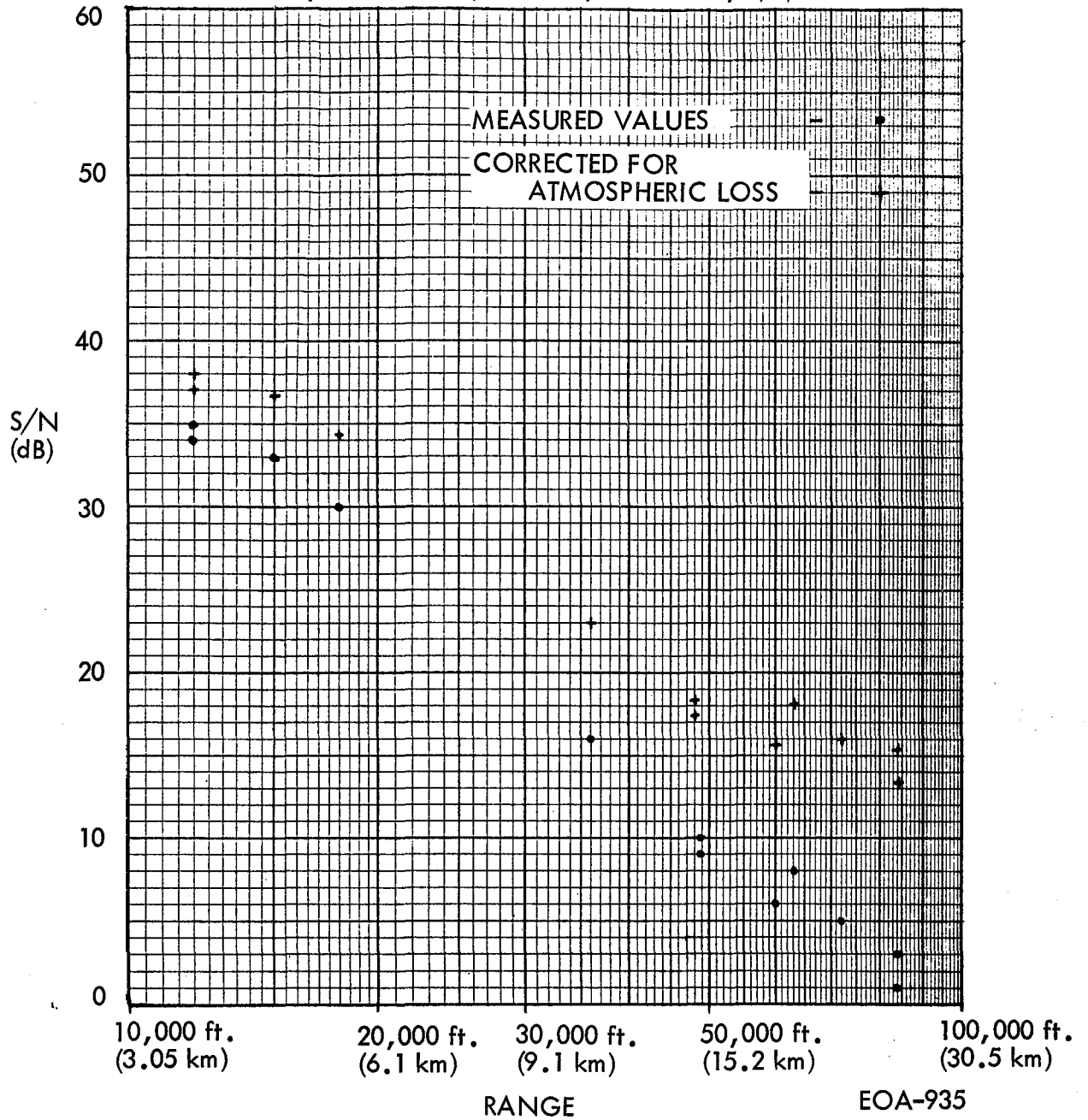
Figure 9-8.   Measured Signal-To-Noise Ratio of CAT
System Against Ground
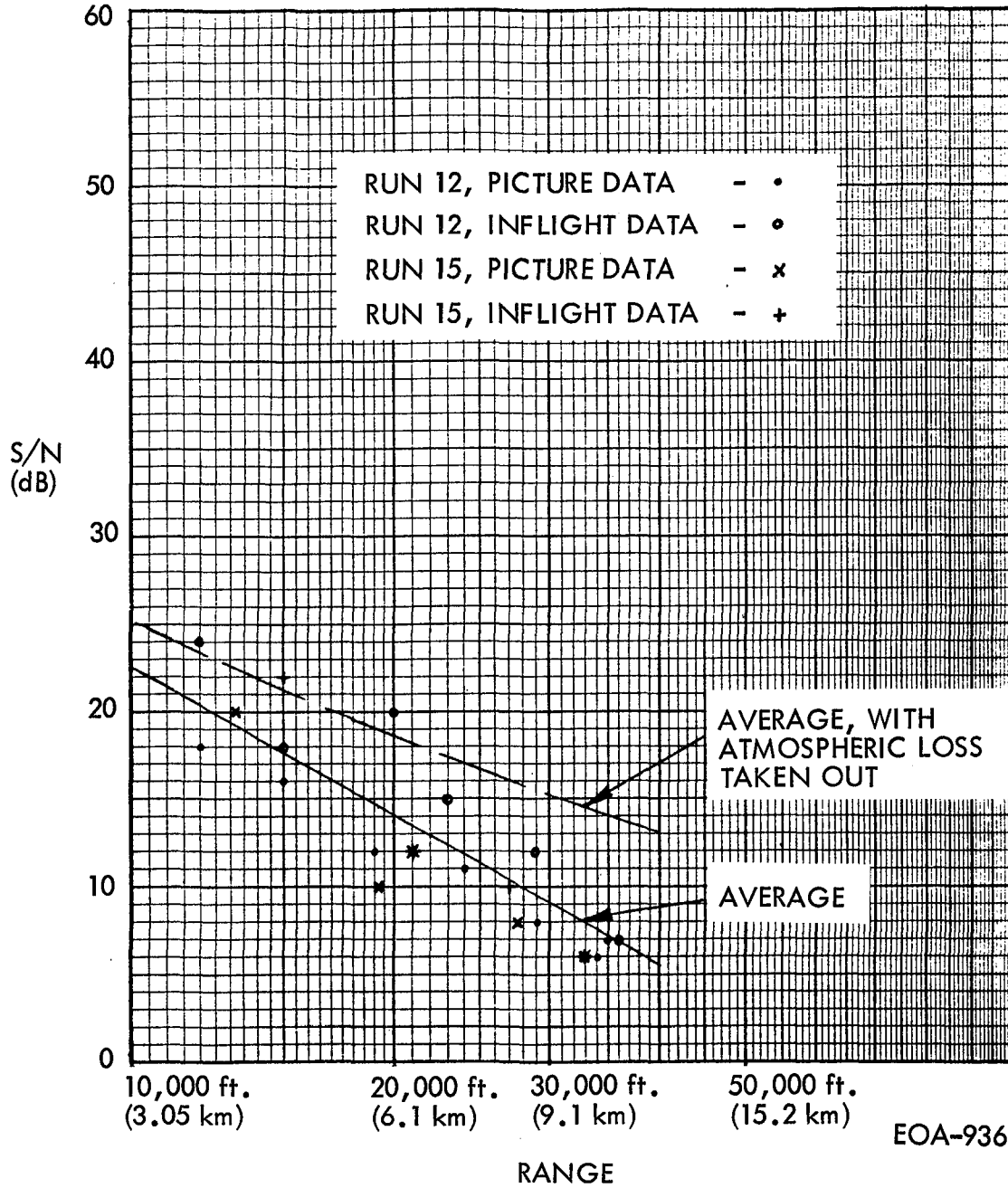
Figure 9-9.   Measured Signal-To-Noise Ratio of CAT
System Against Ground

relative humidity records at Carson Sink, are plotted in Figure 9-10.
The effects of the two major attenuators in the atmosphere at 10.6
microns - water vapor and carbon dioxide - were measured by McCoy,
Rensch and Long[3] and by Yin and Long.[6] The spread of the points from
the line in Figure 9-10 stems from the slight variation in pitch
angle during the runs. For the purposes of this analysis, these
variations can be ignored. The ground returns corrected for atmos-
pheric losses are plotted in Figure 9-8 as crosses and in Figure 9-9
as a dashed line.

In comparing the data at Carson Sink and Edwards, it is evident
that the signals at Carson Sink were much stronger and covered a
wider range. Therefore, the Carson Sink results were emphasized.

9.3.2.2   Theoretical Signal-to-Noise Ratio

Although both the beam and receiver were supposed to be focused
at infinity, there is some doubt as to whether they both were. Also,
the beam may not have filled the optical aperture, as sensitivity tests
involving the closing of the "clam shell" shutter seem to indicate.
Therefore, three possibilities were examined.

1. Both the beam and receiver field-of-view were focused at
    infinity.

2. Both the beam and receiver field-of-view were focused at
    some finite range R_f.

3. The beam was focused at infinity but the receiver field-
    of-view was focused at R_f.

Since the first case is a special variant of the second, the equation
will be derived for the second case. The additional degradation
of the third case will be computed as an extra loss factor. The
aperture effect was considered by varying the diameter.

The signal-to-noise ratio of a heterodyne receiver is:

$$\frac{S}{N} = \frac{\eta_d}{2\,h\nu\,B} \times P_s$$
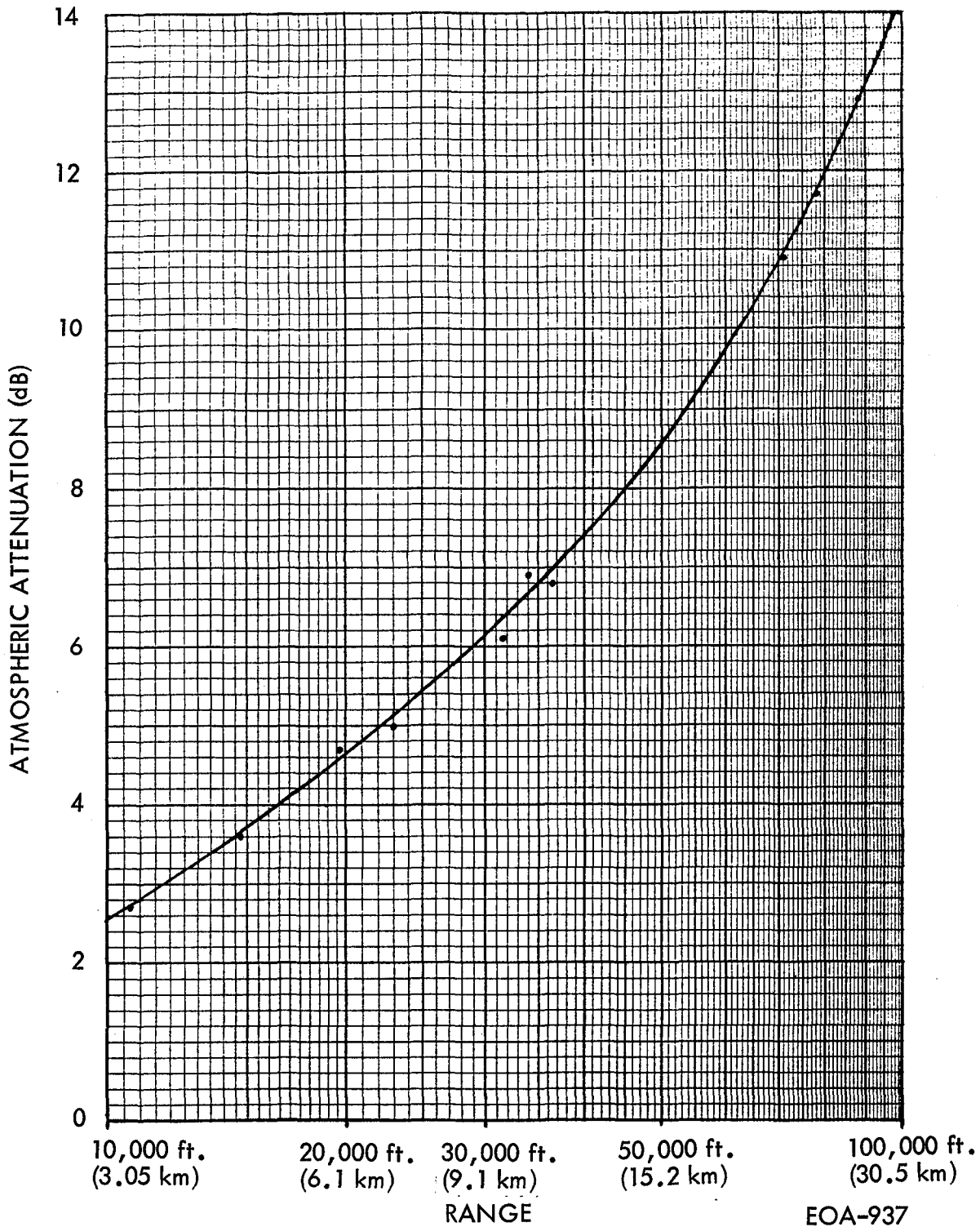
Figure 9-10. Round Trip Atmospheric Loss Based Upon Measured Values of Altitude, Pitch Angle, Temperature and Humidity

The effective signal power P_s of a focused system (Case 2) against the ground not at the point of focus is given by:[8]

$$P_s = P \times \frac{\sigma'}{4\pi} \times \frac{\pi d^2/4}{R^2 + (\pi d^2/4\lambda)^2 (1 - R/R_f)^2} \times \eta_s \eta_a$$

By combining the equations through P_s and substituting $E \approx P/B$, $A_r = (\pi/4)d^2$, and $\eta_a = 1$ (the atmospheric loss was taken out of the measured data), the SNR equation for Case 2 is derived:

$$(\frac{S}{N} \text{ no atm.} \approx \frac{E \sigma' \eta_d \eta_s d^2}{32 \, h\nu \left[R^2 + (\pi d^2/4\lambda)^2 (1 - R/R_f)^2\right]} \tag{1}$$

Here E is the laser pulse energy $= 5$ mjoules

   σ' is the target cross section factor $= 0.25$
     (Calculated below)

   d is the aperture diameter $= 1$ ft. (30 cm)

   η_d is the detector quantum efficiency $= 0.08$

   η_s is the system efficiency $= 0.2$

   $h\nu$ is the energy per photon $= 1.9 \times 10^{-20}$ joule

   R is the range to the ground

   R_f is the range of focus

   λ is the laser wavelength $= 10.6 \times 10^{-6}$ m

For Case 1 (beam and receiver focused at infinity), $R_f = \infty$ in the above equation. For the Edwards Test data the pulse energy was 3.1 millijoules. An aperture diameter of 6 in. (15.2 cm) was also tried.

The radar cross section σ' of a target filling the beam is defined as:

$$\frac{\sigma'}{4\pi} = \frac{\text{Reflected intensity}}{\text{Incident power}}$$

Laboratory measurements of the reflectivity of dirt samples from the test area by R. Seavey showed that this ratio is 0.02 ster^{-1} largely independent of viewing angle. Thus,

$$\sigma' = 4\pi \times 0.02 = 0.25 \text{ ster}^{-1}$$

By substitution into equation (1) the signal-to-noise ratio in the absence of an atmosphere is calculated for Cases 1 and 2. It is plotted in Figure 9-11 for ranges of focus of 10, 20, and 30 thousand ft. (3.05, 6.1 and 9.1 km) and infinity. The 6-in. (15.2 cm) aperture case for infinite focus is also plotted.

For Case 3 - beam focused at infinity and receiver focused at some finite range R_f - an additional loss factor must be included in equation (1). The loss factor is determined by the fraction of the beam within the receiver field-of-view. If the beam is smaller than the field-of-view and therefore wholly contained within it, there is no loss; but if the beam is larger, only the portion within the field-of-view is detected. The remainder is missed because it falls outside the LO beam in the receiver. Hence the SNR degradation is given by:

$$\frac{\text{Receiver FOV area}}{\text{Beam Area}} \quad \frac{d^2(1 - R/R_f)^2 + (\lambda R/d)^2}{d^2 + (\lambda R/d)^2}$$

$$\approx 1 + \frac{R}{R_f} \times \frac{R/R_f - 2}{1 + (\lambda R/d^2)^2} \quad \text{if } R < 2R_f$$

$$\approx 1 \quad \text{if } R \geq R_f \tag{2}$$

The equations are approximate because the field-of-view is not a sharply defined, uniform cone as assumed in the derivation.

The signal-to-noise ratio is plotted in Figure 9-12 as solid lines which are actually asymptotes. The dashed lines represent the SNR with both beam and receiver focused at R_f.

9.3.2.3 Comparison of Experimental and Theoretical Data

None of the theoretical models fit the data points without modification. All must be shifted downward by varying amounts, and then, only a few are reasonable fits. The better fits are plotted in Figure 9-13. The curves are identified as follows:
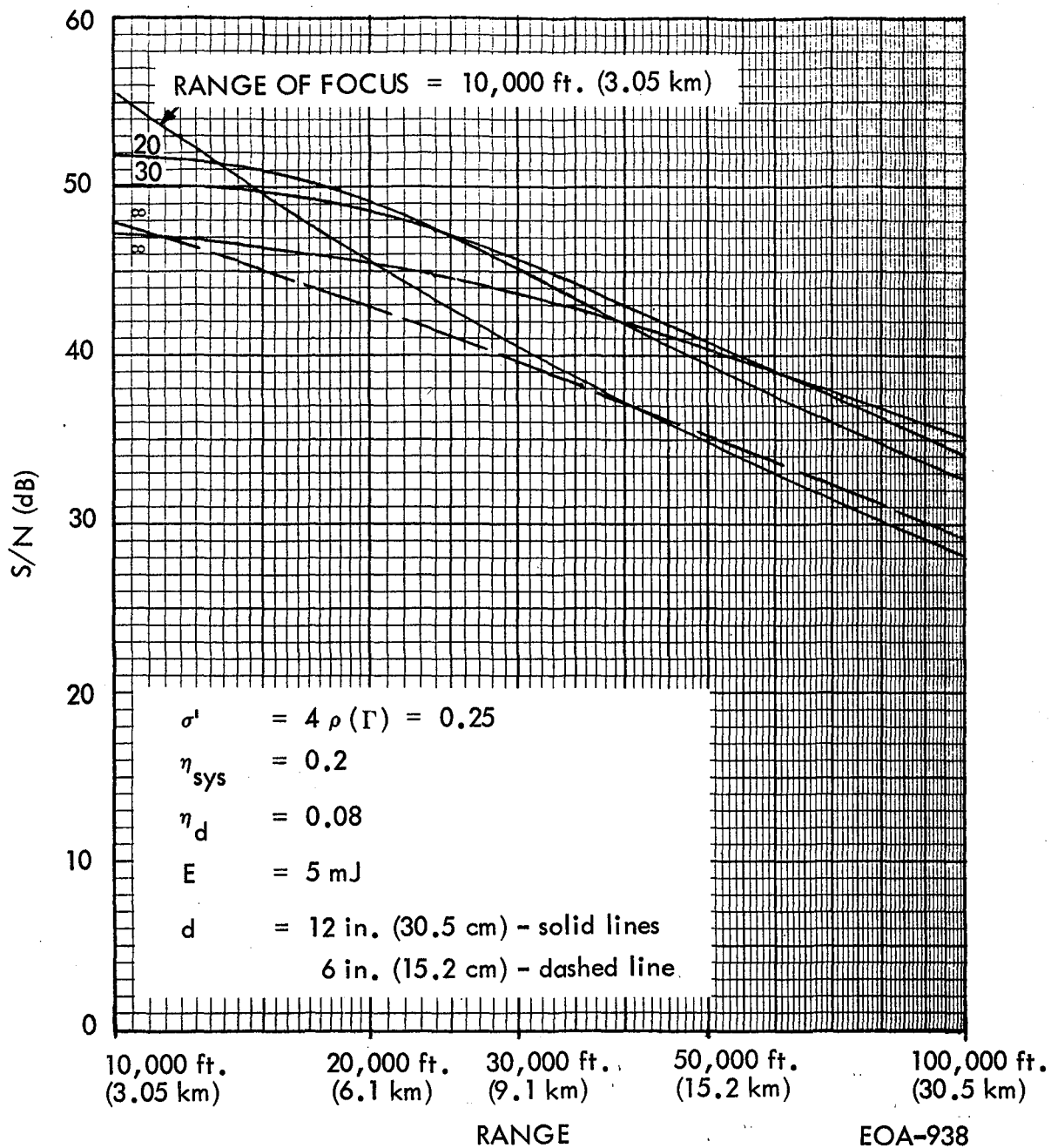
Figure 9-11.   Expected Signal-To-Noise Ratio of CAT System
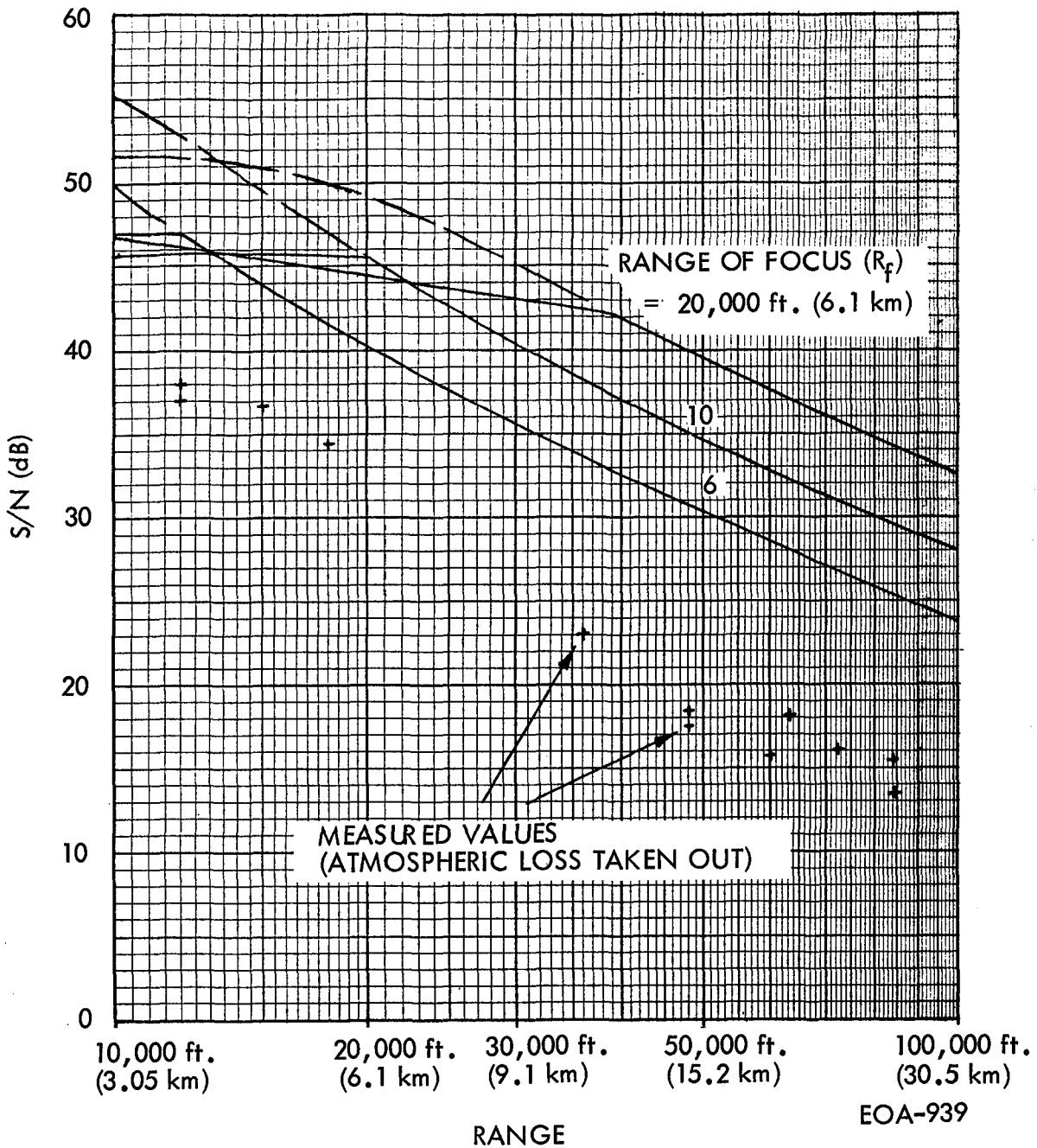Against Ground Assuming No Atmospheric
Attenuation

Figure 9-12. Expected SNR Against Ground with CAT Transmitter Focused At Infinity, Receiver Focused at R_f (No Atmospheric Attenuation)
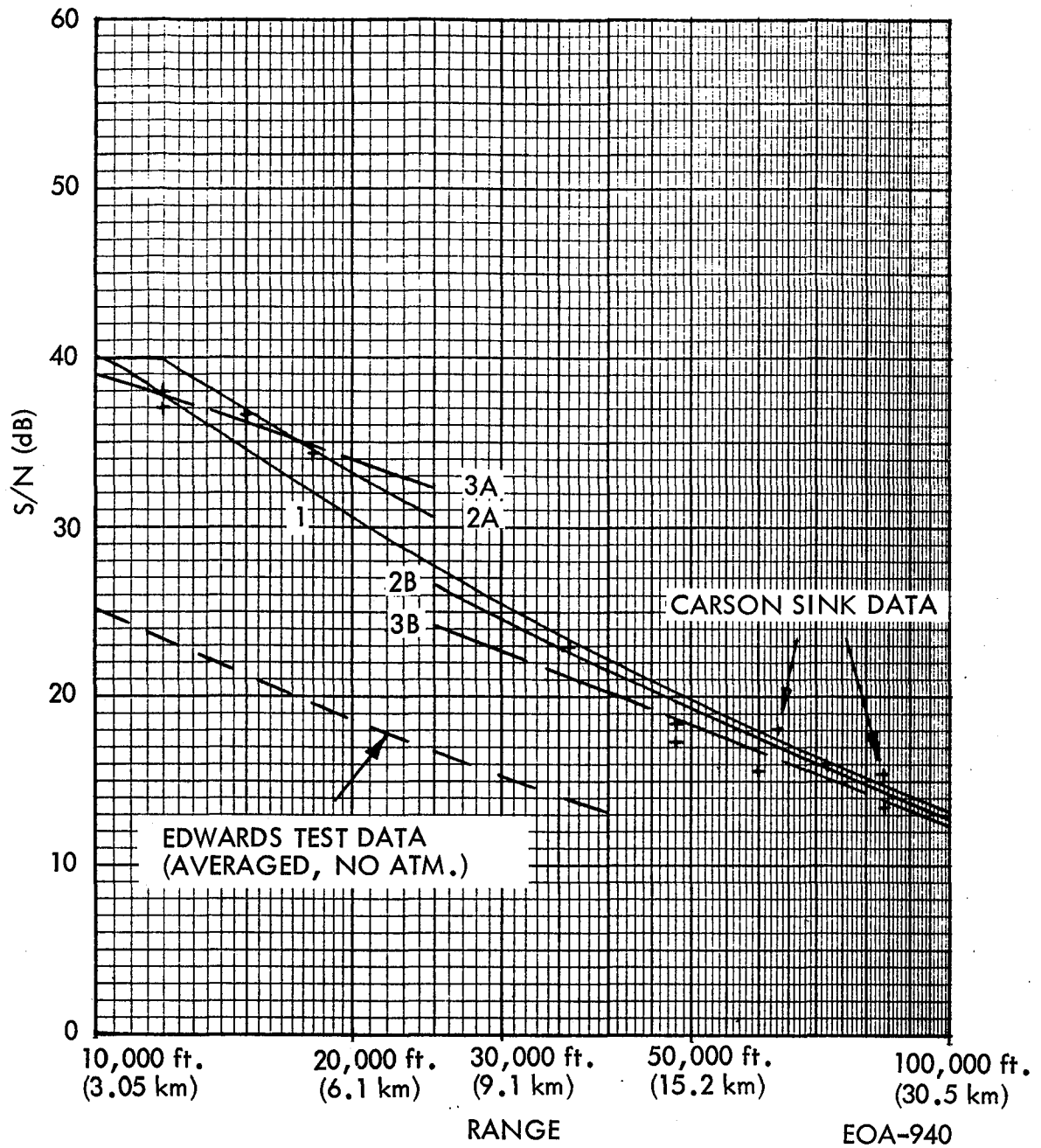
Figure 9-13. Fit of Theoretical Models to Carson
Sink Measurements. (See Text for
Identification of Curves.)

1. $R_{F_t} = R_{F_r}$ = 10,000 ft. (3.05 km),   d - 12 in. (30.5 cm),
    ΔL = 15 dB

2. $R_{F_t} = \infty$, R_{F_r} = 6,000 ft. (1.8 km), d - 12 in. (30.5 cm),
    ΔL_A = 7 dB, ΔL_B = 11 dB

3. $R_{F_t} = R_{F_r} = \infty$, d = 6 in. (15.2 cm), ΔL_A = 9 dB, ΔL_B = 15 dB

Here R_{F_t} and R_{F_r} are the range of focus of beam and receiver respectively, d is the aperture diameter and ΔL is the additional loss factor by which the curves are shifted downward. Note that curves 2 and 3 must be shifted down by different amounts depending upon altitude. The only way to account for the large difference in shift is to postulate a haze or very light cloud layer at 20,000 to 35,000 ft. (6.1 to 10.7 km) slant range; i.e., an altitude of 3,500 to 5,000 ft. (1.1 to 1.5 km) above ground. Although the atmospheric backscatter measurements did not detect a definite haze layer, clouds blocked the beam during parts of the Carson Sink flight, and variations in haze with altitude were clearly evident in the Edwards atmospheric data runs.

Each of the cases indicates a higher operational loss than the predicted 7 dB - anywhere from the extra 7 dB for curve 2 to the 15 dB for curve 1. Possible explanations are:

A. Ground may have lower reflectivity at 10 degrees incidence than what was measured in the lab with loose dirt

B. Turbulence in front of the aperture which reduces the effective area

C. Higher atmospheric attenuation than predicted all along the path.

The extra loss is probably due to some combination of these factors plus higher losses within the receiver under flight conditions.

9.3.3   RETURNS FROM AIR

Tests were run with the beam transmitted horizontally. The received signal was measured as a function of time, i.e., range. The object here is to find the optical model which yields the most constant value of the backscatter coefficient, β, calculated from the measured SNR data. Since the readings on each pulse are at

the same height, β should be a constant. The backscatter coefficient should also be as close to the expected value as possible. However, there is considerable uncertainty as to what this value should be at various altitudes.

9.3.3.1 Test Data

Measurements were made at barometric altitudes of 7,000 ft. (2.1 km), 7,400 ft. (2.3 km), 9,400 ft. (2.9 km), 11,450 ft. (3.5 km), 13,500 ft. (4.1 km), 16,000 ft. (4.9 km) and 17,000 ft. (5.2 km) at ranges out to 3 nautical miles (5.6 km). Since the data at 9,400 ft. (2.9 km) is the most complete, this altitude was selected. In any event, the variation of signal with range is similar at the other altitudes. The data points are plotted in Figure 9-14.

To compare with theory, the atmospheric attenuation was taken out of the measured values. Inspection of typical temperature and humidity readings at that altitude plus application of the Rensch, McCoy and Long[3] data show an attenuation coefficient at 10.6 microns of the order of 0.25 dB/km one way or 0.5 dB/km round trip. If this value is far off, it will show up in the plotted data and a correction can be made. The signal-to-noise ratio without the atmospheric attenuation is plotted in Figure 9-14 as the circled data points.

9.3.3.2 Comparison with Theory

As discussed earlier, there are various possible optical models. To repeat, (1) both the beam and receiver are focused at infinity, (2) both the beam and receiver are focused at some finite range R_F, or (3) the beam is focused at infinity but the receiver is focused at R_F. There is also some flexibility in the selection of the aperture diameter. The flight tests against the ground showed that some of these models fit the data points well, others very poorly. See Page 9-33 for a summary of the cases which gave the best fit in the hard target tests.

The signal-to-noise ratio of a focused system against a soft target is given by[1]:

$$\frac{S}{N} = \frac{\eta_d\ \eta_s\ \eta_a\ \lambda\ E\ \beta}{2\ h\nu}\ (\tan^{-1} X_2 - \tan^{-1} X_2)\ x\ F$$

×   MEASURED SNR FOR H = 13,500 ft. (4.1 km)

•   MEASURED SNR FOR H = 9,400 ft. (2.9 km)

+   MEASURED SNR FOR H = 7,400 ft. (2.3 km)

✝   MEASURED SNR FOR H = 7,000 ft. (2.1 km)

⊙   SNR AT H = 9,400 ft. CORRECTED FOR
     ATMOSPHERIC LOSS

S/N

1 nmi
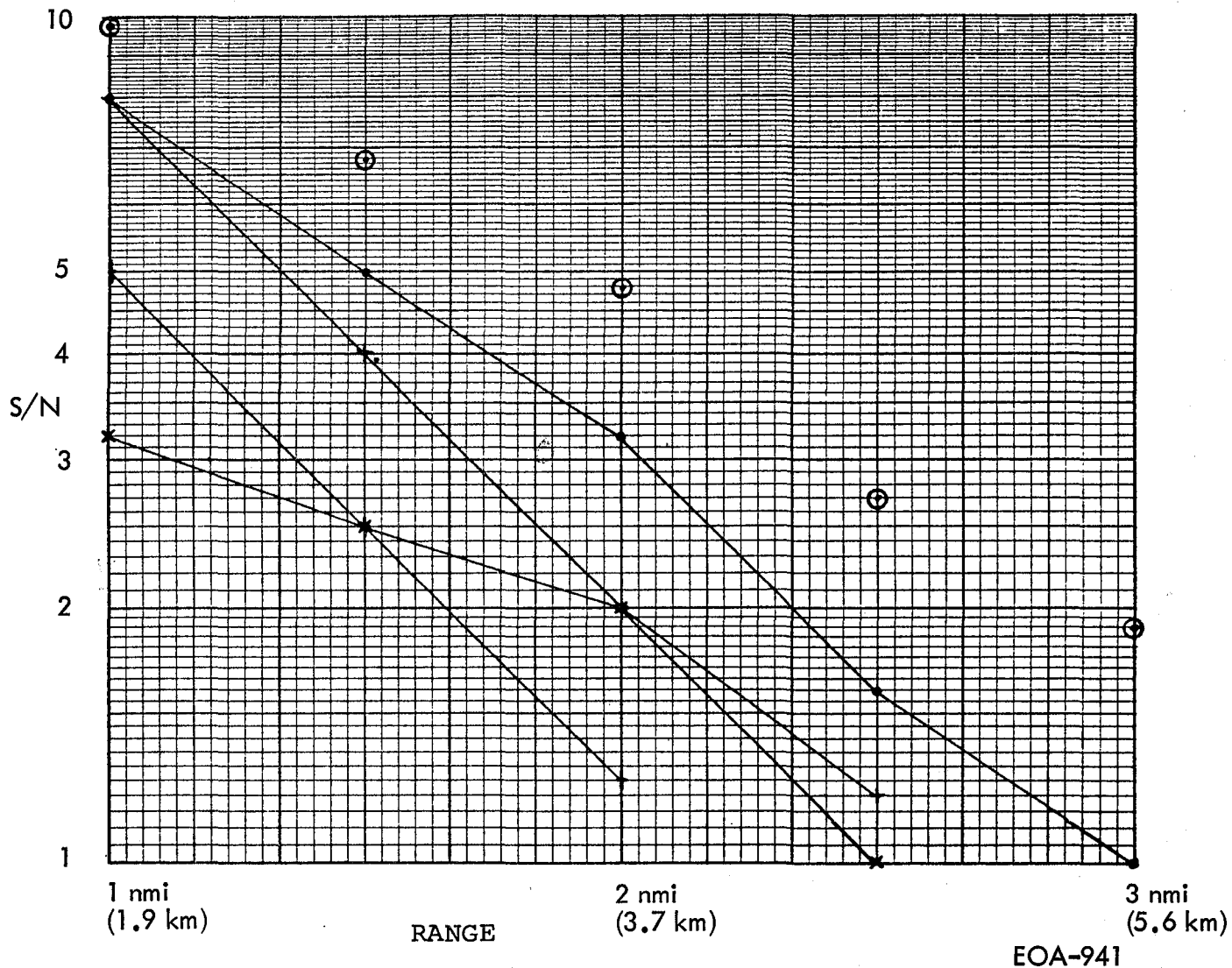(1.9 km)

2 nmi
(3.7 km)

3 nmi
(5.6 km)

RANGE

EOA-941

Figure 9-14.   Signal-To-Noise Ratio Measurements
Horizontally Against Air at Edwards

where

$$X_{1,2} = \frac{4\lambda}{\pi d^2} \; (R \mp \frac{c\tau}{4}) - \frac{\pi \, d^2}{4\lambda \, R_f} \left(1 - \frac{R \mp (c\tau/4)}{R_f} \right)$$

The equation for the loss factor from a difference in focusing, F, was given previously in equation (2). Since the atmospheric attenuation was taken out of the measured data, $\eta_a = 1$. Solving for the backscatter coefficient, β,

$$\beta = \frac{2 \, h\nu \, (S/N)}{\lambda E \; \eta_d \; \eta_s} \quad \frac{1}{(\tan^{-1} X_2 - \tan^{-1} X_1) \; F} \tag{3}$$

The parametric values are the same as for the hard target case except for:

E	= 3	mjoules
τ is the pulse length ($\approx 1/B$)	= 8	μsec
c is the velocity of light	= 3×10^8	m/sec

The backscatter coefficient was calculated with the SNR values at 9,400 ft. (2.9 km) for the various optical situations and plotted in Figure 9-15. The curves are identified as follows:

1. $R_{Ft} = \infty$, $R_{Fr} = 5,000$ ft. (1.5 km), d = 12 in. (30.5 cm)

2. $R_{Ft} = \infty$, $R_{Fr} = 10,000$ ft. (3.05 km), d - 12 in. (30.5 cm)

3. $R_{Ft} = 10$ Kft, $R_{Fr} = 10,000$ ft. (3.05 km), d = 12 in. (30.5 cm)

4A. $R_{Ft} = \infty$, $R_{Fr} = \infty$, d = 6 in. (15.2 cm)

4B. $R_{Ft} = \infty$, $R_{Fr} = 10,000$ ft. (3.05 km), d = 6 in. (15.2 cm)

where R_{Ft} is the range of focus of the transmitted beam, R_{Fr} is the range of focus of the receiver, and d the aperture diameter. The "best fit" curve is one which is most nearly horizontal and closest to the expected value of backscatter coefficient at that altitude. Very few measurements have been made of the backscatter coefficient at 10.6μ, and probably none near 10,000 ft. (3.05 km) altitude. One way of estimating the coeffficient is to extrapolate from the decrease in attenuation from the principal scattering agent, water vapor,
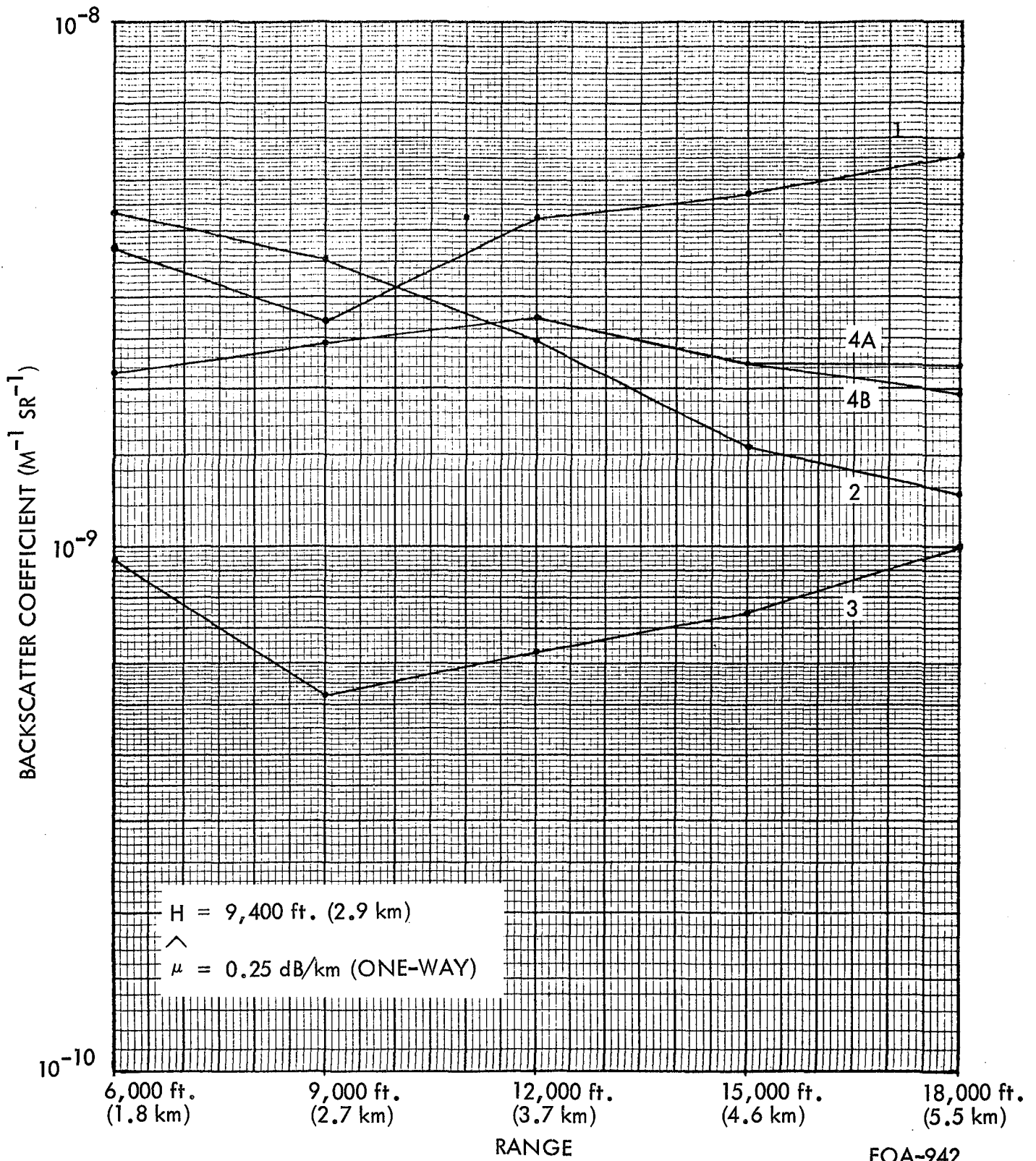
Figure 9-15.   Calculated Backscatter Coefficient From
Air Returns Along Horizontal Path

9-37

with altitude. This approach leads to an estimated reduction of an order of magnitude in the backscatter coefficient, from 10^{-7} per meter per steradian at sea level to roughly 10^{-8} m^{-1} sr^{-1} at 9,400 ft. (2.9 km).

Inspection of Figure **9-15** shows that all the curves except numbers 2 and 3 are reasonably horizontal and all are below the estimated value of backscatter coefficient. (The dip in curve 1 at 9,000 ft. (2.7 km) range is partially due to the approximation of eq. (2) for the loss factor from the difference in focusing. Curve 4A for a six-inch (15.2 cm) aperture size and both beam and receiver focuses at infinity is the most horizontal. However, it is still roughly 6 dB below the estimated backscatter coefficient. Thus, the most probable models based upon the soft target results are:

1. Both the beam and receiver are focused at infinity but the effective aperture diameter is only 6 inches (15.2 cm) and the system losses are roughly 6 dB higher than predicted (with $\beta = 10^{-8}$ m^{-1} sr^{-1})

2. The beam is focused at infinity but the receiver is focused at 5,000 ft. (1.5 km) (the curves at 4,000 and 6,000 ft. (1.2 and 1.8 km) are significantly different and less horizontal) with a 12-inch (30.5 cm) aperture and the system losses are roughl 4 dB higher than predicted with ($\beta = 10^{-8}$ m^{-1} sr^{-1}).

A third, less likely possibility is that both transmitter and receiver were focused at 10,000 ft. (3.05 km) with losses 12 dB higher than predicted (with $\beta = 10^{-8}$ m^{-1} sr^{-1}).

9.3.4   CONCLUSION

The analysis of both the hard and soft target results shows that one of the following optical models of the CAT system applies:

1. $R_{Ft} = \infty$, $R_{Fr} = 5,000$ ft. (1.5 km), $d = 12$ in. (30.5 cm)

2. $R_{Ft} = R_{Fr} = 10,000$ ft. (3.05 km), $d - 12$ in. (30.5 cm)

3. $R_{Ft} = R_{Fr} = \infty$, $d = 6$ in. (15.2 cm)

where R_{Ft} and R_{Fr} are the ranges of focus of transmitter and receiver and d is the aperture diameter. The required extra system loss to fit the above models to the data varies from 7 dB for (1) to 15 dB for (2). The original loss was 7 dB. A summary of how the three models fit the data runs is given in Table 9-3.

Of the three, the most probable model appears to be the third one, provided the existence of a haze layer is possible. It is conceivable that the effective aperture size on transmission and reception was only 6 in. (15.2 cm) even though the physical size was 12 in. (30.5 cm) because the laser output is somewhat Gaussian in intensity distribution. Whichever model does apply, there is little doubt that the losses were roughly an order of magnitude higher than expected. In other words, the total loss is closer to 16 dB than the 7 dB figure originally assumed. Whether these losses are due to sources within the laser system or are external has yet to be determined. Possible external sources are (1) lower ground reflectivity than 0.02 per steradian, (2) turbulence in front of the aperture, and (3) higher attenuation along the path.

There is a good correlation between the test against the ground and the atmosphere which tends to indicate the test data are consistent and the laser system operated at the same setting for both tests. Also, a backscatter coefficient of 2×10^{-8} per meter per steradian is indicated at the 9,400 ft. (2.9 km) altitude, assuming the reflectivity of the ground was 0.02 per steradian in the ground tests. The losses then match as indicated in Table 9-3.

Table 9-3. Comparison of Theoretical Models with Experimental Data

MODEL	GROUND TEST	ATMOSPHERIC TEST
1. T focused at ∞, R focused at 5,000 ft. (1.5 km), d = 12 in. (30.5 cm)	Fits Carson Sink data if: a) Losses are 7 dB higher than predicted b) A haze layer between 3,500 and 5,000 ft. (1.07 and 1.5 km) adds 4 dB more loss	Reasonable fit if system losses are 7 dB higher than predicted with $\beta = 2 \times 10^{-8}$ m^{-1} sr^{-1}
2. T & R focused at 10,000 ft. (3.05 km), d = 12 in. (30.5 cm)	Fits Carson Sink data well if losses are 15 dB higher than predicted	Fair fit if losses are 15 dB higher than predicted with $\beta = 2 \times 10^{-8}$ m^{-1} sr^{-1}
3. T & R focused at ∞, d = 6 in. (15.2 cm)	Fits Carson Sink data if: a) Losses are 9 dB higher than predicted b) A haze layer between 3,500 and 5,000 ft. (1.07 and 1.5 km) adds 6 dB more loss	Best fit to atmospheric data if losses are 9 dB higher than predicted with $\beta = 2 \times 10^{-8}$ m^{-1} sr^{-1}

9.4 SUMMARY OF 1973 FLIGHT TEST ANALYSIS (see Appendix F)

9.4.1 INTRODUCTION

The January 1973 "B" series of flight tests consisted of eight flights in California from January 4 through 19. The tests from these flights fall basically into four groups:

1. Dives at Edwards AFB against a uniform dry lake to check out and calibrate the laser equipment.

2. Measurements of backscatter returns from air at various altitudes.

3. Turbulent cloud tests to evaluate the laser returns from turbulence.

4. Measurements from miscellaneous targets including a mountain, the ground prior to landing, and cumulus, dust and cirrus clouds.

Data from each of these groups were analyzed in detail, and the results presented in Appendix F. The main conclusions are given here.

The data are in the following forms:

a. Sequence camera photographs of the A-scope and Range/Velocity Indicator (RVI). The photographs are spaced at 1.2 second intervals. Each exposure lasts 0.1 second and thus contains the returns from approximately 14 pulses, and the RVI plots frequency versus range for the integrated output of 50 pulses.

b. Intensity/Velocity Indicator. The output from this display is recorded on tape. The IVI plots intensity versus frequency at a selected range for the integrated output of 50 pulses.

c. Polaroid photos of the A-scope taken during flight and in-flight notes of signal-to-noise ratio.

d. Voice recordings. The conversations during flight were recorded on tape.

e. Flight data printouts. The ground and air velocities, wind speed and direction, pitch and roll angle, altitude, heading, latitude and longitude, temperature, dew frost point and acceleration were recorded at ten and one second intervals.

The data analysis was concerned with the sequence camera output only, because this was largely sufficient to describe the system performance. There were two exceptions: (1) the flight data printouts and (2) the IVI data were included in the analysis of the cloud turbulence tests.

9.4.2   RETURNS FROM GROUND AT EDWARDS AFB

The purpose of the flight tests at Edwards AFB was to check out and calibrate the CAT laser system. The aircraft engaged in steep descents against a uniform target, Rogers Dry Lake, with the laser operating continuously. The resulting measurements of signal-to-noise ratio was compared with various theoretical models of the laser system for the calibration. To calibrate the target, a sample of the dry lake bed was taken back to the lab and reflectivity measurements were made at the same angle of viewing.

The conclusions of the Edwards tests are:

1. The CAT laser system worked well, providing consistent results with signal-to-noise ratios as high as 42 dB.

2. The measured signal-to-noise ratios followed roughly the same slope as the 1972 test returns but were 17 dB higher. The improvement was due to a higher laser output and the substitution of the HgCdTe detector.

3. The wide variations in signal level from pulse to pulse, at times exceeding 30 dB, are caused primarily by atmospheric scintillation. The other sources - target scintillation, frequency tuning of the receiver and laser instability - have smaller effects.

4. There was little improvement in signal-to-noise ratio by pulse integration. The variation in signal level from atmospheric scinitillation was so great that the SNR for an integrated series of pulses was hardly better than the peak single-pulse SNR.

The measured data were compared with the theoretical model in Figure 9-16. Good data were recorded on three dives during the flight test series: (a) Flight B2, Run 7; (b) Flight B2, Run 9; and (c) Flight B8, Run 18. The signal-to-noise ratios from these dives are plotted on the graph and are seen to fall into a smooth narrow channel and correlated well with each other. The theoretical model of best fit is drawn as the upper dashed line.

9.4.3 AIR BACKSCATTER RETURNS

The eventual target of the Clear Air Turbulence laser radar is clear air. Therefore, the returns from this target are of interest.

Returns from air were observed throughout the test series, at altitudes as high as 22,000 ft. (6706 m) and at ranges as far as 6 miles (9.65 km). However, the sequence camera was not operated all the time; in fact, it was on only during 20 percent of the good data flights on the average, and much of that was for the dives at Edwards or the Owens Valley runs. Therefore, the sequence camera seldom recorded data at the higher altitudes where some clear air returns were observed on the Intensity/Velocity Indicator (IVI). Hence the data analysis was confined to the lower altitude returns, i.e., below 10,000 ft. (3,048 m).

The conclusions of the analysis are:

1. Based upon the system loss of 15 dB determined from the Edwards data, the backscatter coefficient β at five altitudes between 2,000 and 10,000 ft. (610 and 3048 m) varied from 0.7 to 7 x 10^{-9} per meter per ster. These values are roughly an order of magnitude less than the coefficients observed in the 1972 test series, probably due to the difference in air between summer and winter.
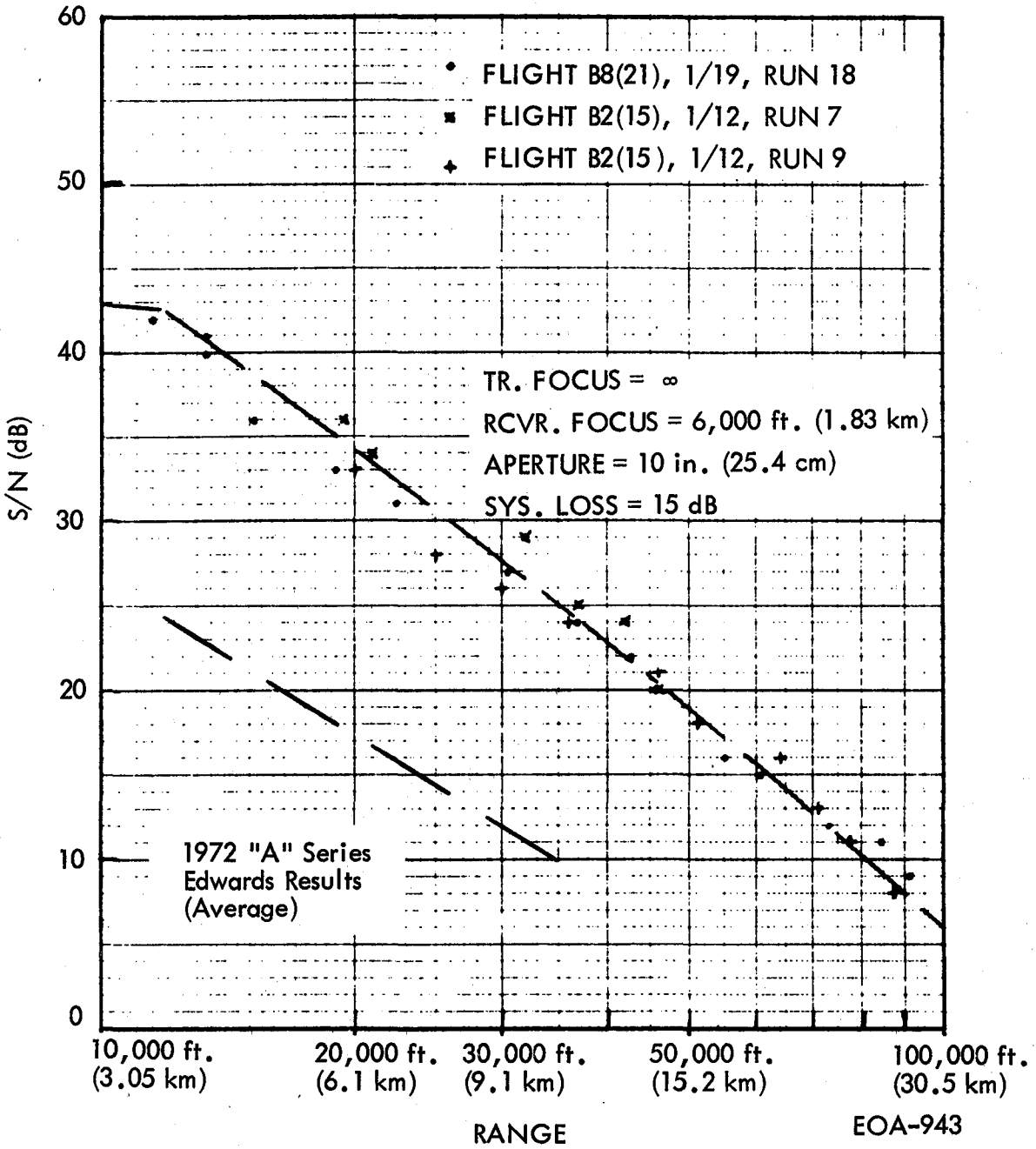
Figure 9-16. Signal-to-Noise Ratio Measurements and Calculated Values for the Dives at Edwards

2. The signal amplitude fluctuated wildly with range on indivi-
    dual pulses, although the envelope remained reasonably con-
    stant from pulse to pulse. Numerous causes were postulated.
    The primary one appears to be target scintillation.

9.4.4   TURBULENT CLOUD TESTS

During the 1973 flight test program the aircraft flew into
regions of severe air turbulence in order to evaluate the CAT laser
performance against turbulence. The flights were conducted over the
Owens Valley in California through cumulus clouds which were fed by
high winds from adjacent mountain ranges. Clouds were detected on
37 occasions. The laser operated continuously during these flights
even though the aircraftt encountered forces as great as 1.25 G above
normal.

The high turbulences were clearly shown on the laser radar
displays well before they were reached. They appear as wide darkened
returns on the Range/Velocity Indicator (RVI).

A study of the cloud returns indicates that:

- As many as three well-separated clouds were detected
  simultaneously by the laser radar (see Figure 9-9a).

- Doppler widths were as large as 5.5 MHz, showing a
  wind velocity spread of 60 mph (27 m/sec) in the space of
  a mile (see Figure 9-9b).

- Clouds were detected at ranges out to 9 nmi (16.7 km).

- Signal-to-noise ratios exceeded 20 dB.

- The extent of laser beam penetration into a cloud was
  as much as 3 nmi (5.6 km).

One conclusion from these observations is that 10.6 micron radiation
pentrates certain types of cumulus clouds well. A visual check
showed the clouds to be opaque to visible radiation. In spite of
the good penetration, the backscatter return was still high - in one

instance when two clouds were detected simultaneously, the signal-to-noise ratio was 13 dB from each one.

9.4.5   DATA EVALUATION

This study demonstrated that the CAT system is a consistent and reliable system, but that improvement is needed to detect CAT at high altitudes.   The measurements of system sensitivity, and the areas and components which could lead to realizing the required improvement are discussed in Section 8 and Appendix G.

REFERENCES

1. W. T. Boord, Yoh-Han Pao, F. W. Phelps, P. C. Claspy, "Far-Infrared Radiation Isolator," IEEE J. Quantum Electronics, Vol. QE-10, p. 273, Feb. 1974.

2. W. E. Webb, "Near-Field Antenna Patterns of Obstructed Cassegrainian Telescopes," 2nd Interim Report, NASA Contract NAS8-25562, p. 14.

3. J. McCoy, D. Rensch and R. Long, App. Op., Vol. 8, No. 7, 7/69, pp. 1471-8.

4. M. Shumate, R. Menzies, J. Margolis and L. Rosengren, App. Op., Vol. 15, No. 10, 10/76, pp. 2480-8.

5. S. S. R. Murty, "Atmospheric Transmission of CO_2 Laser Radiation with Application to Laser Doppler System," NASA Tech. Memo TM X-64987, 11/75.

6. P. Yin and R. Long, App. Op., Vol. 7, No. 8, 8/68, pp. 1551-3.

7. R. McClatchey and J. Selby, AFCRL-72-0611, Envir. Res. Paper #419.

8. C. Sonnenschein and F. Horrigan, App. Op., Vol. 10, No. 7, July 1971, pp. 1600-4.